

Generalised Kerr Microcomb Physics in Synchronously Driven Systems

Présentée le 21 juillet 2023

Faculté des sciences et techniques de l'ingénieur
Laboratoire de photonique et mesures quantiques (STI/SB)
Programme doctoral en photonique

pour l'obtention du grade de Docteur ès Sciences

par

Miles Henry ANDERSON

Acceptée sur proposition du jury

Prof. L. Thévenaz, président du jury
Prof. T. Kippenberg, directeur de thèse
Prof. A. Pasquazi, rapporteuse
Prof. V. Torres-Company, rapporteur
Prof. C. Sophie Brès, rapporteuse

Everything in the world is exactly the same
— Kanye West

Acknowledgements

Firstly I must thank most sincerely my supervisory Professor Tobias Kippenberg, who never failed to give me endless support, *enthusiasm*, and *patience* towards my wildest theories. A very, very special thank you goes towards the group administration Kathleen Vionnet and Antonella Ragnelli who also give me unconditional support, advice and encouragement during all of my organisational adventures and misadventures. To my early academic mentors Erwan Lucas, Maxim Karpov, and Hairun Guo who taught me almost everything I needed to succeed in doing anything. Likewise towards my later senpais and overseers Romain Bouchand, Wenle Weng, Grigory Lihachev, Johann Riemensberger, Rui Ning Wang, Michael Geiselmann, John Jost, Yang Liu, and most of all: Alexey Tikan. Without his aid, I would have gone nowhere very slowly in the final years, particularly since the pandemic. And, for teaching me truly so much of what has underpinned the science of this work, I want to thank again my old professors from Auckland: Stuart, Stephane, and Miro.

I give hearty acknowledgement to all my true comrades in the ‘comb team’: Aleksandr Tusnin, Mikhail Churaev, Junqiu Liu, Arslan Raja, Anton Lukashchuk, Anat Siddarth, Viacheslav Snigerev, and former colleagues Connor Skehan and Jordan Wachs all with whom I spent valuable time in solidarity. Also to honoured colleagues in the optomechanics team, special mention goes to Nils Engelsen, Amirali Arabmoheghi, Alberto Beccari for the same. To the newer students Andrea Triscari, Nikolai Kuznetsov, Dmitrii Pidgaiko, and especially Alisa Davydova, I give my maximum bests.

Lastly, to my family in New Zealand, who were always there even if they were far away.

Abstract

In this thesis, the generation of microcombs under complex, non-trivial, and/or higher-order cavity conditions is explored, both in ideal theory & simulation, and in practical experimentation. Pulse-driving of microresonators is investigated for the generation and temporal guiding of localised dissipative structures. The effect of pulse-driving in contrast to constant-wave driving is explored in terms of energy conversion efficiency and the nonlinear transfer of noise from the input to the output light. The generation of localised dissipative structures under arbitrary dispersion is investigated, including for dissipative solitons in pure or perturbed anomalous dispersion, switching waves in normal dispersion, and zero-dispersion solitons that exist in pure third-order dispersion between anomalous and normal. The existence of these localised dissipative structures in non-trivial resonators where the propagation constants vary with distance is studied, with particular attention for longitudinally modulated dispersion. In these resonators, coherent higher-order dispersive waves on solitons, and the emergence of Faraday-wave satellite structures on switching waves are experimentally observed and analysed according to Floquet theory.

Keywords:

- Nonlinear optics
- Optical frequency combs
- Microresonators
- Localised dissipative structures
- Solitons
- Switching waves
- Dispersion engineering
- Faraday instability
- Floquet dynamics
- Photonic integration

Résumé

Dans cette thèse, la génération de "microcombs" est explorée avec la théorie, la simulation et l'expérimentation pratique. Le pompage pulsé de micro-résonateurs est étudié pour la génération et le guidage temporel de structures dissipatives localisées. L'effet du pompage pulsé par opposition au pompage à ondes constantes est exploré en termes d'efficacité de conversion d'énergie et de transfert non linéaire de bruit de l'entrée à la lumière de sortie. La génération de structures dissipatives localisées sous dispersion arbitraire est étudiée, y compris pour les solitons dissipatifs en dispersion anormale pure ou perturbée, les switching waves en dispersion normale et les solitons à dispersion nulle qui existent en dispersion pure de troisième ordre entre anormal et normal. L'existence de ces structures dissipatives localisées dans des résonateurs non triviaux où les constantes de propagation varient avec la distance est étudiée, avec une attention particulière pour la dispersion modulée longitudinalement. Dans ces résonateurs, des ondes dispersives cohérentes d'ordre supérieur sur des solitons et l'émergence de structures satellites à ondes de Faraday sur des switching waves sont expérimentalement observées et analysées selon la théorie de Floquet.

List of Publications

Primary work

- **M. H. Anderson**, A. Tikan, A. Tusnin, A. Davydova, J. Riemensberger, R. N. Wang, and T. J. Kippenberg, “Dissipative solitons and switching waves in dispersion-modulated Kerr cavities”, *Physical Review X* **13**, 011040 (2023),
<https://journals.aps.org/prx/abstract/10.1103/PhysRevX.13.011040>
- **M. H. Anderson**, W. Weng, G. Lihachev, A. Tikan, J. Liu, and T. J. Kippenberg, “Zero dispersion Kerr solitons in optical microresonators”, *Nature Communications* **13** pp. 4764, (2022)
<https://www.nature.com/articles/s41467-022-31916-x>
- **M. H. Anderson**, R. Bouchand, J. Liu, W. Weng, E. Obrzud, T. Herr, and T. J. Kippenberg, “Photonic chip-based resonant supercontinuum via pulse-driven Kerr microresonator solitons”, *Optica* **8** pp. 771–779, (2021)
<https://opg.optica.org/optica/abstract.cfm?uri=optica-8-6-771>
- D. J. Wilson, K. Schneider, S. Hönl, **M. H. Anderson**, Y. Baumgartner, L. Czornomaz, T. J. Kippenberg, and P. Seidler, “Integrated gallium phosphide nonlinear photonics”, *Nature Photonics* **14** pp. 57–62 (2020)
<https://www.nature.com/articles/s41566-019-0537-9>
- **M. H. Anderson**¹, N. G. Pavlov¹, J. D. Jost, G. Lihachev, J. Liu, T. Morais, M. Zervas, M. L. Gorodetsky, and T. J. Kippenberg, “Highly efficient coupling of crystalline microresonators to integrated photonic waveguides”, *Optics Letters* **43** pp. 2106–2109, (2018)
<https://www.osapublishing.org/ol/abstract.cfm?uri=ol-43-9-2106>

Secondary contributions

- A. Nardi, A. Davydova, N. Kuznetsov, **M. H. Anderson**, C. Möhl, J. Riemensberger, P. Seidler, and T. J. Kippenberg, “Soliton Microcomb Generation in a III-V Photonic Crystal Cavity” (2023), arXiv:2304.12968
<http://arxiv.org/abs/2304.12968>
- G. Lihachev, W. Weng, J. Liu, L. Chang, J. Guo, J. He, R. N. Wang, **M. H. Anderson**, Y. Liu, J. E. Bowers, and T. J. Kippenberg, “Platicon microcomb generation using laser

¹Equally contributing authors

List of Publications

- self-injection locking”, *Nature Communications* **13** pp. 1771 (2022)
<https://www.nature.com/articles/s41467-022-29431-0>
- M. Churaev, R. N. Wang, V. Snigirev, A. Riedhauser, T. Blésin, C. Möhl, **M. H. Anderson**, A. Siddharth, Y. Popoff, D. Caimi, S. Hönl, J. Riemensberger, J. Liu, P. Seidler, and T. J. Kippenberg, “A heterogeneously integrated lithium niobate-on-silicon nitride photonic platform” (2022), arXiv:2112.02018
<http://arxiv.org/abs/2112.02018>
 - W. Weng, **M. H. Anderson**, A. Siddharth, J. He, A. S. Raja, and T. J. Kippenberg, “Coherent terahertz-to-microwave link using electro-optic-modulated Turing rolls”, *Physical Review A* **104** pp. 023511 (2021)
<https://link.aps.org/doi/10.1103/PhysRevA.104.023511>
 - J. Liu, H. Tian, E. Lucas, A. S. Raja, G. Lihachev, R. N. Wang, J. He, T. Liu, **M. H. Anderson**, W. Weng, S. A. Bhave, and T. J. Kippenberg, “Monolithic piezoelectric control of soliton microcombs”, *Nature* **583** pp. 385–390 (2020)
<https://www.nature.com/articles/s41586-020-2465-8>
 - E. Obrzud, M. Rainer, A. Harutyunyan, **M. H. Anderson**, J. Liu, M. Geiselmann, B. Chazelas, S. Kundermann, S. Lecomte, M. Cecconi, A. Ghedina, E. Molinari, F. Pepe, F. Wildi, F. Bouchy, T. J. Kippenberg, and T. Herr, “A microphotonic astrocomb”, *Nature Photonics* **13** pp. 31 (2019)
<https://www.nature.com/articles/s41566-018-0309-y>
 - H. Guo, E. Lucas, M. H. P. Pfeiffer, M. Karpov, **M. H. Anderson**, J. Liu, M. Geiselmann, J. D. Jost, and T. J. Kippenberg, “Intermode Breather Solitons in Optical Microresonators”, *Physical Review X* **7** pp. 041055 (2017)
<https://link.aps.org/doi/10.1103/PhysRevX.7.041055>
 - P. Marin-Palomo, J. N. Kemal, M. Karpov, A. Kordts, J. Pfeifle, M. H. P. Pfeiffer, P. Trocha, W. Stefan, V. Brasch, **M. H. Anderson**, R. Rosenberger, K. Vijayan, W. Freude, T. J. Kippenberg, and C. Koos, “Microresonator-based solitons for massively parallel coherent optical communications”, *Nature* **546** pp. 274–279 (2017)
<http://www.nature.com/articles/nature22387>

Contents

Acknowledgements	i
Abstract (English/Français)	iii
List of Publications	vii
Introduction	1
1 Basic concepts	3
1.1 Optical frequency combs	3
1.1.1 Formulation and discussion	3
1.1.2 Applications of frequency combs	6
1.2 Kerr cavity physics	6
1.2.1 Waveguides and dispersion	7
1.2.2 Nonlinear (Kerr) waveguide optics	10
1.2.3 The resonator (cavity)	12
1.2.4 Modal dispersion	17
1.2.5 The dynamical system equation	19
1.2.6 Numerical modelling	26
1.3 Taxonomy of phase states, modulation instability, dissipative solitons and switching waves	28
1.3.1 Modulation instability	28
1.3.2 Dissipative Kerr solitons	31
1.3.3 Switching waves	35
2 Pulse driven soliton microcomb generation and noise filtering	37
2.1 Pulse-driving motivation vs. CW-pumping	40
2.1.1 Unfavourable scaling in CW microcombs	40
2.1.2 Thermal load avoidance	42
2.1.3 Multi-state avoidance	44
2.2 The electro-optic comb as pulsed input	46
2.2.1 Phase/amplitude modulation	46
2.2.2 Compression (de-chirping)	48
2.3 Basic principles of pulse-driven soliton microcombs	53

ix

Contents

2.3.1	Soliton formation and locking	53
2.3.2	Phase contribution	55
2.4	Broadband, efficient pulse-driven microcomb results and noise propagation	59
2.4.1	Magnesium fluoride crystalline resonator pumping experiment	59
2.4.2	Silicon nitride microcomb experiment - resonator properties and testing setup	60
2.4.3	Soliton formation	62
2.4.4	Numerical modelling with the generalised LLE	64
2.4.5	Comparison with CW driving	67
2.5	Microcomb noise propagation	69
2.5.1	Coherence measurement, noise multiplication	69
2.5.2	Numerical modelling of noise transfer	71
2.5.3	Noise transfer reduction with soliton pushing	74
3	Localised dissipative structures near zero dispersion	79
3.1	Theory	81
3.1.1	Switching wave formation in modulated driving	81
3.1.2	Zero-dispersion formation in pulse-driving	83
3.1.3	Zero dispersion existence and discussion	86
3.2	Experimental observation and probing of normal- and zero-dispersion solitons and structures	90
3.2.1	Switching wave microcomb in pure normal dispersion	90
3.2.2	Zero dispersion soliton microcomb	92
4	Microcombs in the dispersion folded zone and Floquet dynamics	101
4.1	Theory	102
4.1.1	Quasi-phase matching and Floquet theory	103
4.1.2	Upper and lower states resonant radiation curves	104
4.1.3	Faraday instability	106
4.2	Microresonators with tapered mode suppression, with anomalous and normal dispersion	109
4.3	The anomalous dispersion case: solitons with higher-order dispersive waves	113
4.3.1	Theory & Modelling	113
4.3.2	Experimental results	117
4.4	The normal dispersion case: switching waves with satellite structures	119
4.4.1	Theory & Modelling	119
4.4.2	Experimental results and comb tuning	123
4.5	Extended mathematics	130
5	Outlook and conclusion	133
A	Experimental microcomb catalogue	137
B	Electro-optic comb components.	141

C Numerical method	145
C.1 Functions and split-step method	146
C.1.1 Split-step function	146
C.1.2 Homogeneous Kerr cavity solution	147
C.1.3 Live plotter	147
C.2 Script for simulating the dimensionless LLE & basic scenarios	149
C.2.1 Program guide and plotting the output	149
C.2.2 Single dissipative soliton analysis	164
C.2.3 Noise transfer analysis	169
C.2.4 Dissipative solitons in pulse driving example	172
C.2.5 Switching waves and pulse driving	174
C.3 Script for simulating the realistic LLE in Si_3N_4 with advanced examples	176
C.3.1 Program guide and plotting the output	176
C.3.2 Beware numerical Faraday Instability and quasi-phase matching!	190
C.3.3 Modelling repetition rate noise transfer in pulse-driven microcombs . .	190
C.3.4 Generating a zero dispersion soliton microcomb	197
C.3.5 Soliton with HDW analysis	202
C.4 Simulation parameter tables	207
C.5 Tutorial videos online!	211
C.5.1 Dispersion modelling with COMSOL	211
C.5.2 Simulating the GNLSE for supercontinuum generation on Matlab	211
Bibliography	228

Introduction

Over the last half-century, lasers have become a ubiquitous tool in modern technology. But, for the purposes of transferring information, they are akin to measuring distance with a stick of fixed length. New laser systems amounting to *optical frequency combs* are frequency *rulers* and therefore energy rulers, a potential omni-tool for future sensing, communications, and time keeping. While there are several well known specific uses for existing frequency combs in the present day, their fundamental nature portends countless unanticipated applications. At present there exist gaps in the capabilities of existing frequency combs. They are either too sparse in the terahertz domain, or too dense in the megahertz domain. They may require a large amount of optical pump power in order to get little in return. There exists a trade-off between energy efficiency, and spectral bandwidth. Aside from this, there is also the ambition to bring these tools away from the unique, customised laboratory setting on table-top and into foundry-based mass-production in the form of photonic microchips. Such a frequency comb can be most elegantly provided by combining a dissipative micro-cavity with the physics of nonlinear localisation: a *microcomb*. Nonlinear localisation or self-organisation pervades our lives and the natural world. Such environments include multiple layers of dynamical systems each with their own terms and ingredients across physics, chemistry, biology, and even humanity. This gives way to complex distinct regimes and patterns that are challenging to understand easily. Amongst this, the optical cavity provides the purest dynamical system, and hence a most fundamental test-bed.

This thesis merges the interest for the understanding of dynamical systems and self-organised dissipative structures with the technological desire for efficient, precision microcombs on photonic chip. The work presented is the product of feedback between simulation and experiment, and experiment and simulation. The system of choice is the driven dissipative Kerr cavity, in the form of photonic silicon nitride microresonators. Research and development in this area has so far been focused on the continuous-wave-driven soliton microcomb. The physics of this state has been reaching maturity in its base-level understanding. Furthermore, in an application sense, it suffers serious limitations in efficiency and spectral coverage.

This thesis seeks to advance the practical understanding of localised dissipative structures in Kerr cavities, and how we may fill the gaps in achievable chip-integrated frequency comb generation. In Chapter 1, the Kerr cavity system fundamentals will be described, first in the canonical form, and then in the generalised form to be explored in the body of the work.

Chapter 2 will introduce pulsed-driving for the Kerr cavity system, first in theory and then in experiment with the interest of achieving *resonant supercontinuum generation*. The performance of these microcombs are tested in terms of energy conversion efficiency and how input pulse noise transfers, multiples, and is suppressed across the microcomb. In Chapter 3, we move to arbitrary dispersion landscapes. First, to normal dispersion with switching wave microcombs. Then, to the discovery of ‘zero-dispersion’ solitonic dissipative structures as a candidate for broadband efficient microcombs. In Chapter 4, we add longitudinal parametric variation to the system and explore the dramatic effects arising from it, particularly the generation of satellite switching wave microcombs. In the conclusion, steps towards achieving an efficient octave-spanning microcomb is presented, and a future is proposed.

1 Basic concepts

1.1 Optical frequency combs

1.1.1 Formulation and discussion

Consider any complex **signal** in time τ , $a(\tau)$, that amounts to some kind of *solitary* but sudden tonal or frequency excursion. If that signal was made to reliably repeat itself with a certain period T , as if it is constantly cycling around a periodic space so that $c(\tau + T) = c(\tau)$, such a signal could be decomposed as a convolution[1]:

$$c(\tau) = a(\tau) \otimes \sum_{k=-\infty}^{\infty} \delta(\tau - kT) \quad (1.1)$$

where the term on the very right is the ‘shah’ function or *Dirac Comb*, an infinite series of equally spaced Dirac delta functions $\delta(\tau)$, containing unit energy and infinitely narrow duration. Conveniently, from basic Fourier transform theory, the Dirac Comb is its own Fourier transform $\mathcal{F}[\cdot]$, and accordingly in the frequency domain

$$\tilde{c}(\omega) = \tilde{a}(\omega) \times \sum_{m=-\infty}^{\infty} \delta(\omega - m\omega_r) \quad (1.2)$$

which is simply the envelope of the Fourier transform of the solitary signal $\tilde{a}(\omega) = \mathcal{F}[a(\tau)]$, multiplied by the Dirac comb in the frequency domain, spaced by the signal’s *repetition rate*

$$\omega_r = \frac{2\pi}{T} \quad (1.3)$$

If the excursion signal $a(\tau)$ is centred at some optical frequency ω_0 , so that

$$a(\tau) = A(\tau)e^{i\omega_0\tau} \quad (1.4)$$

then

$$\tilde{C}(\omega) = \tilde{A}(\omega) \times \sum_{\mu=-\infty}^{\infty} \delta(\omega - \omega_0 - \mu\omega_r) \quad (1.5)$$

In optics, this whole signal is known as a “frequency comb” [2] although it perhaps really should be called a frequency *ruler* to emphasise the fact that, as it’s derived from a cycling signal, the frequency spacing ω_r is *intrinsically* constant.

A typical thesis on this topic will usually present a frequency comb to you as a plot of uniformly spaced vertical lines (or comb “teeth”) as a function of optical frequency, famously where the comb line frequencies ω_m

$$\omega_m = m\omega_r + 2\pi f_{\text{ceo}} \quad (1.6)$$

with f_{ceo} being the “carrier-envelope offset frequency”: representing the ‘phase slip’ of the underlying oscillating field underneath the signal envelope [3, 4]. In this thesis, I wish to emphasise the frequency comb’s two-dimensional character, presented in Fig. 1.1. Optical frequency combs (OFC) as tools have been most fundamentally considered [5] an *RF-to-optical link* for the fact that the value of the comb line spacing $\omega_r = 2\pi f_r$ typically exists in or slight above the radio frequency (RF) domain (<100s GHz), and the optical centre ω_0 and its bandwidth exists firmly in the optical domain of 100s THz. Hence, with having sure knowledge of m , ω_r , and f_{ceo} , OFCs are able to *transfer* knowledge of optical frequencies, and therefore energies [3, 6, 7, 8, 9, 10, 11] (atomic, molecular response signals and so forth) from the optical domain down to the radio level where they can be measured ‘exactly’ with electronic circuitry. Likewise in reverse, information originating in the radio frequency domain (data communications) can be *imposed* on well known optical wavelengths for data transmission [12, 13, 14] and optical frequency synthesis [15, 4, 16]. This relationship between the radio and optical domains is fundamental to frequency comb optics, and in this way I would liken it fundamentally to music where, the optical carrier and envelope represents *pitch* and *timbre*, while the RF signal/response corresponds to *rhythm* and the constant *beat*.

Presenting the frequency comb as it is in Fig. 1.1 will be a mainstay of this thesis. It allows a ‘birds-eye’ view of the OFC response to phenomenon over the rapid short term – the fast or optical frequency – and the gradual long term – the slow or radio frequency. One useful visualisation involved here is the OFC noise or instability. When the optical carrier frequency varies and drifts for whatever reason over the long term t (as opposed to the short term τ) $\omega_0(t) = 2\pi(\hat{f}_0 + \delta f_0(t))$, then the comb grid experiences noise/uncertainty on each line uniformly. When the cycle velocity of the signal envelope $A(\tau)$ speeds up or slows down

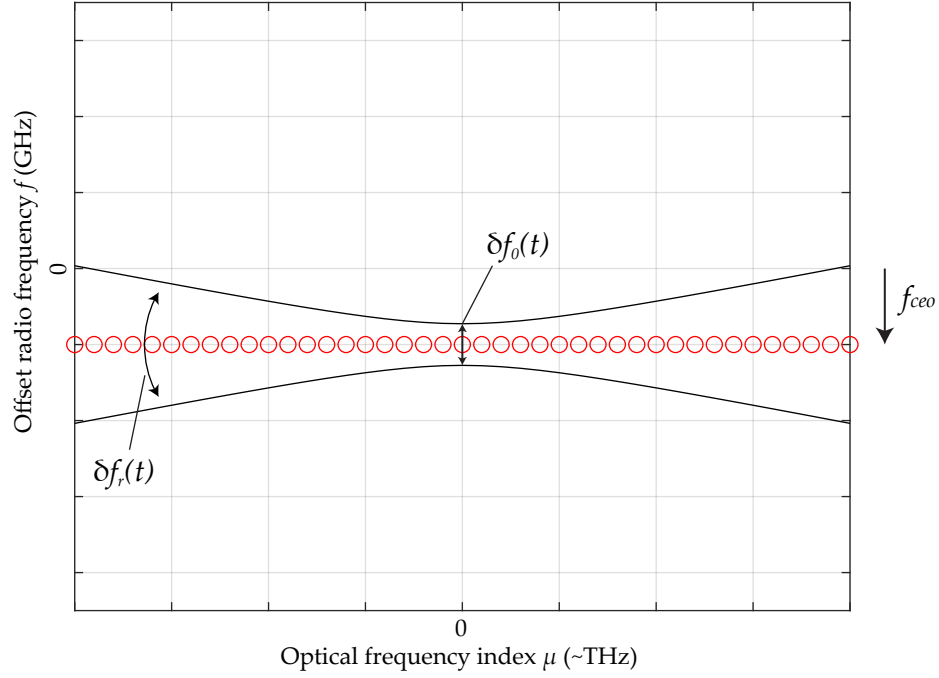


Figure 1.1: **Two-dimensional representation of a frequency comb.** The red circles represent comb teeth in slow vs. fast frequency space ie. RF vs. optical, rhythm vs. pitch. Noise or instability may cause this ‘comb grid’ to jitter up and down in carrier frequency with $\delta f_o(t)$ and lean high and low with $\delta f_r(t)$, inside the black lines.

(timing jitter) then the comb grid leans with an additional high or low gradient in the offset (slow) frequency dimension. In order for an OFC to be *useful* as an RF-to-optical link, then both f_{ceo} and f_r must be *stabilised*, or locked to another highly stable reference frequency [3, 2], and the noise (incoherence) of $\delta f_o(t)$ and $\delta f_r(t)$ must be ‘cooled’ or ‘quietened’ down to human timescale of single-Hz variation.

Finally, while having a stabilised OFC is sufficient a tool to measure relative signals accurately[17], in order to *know* the f_{ceo} , the OFC has to be ‘self-referenced’, for instance, with the **f – 2f** scheme. If an OFC has a spectral envelope that encompasses an octave in bandwidth, that means at the low end of the spectrum there exists a comb line frequency that, if doubled, would be able to be measured via heterodyne with a comb line at the high end, where

$$\begin{aligned}
 2\omega_{m1} &\approx \omega_{m2} \\
 \Rightarrow \\
 2(mf_r + f_{ceo}) &\approx (2mf_r + f_{ceo}) \\
 \Rightarrow \\
 2\omega_{m1} - \omega_{m2} &= 2\pi f_{ceo}
 \end{aligned} \tag{1.7}$$

which is why an OFC that spans an octave is the ultimate nice-to-have.

1.1.2 Applications of frequency combs

Optical atomic clockwork, low-noise microwave generation, and optical frequency synthesis

As discussed above, a self-referenced frequency comb can transfer the relative purity of an atomic transition at 100s THz down the human scale of seconds, imparting a relative stability to the definition of second at the order of 10^{-17} [18, 19, 20, 21, 22]. OFCs are now able to go in to orbit to strengthen GPS and conduct relativistic measurements of Earth's gravity by comparing minute timing differences. [23, 24, 25, 26], including on land [27].

Without interacting with trapped atoms, self-referenced OFCs locked to ultra-stable cavities and coherent lasers [28, 29, 30] can divide the relative phase noise of that laser by factors of $(10,000)^2$ transferring from the 100s THz domain down to 10s GHz, enabling high purity RF signals for radar and communications.

When operated in reverse, a highly stable RF signal can be transferred to the optical domain via a self-referenced frequency comb, enabling the specification of laser frequencies to sub-Hz precision [15, 4, 31, 32, 33].

Astro-spectrometer calibration

The stability of an ultra-broadband OFC can be used to provide calibration (ie. frequency ruler) for astro-spectrometers, replacing ageing gas lamps [34, 9, 35] and providing a stable reference sufficient to enable detection of exo-planets via the radial Doppler shift of the stars emission spectrum [36, 37, 38, 39]. An OFC having its comb line spacing in the GHz domain is particularly important, as the individual comb teeth can be separated via diffraction [40].

Parallel telecommunications and ranging

OFCs, particularly those in the GHz spacing area are naturally suited as massively parallel multi-channel sources and receivers of information, for data communications [12, 13, 41, 42] and for distance ranging and lidar [43, 11, 44, 45]. This replaces the need for high number of individual laser devices requiring mutual stabilisation and electricity usage.

1.2 Kerr cavity physics

This section will briefly define everything necessary to interpret the results of this thesis.

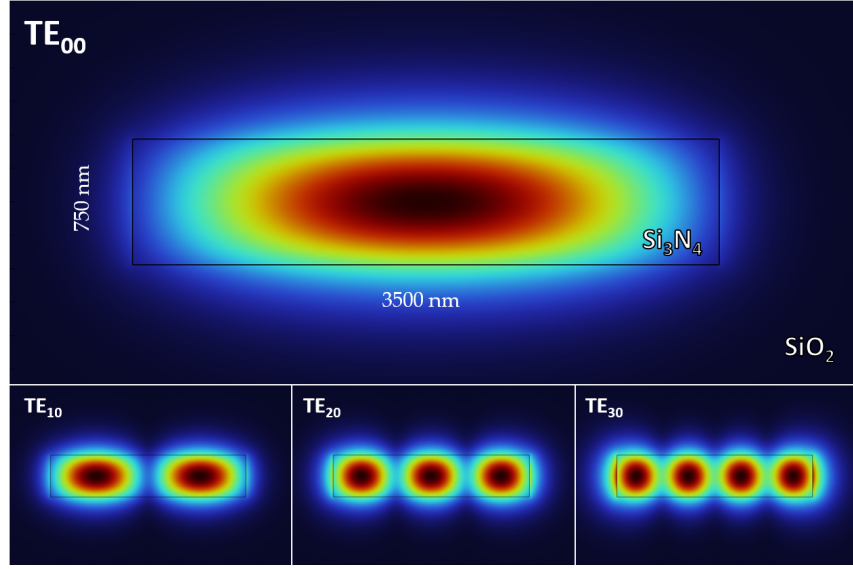


Figure 1.2: **Transverse eigenmodes of a wide Si_3N_4 waveguide cross-section, x -polarisation (quasi-“TE”).** First four transverse harmonics $|G(x, y)|$ for the propagating mode in an example $3.5 \times 0.75 \mu\text{m}^2$ Si_3N_4 waveguide (featured in chip design D62.C5), calculated using COMSOL Multiphysics 6.1. Each mode depicted here is also paired with a y -polarised mode (“TM”).

1.2.1 Waveguides and dispersion

Transverse eigenmodes

If we consider light as a constant travelling electromagnetic field propagating through a photonic waveguide, having a separable form

$$\mathbf{E}(x, y, z, t) = \mathbf{G}(x, y) A(z, t) \exp \left[(i\beta(\omega) - \alpha(\omega))z - i\omega t \right] \quad (1.8)$$

where $A(z, t)$ is the above discussed signal envelope function, with a transverse density of $\mathbf{G}(x, y)$ (normalised so that $\iint |\mathbf{G}(x, y)|^2 dx dy = 1$) governing a travelling wave with frequency ω [s^{-1}], loss α [m^{-1}], and propagation phase constant [m^{-1}]

$$\beta(\omega) = \frac{\omega n_{\text{eff}}(\omega)}{c} \quad (1.9)$$

where n_{eff} the effective refractive index is the eigenvalue solution, with eigenmode solution $\mathbf{G}(x, y)$, found from solving Maxwell’s equations for a focusing refractive index profile $n(x, y)$, such as those depicted in Fig. 1.2 for an example Si_3N_4 waveguide in full silica (SiO_2) cladding. Such modes can be found for arbitrary non-uniform anisotropic transverse dielectrics with the use of commercial mode solvers such Comsol Multiphysics in this instance, or Ansys, or

programs freely available online [46, 47].

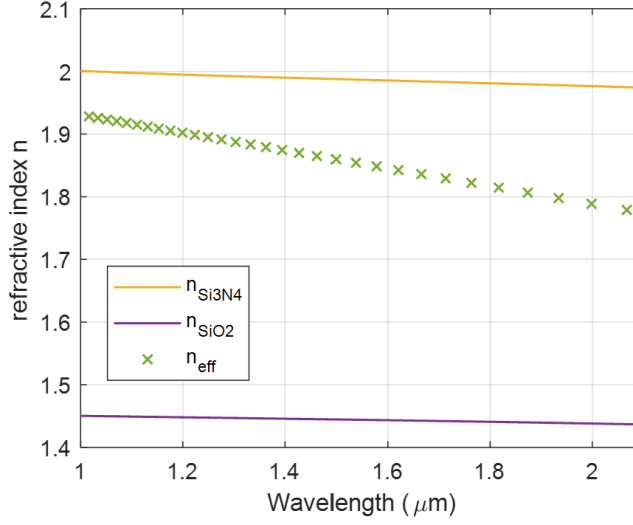


Figure 1.3: **Numerically calculated values of n_{eff} at many wavelengths Si_3N_4 waveguide**, for the TE00 mode in Fig. 1.2. As wavelength increases, the mode expands to have more of itself located out of the Si_3N_4 core and into the surrounding SiO_2 cladding, so that n_{eff} tends from the core $n(\lambda)$ to the cladding $n(\lambda)$.

Dispersion

Modes at different frequencies ω travel at difference phase velocities ie. *dispersion*, a crucial phenomenon underpinning all the presented work. As we are interested in nonlinear optics and wave-coupling, self-organisation, and phase matching, we have to decompose $\beta(\omega)$ into Taylor series components

$$\beta(\omega) = \beta_0 + \beta_1(\omega - \omega_0) + \frac{\beta_2}{2}(\omega - \omega_0)^2 + \frac{\beta_3}{6}(\omega - \omega_0)^3 + \dots + \frac{\beta_\ell}{\ell!}(\omega - \omega_0)^\ell \quad (1.10)$$

for $\ell \geq 2$ up to however many is necessary to model and predict the system over a large spectral bandwidth, with constant coefficients evaluated at the centre frequency ω_0

$$\beta_\ell = \left. \frac{d^\ell \beta}{d\omega^\ell} \right|_{\omega_0} \quad (1.11)$$

with each coefficient playing an important role: β_0 the phase constant (phase velocity $v_p = c/n_{\text{eff}} = \omega_0/\beta_0$); β_1 the group *delay* (group velocity $v_g = c/n_g = 1/\beta_1$) the speed of travel for the envelope function $A(z,t)$; and β_2 specifically the group ‘delay dispersion’ (but hereafter group velocity dispersion (GVD)) quantifying the spread or dispersal in time for a group of waves travelling at different frequencies in a linear medium. When $\beta_2 > 0$ the dispersion

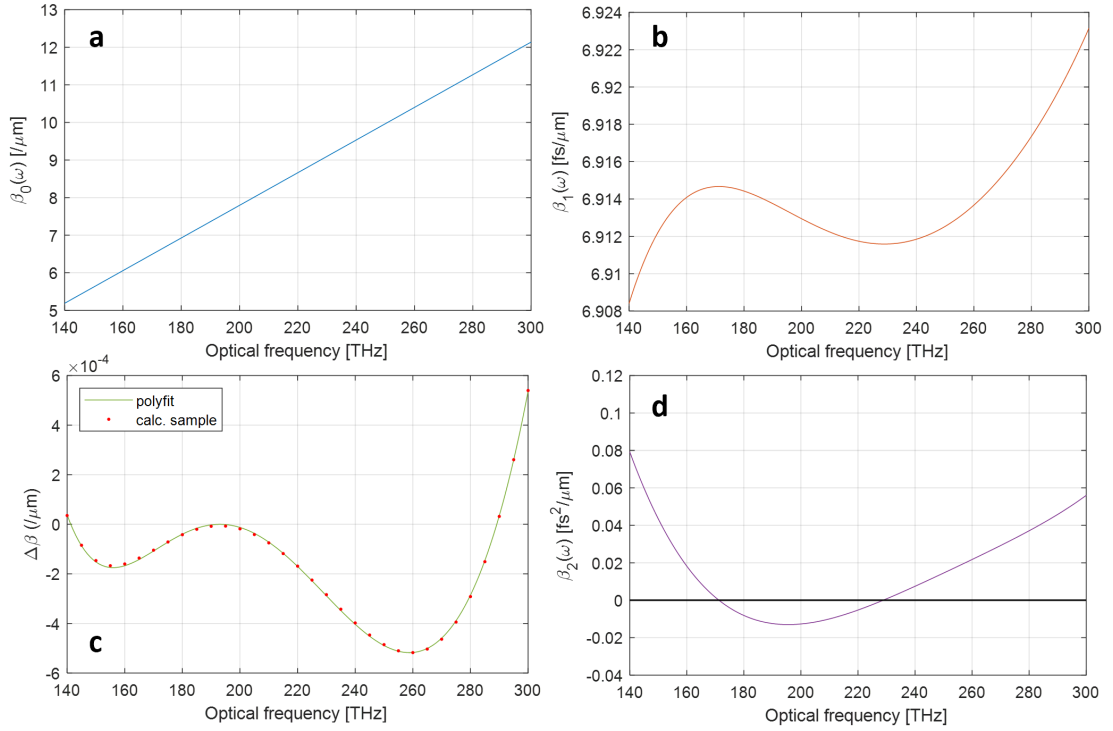


Figure 1.4: Numerically calculated and fitted dispersion values from the above n_{eff} in four useful forms as a function of optical frequency. (a) Phase constant. (b) Group delay. (c) Relative phase delay, or integrated dispersion, the 6th-order polynomial fit plotted with the original calculated sample points to verify the fit. (d) Group velocity dispersion.

is said to be *normal* as when ‘red’ frequencies travel with a faster group velocity than blue frequencies, and for when $\beta_2 < 0$ the dispersion is said to be *anomalous* in the opposite case. The dispersion slope term β_2 governs at what frequency the GVD changes sign from normal to anomalous and whether this will cause radiation to be emitted away from a travelling pulse. β_2 and β_3 will be a fundamental role in this thesis, but all higher orders β_{4+} will also serve to complicate any emitted radiation. Fig. 1.4 shows how these orders of dispersion appear when calculated and isolated for the realistic Si_3N_4 waveguide modelled above.

Fig. 1.4(b) can tell us where any two propagating signals will be travelling at the same velocity, and Fig. 1.4(d) tells us where and whether dispersion is anomalous and so can allow for nonlinear self-organisation of our optical system. If we wish to know how the *relative* phase of co-travelling waves evolves with distance, we take the ‘integrated dispersion’

$$\Delta\beta(\omega) = \beta(\omega) - \beta_0 - \beta_1(\omega - \omega_0) \quad (1.12)$$

which is essentially Fig. 1.4(d) integrated twice back into the phase domain centred at ω_0 . In the example shown here, we can see that an optical signal (for instance, our pump wavelength)

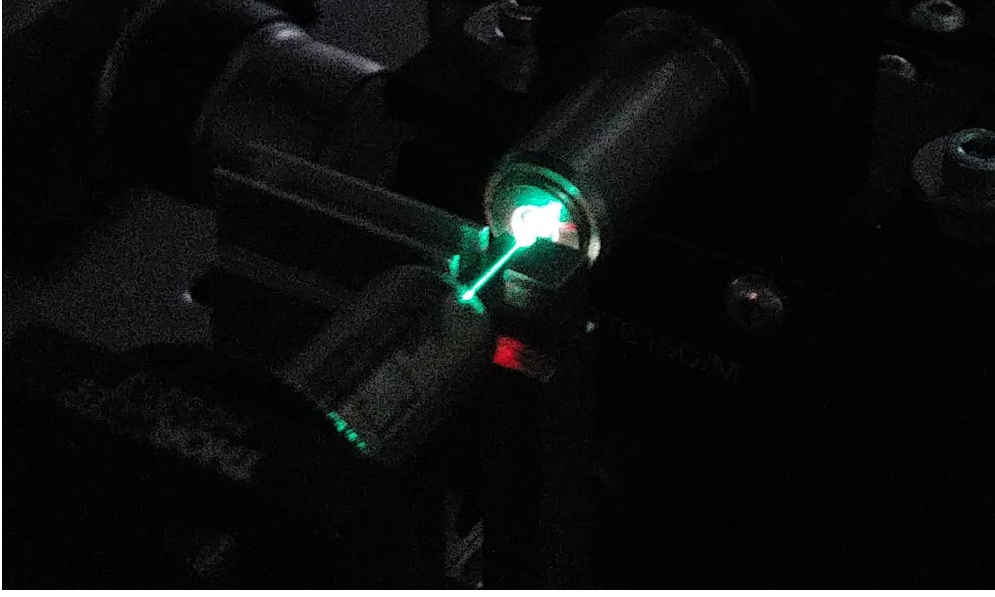


Figure 1.5: **Photo of triple-frequency generation occurring during a supercontinuum generation experiment on Si_3N_4** . Here, light propagating at 200 THz is strong enough to stimulate the creation of light at 600 THz.

located at $\nu_0 = 192$ THz will find *phase matching* with a co-travelling wave at $\nu = 140$, or 290 THz, and could become nonlinearly resonant.

1.2.2 Nonlinear (Kerr) waveguide optics

For anisotropic dielectric media (vacuum permeability and permittivity expressed here as μ_0 and ϵ_0), the polarisability faces an escalating series of nonlinear distortion, of which the second-order and third-order nonlinear polarisation are considered for moderately strong optical fields.

$$\mathbf{P} = \epsilon_0 \left[\chi^{(1)} \cdot \mathbf{E} + \chi^{(2)} : \mathbf{E}\mathbf{E} + \chi^{(3)} :: \mathbf{E}\mathbf{E}\mathbf{E} + \dots \right] \quad (1.13)$$

For the majority of this work involving silicon nitride nonlinear photonics, and not gallium phosphide or lithium niobate, the nonlinear polarisation is considered isotropic, and with no preferred axes in the material the second-order nonlinearity is negligible. Hence, we consider that $\mathbf{P} = \mathbf{P}_L + \mathbf{P}_{NL}$, with the latter including $\chi^{(3)}$ only.

So, considering a propagating OFC of M different frequencies, and the same polarisation and transverse mode (for simplicity)

$$A(z, t) = \sum_{m=1}^M A_m \exp[i\beta_m z - i\omega_m t] \quad (1.14)$$

the resulting polarisation field would then be a sum of every triple product of this wave

$$P_{\text{NL}m} = \epsilon_0 \chi^{(3)} \left[\frac{1}{8} \sum_{j,k,l} E_j E_k E_l \exp[i\Lambda_{+jklm}] + \frac{3}{8} \sum_{j,k,l} E_j E_k E_l^* \exp[i\Lambda_{-jklm}] \right] + c.c. \quad (1.15)$$

where Λ stands for the momentum and energy conservation requirements, firstly for sum-frequency generation

$$\Lambda_{+jklm} = (\beta_j + \beta_k + \beta_l - \beta_m)z - (\omega_j + \omega_k + \omega_l - \omega_m)t \quad (1.16)$$

which results in *triple-harmonic* generation in the degenerate pump case (an experimental view shown in Fig. 1.5), and secondly for difference-frequency generation

$$\Lambda_{-jklm} = (\beta_j + \beta_k - \beta_l - \beta_m)z - (\omega_j + \omega_k - \omega_l - \omega_m)t \quad (1.17)$$

for which there are three times as many photon coupling (or throupling) opportunities. This second event is responsible for *four-wave mixing* (FWM), as well as cross-phase modulation for considering only two frequencies if $j = k$ and $l = m$, and for self-phase modulation (SPM) for a single frequency and $j = k = l = m$.

The NLSE, solitons, and dark solitons

From Eq. 1.13 considering only $\chi^{(3)}$, this leads us to the intensity driven nonlinear wave equation

$$\left(\nabla^2 - \frac{n^2}{c^2} \frac{\partial^2}{\partial t^2} \right) \mathbf{E}(\mathbf{r}, t) = -\mu_0 \frac{\partial^2 \mathbf{P}_{\text{NL}}}{\partial t^2} \quad (1.18)$$

where the nonlinear polarisation acts as a source. Applying this to our travelling wave from Eq. 1.8, we ultimately are able to condense the nonlinear wave equation down to a single-envelope nonlinear dispersive wave equation: the *nonlinear Schrödinger equation* (NLSE)

$$\frac{\partial A}{\partial z} = -i \frac{\beta_2}{2} \frac{\partial^2 A}{\partial \tau^2} + i\gamma |A|^2 A \quad (1.19)$$

which has taken a number of assumptions to reach. This includes taking $G(x, y)$ and $A(z)$

as separable and G not affected by nonlinearity; finding a modified intensity-dependent refractive index

$$\tilde{n} = n + n_2|E|^2 \quad (1.20)$$

where the nonlinearity is still small enough so that $\varepsilon = (n + \Delta n)^2 \approx n^2 + 2n\Delta n$; and, importantly that the envelope $A(z)$ is sufficiently slow so that $\partial^2 A / \partial z^2 \approx 0$. In Eq. 1.19 we have introduced the envelope nonlinear phase constant¹

$$\gamma = \frac{n_2 \omega_0}{c A_{\text{eff}}} \quad (1.21)$$

which is in units of $[(\text{m.W})^{-1}]$, clarifying that $|A(\tau)|^2$ is similarly in units of Watt. The phase constant γ encompasses the transverse mode density with

$$A_{\text{eff}} = \frac{(\int \int_{\infty}^{\infty} |G(x, y)|^2 dx dy)^2}{\int \int_{\infty}^{\infty} |G(x, y)|^4 dx dy} \quad (1.22)$$

Finally, there has been a coordinate transform, hinted at in section 1.1

$$\tau = t - \beta_1 z \quad (1.23)$$

where the new *fast time* coordinate follows our rapid signal A as it *gradually* changes over distance z . GVD is included here only at the second order, but we will see the higher orders later in the cavity system. The linear loss term

$$\frac{\partial A}{\partial z} = -\frac{\alpha_l}{2} A \quad (1.24)$$

with α_l in $[\text{m}^{-1}]$, brought back from Eq. 1.8, could also be included in to Eq. 1.19 to change it from the conservative NLSE to the dissipative form. In more interesting systems, the loss can be nonlinear as in two-photon absorption in materials such as silicon, and/or dispersive as in gain dispersion in an erbium doped amplifier.

1.2.3 The resonator (cavity)

Although Fabry-Perot Kerr resonators have recently become available for microcomb generation, including in our group, our Kerr cavity system is an evanescently coupled ring resonator shown in Fig. 1.6. Such resonators can be represented alternatively in frequency units (Fig.

¹Here, A for area is non-italicised, to be distinguished apart from $A(z, \tau)$.

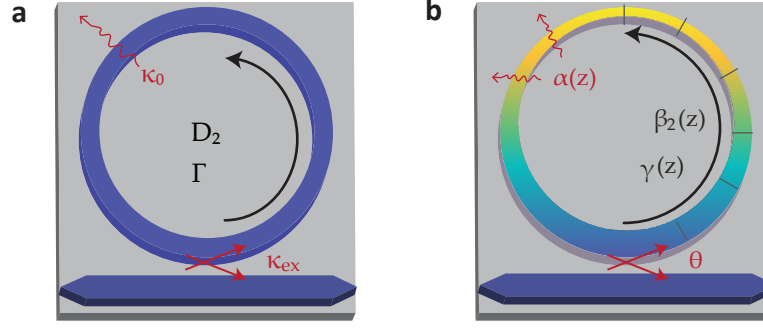


Figure 1.6: **Schematic ring resonators.** (a) Trivial, mean-field resonator. Appropriate for parameters in the frequency domain. Evaluation step can be of any duration, even longer than the roundtrip time. (b) Non-trivial resonator. Appropriate with per-metre phase coefficients. Propagation constants may change with distance, and evaluation rate must be much higher than the FSR accordingly.

1.6(a)), which is conceptually appropriate for more ‘monolithic’, small ultra-high quality ring resonators; or, in phase/loss per metre units (Fig. 1.6(b)) more familiar in longer fibre-based loop cavities and may have different internal segments with different propagation constants. The latter can be termed as a ‘lumped’ model. In this thesis, particularly in chapter 4, longer Si_3N_4 racetrack resonators are featured that possess changing propagation constants, so this model is generally preferred as a starting point. However, frequency units possess a genuine elegance and are very suited to the ‘frequency vs. frequency’ theme of this thesis, so both formalisms are referred to.

Loss, coupling, resonance

Consider a signal envelope incident at the resonator $A_{in}(z, \tau)$, travelling along through the “bus” waveguide. Light $A(z, \tau)$ circulates around the ring and is coupled with A_{in} every roundtrip. Over one complete roundtrip, $|A|^2$ experiences overall internal reflection ρ and output transmission θ , with $\rho + \theta < 1$ because the system is lossy (not unitary). θ is the power coupling coefficient between the bus waveguide and the resonator waveguide, and $\rho = (1 - \theta) \exp[-\alpha_l L]$. During propagation, A is governed by Eq. 1.19. At the *boundary* of the ring cavity at the coupling location, the intracavity field has the following condition

$$A^{(r+1)}(z=0, \tau) = \sqrt{\rho} A^{(r)}(z=L, \tau) e^{i\phi} + \sqrt{\theta} A_{in} \quad (1.25)$$

with L the ring length, r the roundtrip index, and ϕ the roundtrip *accumulated relative phase*² of the travelling field determining the condition for resonance. Considering linear phase shift, we find the *equilibrium* solution for when $A^{(r+1)}(0, \tau) = A^{(r)}(L, \tau)$

²This ϕ corresponds to the phase of a travelling signal, to distinguish itself from φ later appearing as the angular *spatial* coordinate $\varphi = \tau D_1$.

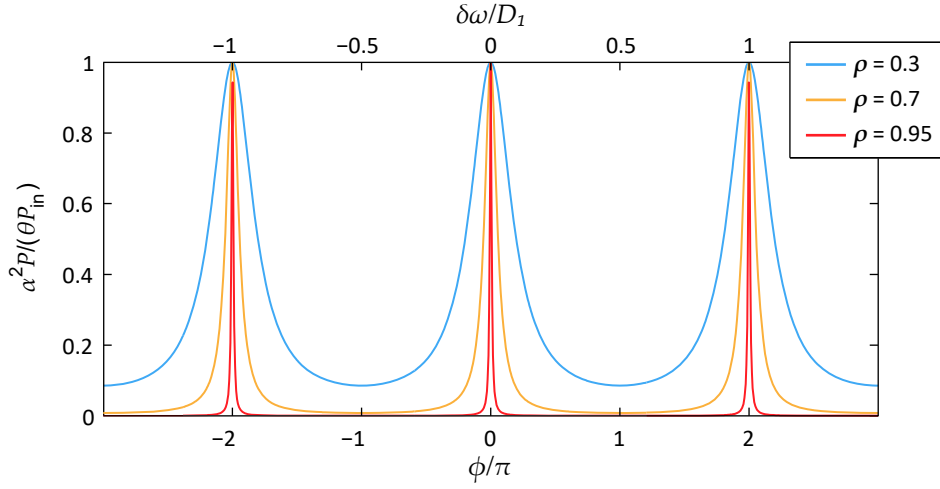


Figure 1.7: **Resonance, internal absorption of cavity as function of tuning ϕ .** The intracavity enhancement factor is given by $\theta/\alpha^2 = 2\eta\mathcal{F}/\pi$. Adapted from [48].

$$A = \frac{\sqrt{\theta}}{1 - \sqrt{\rho} \exp(i\phi)} A_{\text{in}} \quad (1.26)$$

and

$$\frac{|A|^2}{|A_{\text{in}}|^2} = \frac{\theta/(1 - \sqrt{\rho})^2}{1 + K \sin^2(\phi/2)} \quad (1.27)$$

where $K = 4\sqrt{\rho}/(1 - \sqrt{\rho})^2$, giving the Airy function for a linear cavity homogenous solution shown in Fig. 1.7. The most relevant figure of merit for resonant cavities is the *Finesse*, which is defined as the ratio of the frequency/phase separation of each resonance to the resonance full-width at half maximum, from Eq. 1.27,

$$\mathcal{F} = \frac{\pi}{2 \arcsin\left(\frac{1 - \sqrt{\rho}}{2\sqrt[4]{\rho}}\right)} \approx \frac{\pi}{\alpha} \quad (1.28)$$

introducing the single roundtrip loss constant $\alpha \equiv (1 - \rho)/2$, where the above approximation is appropriate for total roundtrip losses less than 5-10%, or values of $\mathcal{F} \gtrsim 60$. With α and \mathcal{F} , we can now define the photon *lifetime*

$$t_{\text{ph}} = \frac{1}{2\alpha} T = \frac{\mathcal{F}}{2\pi} T = \frac{1}{\kappa} \quad (1.29)$$

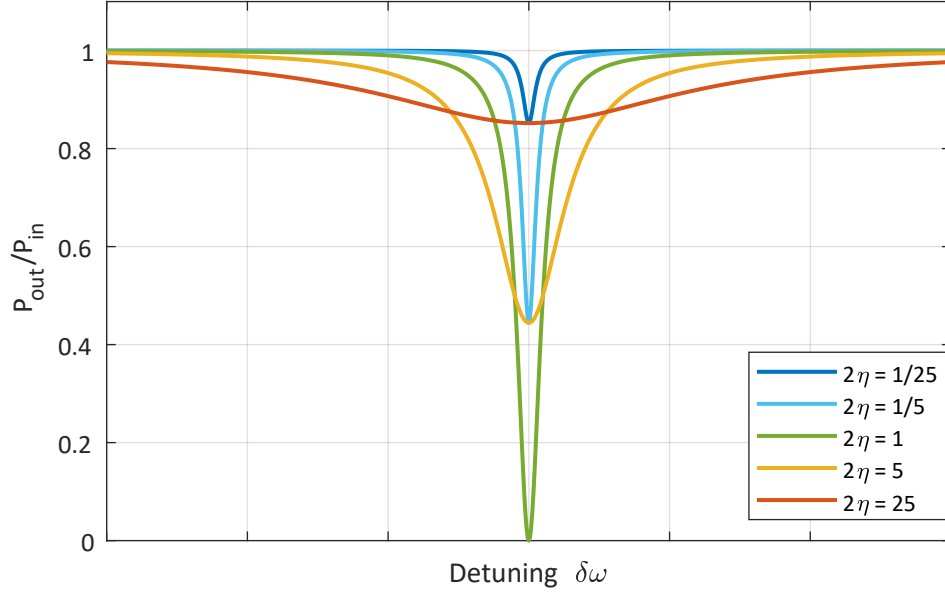


Figure 1.8: **Power transmission of cavity resonance through direct bus waveguide route** as a function of detuning and loading factor η .

now establishing the cavity *linewidth* κ in 2π .Hz. Similarly, we can convert the coupling coefficient to frequency units as well

$$\kappa_{\text{ex}} = \frac{\theta}{T} \quad (1.30)$$

with κ_{ex} representing the ‘external’ cavity linewidth, and

$$\kappa_0 = \frac{\theta_l}{T} \quad (1.31)$$

the ‘internal’ linewidth, originating from internal roundtrip loss coefficient $\theta_l \approx 1 - \exp[-\alpha_l L]$. The total linewidth is a simple sum: $\kappa = \kappa_0 + \kappa_{\text{ex}}$. As the photon lifetime t_{ph} represents the timescale for exponential decay of photons circulating the coupled cavity ie. the measure of time a photon can stay and build up inside the resonator, this gives us the maximum enhancement factor on resonance

$$\left(\frac{P}{P_{\text{in}}} \right)_{\text{max.}} = \frac{\theta}{\alpha^2} = \frac{2\eta}{\pi} \mathcal{F} \quad (1.32)$$

where this time we include the cavity ‘loading factor’

$$\eta = \frac{\theta}{2\alpha} = \frac{\kappa_{\text{ex}}}{\kappa} \quad (1.33)$$

which will become highly relevant later when discussing conversion efficiency. In frequency domain units, assuming a very high finesse so as to approximate resonances as solitary (where $\phi \ll 2\pi$), Eqs. 1.26 and 1.27 simplify to

$$A = \frac{\sqrt{\kappa_{\text{ex}}/T}}{\frac{\kappa}{2} - i\delta\omega} A_{\text{in}} \quad (1.34)$$

now with the frequency *detuning* $\delta\omega = \phi/T$, and the power enhancement

$$\frac{|A|^2}{|A_{\text{in}}|^2} = \frac{\kappa_{\text{ex}}/T}{\left(\frac{\kappa}{2}\right)^2 + \delta\omega^2} = \frac{\mathcal{F}}{\pi} \frac{2\eta}{1 + \left(\frac{\delta\omega}{\kappa/2}\right)^2} \quad (1.35)$$

If we are interested in the *throughput* bus waveguide transmission, as we often are in experiment, then

$$\frac{|A_{\text{out}}|^2}{|A_{\text{in}}|^2} = \frac{|A_{\text{in}} - \sqrt{\kappa_{\text{ex}}T}A|^2}{|A_{\text{in}}|^2} = 1 - \frac{4\eta(1-\eta)}{1 + \left(\frac{\delta\omega}{\kappa/2}\right)^2} \quad (1.36)$$

which is graphed in Fig. 1.8. Here, we see that at $2\eta = 1$, input power is completely absorbed and dissipated into the cavity on resonance. This is “critical” coupling. For $2\eta < 1$, under-coupling, light stays in the cavity longer to dissipate there before exiting, and intracavity power becomes very low. For $2\eta > 1$, over-coupling, light tends to exit the cavity into the bus waveguide before dissipating inside the cavity, and intracavity power is also low. While the finesse of the cavity stays high for under-coupling, over-coupling allows more of the intracavity light to be retained and collected in the bus waveguide. This will be relevant later when discussing soliton conversion efficiency.

Nonlinear frequency shift

Recalling the Kerr nonlinear effect and the NLSE above, we can incorporate the nonlinear phase shift to the cavity solution from Eq. 1.27, so that

$$\frac{|A|^2}{|A_{\text{in}}|^2} = \frac{\theta/(1-\sqrt{\rho})^2}{1 + K \sin^2((\phi_0 + \gamma L|A|^2)/2)} \quad (1.37)$$

as depicted in Fig. 1.37, creating a linear ‘tilt’ to the resonance condition, and very importantly,

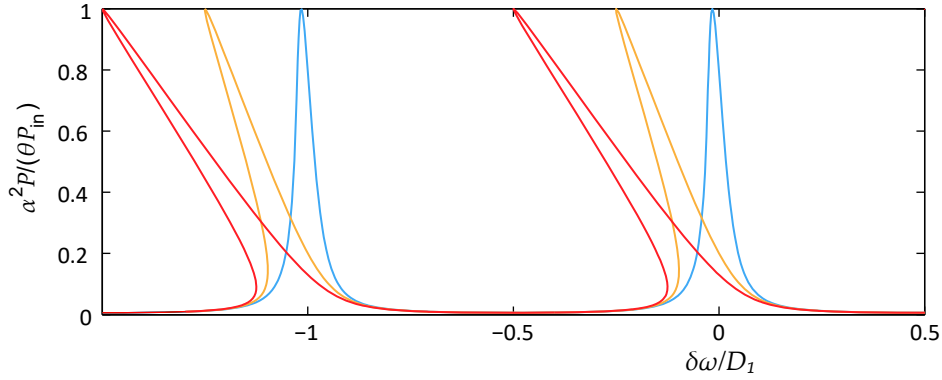


Figure 1.9: **Intracavity power enhancement as function of tuning ϕ and increasing nonlinear phase shift.** Adapted from [48].

a region of *bistability* underneath this tilt with a hysteresis depending on which direction you would tune into this resonance. In the high-finesse picture with frequency units,

$$\frac{|A|^2}{|A_{\text{in}}|^2} = \frac{\kappa_{\text{ex}}/T}{\left(\frac{\kappa}{2}\right)^2 + (\delta\omega + \Gamma|A|^2)^2} \quad (1.38)$$

where we introduce the nonlinear detuning coefficient in units of Hz/W

$$\Gamma = \frac{\gamma}{\beta_1} = \gamma \frac{L}{T} = \frac{n_2 \omega_0 L}{c T A_{\text{eff}}} \quad (1.39)$$

1.2.4 Modal dispersion

Returning to the topic of waveguide dispersion, while per metre dispersion coefficients are highly useful in design and modelling for resonators, *experimentally* it may sometimes be more useful to characterise dispersion with frequency units. In linear dispersive cavities, the above mentioned accumulated roundtrip phase varies with mode frequency $\phi \rightarrow \phi(\omega)$, where from Eq. 1.12,

$$\begin{aligned} \Delta\phi(\omega) &= \Delta\beta(\omega)L \\ &= \frac{\beta_2 L}{2}(\omega - \omega_0)^2 + \frac{\beta_3 L}{6}(\omega - \omega_0)^3 + \frac{\beta_4 L}{24}(\omega - \omega_0)^4 + \dots \end{aligned} \quad (1.40)$$

which causes every resonance frequency ω_μ to deviate from a uniformly spaced grid over a broad bandwidth. If we fix our reference point for the cavity repetition period T , we can obtain

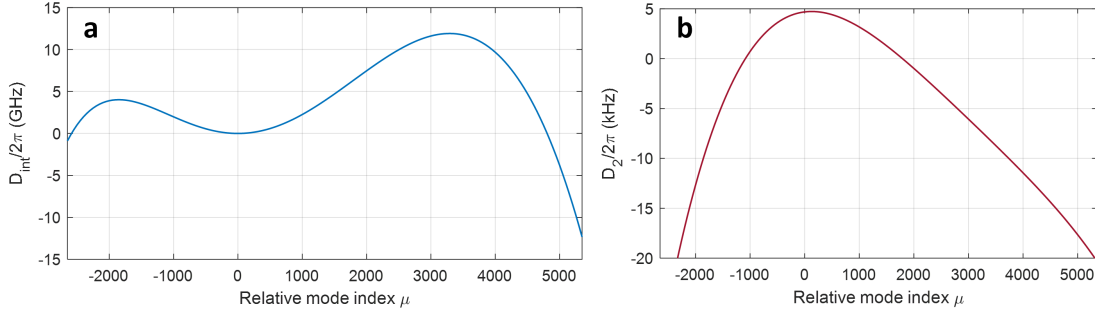


Figure 1.10: **Resonator mode dispersion, with calculated data converted from Fig. 1.4.** (a) Resonance mode deviation spectrum D_{int} of test Si_3N_4 waveguide. The resonance frequencies are seen to ‘return’ to the comb grid at two locations. (b) D_2 : the *change in FSR* D_1 as a function of mode index μ .

the deviation of modal frequencies away from the median FSR, (several different ways)

$$\frac{\Delta\beta(\omega)L}{T} = \frac{\Delta\beta(\omega)}{\beta_1} = \frac{\Delta\beta(\omega)LD_1}{2\pi} = D_{\text{int}} \quad (1.41)$$

fixing the group velocity as $\beta_1 = T/L$, re-introducing the FSR as

$$D_1 = \frac{2\pi}{T} = \frac{2\pi}{\beta_1 L} \quad (1.42)$$

and introducing the “integrated dispersion”

$$D_{\text{int}} \equiv \omega_\mu - \omega_0 - D_1\mu = \frac{D_2}{2}\mu^2 + \frac{D_3}{6}\mu^3 + \frac{D_4}{24}\mu^4 + \dots \quad (1.43)$$

with second-, third, fourth-order coefficients and so on

$$D_\ell = -\frac{D_1^{\ell+1}}{2\pi}\beta_\ell L \quad (1.44)$$

and corresponding with the OFC mode *index*

$$\mu = \frac{\omega - \omega_0}{D_1} \quad (1.45)$$

Similar to $\Delta\beta$, D_{int} expresses the deviation frequency of every resonance away from the *tangent* of the mode spectrum: the pump/centre frequency ω_0 and the FSR *evaluated* at that pump wavelength. The coefficients themselves are originally defined as

$$D_\ell = \frac{\partial^\ell}{\partial \mu^\ell} \omega_\mu \quad (1.46)$$

expressing the change in mode frequency per mode (the FSR D_1), the change in FSR per mode (the second-order dispersion D_2), the change in dispersion per mode (third-order D_3) and so on. In experiment, we characterise real microresonator devices by measuring ω_μ *directly*, and fit the coefficients D_ℓ , by conducting *frequency-comb calibrated swept-laser spectroscopy* of every real microresonator mode [49, 50]. The details of this technique are given in the references and a similar experimental schematic for measuring the live OFC is given later in Fig. 4.9. In brief, we use a separate full self-referenced frequency comb to accurately calibrate a series of 3 spectrally overlapping external-cavity diode lasers (ECDL) as they sweep from 1250 nm to 1640 nm. The sweeping lasers probe the transmission of every resonator mode (Eq. 1.36 and Fig. 1.8), and the result can be graphed in 2-dimensional form as in Fig. 1.1, where the total linear signal is chopped into fixed segments of the ‘repetition rate’ f_r and displayed column-wise on the y-axis, leaving each segment to be sorted on the x-axis in terms of mode index and optical frequency. An example result of this is plotted in Fig. 1.11.

1.2.5 The dynamical system equation

Considering the resonator depicted in Fig. 1.6(b), this system can be accurately described as a lumped model, specifically with the following two segments from Eqs. 1.19 and Eq. 1.25

$$A^{(r+1)}(z=0, \tau) = \sqrt{1-\theta} A^{(r)}(z=L, \tau) e^{i\phi_0} + \sqrt{\theta} A_{\text{in}} \quad (1.47)$$

$$\frac{\partial A}{\partial z} = -\frac{\alpha_l(z)}{2} A - \sum_\ell \frac{i^{\ell+1} \beta_\ell(z)}{\ell!} \frac{\partial^\ell A}{\partial \tau^\ell} + i\gamma(z)|A|^2 A \quad (1.48)$$

with the coupler equation setting $\rho = 1 - \theta$, and the NLSE component including the remaining waveguide dissipation via propagation, and higher orders of dispersion. This pair of conditions is often referred to as the “Ikeda Map” named for a 1979 work on such a system [51]. Although the lack of a single system equation makes finding well known solutions more complicated, this model represents the most reliable option, and is essential for accurately describing resonator systems with high loss and that have dramatic internal changes.

The LLE

For the sake of elegance and simplicity, the Ikeda map can be consolidated into a single ‘mean field’ model:

$$T \frac{\partial A}{\partial t} = (i\phi_0 - \alpha) A - i \frac{\beta_2 L}{2} \frac{\partial^2 A}{\partial \tau^2} + i\gamma L |A|^2 A + \sqrt{\theta P_{\text{in}}} \quad (1.49)$$

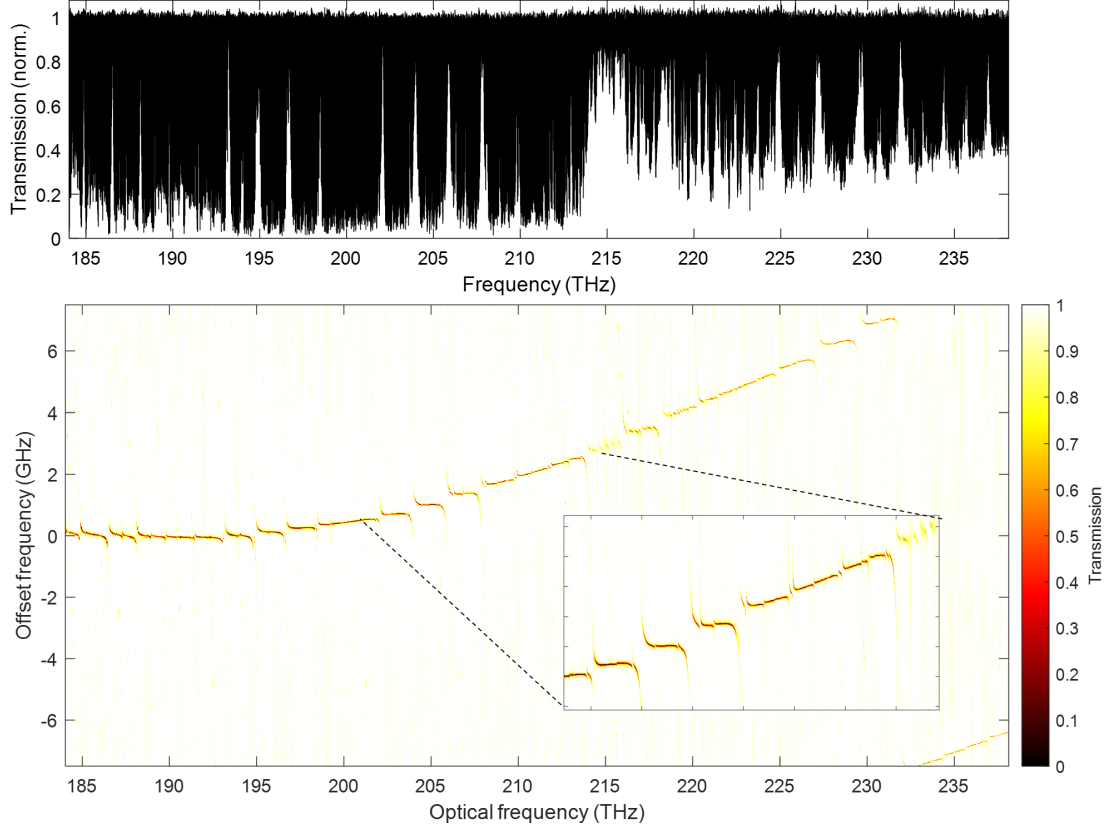


Figure 1.11: **Experimentally mapped dispersion/loss of resonator designed with waveguide from Fig. 1.2 and 1.10.** (Top) Frequency comb-calibrated transmission trace of microresonator (device ID: D62-2.F8.C6.R4(TE)), containing over 3,000 resonances. (Bottom) The trace above sorted into vertical segments of $f_r = 15.057$ GHz (the median FSR), revealing both D_{int} and the resonance κ and η .

known as the *Lugiato Lefever equation* [52] (LLE) in phase units for a dispersive resonator (now specifying pump *power* $P_{\text{in}} = |A_{\text{in}}|^2$ in W). Deriving this equation from Eqs. 1.47, 1.48 takes several assumptions. Firstly, the loss and change in phase over one roundtrip is small and so can be linearised, and particularly that the high-finesse approximation from Eq. 1.28 holds valid so that total roundtrip loss can be expressed by α . For the same reason, the first-order approximation is taken for coupler transmission $\sqrt{1-\theta}\exp(i\phi_0)$ so we must be able to assume that $\phi_0 \ll \pi$, that the detuning is only ever in the vicinity of one resonance, otherwise the Ikeda Map or a higher-order modified LLE should be used [53, 54].

Furthermore, we have related the long-term propagation of a pulse over distance z from the NLSE to the long-term behaviour of the intracavity field over “slow” time t , with

$$t = \frac{z}{L} T = \frac{2\pi z}{LD_1} = z\beta_1 \quad (1.50)$$

with attention paid to the factor of T existing on the lefthand side of Eq. 1.49. This model is conceptually best for modelling dynamics at fractions of the roundtrip time even though, as a mean-field model, it can be evaluated at steps arbitrarily longer than the roundtrip time provided that $t_{\text{ph}} \gg T$, which is commonly the case in crystalline microresonators or THz-rate Si_3N_4 resonators with finesse on the order of $\mathcal{F} \gtrsim 100,000$. For such tiny cavities, more like that depicted in Fig. 1.6(a), the system units of Eq. 1.49 may be mentally cumbersome and not directly applicable to experiment as briefly touched on in section 1.2.4. For that, the LLE can alternatively be re-expressed having coefficients in frequency units

$$\frac{\partial A}{\partial t} = -\left(\frac{\kappa}{2} + i\delta\omega\right)A + i\frac{D_2}{2}\frac{\partial^2 A}{\partial \varphi^2} + i\Gamma|A|^2A + \sqrt{\kappa_{\text{ex}}T^{-1}P_{\text{in}}} \quad (1.51)$$

this time assuming a whole resonator intracavity field directly bound within the spatial angular coordinate $\varphi \in (-\pi, \pi]$, related to the earlier fast time coordinate $\varphi = \tau D_1$. This time, the field A has units of \sqrt{W} and Γ as nonlinear frequency shift in Hz/W. In many publications from our group historically, the field A instead represents the sum of photons present at each cavity mode frequency. In that case, Eq. 1.51 is the same, but with nonlinear coefficient g_0 instead of Γ used here, with g_0 being the nonlinear frequency shift *per photon*. The two are related thus

$$g_0 = \frac{\hbar\omega_0^2 D_1}{2\pi} \Gamma = \frac{\hbar\omega_0^2 c n_2}{n_g^2 V_{\text{eff}}} \quad (1.52)$$

assuming the cavity mode volume $V_{\text{eff}} = LA_{\text{eff}}$. In either case, in my view it is conceptually useful to describe Kerr cavity phenomenon in relative units that are invariant to the peculiar properties of the real experimental resonator, whether it be a fibre-optic loop or photonic waveguide resonator large or small, made of material of high or low loss and nonlinearity and so on. This LLE is expressed as follows, alternatively as the two normalised forms

$$\frac{\partial \psi}{\partial t} = -(1 + i\zeta_0)\psi + i\mathfrak{d}_2 \frac{\partial^2 \psi}{\partial \varphi^2} + i|\psi|^2\psi + F \quad (1.53)$$

$$\frac{\partial \psi}{\partial t} = -(1 + i\zeta_0)\psi + id_2 \frac{\partial^2 \psi}{\partial \tau^2} + i|\psi|^2\psi + F \quad (1.54)$$

with Eq. 1.53 retaining the spatial angular coordinate φ , and Eq. 1.54 being unbound in the relative fast time domain. In all the above four versions of the LLE higher-order dispersion terms can be included ie.

$$+i^{\ell+1}\frac{\beta_\ell}{\ell!}\frac{\partial}{\partial \tau^\ell}, \quad +i^{\ell+1}\frac{D_\ell}{\ell!}\frac{\partial}{\partial \varphi^\ell}, \quad +i^{\ell+1}\mathfrak{d}_\ell\frac{\partial}{\partial \varphi^\ell}, \quad +i^{\ell+1}d_\ell\frac{\partial}{\partial \tau^\ell}$$

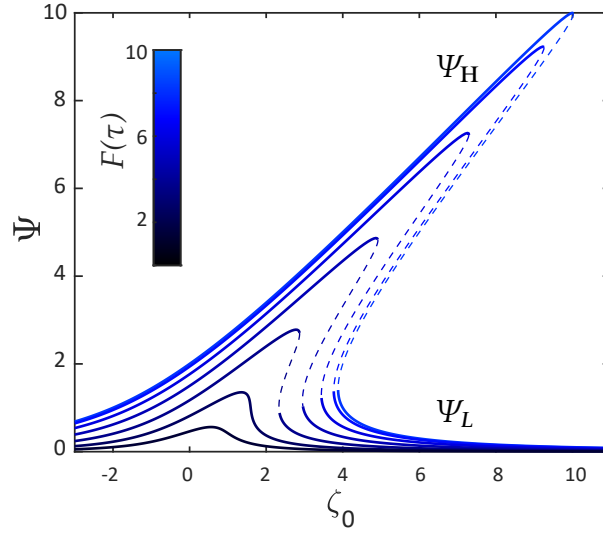


Figure 1.12: CW intracavity power in dimensionless units vs. detuning ζ_0 and increasing nonlinear driving F^2 . The dashed-line solutions are never stable.

In the end, the following transformations are used³

$$\begin{aligned}
 t &= t \frac{\alpha}{T} & \tau &= \tau \sqrt{\frac{2\alpha}{|\beta_2|L}} & \psi &= A \sqrt{\frac{\gamma L}{\alpha}} \\
 t &= t \frac{\kappa}{2} & \tau &= \tau \sqrt{\frac{\kappa}{|D_2|}} & \psi &= A \sqrt{\frac{2\Gamma}{\kappa}} \\
 \zeta_0 &= \frac{-\phi_0}{\alpha} & d_\ell &= \frac{\beta_\ell L}{\alpha \ell!} \left(\frac{2\alpha}{|\beta_2|L} \right)^{\ell/2} & F &= A_{\text{in}} \sqrt{\frac{\gamma L \theta}{\alpha^3}} \\
 \zeta_0 &= \frac{2\delta\omega_0}{\kappa} & d_\ell &= \frac{2D_\ell}{\kappa \ell!} \left(\frac{\kappa}{|D_2|} \right)^{\ell/2} & F &= A_{\text{in}} \sqrt{\frac{4\kappa_{\text{ex}} D_1 \Gamma}{\pi \kappa^3}} \\
 \varphi &= \tau D_1 & \vartheta_\ell &= \frac{2D_\ell}{\kappa \ell!} & \varphi &= \tau \sqrt{\vartheta_2}
 \end{aligned} \tag{1.55}$$

Importantly, $d_2 = 1$ or -1 properly, but it is useful to include regardless. In that case, for Eq. 1.54, the only two control parameters are now ζ_0 and F . Even in experiment, regardless of platform or FSR and so on, knowing just these two values tells you everything you need to know about the basic dynamical behaviour of individual dissipative phenomenon.

Returning to the equilibrium solutions from earlier, if we consider a only constant-wave (CW) field existing in the cavity governed by Eq. 1.54, then the dispersion terms vanish and, if we set the lefthand side to zero we find

³Pay attention to the difference in typesetting between normalised t and real t , and normalised τ and real τ

$$F = [1 + i(\zeta_0 - |\psi_{\text{CW}}|^2)]\psi_{\text{CW}} \quad (1.56)$$

which gives us the normalised form of the tilted resonance Eq. 1.38, shown later on in Fig. 3.2. By taking the modulus on both sides, we can obtain a cubic equation

$$\Psi^3 - 2\zeta_0\Psi^2 + (1 + \zeta_0^2)\Psi - F^2 = 0 \quad (1.57)$$

with $\Psi = |\psi|^2$. By finding the roots of this equation, we are able to solve for the complex amplitude solutions to Eq. 1.56, particularly to find the stable high and low CW solutions ψ_H and ψ_L which are relevant to chapters 3 and 4. The tilted CW resonance is shown in Fig. 1.12 for increasing relative nonlinear driving power F^2 . Bistable solutions begin to exist for $F^2 > (2/\sqrt{3})^3$ [55].

The generalised dynamical system

A real photonic microresonator will not be fully described by the LLE described above, and higher-order terms should sometimes be included to create an accurate prediction. The following is the *generalised* LLE (GLLE) containing all effects present in this thesis, with descriptions below:

$$\begin{aligned} \frac{\partial A}{\partial t} = & \mathcal{F}_\tau \left[(i\hat{D}_\mu(t) + \hat{K}_\mu(t))\tilde{A}_\mu \right] \\ & + i\Gamma(t) \left[(1 - f_R)|A|^2 A + f_R(h_R(\tau) \otimes |A|^2)A \right] \\ & + T^{-1}(\Theta(\tau) \otimes A_{\text{in}}(\tau)) \end{aligned} \quad (1.58)$$

High-order dispersion

The linear operator \hat{D} contains every imaginary frequency response of the cavity ie. detuning, desynchronisation (drift or convection[56]), and dispersion. For instance

$$\hat{D} = \delta\omega(t) + \mu(2\pi\delta f_r(t)) + D_{\text{int}}(\mu, t) + \delta\hat{D}_\mu \quad (1.59)$$

where included now is the offset relative repetition rate (or desynchronisation) δf_r which models a field constantly “moving” faster or slower than it is recorded, perhaps relative to the ‘stationary’ pump function $P_{\text{in}}(\tau)$. More on this in chapter 2 and further. The integrated dispersion D_{int} can as usual be modelled as a polynomial expansion, including up to many orders of D_ℓ (typically 6 is enough for Si_3N_4 microcombs), but there is no requirement for this. It can be arbitrarily curved to include, for instance, broadband deviations due to transverse

mode hybridisations (avoided-mode crossings)[57, 58]. Recently, microcomb experiments and modelling involving arbitrary individual comb mode shifts have been taking place, where $\delta\hat{D}_\mu = \epsilon(1 - \delta(\mu))$ with mode shift ϵ at the mode index given by Kronecker delta function $\delta(\mu)$.

Spectrally dependent dissipation

Over a broad spectral bandwidth, different wavelengths experience different dissipation due to material absorption and sidewall roughness. In addition, different wavelengths also couple between the bus waveguide and resonator at different rates. So that inside the resonator

$$\hat{K} = \hat{\kappa}_0(\mu, t) + \hat{\kappa}_{\text{ex}}(\mu) \quad (1.60)$$

and also the output microcomb may be *skewed* to higher or higher lower wavelengths (usually lower) with

$$\Theta(\tau) = \mathcal{F}[\sqrt{\hat{\kappa}_{\text{ex}}(\mu)}]_\tau \quad (1.61)$$

Forgetting this latter point especially has led to several overly-optimistic predictions about octave-spanning microcombs! Even if the comb lines are populated inside the resonator, they may never leave through the bus waveguide to be measured[59].

Temporal (pulsed) driving

The incident power can be any profile with varying phase and intensity

$$A_{\text{in}}(\tau) = \sqrt{P_0(t)}F_p(\tau, t)e^{i\phi_p(\tau)} \quad (1.62)$$

with peak power P_0 , pulsed or modulated envelope F_p , and input phase curvature or chirp $\phi_p(\tau)$. This will be addressed in substantial detail in the following chapter.

Floquet dynamics, parametric variation

In general, any resonator parameter may, and does, vary with distance and therefore slow time t . Waveguide roughness for instance is a key reason transverse spatial modes are able to couple together creating mode mixing. This, and the consequent *Floquet* dynamics, are covered in detail in chapter 4.

Noise

Looking above, note that key parameters may vary with slow time as noise, such as $\delta\omega(t)$ representing pump laser frequency noise, $P_0(t)$ pump intensity noise, or $F_p(\tau - \delta\tau(t))$ corresponding to timing jitter. The cavity itself may flex in length, and therefore *duration* $f_r(t)^{-1}$ due to thermal noise. Timing jitter specifically is investigated in the next chapter.

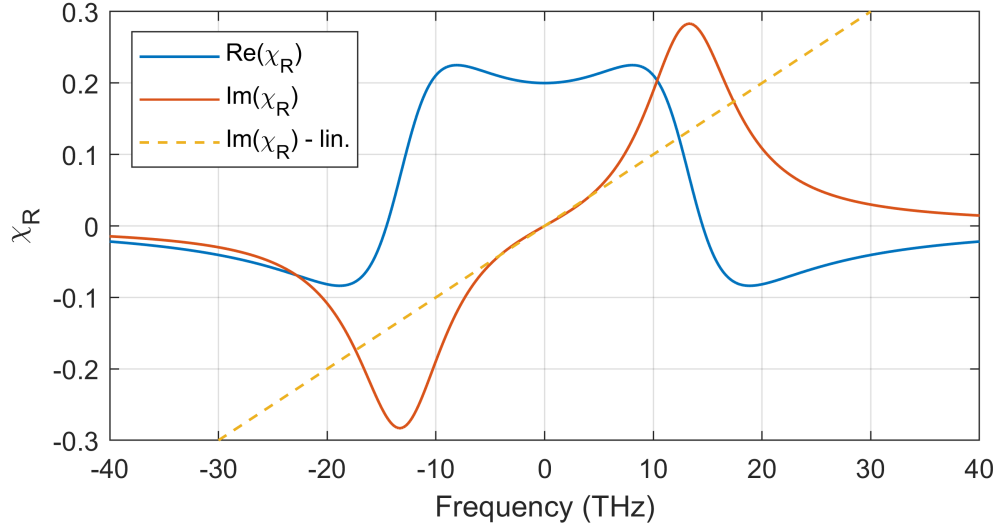


Figure 1.13: **Real and imaginary component of the Raman contribution to the Kerr effect.**

Stimulated Raman scattering (SRS)

Finally, the intracavity field may be subject to the Raman scattering effect, exhibited strongly in SiO_2 and GaP, where the power envelope of the travelling light couples to molecular vibrations in the waveguide, such that a pump photon is absorbed and an acoustic phonon along with a lower energy photon is emitted in exchange. This effect is manifested with a delayed response to the imaginary component of the $\chi^{(3)}$ nonlinearity and therefore Γ , with a contribution factor f_R . The associated Raman response in glass can be approximated as a ringing impulse response

$$h_R(\tau) = \frac{\tau_1^2 + \tau_2^2}{\tau_1 \tau_2^2} e^{-\tau/\tau_2} \sin(\tau/\tau_1) \quad (1.63)$$

with a frequency τ_1^{-1} and decay constant τ_2 , the Fourier transform of which is shown in Fig. 1.13, exhibiting a maximum gain at a downward frequency shift of about 13 THz. In narrow band, the response can be approximated as linear [60, 61].

1.2.6 Numerical modelling

All work in this thesis on simulating the LLE or GLLE utilises the split-step Fourier method [62], where the LLE is considered analytically solvable over distances short enough that the dispersion and nonlinearity do not contradict each other, and hence are treated *separably*. Here it is shown directly in my Matlab code:

```
function C3 = LLE_splitstep(C1,L,S,g,x)

N = 1i*g*abs(C1).^2;

C2 = exp(x*N).*(C1 + S./N) - S./N;

C3 = fft(exp(x*L).*ifft(C2));
```

for evaluating the LLE without Raman scattering. The LLE is integrated step wise over distance x , g the nonlinear coefficient, and S the driving pump array. The linear operator

$$\hat{L} = i\hat{D} + \hat{K} \quad (1.64)$$

as above in Eq. 1.58, including all losses and detuning/dispersion. For when Raman scattering is enabled:

```
function C3 = LLE_splitstepR(C1,L,S,g,fr,ChiR,x)

I = ifft(abs(C1).^2);
N = 1i*g*((1-fr)*abs(C1).^2 + fr*fft(ChiR.*I));

C2 = exp(x*N).*(C1 + S./N) - S./N;

C3 = fft(exp(x*L).*ifft(C2));
```

with Raman contribution factor fR and the Raman response in the frequency domain $\tilde{\chi}_R^{(3)}$ from Fig. 1.13.

In order for this to be accurate, x should be less than the dispersion length $L_D \approx (\beta_2 \Omega^2)^{-1}$ (for pulse bandwidths of Ω) and the nonlinear length $L_N = (\gamma P)^{-1}$ with P the peak power inside the cavity. Furthermore, for a very broadband simulation with thousands of comb lines to model, the step length has to be sufficiently short so as not to stimulate the growth of false sidebands at the edges of the spectral window. The rapid switching between dispersion step and nonlinear step creates a simulated ‘grating’, and enables quasi-phase matching between the pump and far away modes with very strong phase-shifts due to the dispersion. Ironically,

this leads to ‘numerical’ Faraday instability, not unlike the phenomenon discussed in chapter 4.

1.3 Taxonomy of phase states, modulation instability, dissipative solitons and switching waves

This section will detail the foundational set of dissipative Kerr cavity regimes and structures, including a look at their would-be Kerr microcomb properties through the slow vs. fast frequency diagram (as in Fig. 1.1) (sometimes referred to as the ‘nonlinear dispersion relation’ (NDR)) [63, 64, 65]:

$$\tilde{\psi}(\Omega, \zeta) = \mathcal{F}_t \left[W_t \mathcal{F}_\tau [\psi(t, \tau)] \right] \quad (1.65)$$

In terms of *resonant radiation* and gain for laterally spaced frequencies oscillating in 2D frequency space at $\exp[\pm i\Omega\tau \pm i\zeta t]$, in a quasi-CW driven Kerr cavity, we have the following resonant radiation conditions (RRC) from linearising Eq. 1.54 [66, 67, 68]:

$$\zeta_{L\pm}(\mu) = -\delta d_1 \Omega + d_3 \Omega^3 \mp \sqrt{(\zeta_0 - d_2 \Omega^2 - d_4 \Omega^4 - 2|\psi_L|^2)^2 - |\psi_L|^4} \quad (1.66)$$

$$\zeta_{H\pm}(\Omega) = -\delta d_1 \Omega + d_3 \Omega^3 \mp \sqrt{(\zeta_0 - d_2 \Omega^2 - d_4 \Omega^4 - 2|\psi_H|^2)^2 - |\psi_H|^4} \quad (1.67)$$

here associated to either the intracavity field existing in the upper or lower CW state solution ψ_H and ψ_L . Where ζ_{\pm} is real and intersects with the horizontal microcomb four-wave mixing grid, we find resonant radiation ie. dispersive wave (DW) emission [67, 69]. Where the ζ_{\pm} is imaginary, we see spontaneous gain: *modulation instability* (MI) [70], and in parametrically modulated cavities as *Faraday instability* (FI) [71, 72].

1.3.1 Modulation instability

For anomalous dispersion $d_2 = -1$ when the cavity field is in the upper state $\psi = \psi_H$, and neglecting other orders of dispersion ($d_{1,3,4} = 0$), the above RRC simplifies to

$$\zeta_{\pm}(\mu) = \mp \sqrt{(\zeta_0 + \Omega^2 - 2|\psi|^2)^2 - |\psi|^4} \quad (1.68)$$

and MI gain exists for some sideband frequency $\pm\Omega$ when the imaginary component of $\zeta_{\pm}(\mu)$ is non-zero [70, 55], which in anomalous dispersion corresponds simply to the intracavity field power $\Psi = |\psi|^2 > 1$. Above threshold this requires a detuning (from Eq. 1.57)

$$\zeta_0 > 1 - \sqrt{F^2 - 1} \quad (1.69)$$

with first sideband gain at threshold located at

1.3 Taxonomy of phase states, modulation instability, dissipative solitons and switching waves

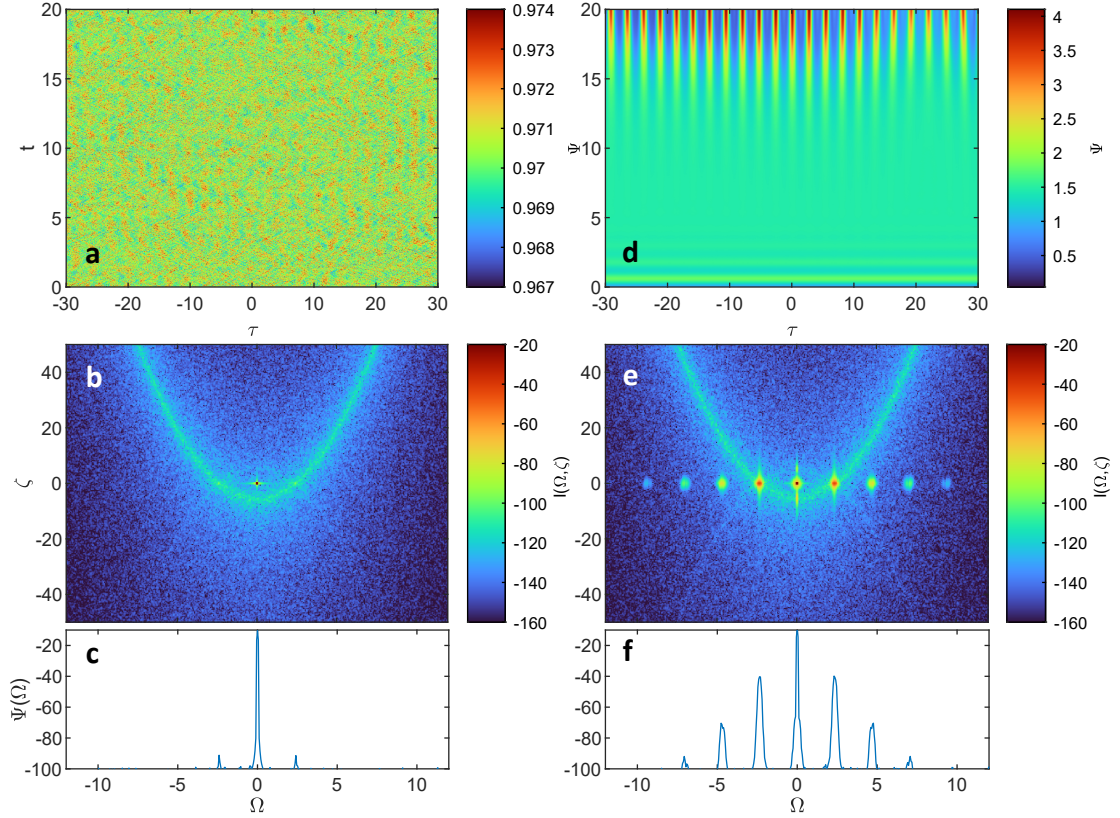


Figure 1.14: **Simulation for onset of modulation instability (MI) from Eq. 1.54 at $F^2 = 25$, and for (a-c) $\zeta_0 = -4$ and (d-f) $\zeta_0 = -2.5$.** (a,d) Intracavity field $|\psi(t, \tau)|^2$ propagating over slow time vs. fast time. (b,c) The same field converted to slow vs. fast frequency field density $|\tilde{\psi}(\Omega, \zeta)|^2$. (c,f) The resulting averaged spectral envelope $\tilde{\Psi}(\Omega)$ one would observe in experiment.

$$\Omega_{\text{th}} = \pm \left[1 + \sqrt{F^2 - 1} \right]^{1/2} \quad (1.70)$$

If we simulate the LLE (Eq. 1.54), with a small amount of continuously injected random Gaussian noise onto the field, we observe the behaviour depicted in Fig. 1.14(a-c) at the MI threshold and in Fig. 1.14 for above the threshold, with the detuning $\zeta_0 < 0$ on the ‘blue’ side of the resonance behind the Kerr tilt (see Fig. 1.12). In Fig. 1.14(a) at threshold, we see the noisy field is CW, but exhibits pockets of a below-threshold wave pattern. In the ‘NDR’ in (b), a pair of conjugate nonlinear dispersive resonance curves is observed, following the parabolic lines predicted by the RRC $\zeta_{H\pm}$. The bright band corresponds to ζ_{H-} , approximately following the cavity $d_{\text{int}} = -d_2\Omega^2$. Importantly, at the pump frequency located at $\Omega = 0$, the offset location of this resonance is roughly equal to the detuning ζ_0 and has appeared in experiments as the “C-resonance” detected using phase-modulated probing of the resonator and a network analyser [73, 74]. The other dispersive resonance curve ζ_{H+} appears very weak as it is the anti-Stokes four-wave mixing conjugate for ζ_{H-} and has low efficiency due to the low level of intracavity power at this detuning. Increasing the detuning to $\zeta_0 = -2.5$ raises the intracavity

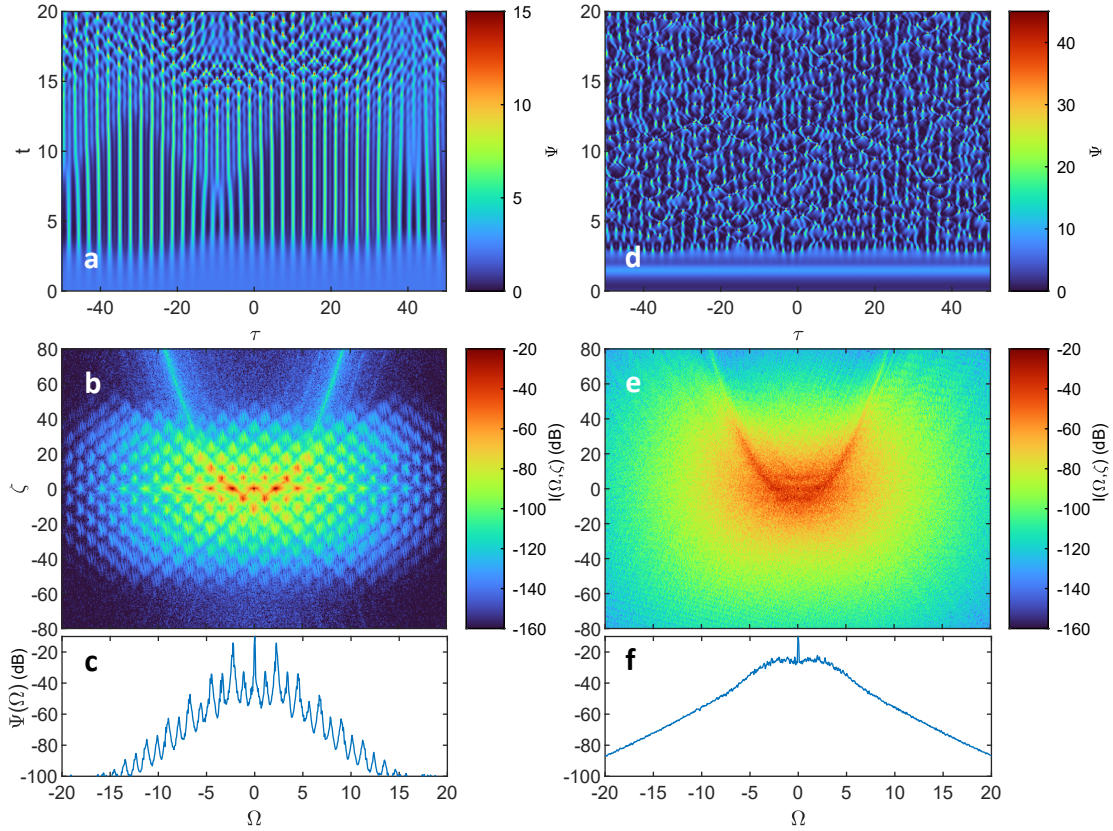


Figure 1.15: **Simulation for intermittent MI from Eq. 1.54 at $F^2 = 25$, for (a-c) $\zeta_0 = -1$ and turbulent MI in (d-f) at $\zeta_0 = 4$.** (a,d) Intracavity field $|\psi(t, \tau)|^2$ propagating over slow time vs. fast time. (b,c) The same field converted to slow vs. fast frequency field density $|\tilde{\psi}(\Omega, \zeta)|^2$. (c,f) The resulting averaged spectral envelope $\tilde{\Psi}(\Omega)$ one would observe in experiment.

CW power Ψ above 1, and MI gain is realised at the intersection of $\zeta_{H\pm}$, close the prediction from Eq. 1.70, and we see the emergence of a patterned solution to the cavity field. When stable, these first spectral/comb lines are called “primary lines”, and the intracavity pattern is referred to sometimes as ‘Turing rolls’.

With the power level set relatively high at $F^2 = 25$, if we continue to increase the detuning ζ_0 we observe transition from stable MI to “intermittent” MI [75] in Fig. 1.15(a-c), where the patterned solution is oscillatory in time and so acquires frequency components off the middle comb axis and into the $\pm\zeta$ direction, a phenomenon referred to as “sub-combs” [76]. The instability overt the long term is relatively gentle and so individual sub-comb lines are still resolvable. When ζ_0 is increased further we enter the full chaotic or ‘turbulent’ regime [75] in Fig. 1.15(d-f), where all comb lines have completely dissolved into each other. In the time domain in (d), this can be seen due to chaotic lateral motion of dissipative structures, sometimes generating *rogue waves*. In microresonators before dissipative solitons were discovered, this state (as seen in Fig. 1.15(f)) was most often the object of research [77, 78, 76].

1.3 Taxonomy of phase states, modulation instability, dissipative solitons and switching waves

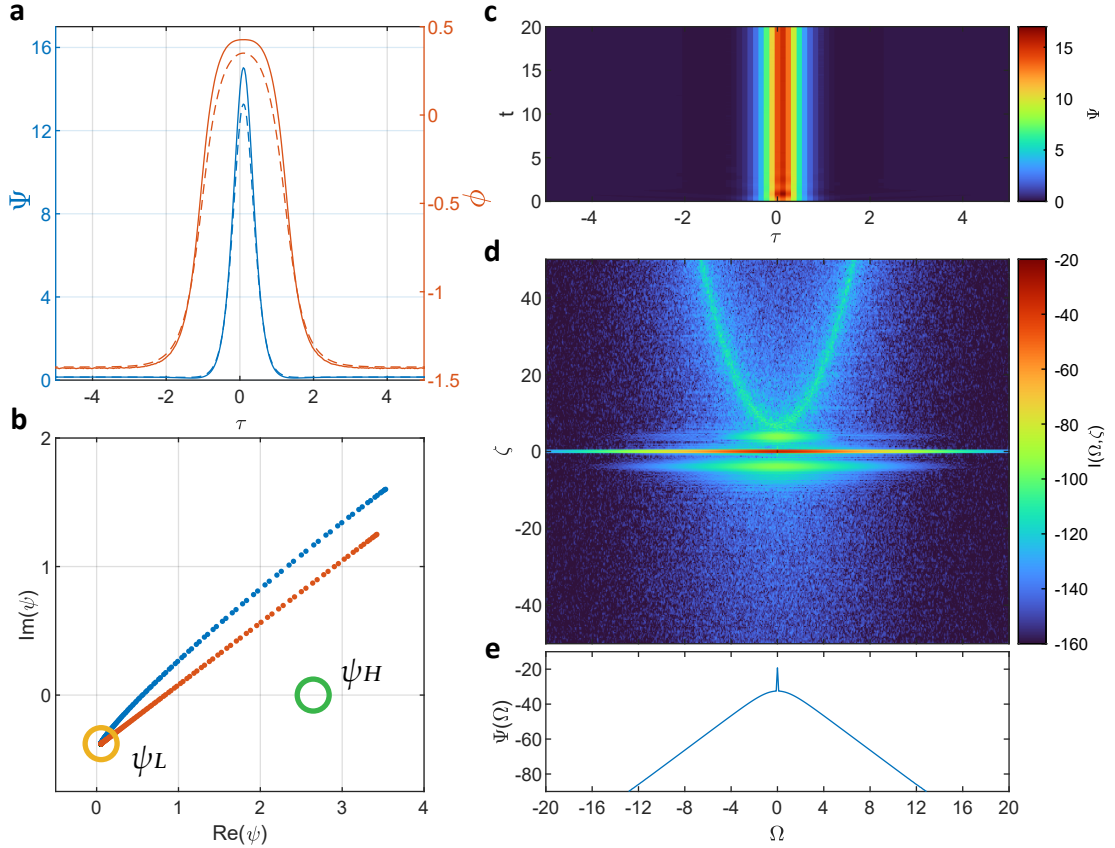


Figure 1.16: **Dissipative Kerr soliton (DKS), numerical solution to the LLE (Eq. 1.54).** $F^2 = 7$, $\zeta_0 = 7$. (a) Numerically obtained solution for intracavity DKS, in intensity and phase. Overlaid is the analytical solution as an approximation. (b) DKS solution ψ_{DS} in complex space, (blue) numerical and (red) analytical solution. Circles mark the CW states ψ_L and ψ_H . (c) Stable intracavity DKS propagation over the slow time t . (d) Slow vs. fast frequency diagram of DKS long term state. (e) Average DKS spectral envelope over the total propagation time.

1.3.2 Dissipative Kerr solitons

Dissipative Kerr solitons (DKS), also often just called dissipative solitons or temporal cavity solitons, are a primary type of *localised dissipative structure* (LDKS) featured in the research of this thesis. DKS are solitary pulses that are able to exist in continuously driven Kerr cavities stably and indefinitely. Whereas conservative solitons, as solutions to the NLSE (Eq. 1.19), exist as part of a continuous family of solutions, DKS have a peak power and duration that is uniquely set by the driving parameters F and ζ_0 . Existing within the *bistable* region of the nonlinear Kerr-tilted cavity resonance (Fig. ?? and ??), dissipative solitons essentially represent a rapid excursion in complex amplitude that *connects* the lower stable CW state of the cavity ψ_L with the MI-driven patterned solution that exists along the upper state [80, 81]. As the dynamics of the LLE are invariant to temporal translation, DKS can exist individually in high numbers throughout the angular/temporal ‘space’ of the cavity provided they are outside each

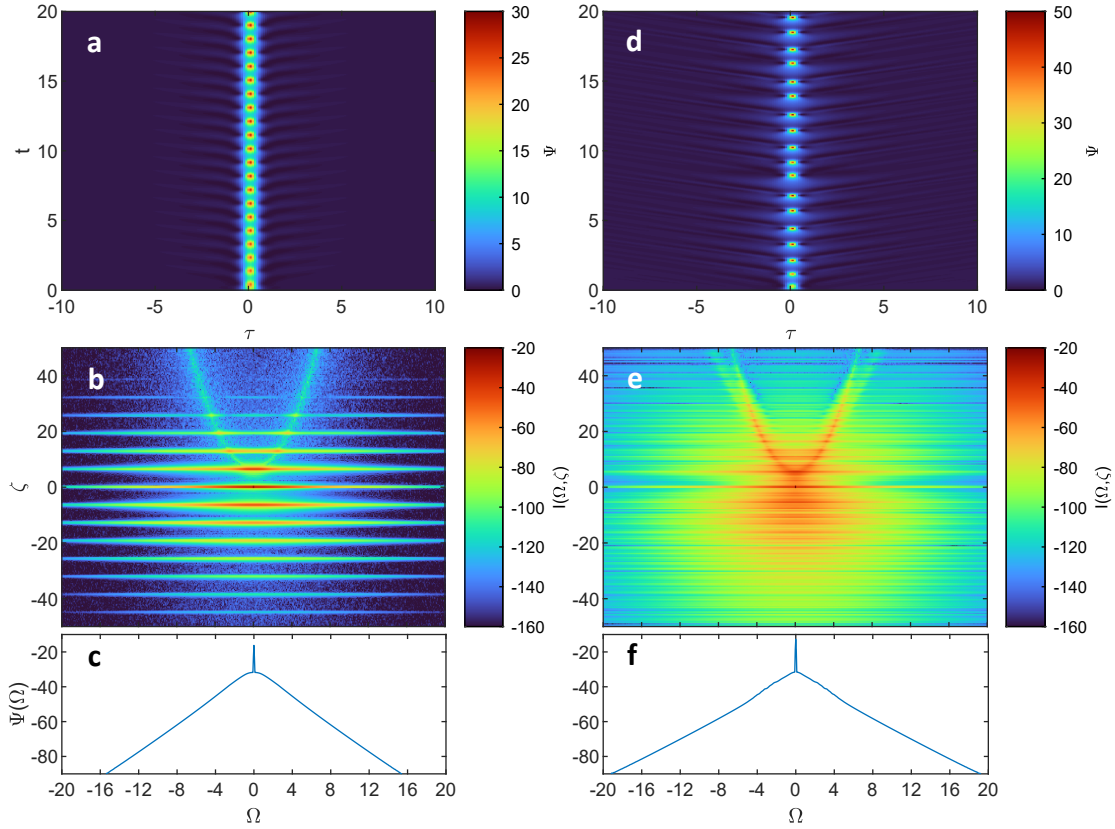


Figure 1.17: **Simulation for constant breathing soliton at $\zeta = 7$, for (a-c) $F^2 = 14$ and a soliton breathing chaotically in (d-f) at $F^2 = 25$.** (a,d) Intracavity field $|\psi(t, \tau)|^2$ propagating over slow time vs. fast time. (b,c) The same field converted to slow vs. fast frequency field density $|\tilde{\psi}(\Omega, \zeta)|^2$. (c,f) The resulting averaged spectral envelope $\tilde{\Psi}(\Omega)$ one would observe in experiment.

other's influence, shown in Fig. 1.16(a) analytically and numerically.

An analytical approximation for the soliton can be found[82, 83, 84] if the LLE Eq. 1.54 were considered in the limit of low loss:

$$\psi_{\text{DS}}(\tau) = \sqrt{2\zeta_0} \text{sech}(\sqrt{\zeta_0}\tau) e^{i\phi_{\text{DS}}} \quad (1.71)$$

$$\phi_{\text{DS}} = \cos^{-1} \left(\frac{2\sqrt{2\zeta_0}}{\pi F} \right) \quad (1.72)$$

which is in general a good approximation (also plotted in Fig. 1.16) in cases of moderately strong nonlinear driving $F \gtrsim 3$ [85], and is a good starting point for forcing the solution in dynamical split-step simulations. In the slow vs. fast time picture, Fig. 1.16(c), the DKS

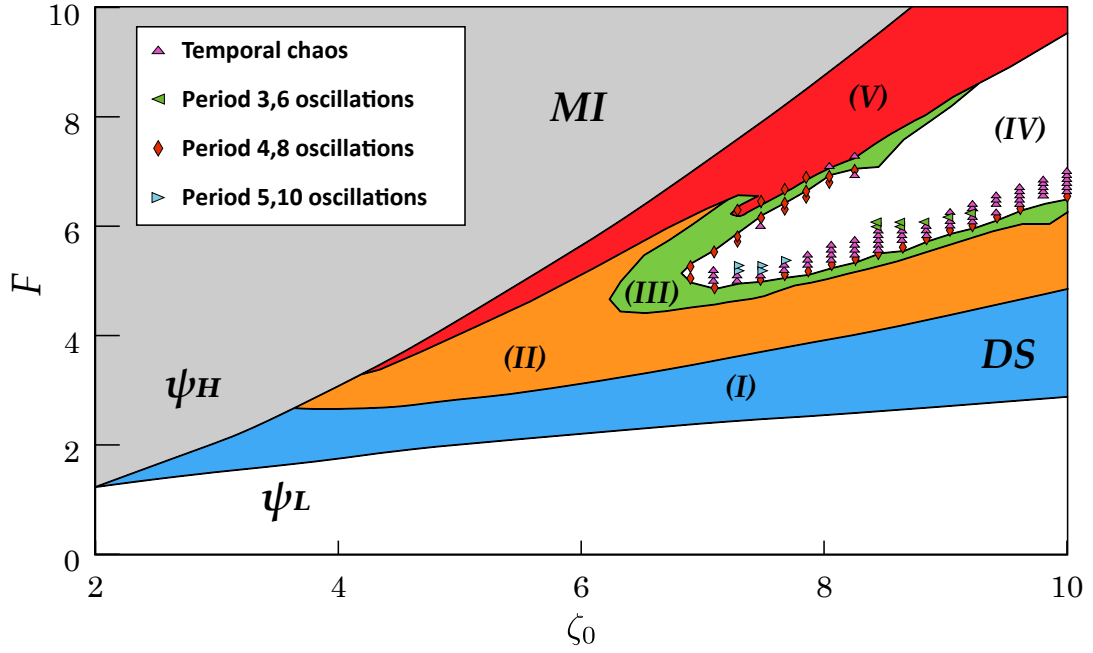


Figure 1.18: Adapted from [79], a full numerically obtained survey of dynamical states for DKS in the Kerr bistable region. (I) Stable soliton with constant profile over t . (II) Defined breathing cycle/orbit. (III) Breathing with a split limit cycle over 2 alternating periods. (IV) Transient chaos. (V) Spatiotemporal chaos.

exists as a constant in slow time t and accordingly in slow vs. fast frequency picture in (d) forms the horizontal comb grid locked together by the energy transfer of FWM and spectral nonlinear phase shift \hat{N} counter-acting the linear operator L , the residue of which is seen in the background dispersive RRC ζ_{L-} as the bright parabolic band.

Also seen above and below the DKS in the ζ dimension are a pair of parallel relaxation frequencies, identified as the S-resonance in live cavity probing measurements of the DKS state in experiment [73, 74]. If the power and detuning are brought to a point where these frequencies coincide with ζ_{L-} , the DKS begins to acquire a ‘ladder’ of offset combs [86] oscillating in the slow frequency $\pm\zeta$ dimension similar to unstable MI, shown next in Fig. 1.17. Here, we observe two regimes of dissipative soliton *breathing*[79, 87] where the DKS undergoes a repeating cycle of temporal compression, absorbing energy from the pump, and then partial collapse and radiation of energy into the surrounding field. In Fig. 1.17(a-c), the breathing frequency ladder is defined and the breathing limit cycle is fixed. In Fig. 1.17(d-f) further into the nonlinear driving regime, this ladder has dissolved into a broad band similar to the MI state above in Fig. 1.15(d-f). In the time domain, this corresponds to a *chaotic* breathing cycle [88]. The effect in the frequency domain is to turn the soliton sech^2 envelope into more of a triangular form[87]. Knowing when and whether the DKS will be stable or breathing is naturally relevant for microcomb applications, which is why being informed on the dynamical attractor chart,

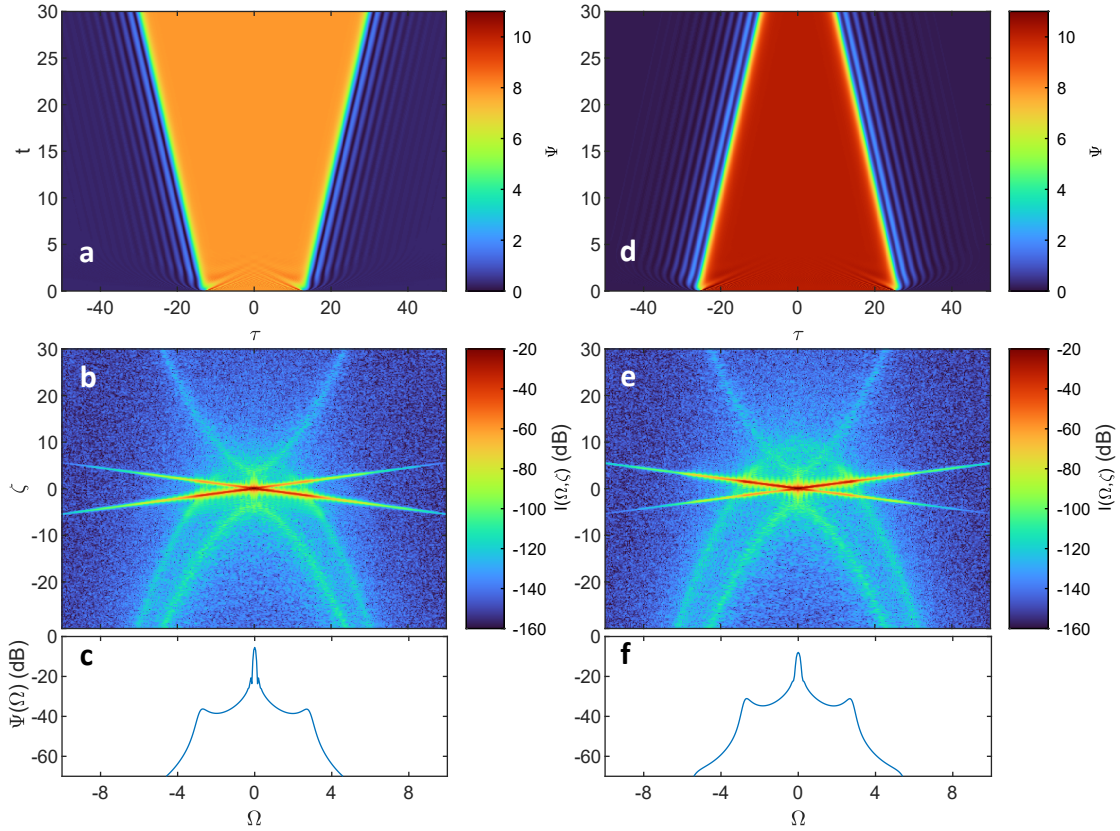


Figure 1.19: **Dissipative Kerr soliton (DKS), numerical solution to the LLE (Eq. 1.54).** $F^2 = 7$, $\zeta_0 = 7$. (a) Numerically obtained solution for intracavity DKS, in intensity and phase. Overlaid is the analytical solution as an approximation. (b) DKS solution ψ_{DKS} in complex space, (blue) numerical and (red) analytical solution. Circles mark the CW states ψ_L and ψ_H . (c) Stable intracavity DKS propagation over the slow time t . (d) Slow vs. fast frequency diagram of DKS long term state. (e) Average DKS spectral envelope over the total propagation time.

adapted from the investigation of *Leo et al.*[79] and *Parra-Rivas et al.*[80] presented in Fig. 1.18, is essential. In the phase space of driving F and detuning ζ_0 , the soliton regimes observed above are mapped out in regions (I) for stable DKS, and (II) for ‘stable’ breathing DKS. The chaotic breathing DKS shown in Fig. 1.17(d-f) is located at the rim of region (IV) where DKS transition from harmonic breathing to fully a-periodic breathing via region (III), the *period-doubling* cascade route to chaos[55]. Importantly, within regions (IV) and (V), single DKS can no longer exist over the long term[88, 48]. In the former, DKS will eventually leave their breathing orbits spontaneously and the field returns to the homogenous CW ψ_L solution. In the latter by contrast, the lower CW field ψ_L itself becomes unstable surrounding the breathing DKS, and the DKS is liable to nucleate an expanding domain of chaotic modulation instability, eventually filling the cavity field.

1.3.3 Switching waves

Here, we turn attention away from the anomalous dispersion regime and towards *normal* dispersion with $d_2 = +1$. In conservative systems of continuous propagation with the NLSE, the localised solution here is not a ‘bright’ soliton, but rather a ‘dark’ soliton. The NLSE dark soliton corresponds to a phase-flip within a travelling CW field forming an intensity dip or kink[89]. For Kerr cavities with normal dispersion, things are different. Instead, both CW solutions in Kerr bistability ψ_H and ψ_L are completely nominally stable, however, a solitary connection between the two is able to exist called a *switching wave* (SW) [90] (complex profiles are shown later in Fig. 3.7). In periodic cavity fields, SWs must naturally come in pairs but, just as with multiple soliton states, the two SWs act independently. Fig. 1.19 shows the excitation of a pair of SW fronts in the LLE system. The seed is a rectangular function connecting the pre-solved ψ_H on the inside and ψ_L on the outside. The two individual SW profiles in the frequency domain, unlike solitons, are spectrally unbalanced, and thus have an equilibrium tilt or ‘lean’ in the ζ vs. Ω space, opposite to each other. For this reason, they acquire opposite group velocities [56] depending on the value of F and ζ_0 .

With a fixed value of $F^2 = 14$, in Fig. 1.19(a-c) $\zeta_0 = 7$, the SW fronts have an outward or expanding velocity, and the lower state ψ_L is effectively invaded by ψ_H akin to an explosive shockwave. In Fig. 1.19(b), we see in the slow vs. fast frequency domain *both* upper and lower state RRCs (Eq. 1.66) are represented. Due to the higher power of the ψ_H field, ζ_{H+} is highly visible, and because of the low level of ψ_L , ζ_{L+} is not. We can see that the comb grids of ψ_{SW} in this scenario intersect with the ζ_{L-} RRC, causing the formation of dual shockwaves and the termination of the SW spectrum at the wings, creating the signature SW spectral envelope seen in Fig. 1.19(c). In Fig. 1.19(d-f), $\zeta_0 = 9$ and the SW velocities have reversed and ψ_H is invaded by ψ_L . There exists a value of ζ_0 between these two examples where the SW velocity is zero, termed the “Maxwell Point”. Although such a point exists, it is not a stable locked state and, in general, SWs are always free running and require an element of non-locality in order to ultimately stabilise their front motion. This is covered in chapter 3.

2 Pulse driven soliton microcomb generation and noise filtering

At the start of this research thesis, the idea of improving the microcomb generation process and efficiency by replacing the usual continuous-wave (CW) laser input with an optical pulse train, synchronised to the resonator repetition rate, was gaining interest. The driven Kerr cavity system, governed by the LLE (Eq. 1.49), is said to be *locally* coupled in terms of optical nonlinear frequency conversion[91], and *invariant* to temporal translation, ie. what happens at one end of the resonator is no business of the other end[92]. As such, unlike in a mode-locked laser with an active gain-medium, each dissipative soliton derives its energy from its *immediate* temporal overlap with the background pump. In terms of power budget, this makes the all pump energy temporally outside the soliton *waste*. For many years, synchronous pulse-driving was used in optical fibre-loop resonators[71, 93, 88, 53] mainly for two reasons: pulse-driving effectively *windows* the temporal gain region inside the cavity to ensure we can isolate a single soliton state (see Fig. 2.2) and, given a strongly decreased input pump duty-cycle and the use of an EDFA, a significantly higher peak power can be made available for soliton generation for either efficiency purposes, or to observe chaotic behaviour[88]. Pulse-driving for soliton microcomb generation was demonstrated by *Obrzud et al.*[94] just before this work began, where they made use of an *electro-optic* comb (EO-comb) to create the optical pulse train with a repetition rate necessary to match with a 10 GHz fibre Fabry-Perot cavity.

In my work, the goal was to use this method to explore single-soliton microcomb generation in a Si_3N_4 microresonator, with its dispersion specifically designed to deliver a frequency comb spectrum as wide as possible, ideally reaching an octave in bandwidth. The comb line spacing had to be accessible to microwave electronics ($< 20 - 40$ GHz), so as to avoid requiring further modulation-transfer techniques[95]. This goal was likened by us to *resonant* supercontinuum generation[96] (SCG). This, along with the specific goal of reaching an octave-spanning microcomb spectrum, will be covered further in chapter 5. I further investigate, numerically and experimentally, the nature of the bonding between the generated dissipative soliton (DKS) and the driving pulse, particularly the *nonlinear* filtering[97] of noise transfer this weak bonding gives rise to. This nonlinear filtering is found, remarkably, to combat

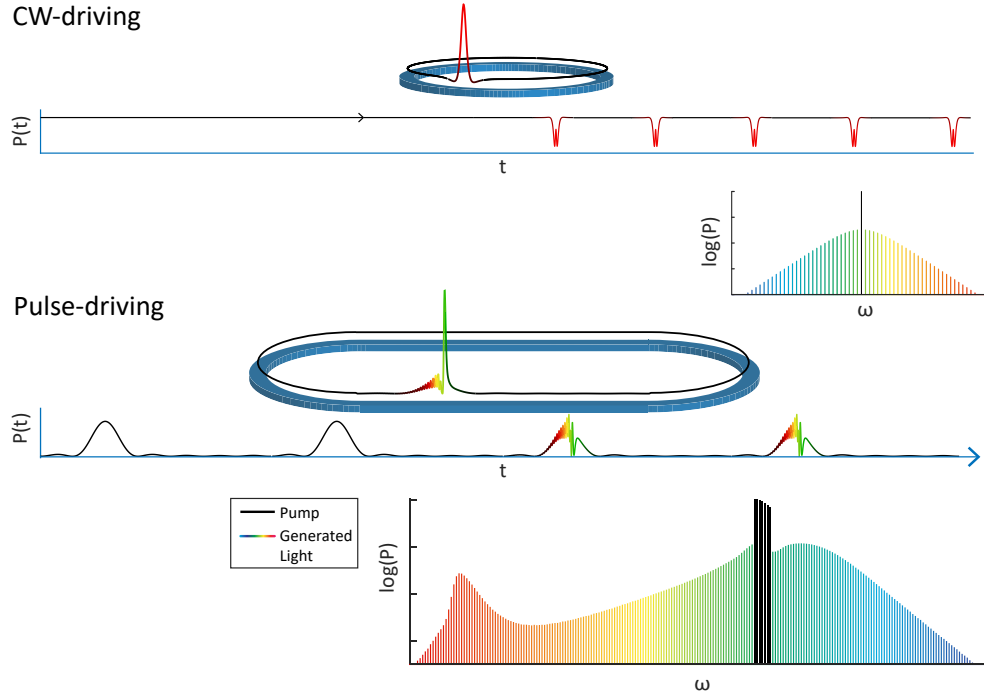


Figure 2.1: **Traditional continuous-wave vs. pulse driven soliton microcomb systems.** In a typical Kerr cavity system, dissipative solitons derive their energy locally from the background CW. Hence, overall power efficiency is maximised with the ratio of soliton duration to total roundtrip time ie. when a low number of comb lines are generated, as in the top case. In Si_3N_4 , this corresponds to THz-rate microcombs. For temporally larger systems with many comb lines (GHz-rate in our case), it is better to concentrate the input pump energy around the single soliton in the form of a synchronous pulse-pump, as in the bottom case.

noise multiplication, a known drawback of EO-comb-driven SCG, where frequency noise on the input pulse repetition rate is transferred and multiplied over the generated optical lines destroying their coherence [98, 31]. I present a way to optimise this filtering in both simulations and experiment.

This chapter will cover the theory, simulation, and experiment of dissipative soliton microcomb generation with a synchronous pulsed input. First, how pulse-driven dissipative soliton generation differs practically with CW-driving, particularly its advantages; Second, the basic physics of how dissipative solitons form in this system and how they are guided by it; Third, how we implement pulse-driven Kerr microcombs experimentally with an electro-optic comb (EO-comb); Fourth, the experimental results of 1000-line microwave-rate, single-state soliton microcomb generation in a dispersion-engineered Si_3N_4 microresonator; and Fifth, how the fundamental noise on the repetition rate of the injected pulses transfers to, and is filtered by, the dissipative soliton state.

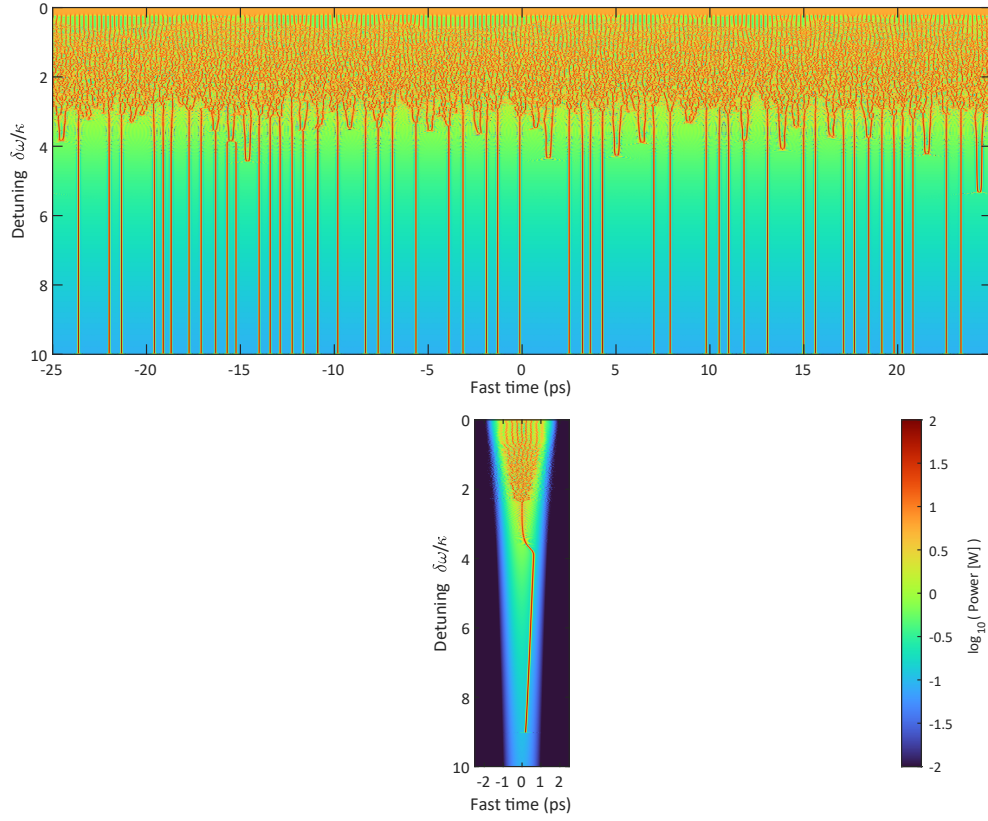


Figure 2.2: **Dissipative soliton generation in space/time by scanning over resonance, with CW (top) compared with pulse-driven (bottom).** In CW systems, four-wave mixing (FWM) and soliton generation goes on forever to the left or right, or is periodically bounded (to the real angular resonator space, or the simulation frame). By contrast, a pulse-driven system is ‘windowed’ in the fast time domain. Provided the same intracavity power level, the dynamics are invariant to resonator FSR (in the absence of long range wave coupling). The top field exactly represents a 20 GHz Si_3N_4 resonator, but the bottom field may represent 200 GHz maximum, or 20 GHz, or 20 MHz, or any temporally large resonator, where the rest of the space is considered unoccupied. Parameter values used here given in supplementary Table C.2.

2.1 Pulse-driving motivation vs. CW-pumping

While CW-driving is the traditional method of generating a microcomb [99], it does not guarantee successful formation of a smooth and efficient coherent soliton state. Depending on the properties of the microresonator, and the target power and repetition rate of the microcomb, CW-driving may be ineffective or inefficient, and instead pulse-driving may be better suited [94]. Problems with CW-driving might be unavoidable. There were three key motivations behind pulse-driving for soliton microcomb generation as opposed to CW-driving.

2.1.1 Unfavourable scaling in CW microcombs

In a waveguide resonator with fixed propagation constants (loss α_l [m^{-1}], inverse group velocity β_1 [ps.m^{-1}], dispersion β_2 [ps^2m^{-1}], and nonlinearity γ [$\text{W}^{-1}.\text{m}^{-1}$]), output soliton power does *not change* with FSR (Eq. 1.71). However, the resonator *Finesse* $\mathcal{F} = D_1/\kappa$ decreases with FSR, and so the incident power P_{in} required to sustain that soliton increases. For a single-soliton state, this results in a decrease in power efficiency with a decrease in the FSR D_1 .

In CW-driving, based on Eq. 1.71 and 1.72, *maximum* achievable power efficiency (soliton output power divided by input CW power) is given by

$$\epsilon_{cw} = \sqrt{\frac{2\pi\kappa|\beta_2|D_1\eta^3}{\gamma P_{\text{in}}}} \quad (2.1)$$

which is assuming that the soliton exists at its maximum detuning $\delta\omega$ [100, 101] (see Eq. 1.72 and 1.55)

$$\delta\omega_{\text{max}} = \frac{\pi^2 F^2 \kappa}{4} \quad (2.2)$$

Eq. 2.1 can be re-expressed in terms of the normalised relative driving strength F , from Eq. 1.55

$$\epsilon_{cw} = \frac{2\eta^2 D_1}{F} \sqrt{\frac{2|\beta_2|}{\beta_1 \kappa}} \quad (2.3)$$

which may be more helpful considering the practical desire to minimise the required input power for soliton generation, corresponding to a value of $F > \sqrt{1.54}$ [79] or, more realistically, $F \lesssim 3$. This is evidently doubly beneficial for soliton conversion efficiency, as it decreases by over-driving with a high F .

The scaling of soliton efficiency ϵ_{cw} with D_1 is demonstrated with the simulation presented in Fig. 2.3 based on Eq. 1.49, with a relative driving strength and detuning set to be $F = 10$

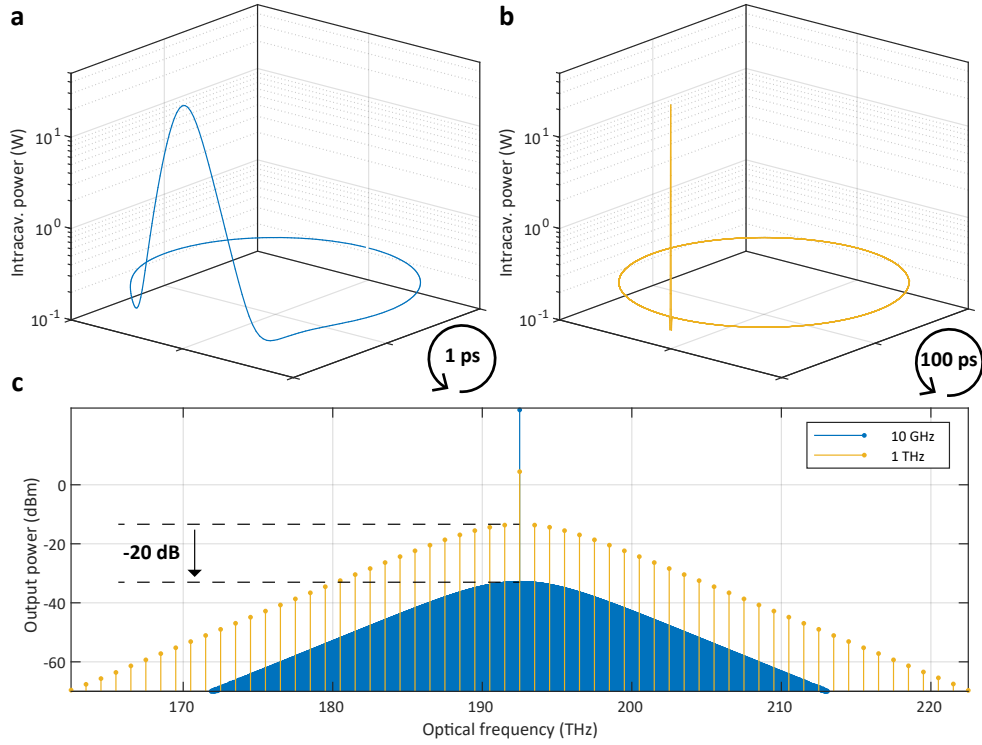


Figure 2.3: **Unfavourable scaling for DKS in ‘large’ resonators.** Simulation of Si_3N_4 resonators with the same Q -factor (κ and η) and dispersion $\beta_{1,2}$. (a,b) Intracavity field for DKS in microresonator with FSR = (a) 1 THz and (b) 10 GHz. The solitons have equal pulse duration. (c) Output microcomb for each resonator. Parameter values given in supplementary Table C.2.

and $\zeta_0 = 10$, as is most of the demonstration simulations presented going forward. In brief, compared with the 1 THz resonator, the 10 GHz resonator with a single-state DKS suffers 100 times less conversion efficiency for the same soliton profile, and also requires 100 times higher incident pump power in order to maintain the same intracavity pump power background level. The solitons in both resonator have the same duration and the same intracavity peak power. The DKS in Fig. 2.3(a) requires 3.5 mW of incident pump power, while the one in (b) requires 350 mW. The DKS in (b) compared to (a) exits the resonator with 100 times more energy, 100 times less frequently, requiring 100 times more incident pump power, giving 100 times more comb lines, but each with 100 times less individual power. As such, the pump-to-comb line contrast increases by a staggering 40 dB, rising to 59 dB. This would be the required extinction ratio any pump-line Bragg grating or notch-filter would need to flatten the pump for further use in, for instance, WDM applications [12, 11].

Soliton physics in the pure Lugiato-Lefever Equation (LLE) system is local, and therefore all the unused energy in the cavity temporal space can be vacant and the single soliton properties will not change. So if we now consider a single soliton sustained by a *synchronised input pump pulse* of duration τ_p

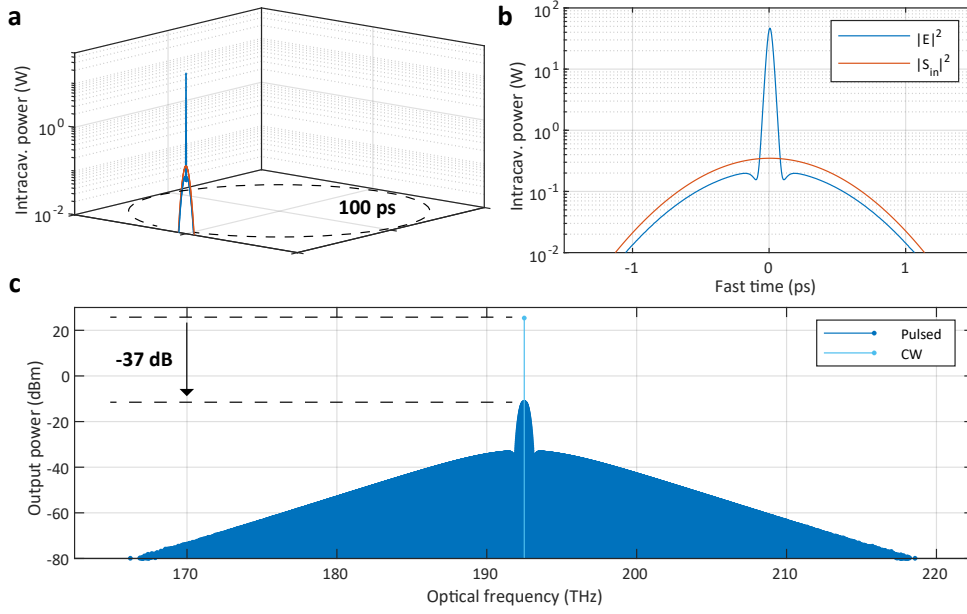


Figure 2.4: **Favourable scaling for pulse-driven DKS in large resonators.** Simulation in same 10 GHz resonator as in Fig. 2.3(b), now with 1 ps incident pump function. (a) Total intracavity field in angular space. (b) Only the active part of the resonator. (c) Output microcomb spectrum, with the previous required CW-pump line to compare. Parameter values given in auxiliary Table C.2.

$$\epsilon_{pd} \approx \frac{T_R}{\tau_p} \epsilon_{cw} = \frac{4\pi\eta^2}{\tau_p F} \sqrt{\frac{2|\beta_2|}{\beta_1\kappa}} \approx N\epsilon_{cw} \quad (2.4)$$

where the total time inside the resonator $T_R = 2\pi/D_1$. This factor can be *roughly* approximated by the number of additional comb teeth injected into the resonator N making up the input pulse train, assuming the input pulse is Fourier-transform limited. In this way, soliton microcomb power efficiency in a resonator with fixed waveguides constants *no longer scales with the FSR*, but instead the inverse driving pulse duration τ_p . This is demonstrated in the model shown in Fig. 2.4, where replacing the incident CW pump with a 10 GHz picosecond pulse train with *the same* peak power $P_0 = 350$ mW as required in Fig. 2.3(b), in this case a Gaussian pulse with a 1 picosecond duration (FWHM), the average incident pump power has dropped to 3.7 mW for the same soliton microcomb, representing 94-fold increase in conversion efficiency and a 37 dB decrease in the peak pump-to-comb line contrast.

2.1.2 Thermal load avoidance

In most realistic microresonators the temperature rises with some function of intracavity average power [102]. Rising temperature causes an expansion of the resonator volume, a decrease in the FSR, and therefore a negative shift to every resonance mode frequency ω_μ . When

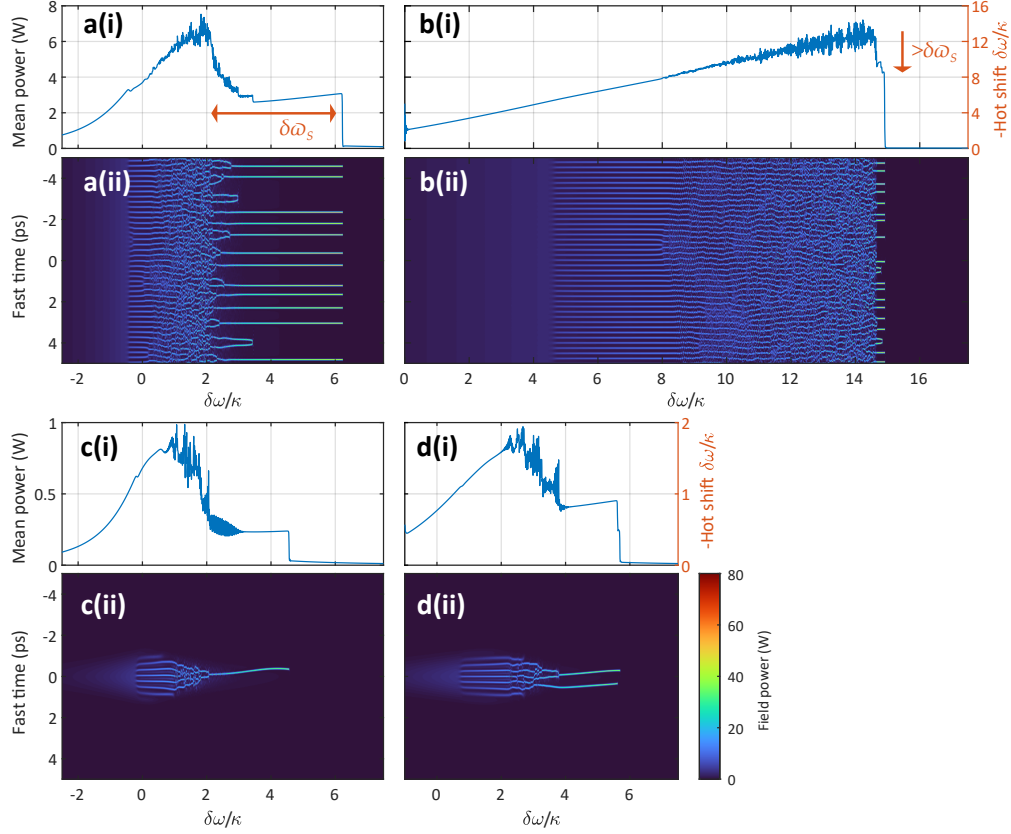


Figure 2.5: **Avoiding thermal-shift in pulse driving.** Intracavity field/power during scan over resonance in example 100 GHz Si_3N_4 resonator. (a,c) No thermal-shift to detuning. (b,d) Thermal shift enabled. (a,b) CW-driving. (c,d) Pulse-driving. (i) Mean intracavity power during scan. Right-hand axis indicates long-term negative detuning shift proportional to mean intracavity power. (ii) Instantaneous intracavity field power during scan. Parameter values given in auxiliary Table C.2.

generating a soliton microcomb, we scan the laser frequency negatively over the resonance from blue to red-detuned. When doing this, the rising mean intracavity power causes the detuning value to shift negatively, effectively delaying the point where the hot-cavity state falls from the blue-detuned MI region to the red-detuned soliton region. In this way, the cavity state is effectively pulled back like a slingshot. If the excess ‘hot’ detuning shift is greater than the whole soliton existence range $\delta\omega_s$, the soliton regime will be completely skipped, forbidding stable soliton microcomb generation [103]. Fig. 2.5 shows a demonstrative simulation where the thermal hot-shift coefficient, the change in detuning $\delta\omega$ with intracavity average power \bar{P}_{int} is set as

$$\frac{d}{d\bar{P}_{\text{int}}}(\delta\omega) = 2\kappa[\text{W}^{-1}] \quad (2.5)$$

with a rise time constant of 10 photon lifetimes to mimic a relatively fast thermal response. In the CW-driven example shown in Fig. 2.5(b), the drop in \bar{P}_{int} as MI transitions to solitons

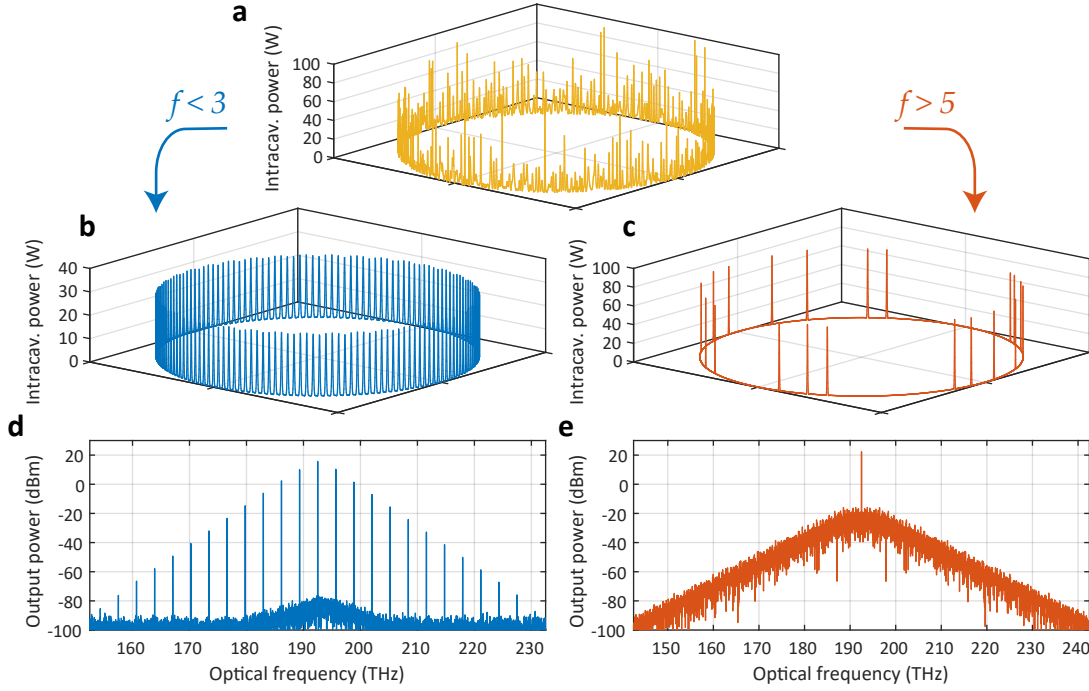


Figure 2.6: Multi-state soliton formation in CW-driven resonators. Simulated result of scan over resonance in example 20 GHz Si_3N_4 microresonator. (a,b,c) Intracavity field in angular temporal domain in (a) MI state, (b) perfect soliton crystal state if driving power is low, and (c) disordered multi-soliton state if driving power is high. (d,e) Frequency domain spectral envelopes of (b,c) respectively. Parameter values given in auxiliary Table C.2.

causes the detuning to lurch forward by more than the soliton existence range, throwing the cavity out of the soliton regime. In Fig. 2.5(d), pulse-driving decreases the intracavity ‘occupancy’ – and therefore the hot-shift – by that same factor of $T_R/\tau_p \approx N$, which may make soliton generation available.

2.1.3 Multi-state avoidance

In CW-driven Kerr resonators, soliton formation is possible across all the intracavity time-space. In resonators with low relative modal dispersion \mathfrak{D}_2 , there is more effective temporal space for a higher number of solitons to exist. Depending on the relative driving strength F , solitons may form in a highly-ordered lattice (perfect soliton crystal) [104], a defective lattice [105], or a completely random disordered state. In the crystalline states, intermediate comb lines will be suppressed (see Fig. 2.6(b,d)), whereas in the disordered state the microcomb envelope will be rough and unpredictable (Fig. 2.6(c,e)). Only a single-state soliton will guarantee a smooth envelope, but achieving this in a CW-driven system requires either the presence of mode-crossings violating the locality of the LLE [106, 107], or thermally-mediated soliton number-‘switching’ [73], which requires an extra high pump power ($F > 5$). As shown in above demonstrative models, for a sufficiently short input pulse, solitons are formed naturally

in a single state.

Soliton crystal states

It has been found recently by *Karpov et al.* [104] that when the effective pump strength is low ($F < 3$), a *soliton crystal state* is likely to be formed in a microresonator that has mode-crossings in its mode spectrum. This is the case in most multi-transverse mode Si_3N_4 microresonators, and it has been found that modal deviations need only be weak ($\varepsilon < \kappa$) for crystal states to become likely to appear. The mode-crossing causes a weak dispersive wave to be emitted by each soliton. With many solitons, these waves accumulate to form a powerful modulated background potential [92] that forces all solitons in to a crystalline lattice, the number (and therefore spacing) of the solitons determined by the relative index of the mode crossing. In the simulated case shown in Fig. 2.6(b,d) for an example 20 GHz microresonator, there is a 160-soliton crystal state resulting from a small modal deviation at mode $\mu = +160$ of $\varepsilon_{160} = -\kappa/2$ (see Eq. 1.59). As a result of the perfect crystal lattice, only every 160 comb modes is populated with energy (although there exists elevated noise in the intermediate modes due to tension in the crystal state). In other work, varieties of soliton crystal ‘defect’ states have been observed under similar conditions [105], where there exist gaps, flexes, or a-periodicities in the lattice. In all cases, the intermediate comb modes in between the “supermodes” are strongly suppressed. Therefore, if the application of this example microcomb were in the 20 GHz RF domain, it would unfortunately be ineffective and, at this lower relative pump power, there is little feasible way of decreasing the soliton count down to one.

Soliton number-switching

In the case where the effective pump strength is high, $F > 5$, when scanning the laser over resonance, nascent solitons emerging from MI will traverse a kind of ‘death zone’, or transient chaos [79, 88] (region IV from Fig. 1.18). As explained in section 1.3.2, in this regime solitons undergo a chaotic breathing cycle and have a survivability that decays with time. Tuning the laser *into* this region is precisely the way that we can reduce the soliton number in the cavity deliberately [73, 104]. In fact, in the absence of strong mode crossings or any other higher-order effects from the GLLE, this is likely the *only* way to deterministically reduce the soliton number in a pure CW-driven system. This is unfortunate since it requires a peak power over 5 times higher, $F^2 > 25$, than what is necessary for soliton generation which, as explained above, further decreases single soliton efficiency.

2.2 The electro-optic comb as pulsed input

The following section provides a guide on how an electro-optic comb (EO-comb) is formed experimentally and how it can be fashioned into a pulse train that is *best* appropriate for soliton microcomb generation. However, any synchronisable pulsed-source, with the correct chirp, can theoretically (and hopefully) be used for soliton microcomb generation [108, 109]. Proceed to the following section 2.3 to skip the details of an electro-optic pulse generator.

Our research targets photonic microresonators with FSRs throughout the GHz+ domain. Therefore, a pulsed-source with a completely flexible GHz repetition rate is needed, and this mostly disqualifies mode-locked lasers. Our pulses are provided by an *electro-optic comb* (EO-comb), where the repetition rate can be reconfigured to any frequency carried by the microwave components, in this case <18 GHz. The repetition rate can also be fine-adjusted *in-situ* with the experiment at a level of Hz to MHz without having to make mechanical adjustments.

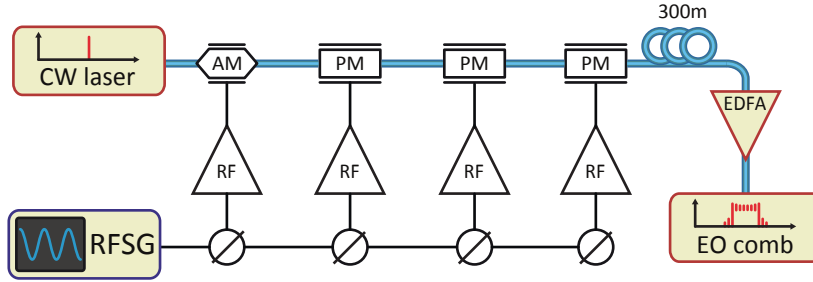


Figure 2.7: **Experimental setup for our electro-optic comb and pulse generator.** AM: Amplitude modulator; PM: Phase modulator; RFSG: Radio frequency signal generator; EDFA: Erbium-doped fibre amplifier. Credit: Alisa Davydova.

2.2.1 Phase/amplitude modulation

The operation principle behind our EO-comb setup is given in *Kobayashi et al.* (1988) and *Fujiwara et al.* (2003) [110, 111]. As shown in the setup diagram in Fig. 2.7, a CW laser is modulated in series by a Mach-Zehnder amplitude modulator (AM) and several electro-optic phase modulators (PM) whose effects all stack, provided they are in phase. When all modulators are acting in phase, in the RF domain, the throughput optical field envelope is expressed by

$$E_{eo}(\tau) = \cos\left(\frac{\pi}{4} a_1 \sin(2\pi f_{eo} \tau) - \frac{\pi}{2} a_0\right) \times \exp\left(i\left(c\frac{\pi}{4} a_1 + \frac{\pi}{2} b_1\right) \sin(2\pi f_{eo} \tau) - i c \frac{\pi}{2} a_0\right) \quad (2.6)$$

where a_1 is the amplitude modulation index (V_{am}/V_{π}), and a_0 is the modulation offset (V_{bias}/V_{π} , D.C.). The phase modulation index is given by b_1 (V_{pm}/V_{π}). The parameter c

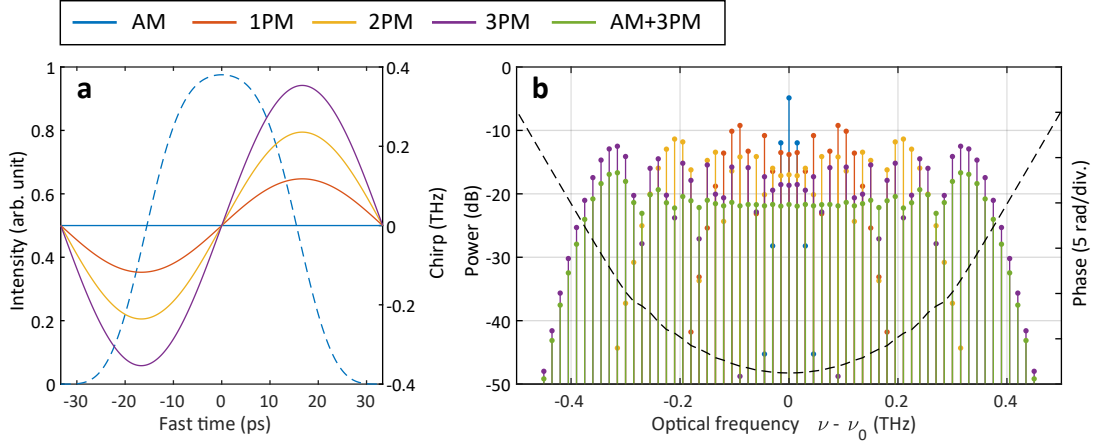


Figure 2.8: **Modelling the EO-comb waveform in (a) time and (b) frequency.** Here $f_{eo} = 15$ GHz. (a) Intensity of final waveform in dashed line, and instantaneous frequency (chirp) in solid lines. (b) Individual comb line power in solid line, phase of the final AM+3PM spectrum in dashed line.

is the relative chirp of the Mach-Zehnder modulator. In our system, because $b_1 \gg c$, we can ignore c . In our experimental EO-comb, each PM has a $V_\pi \approx 3$ V. When we drive all three PM with an RF power of about 2 W each ($V_{pm} = 15$ V peak), we reach a combined $b_1 \approx 15$, forming 48 spectral sidebands or additional comb teeth making up the EO-comb (see Fig. 2.8 and 2.9). Each new comb line in Fourier space evolves with the modulation index b_1 [1] according to

$$E_{eo} = \sum_{n=-\infty}^{\infty} \hat{E}_n e^{2i\pi(\nu_0 - n f_{eo})\tau} \quad (2.7)$$

$$\hat{E}_n = J_n\left(\frac{\pi}{2} b_1\right) \quad (2.8)$$

with J_n being the n th order Bessel function of the first kind. In the time domain, this forms a strongly frequency-modulated CW field, with a maximum frequency deviation of

$$\Delta\nu = \frac{\pi}{2} b_1 f_{eo} \quad (2.9)$$

so that the EO-comb significant bandwidth is approximately limited to $2\Delta\nu = \pi b_1 f_{eo}$, and all comb teeth $n > \pi b_1/2$ fall quickly in power to zero. The maximum linear *frequency chirp* of the waveform

$$\frac{d\nu_{eo}}{d\tau} = \nu'_{eo} = b_1 \pi^2 f_{eo}^2 \quad (2.10)$$

$$\nu_{eo} = -\frac{\partial\phi(\tau)}{\partial\tau} \quad (2.11)$$

where the phase of the field $\phi(\tau) = \arg(E_{eo})$. When we use the fourth RF branch to supply the AM, we target a_1 around 0.9-1 and $a_0 = 1 - a_1/2$, shown in Fig. 2.8(a). This effectively forms an intensity ‘window’ containing primarily the maximum linear chirp region of the waveform. This removes the interference fringes in the PM-only EO-comb spectrum effectively flattening it, as demonstrated in Fig. 2.8(b) and 2.9(c,d).

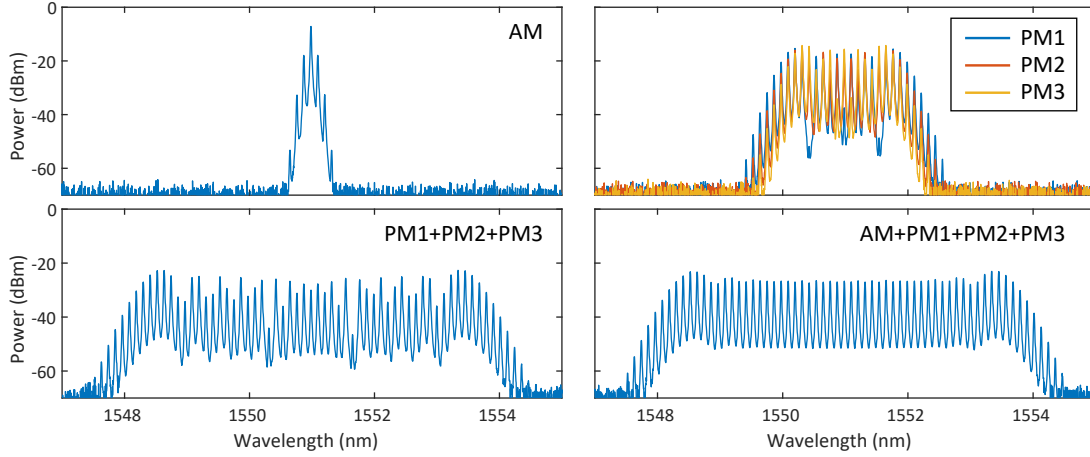


Figure 2.9: **Experimental EO-comb build-up.** Here $f_{eo} = 14$ GHz. (a) Amplitude modulator engaged only. (b) Each phase modulator engaged individually. (c) Three combined phase modulators engaged. (d) Amplitude and all phase modulators engaged.

2.2.2 Compression (de-chirping)

The EO-comb in this pure frequency-modulated state is already useful as a frequency comb, which can be used to coherently extend the spectra of laser lines, or bridge the gap between microcomb teeth that have a large frequency spacing (50 GHz+) so that they can be compared via heterodyne measurement on photodiode [112, 113]. For pulse-driving microresonators, we can turn the EO-comb waveform into pulses by cancelling its frequency chirp via propagation through a waveguide with group velocity dispersion (GVD), given by the β_2 parameter measured in s^2/m . Taking Eq. 2.10 as a guide, we will need a waveguide length L where

$$\beta_2 L \approx (2\pi v'_{eo})^{-1} \quad (2.12)$$

This represents the required ‘dispersion compensation’ to turn the chirped waveform into a Fourier transform-limited pulse. Fig. 2.10(a-d) shows modelling for the propagation over of the final waveform from Fig. 2.8 through dispersion, using the solution to the linear Schrödinger equation in the frequency domain

$$\hat{E}_{eo}^{\text{final}} = \hat{E}_{eo}^{\text{initial}} \times \exp \left[\frac{i\beta_2 L}{2} (2\pi(\nu - \nu)) ^2 \right] \quad (2.13)$$

Since the spectral phase of the initial central EO-comb is quadratic, this phase can be completely flattened at the point where $\beta_2 L = 1/(b_1 \pi^2 f_{eo}^2) = 4.8 \text{ ps}^2$ in our 15 GHz EO-comb example, which is shown by the dotted line in Fig. 2.10(c). However, this waveform is not Gaussian. Due to the nonlinear sinusoidal chirp at the pulse edges, the real compression point for the pulse in the time domain, shown by the dashed line in Fig. 2.10(a-d), occurs slightly later at $\beta_2 L = 5.6 \text{ ps}^2$. In our experiment, this value of dispersion can be provided by about 260 m of basic SMF-28 having $\beta_2 = -0.022 \text{ ps}^2/\text{m}$. According to Eqs. 2.10 and 2.12, the required length L scales with the inverse square of f_{eo} for a fixed b_1 . Hence, as shown in Fig. 2.10(e) and (f), the same EO-comb at $f_{eo} = 10 \text{ GHz}$ requires around double the dispersion length, and half with 20 GHz.

In-phase modulation

In our practical experiment, each of the microwave phase-shifters shown in Fig. 2.7 have to be adjusted so each modulator is acting in phase. The EO-comb bandwidth and b_1 will be maximised as long as the three PM are acting in phase. In addition to that, the relative phase between the chirped waveform and the intensity waveform can be set (see Fig. 2.11), in particular so that the initial linear chirp of the long pulse is either positive (increasing with time delay) or negative (decreasing). If we are using SMF-28 as dispersion compensation, which has anomalous dispersion $\beta_2 = -0.022 \text{ ps}^2/\text{m}$, then we need to set the chirp to be positive.

In the real world, it is impractical to fine-tune the length or total dispersion of a solid-state dispersive medium, such as an optical fibre or chirped Bragg grating. This is done approximately in our lab for instance by starting with too much dispersion (300 m of SMF), and then adding incremental lengths of opposite-sign dispersion-compensating fibre, so as to go ‘back up’ the compression profile shown in Fig. 2.10 in order to reach the ideal. However, once you have settled on a fixed amount of dispersion, the pulse profile can be *fine-tuned* by adjusting the EO-comb PM index b_1 after the fact. As shown in Fig. 2.12, this will ensure you have the highest peak-power enhancement in pulse formation. Importantly, this can also determine whether the *residual* chirp (shown here as phase curvature) is positive or negative. This has important consequences for soliton generation!

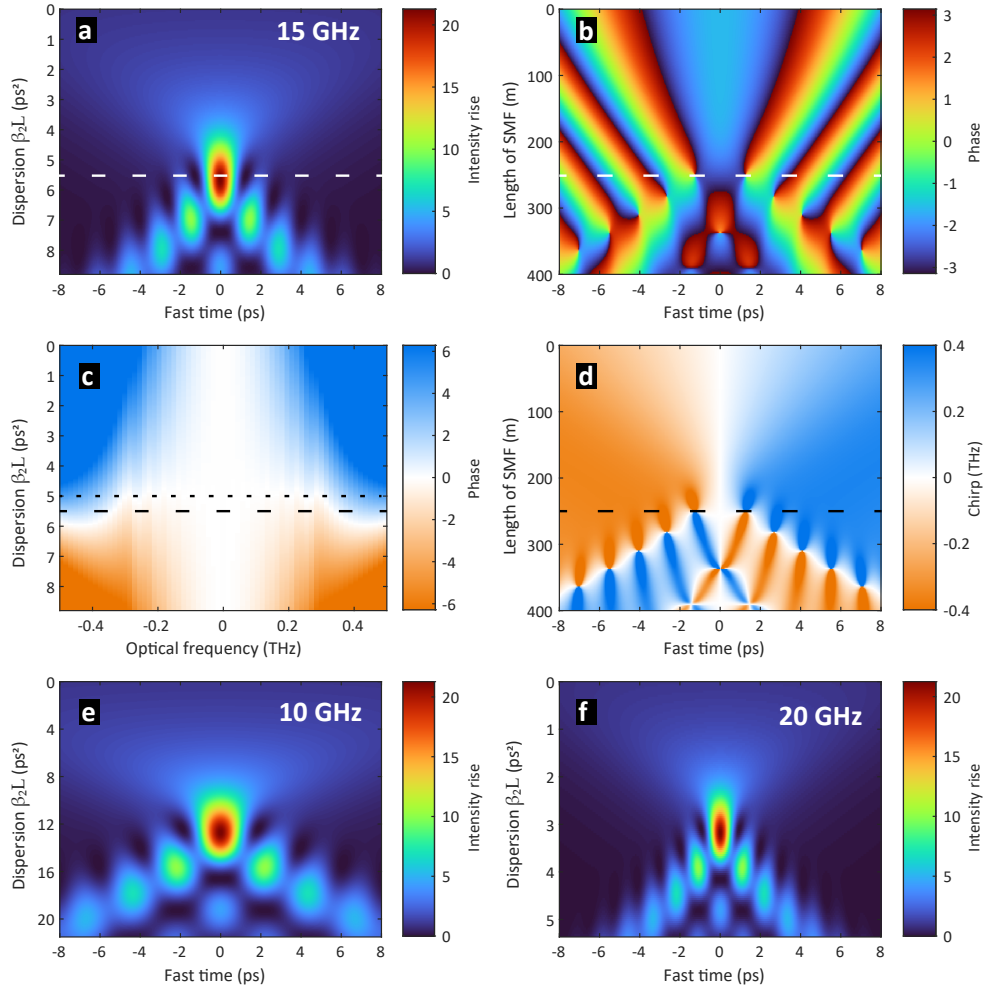


Figure 2.10: **EO-comb linear temporal-compression (de-chirp)**. (a) Time-domain field intensity, normalised to starting peak intensity, (b) phase, (c) frequency domain phase, and (d) time-domain instantaneous frequency (chirp), in propagation through dispersive waveguide or equivalent single-mode fibre (SMF), for $f_{e0} = 15$ GHz and other parameters given above. Long-dashed lines mark minimum pulse duration / maximum peak intensity enhancement. Short dashed line corresponds to where chirp of the EO-comb centre is first flattened. (e) Time-domain pulse intensity compression for (e) $f_{e0} = 10$ GHz and (f) $f_{e0} = 20$ GHz and the same modulation indices.

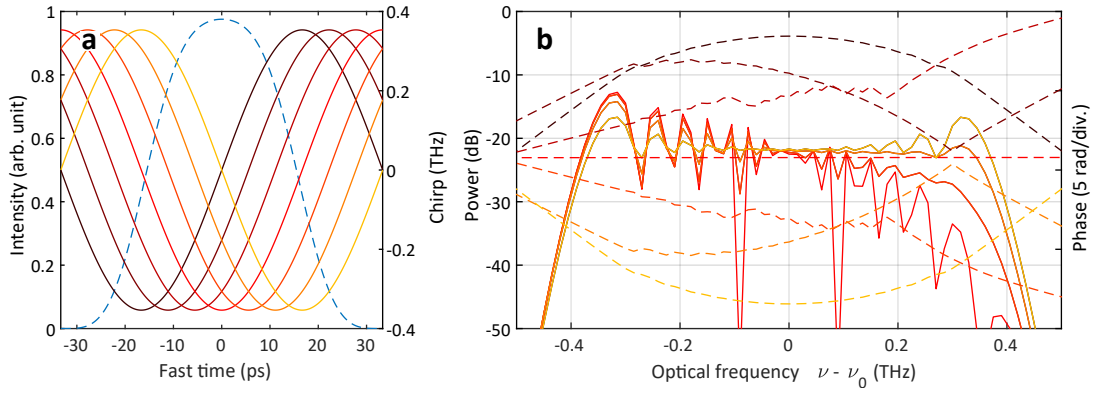


Figure 2.11: **Chirp reversal.** When the AM is out of phase with the PM, the spectral profile becomes tilted. When the phase difference becomes π , the chirp of the EO-comb waveform reverses.

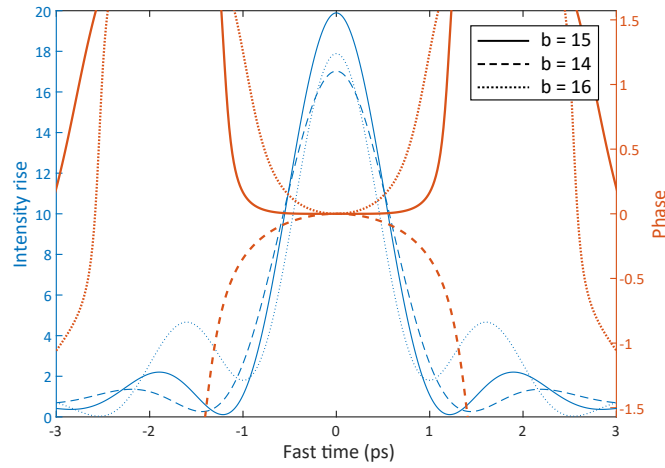


Figure 2.12: **Fine-tuning the final EO-comb pulse after linear compression.** Pulse (blue) relative intensity and (orange) phase where the phase modulation index b_1 is fine-adjusted, giving a phase-flat pulse, or under- or over-compressed leaving a phase curvature (linear chirp).

Nonlinear compression (broadening)

The most sure-fire way to know whether an optimal pulse has been successfully formed, a frequency-resolved optical gating (FROG) measurement will have to be carried out. This will confirm the final pulse width and phase profile. However, another far simpler check is to amplify the EO-comb pulse through an EDFA to the level of 100s of mW. According to Figs. 2.10 and 2.12, this would make a pulse with peak power on the order of several Watts, which is enough to exhibit *nonlinear* spectral broadening based on self-phase modulation (SPM) of the pulse [62]. When measured on an optical spectrum analyser (OSA) this gives the signature of additional broadening of the EO-comb spectrum and FWM. If the EO-comb ‘pulse’ is not demonstrating SPM after strong amplification, then the initial EO-comb chirp is probably the wrong sign (see Fig. 2.11).

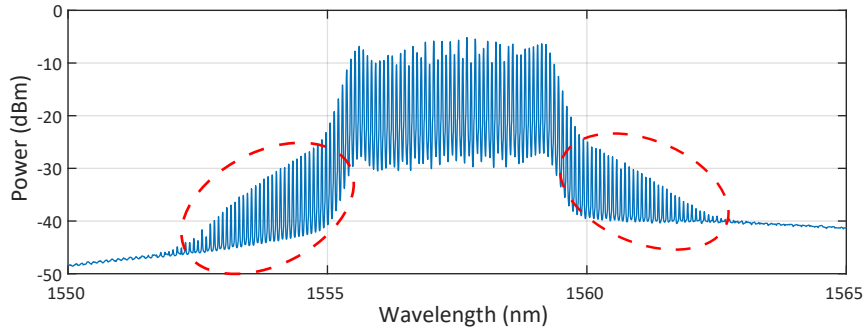


Figure 2.13: **Broadening under high power gives a spectral signature of successful pulse profile.** Here $f_{\text{eo}} = 10$ GHz, and the average power out from the EDFA ≈ 500 mW.

2.3 Basic principles of pulse-driven soliton microcombs

Consider the dimensionless Lugiato Lefever equation (LLE):

$$\frac{\partial \psi}{\partial t} = \left(-d_1 \frac{\partial}{\partial \tau} - i d_2 \frac{\partial^2}{\partial \tau^2} + d_3 \frac{\partial^3}{\partial \tau^3} \right) \psi + (i|\psi|^2 - i\zeta_0 - 1)\psi + F(\tau) \quad (2.14)$$

for field ψ (power field $\Psi = |\psi|^2$) with the second-order dispersion set to be anomalous here ($d_2 = -1$), and driven by pulse-envelope

$$F(\tau) = F_0 \exp[\tau^2/\tau_p^2] \quad (2.15)$$

with $F_0 = \sqrt{10}$ and $\tau_p = 16$, representing a pulse profile much wider than the typical duration of a DKS. These normalised parameters can apply to *any* predominantly Kerr material resonator platform [85]. For the relationship to real experimental parameters, see Eqs. 1.55.

For generating a soliton microcomb, we may proceed in the same way as for CW driving as described in section 2.1. For pulse-driving, the pulse train needs to be finely matched to the resonator in two ways before the soliton step will appear: correct repetition rate (synchronisation), and correct pulse chirp. Soliton existence requires it ‘sits’ on a background of pump light, and if the pulse pump envelope is circulating the resonator at a different rate to the soliton, the soliton may ‘fall off’ and collapse during formation. Thankfully, there’s a range in difference between soliton and driving pulse repetition rate where the soliton locks itself temporally to the driving pulse: the locking range. The input pulse repetition rate must be within this range for the soliton step to appear, and the step length is maximised by optimising the repetition rate and the driving pulse chirp.

2.3.1 Soliton formation and locking

Fig. 2.14 demonstrates input pulse synchronisation for forming solitons, by scanning over resonance. For an un-chirped pulse, it has been found in numerical studies [114, 115, 116] that the soliton tends to find itself at a ‘trapping’ position located at a certain background driving power level. This trapping or equilibrium position is defined where the relative soliton *temporal velocity* v_S , $[\partial \tau / \partial t]$ reaches zero. For a pump function with a varying intensity

$$v_S = y(\zeta_0, F) F'(\tau) \quad (2.16)$$

which is proportional to the slope or derivative of the driving pulse envelope $F(\tau)$, and also proportional to some function $y()$ of detuning ζ_0 and local driving strength F . As found in [114], $y = 0$ when $F(\tau) = F_C$, a critical value of the background pump power upon which the soliton sits. For large values of the normalised detuning ζ_0 , $F_C^2 \gtrsim 8\zeta_0/\pi^2$, which happens to be

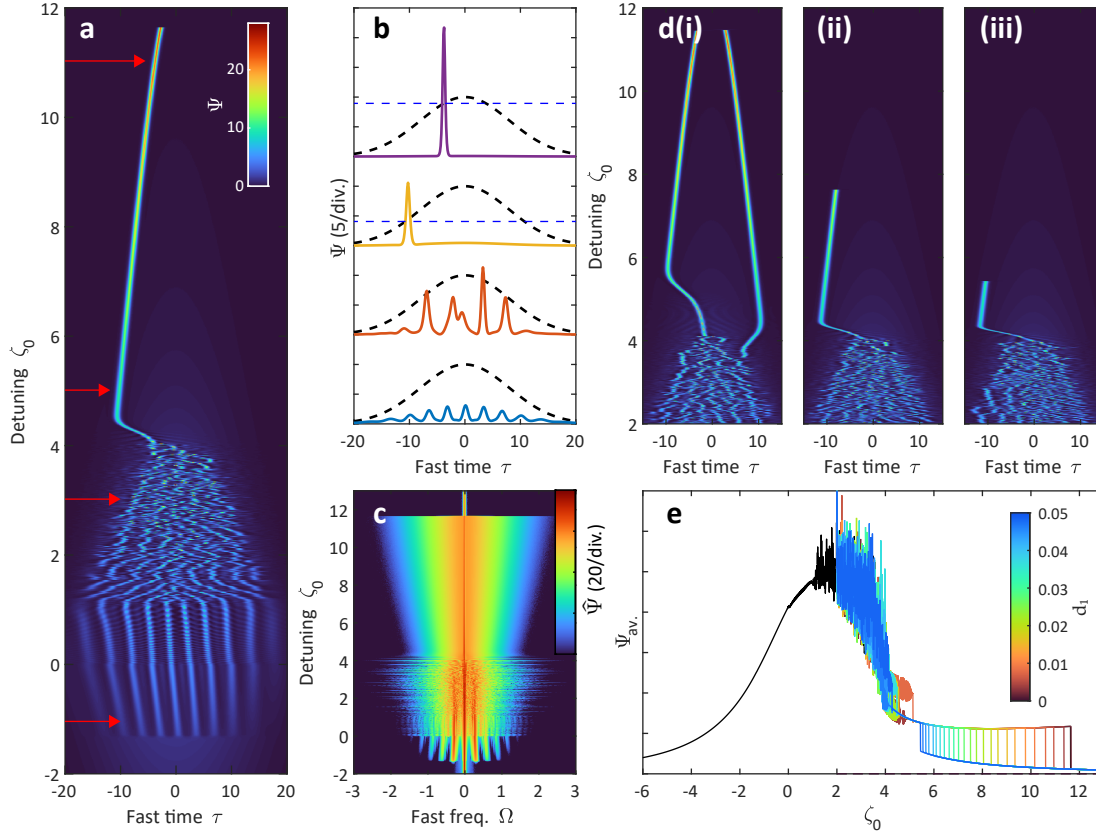


Figure 2.14: **Soliton formation and locking in pulse-driven Kerr resonator.** (a) Intracavity optical field in pulse-driven resonator as a function of detuning ζ_0 , and slightly desynchronised with $d_1 = 0.002$. (b) Slice of intracavity field at points given by red arrows in (a), showing Turing rolls, chaotic MI, and soliton at low, and high detuning. Black dashed line is the pulse function $|F(\tau)|^2$. Blue dashed line is the predicted trapping power F_C^2 . (c) Optical spectrum of (b). (d) (i-iii) Other examples for soliton formation with $d_1 = 0, 0.25, 0.5$ respectively. (e) Intracavity average power vs. detuning, with unfurling of the soliton step as a function of desynchronisation d_1 . The scan duration $\Delta t / \Delta \zeta_0 = 512$.

the minimum power for soliton existence. Hence, for an un-chirped pulsed driving function, a soliton will tend to move towards and trap itself at an *edge* of the driving pulse envelope, as demonstrated in Fig. 2.14(a,b).

When the driving pulse repetition rate does not equal the natural soliton repetition rate, there will be an effective group velocity offset (delay) d_1 in the intracavity optical field, manifesting as a forward/backward drift. For a soliton to be stably trapped to the driving pulse, its trapping velocity has to match this resonator velocity offset so that $v_s - d_1 = 0$. As implied by Eq. 2.16, as detuning increases, the soliton moves along its trapping position higher towards the top/centre of the driving pulse envelope, and the ‘tightness’ of this trapping becomes weaker as $F'(\tau)$ decreases there. For that reason, for larger values of d_1 , the detuning range for stable soliton trapping decreases. This results in the smooth ‘step unfurling’ behaviour seen in Fig.

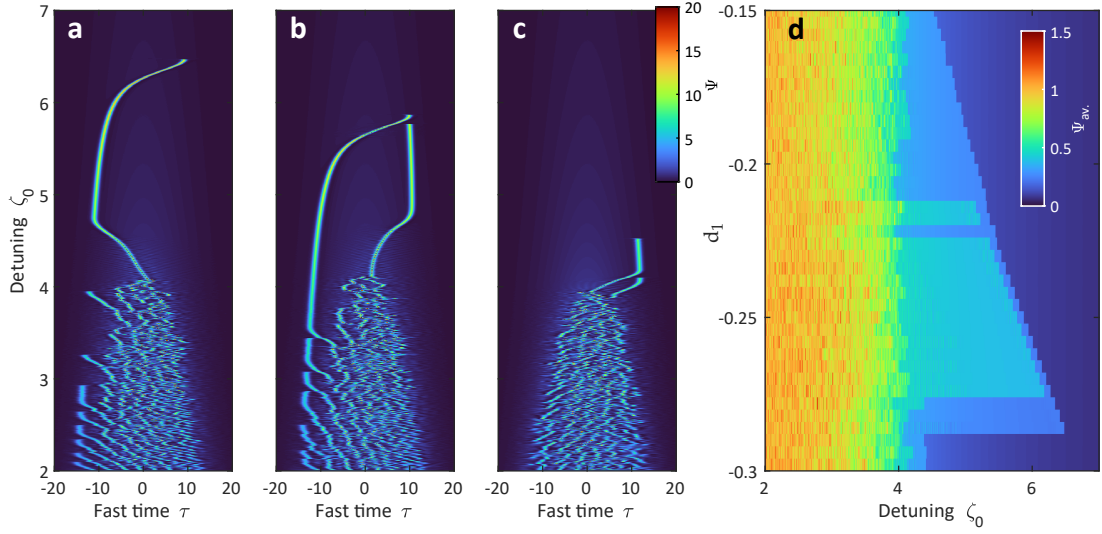


Figure 2.15: **Soliton formation with asymmetry.** In this case $d_3 = 0.05$. (a) Intracavity optical field during scan and soliton formation examples for $d_1 = 0.28$, (b) $d_1 = 0.25$, and (c) $d_1 = 0.15$. (d) Unfurling of soliton step vs. d_1 . The scan duration $\Delta t / \Delta \zeta_0 = 512$.

2.14(e) as $v_S - d_1 \rightarrow 0$. This is what is seen in experiment when reaching synchronisation between the input pulse driving rate and the soliton natural repetition rate.

If there is an asymmetry in the soliton spectrum – as a result of Raman self-frequency shift, dispersive wave emission etc. – the soliton will incur its own intrinsic group velocity offset $v_I(\zeta_0, f)$ which may change with detuning and power, and $v_S + v_I - d_1 = 0$ for stable trapping. This will mean the soliton has a *bias* on whether it will last longer existing on the leading or trailing edge of driving pulse envelope[115], resulting in a step unfurling that is asymmetric for desynchronisation d_1 . This is demonstrated in Fig. 2.15, where the soliton generation simulation includes third order dispersion with $d_3 = 0.05$.

2.3.2 Phase contribution

Consider a pump profile modulated only in phase, as

$$F(\tau) = F_0 \exp[i\Delta\phi * \cos(\pi\tau/\Delta\tau)] \quad (2.17)$$

where $\Delta\phi = 2\pi\Delta\tau * 0.005$. $\pm\Delta\tau$ represents the fast time-span inside the cavity. As demonstrated in previous experiments and investigations [117, 116], unlike for intensity variation in the pump function, in the presence of *phase* variation instead

$$v_S = 2\phi'(\tau) \quad (2.18)$$

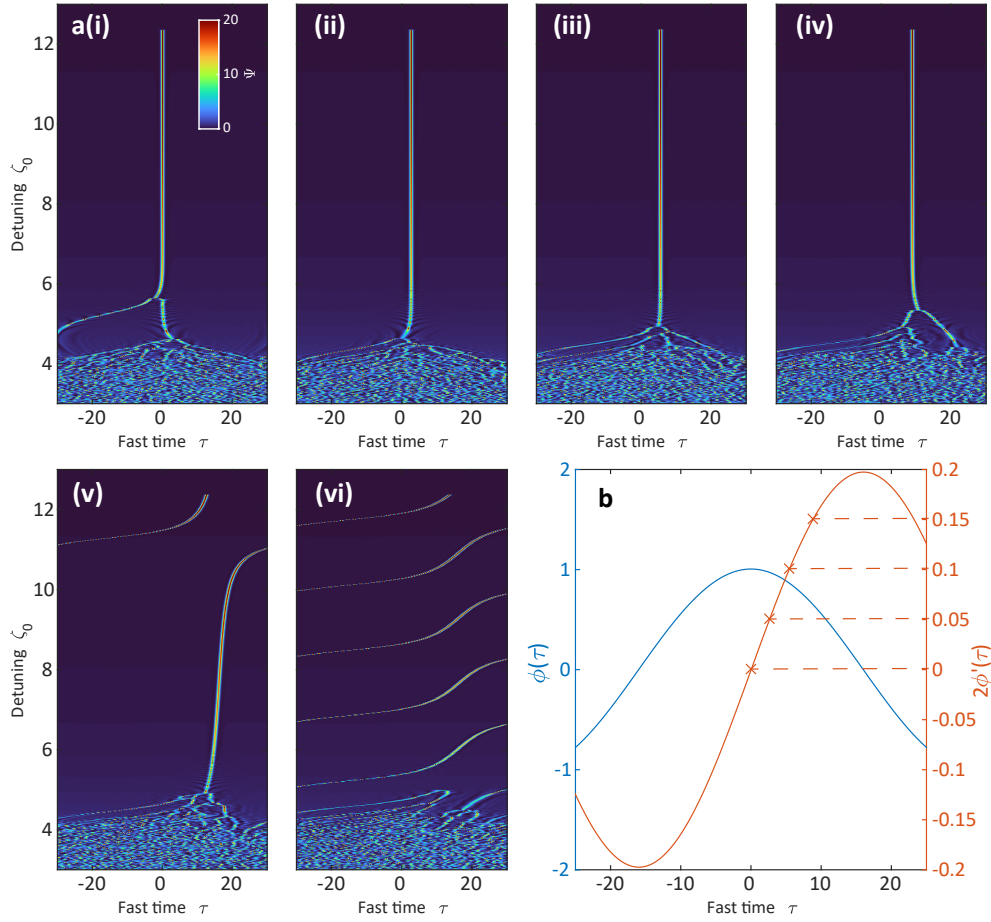


Figure 2.16: (a) Formation of DKS while scanning over resonance with CW-driving, with a phase-modulated background according to (b). (i-vi) $d_1 = 0, 0.05, 0.1, 0.15, 0.2, 0.25$. (b) Left: Background relative phase of the pump $F(\tau)$; Right: $2\times$ the pump chirp. The equilibrium locations of each scenario (i-vi) are marked with an 'x'. This point equals $2\phi'(\tau)$. The scan duration $\Delta t/\Delta\zeta_0 = 256$.

where $\phi(\tau) = \arg(F(\tau))$. Dissipative solitons in Kerr cavities inherit the instantaneous frequency of the background pump wave as their own carrier frequency. As such, a DKS with its own frequency shifted will experience a shift in group velocity due to *group velocity dispersion* (GVD). Thus, solitons will move towards the *peak* of the background phase curve (where the carrier frequency-shift is zero) at a speed proportional to the phase gradient. This is demonstrated in Fig. 2.16 where a formed DKS finds itself at an equilibrium location where $v_S = d_1$ ie. 'locked'. If the desynchronisation is greater than can be compensated by v_S , the soliton will become unlocked, and return closer to its natural group velocity (seen in Fig. 2.16(a(v-vi))). In this way we can trivially predict the locking range as

$$|d_1| \leq 2\phi'_{\max} \quad (2.19)$$

where, in this example, $\phi'_{\max} = 2\pi^2 * 0.005$. In this thesis however, we are primarily concerned with chirped pulse-driven dissipative solitons where phase variation plays a role. While Eq. 2.19 can give us the ball park of the locking range experimentally, the nonlinear function $y(\zeta_0, F)$ from Eq. 2.16 makes the precise locking range due to intensity modulation harder to define, but we can still predict using simulations.

As shown before in Fig. 2.10 and 2.12, our final driving pulse may have residual dispersion, with either positive or negative phase curvature, so a soliton formed here will experience a group velocity shift in any direction due to both influences of the pulse phase and intensity. In the asymmetrical case presented in Fig. 2.15, a residual negative phase curvature could help the soliton stay within the driving pulse envelope. This scenario is presented in Fig. 2.17, where the input driving pulse function has received varying initial dispersion, expressed in frequency domain:

$$\hat{f}(\Omega) \rightarrow \hat{f}(\Omega) e^{id_p\Omega^2} \quad (2.20)$$

similar to Eq. 2.13 (Ω being dimensionless frequency), where d_p is the normalised equivalent of $\beta_2 L$ during the EO-comb compression. In Fig. 2.17(a), we prepare 6 input pulse functions (i)-(vi) with input dispersion (chirp) from $d_p = -20$ (positive phase curvature) to $+80$ (negative phase curvature). In Fig. 2.17(b) and (c), we compare step behaviour for $d_p = 0$ and $d_p = +20$ respectively. In (c), we see the soliton existence range has increased overall, over both detuning ζ_0 and d_1 . For cases in (d) and (e)(i) to (vi), we show the longest step achievable for a given d_1 , for each value of pulse chirp d_p . In general, the stronger the pulse chirp (with negative phase curvature), the more the soliton is pulled towards the centre of the input pulse envelope (e(vi)) instead of being pushed against the pulse edges (e(i)). This reaches an optimum in the case (iv) (the darker red) where, as shown in (a), the pulse phase is maximally negatively curved *before* the pulse intensity begins to drop significantly due to strong dispersion.

Armed with this knowledge, the soliton generation step can be maximised when pulse-driving through *iterating* the exact input pulse repetition rate, and its chirp. In our practical experiment this meant spinning the dial on the EO-comb RF synthesiser to set its frequency *and* its RF power to the phase modulators, whilst the soliton step is observed, watching for the ‘unfurling’.

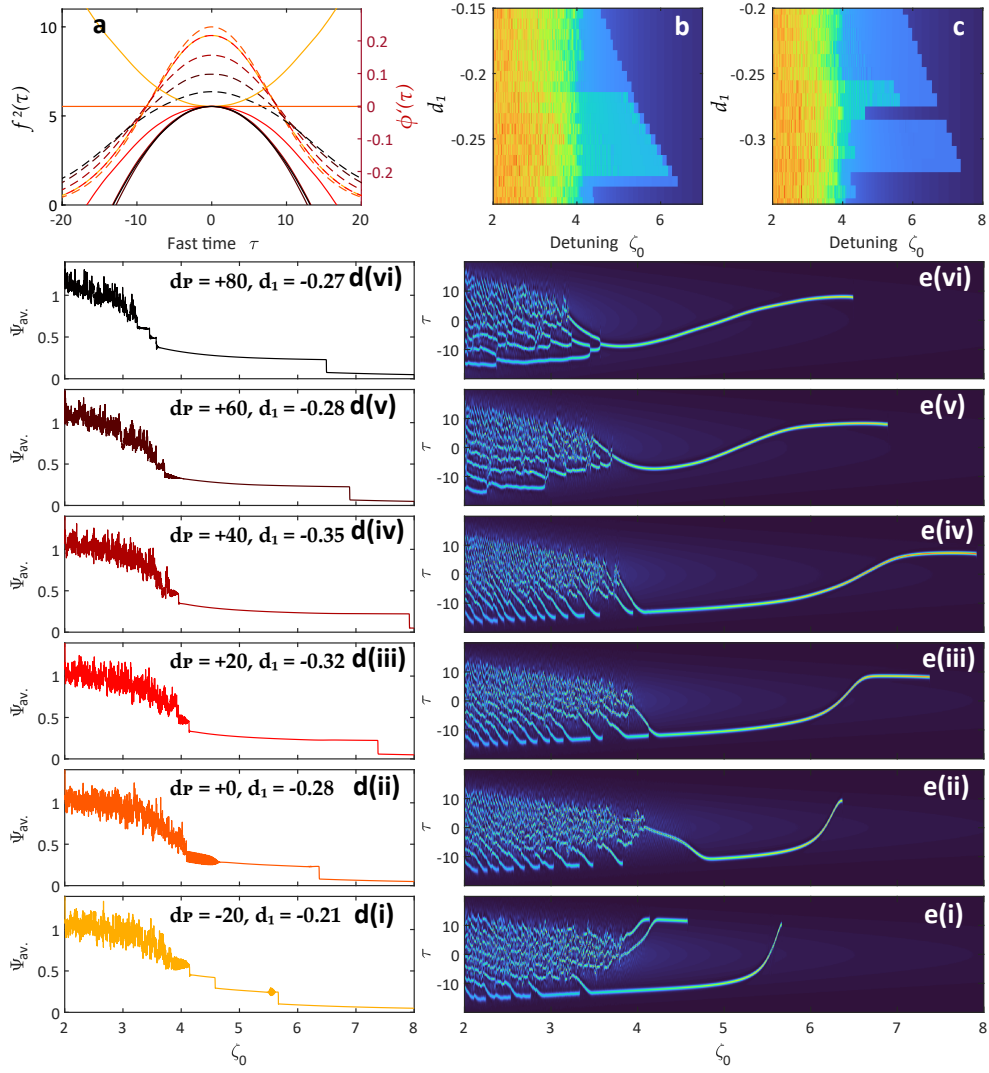


Figure 2.17: **Optimising soliton generation by fine-tuning the input pulse chirp.** (a) Phase (solid) and intensity (dashed) profile of the driving input pulse function. Colour-coded with (i-vi). (b,c) Step unfurling profile for $d_P = 0$ and $+20$ respectively. (d) Intracavity average power during soliton formation. (e) Intracavity optical field during soliton formation. (i-vi) Obtained d_1 giving maximum soliton existence over detuning for each value of input dispersion d_P . The scan duration $\Delta t / \Delta \zeta_0 = 512$.

2.4 Broadband, efficient pulse-driven microcomb results and noise propagation

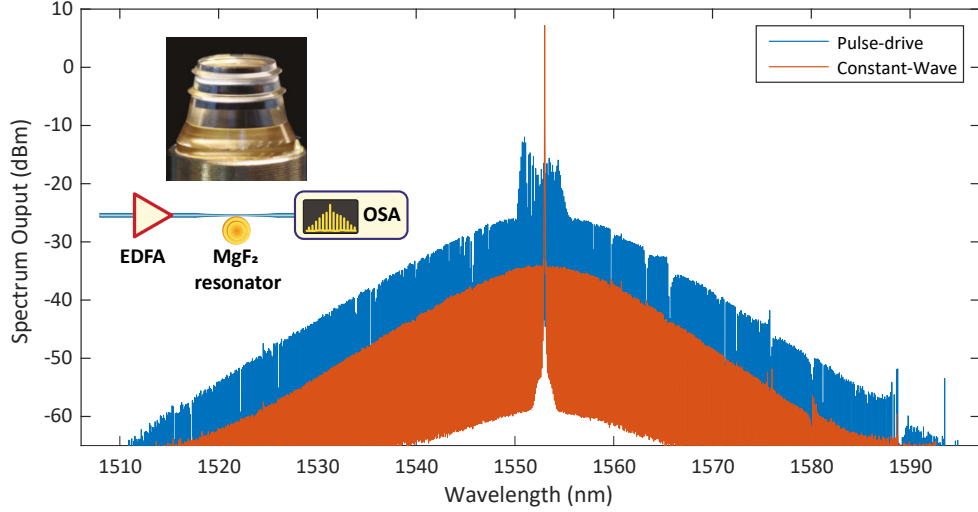


Figure 2.18: **Pulse-driving result in MgF_2 whispering gallery mode resonator.** Output soliton microcomb spectrum for pulse-driving and CW experiment in comparison. Upper-left: basic scheme of the experiment with tapered-fibre coupling and picture of resonator.

2.4.1 Magnesium fluoride crystalline resonator pumping experiment

In a short experiment, for the purpose of verifying our expectations of pulse-driving in a *known* system, we tested soliton microcomb generation in our crystalline whispering gallery-mode Magnesium Fluoride (MgF_2) microresonator. This microresonator is similar to that used in the first soliton microcomb generation experiment [99], and is used particularly in the works by Erwan Lucas [74, 87, 30] and is described in further detail in his thesis[58]. Originally formed from diamond turning, its ring protrusion is further polished by diamond slurry to reach an intrinsic quality factor of $Q_0 = 2 \times 10^9$, or $\kappa_0/2\pi \approx 100$ kHz. It has an FSR of 14 GHz. Fig. 2.18 displays the obtained soliton microcombs with CW driving compared with pulse-driving, focusing on both achievable *soliton power* and *efficiency*. We couple the pump light to the *whispering gallery mode* evanescently via a tapered optical fibre suspended by the resonator.

For the CW case, we placed the tapered fibre at a distance from the resonator to get slightly over critical coupling $\kappa_{\text{ex}}/2\pi = 200$ kHz, and drive with a CW power of 200 mW in order to obtain a single soliton at a high detuning. When instead driving with the EO-comb pulsed source, at a synchronised repetition rate of 14 GHz, we placed the tapered fibre very close to resonator in order to over-couple by an estimated factor of 20:1, or $\kappa_{\text{ex}} \approx 2$ MHz. Here, the average pump power was 4 times less at 50 mW, yet the achievable soliton microcomb with the *same* spectral bandwidth was almost 10 times more energy dense. And, the measured efficiency – the ratio of total soliton comb line power (excluding pump teeth) to total output

power – had increased from 0.95% in the CW case, to 24% in the pulse-driven case, a factor of 25 improvement.

2.4.2 Silicon nitride microcomb experiment - resonator properties and testing setup

In the Si_3N_4 experiment, the aim shifts from soliton power and conversion efficiency to spectral bandwidth. The resonator used in this experiment (internal ID: D42-1.F8.G0.R7), was the seventh resonator of nine, on a chip containing racetrack resonators designed for an FSR of 28 GHz (originally so it could become synchronised with the 14 GHz MgF_2 resonator, but this experiment was not attempted in the end). It was part of the overall D42 wafer series of chip designs, which was the second series of resonators designed by me as part of the goal to generate an octave-spanning soliton microcomb through pulse-driving. D42 was fabricated using the *photonic Damascene* process [118]. The properties of the resonator are shown in Fig. 2.19. The total frequency calibrated resonance spectrum was obtained through frequency comb-calibrated swept-laser spectroscopy [49, 50]. The Si_3N_4 waveguide cross section was designed and intended to be 2,350 nm wide and 770 nm deep. According to FEM calculations at the time, this was supposed to give a low integrated dispersion profile with two zero-crossings around an octave apart at 140 and 280 THz. In fact, our model of the Si_3N_4 material refractive index at the time (more about this online, see C.5.1) was out of date, so instead we saw the more cubic D_{int} profile seen in Fig. 2.19(d). The intended dispersion was further changed unpredictably by the inclusion of the ‘mode-suppression section’ described in more detail in section 4.2.

At the time in 2018, we could only reliably measure D_{int} from 185-200 THz, which only gave an accurate fitting for the second-order dispersion $D_2 = 2\pi \cdot 7.2$ kHz. After observing the soliton microcomb shown below, I inferred the value of $D_3 = 2\pi \cdot 15$ Hz based on the dispersive wave location (giving the red-dashed fit in the figure (d)). Since 2020, we are able to measure D_{int} over 185-240 THz, which gives the blue-dashed fit. This fit must be wrong unfortunately, as it is still too inaccurate at low wavelengths (<185 THz), and does not agree with the results presented below. Other than the dispersion, the spectrum for the resonator linewidth κ is shown in Fig. 2.19(b). This resonator on the chip R7 gave critical coupling at the pump wavelength, with a total loaded linewidth of approximately 150 MHz. Due to the ‘straight-straight’ coupling section seen in Fig. 2.19(a), the coupling rate κ_{ex} tails off with higher optical frequency[59].

The full experimental setup is depicted in Fig. 2.20. The source laser is a *Toptica* CTL1550. The EO-comb is configured as described in Fig. 2.7 section 2.2, and uses *EO-space* modulators. Using the frequency-resolved optical gating method (FROG), we retrieve a minimum input pulse duration of 1.1 ps (see Fig. 2.20(c)). An RF synthesiser supplies the EO-signal $\hat{f}_{\text{eo}} = 13.94$ GHz. In this way, the microresonator is sub-harmonically pumped every two roundtrips. Half the EO-comb teeth are off resonance, and so can effectively be ignored in terms of soliton

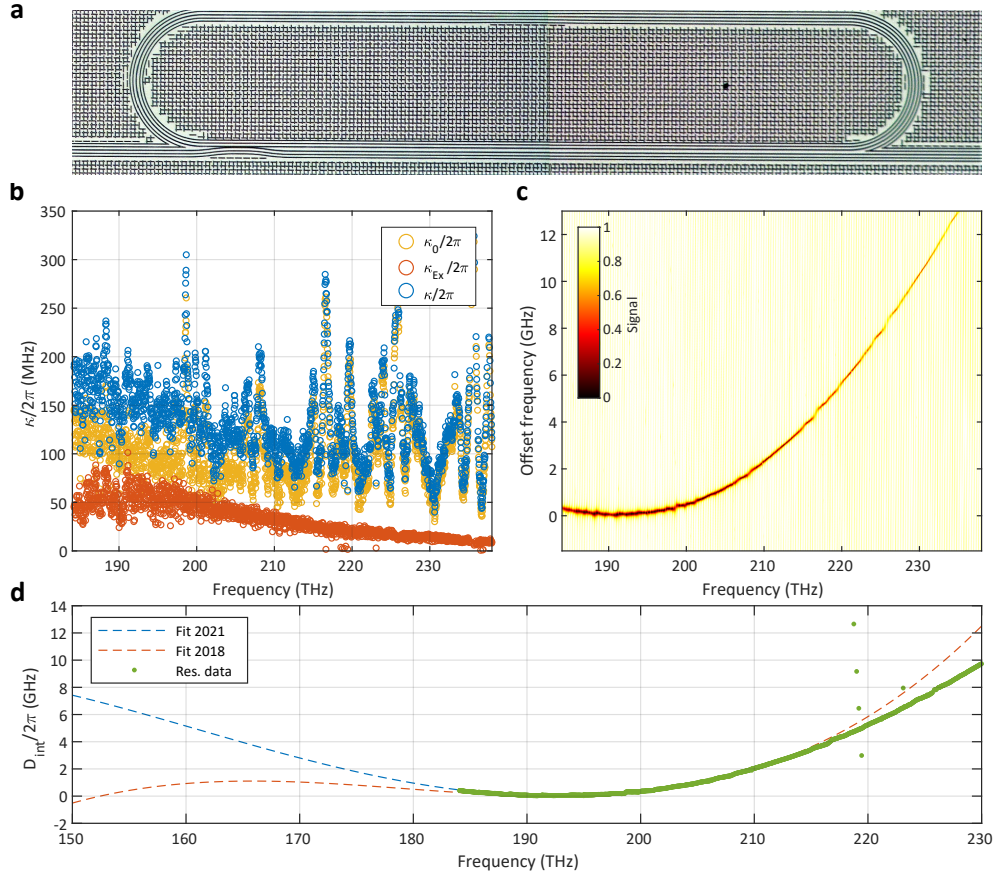


Figure 2.19: **Experimental resonator characteristics (D42-1.F8.G0.R7).** (a) Microscope image of the resonator, showing its semi-circular racetrack design and straight-straight coupler section. (b) The fitted linewidth values of each measured resonance. (c) The total transmission trace measured using the calibrated swept-laser spectroscopy, graphed in Eschelle form with a repetition sampling rate of 27.885 GHz. (d) Calibrated measured D_{int} and two possible fits.

pumping, as if we were driving at 27.89 GHz with half power-efficiency (hence from this point $f_{eo} = 2\hat{f}_{eo}$). Importantly, we employ the use of two separate RF synthesisers for comparison in how noise transfers to the soliton microcomb: A Rhode & Schwarz SMB100A, and an ultra-low phase noise Keysight E8267D, hereafter referred to as RF-1 and RF-2 respectively. Their frequency noise profile at 14 GHz is given in Fig. 2.20(a). After amplification with an EDFA, the EO-comb pulse pump is sent into and out of the Si_3N_4 microchip via lensed fibres and inverse-tapered waveguide ports [119].

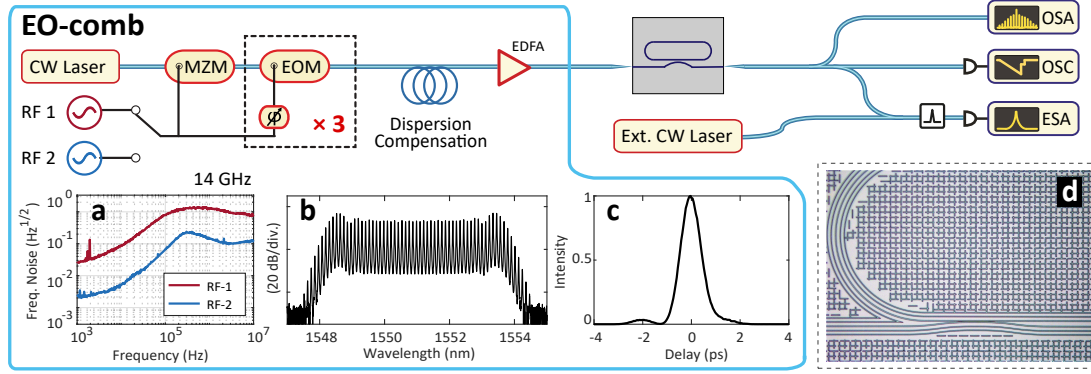


Figure 2.20: **Experimental setup for pulse-driven DKS generation using dispersion-engineered Si_3N_4 photonic chip.** (a) Experimental layout. MZM: Mach-Zehnder modulator, EOM: electro-optic modulator, EDFA: erbium-doped fiber amplifier, ESA: electronic spectrum analyser, OSA: optical spectrum analyser, OSC: oscilloscope. The input pulse train is coupled into and out of the microresonator chip via lensed fibres. Output light is filtered and mixed with a second laser for heterodyne measurement. (b) Frequency noise of two RF signal generators at 14 GHz. (c) Spectrum of the 14 GHz EO-comb before amplification. (f) Retrieved FROG measurement of the optimum pulse duration. (d) Microscope image of part of the microresonator, depicting the coupling section.

2.4.3 Soliton formation

Fig. 2.21 shows the results of soliton microcomb formation, after scanning over resonance and stopping at the state existing at maximum detuning, for many average input power levels. At the lowest power, below the soliton existence requirement, we see the ‘primary comb’ stage of MI (‘Turing Rolls’) in Fig. 2.21(a). As expected, the side-lobes inherit the same bandwidth as the input EO-comb, since this is a pulse-driven event. Fig. 2.21(b) shows the soliton microcomb accessible at the lowest input power. This microcomb has a 3-dB bandwidth of 9.5 THz, and an estimated pulse duration of 55 fs based on a sech^2 fit. The conversion efficiency is approximately 4%, or 8% if not including the $2\times$ sub-harmonic driving efficiency. As said in Eq. 2.3, soliton conversion efficiency is highest at the minimum pump power. Fig. 2.21(c) shows the progressive increase in the microcomb bandwidth with higher power at maximum detuning, with the most broad microcomb shown in Fig. 2.21(d). Here, the conversion efficiency has decreased from 8% to 2.8%. The spectral envelope includes 2,300 detectable comb lines, about 1,400 within the top 10 dB of power near the centre, spanning 64 THz or 600 nm. At the time the result was first posted, to our knowledge, this demonstrated the highest reported line-count for a single-state soliton microcomb, with a repetition rate over 10 GHz. This chapter reports the results acquired in early 2019, but more powerful and efficient soliton microcombs from later times are reported later in section 4.3.2, and in chapter A.

The spectrum is strongly enhanced on the long-wavelength side due to the prominent third-order dispersion, forming a dispersive wave at 1957 nm [120]. While normally there should be

2.4 Broadband, efficient pulse-driven microcomb results and noise propagation

spectral recoil resulting from the photon energy imbalance, the presence of soliton Raman self-frequency shift [121, 61, 122, 123] may have cancelled this recoil, as was observed before in a similar Si_3N_4 microresonator by *Karpov et al.*[60].

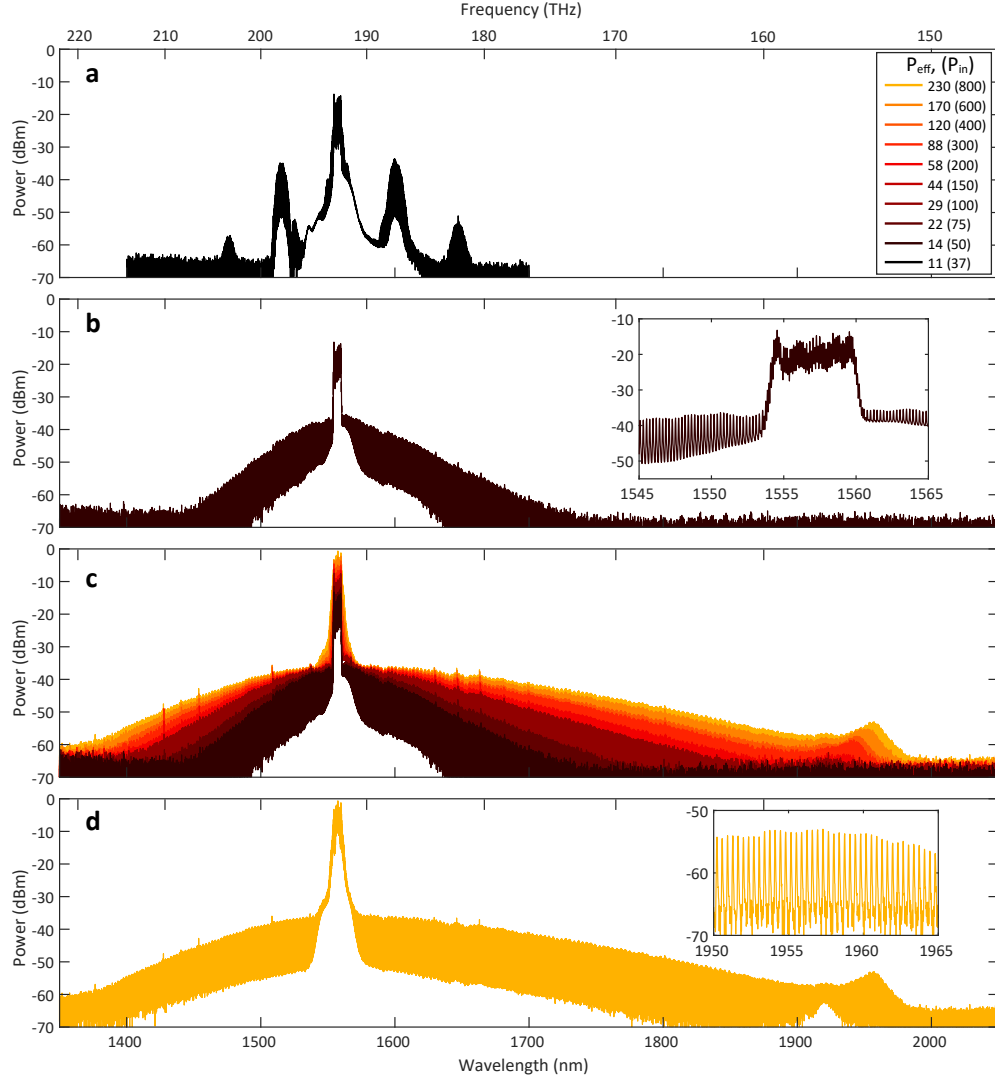


Figure 2.21: **Results for pulse-driven soliton microcomb generation in Si_3N_4 microresonator.** Legend: Input power noted as effective power coupled to the microresonator (and total power incident on chip) taking into account chip insertion loss and $\times 2$ pulse inefficiency. (a) Primary MI comb state. (b) Lowest power and most efficient soliton microcomb. Inset: Close-up of EO-comb pump showing the half comb line separation. (c) Growth of soliton microcomb spectrum with P_{in} according to the legend above. (d) Soliton microcomb at highest P_{in} and detuning. Inset: comb lines in the dispersive wave region.

Fig. 2.22(a) shows examples of the transmission traces measured at the output of the Si_3N_4 chip while the laser centre frequency is scanned over the cavity resonance, from the blue-

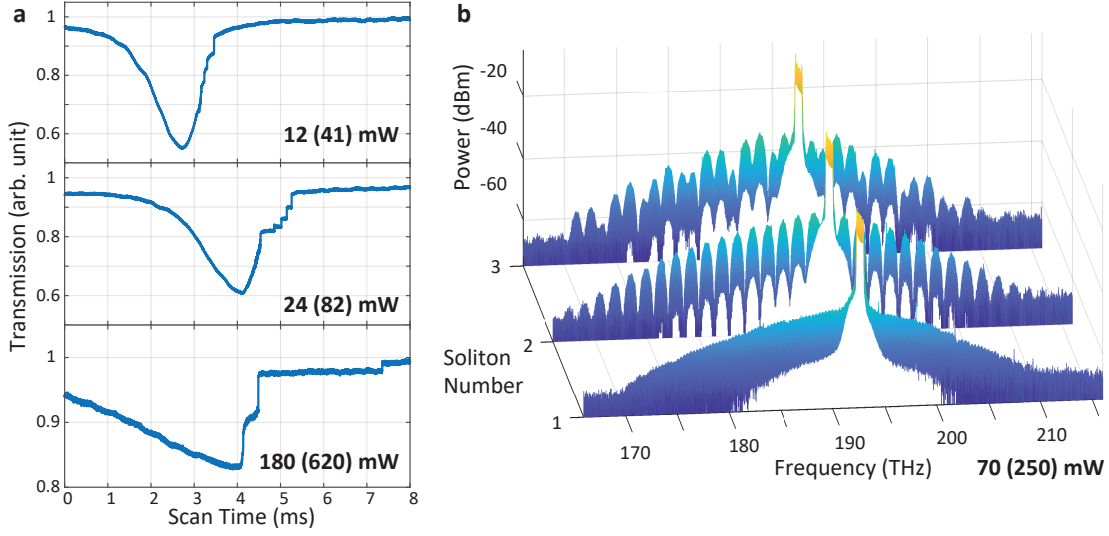


Figure 2.22: **Pulse-driven DS multi-states.** (a) Transmission traces detected at the output of the resonator while the laser is tuned over resonance (in the negative frequency direction), for different input power levels, marked as effective power coupled to resonator (and total power towards chip). (b) Example of multi-soliton spectra.

detuned to the red-detuned side. Three power levels are shown. The soliton step first appears at 12 mW average coupled to the resonator. At a mid-range power of 24 mW, DS tend to form in numbers from 1-3. Examples of the experimentally obtainable multi-soliton microcombs are shown in the panel (b). For the 2-state, since the fringe spacing corresponds to the input pulse width, we can surmise the two solitons are locked at opposite edges of the pulse. In the 3-state, a third soliton likely exists between them. In the bottom high-power trace at $P_{\text{eff}} = 180$ mW, only a single-state is accessible and the step has become substantially longer, enabling easy access to the DS state using slow tuning of the laser frequency.

2.4.4 Numerical modelling with the generalised LLE

I model the realistic spectrum of the generated DS states using the generalised LLE (GLLE, see section 1.2.5) evaluated in the frequency domain:

$$\frac{\partial \tilde{A}_\mu(t)}{\partial t} = i\hat{D}_\mu \tilde{A}_\mu - \frac{\kappa(\mu)}{2} \tilde{A}_\mu + i\Gamma \mathcal{F} \left[(1 - f_R) |A|^2 A + f_R (h_R(\varphi) \otimes |A|^2) A \right]_\mu + \sqrt{\kappa_{\text{ex}}(\mu)} \tilde{F}_\mu(t) \quad (2.21)$$

including higher order dispersion in the form of

$$\hat{D}_\mu = \delta\omega + 2\pi\delta f_{\text{eo}}\mu + \frac{D_2}{2}\mu^2 + \frac{D_3}{6}\mu^3 \quad (2.22)$$

2.4 Broadband, efficient pulse-driven microcomb results and noise propagation

with microresonator longitudinal modes relative to the centre wavelength ($\mu = (\omega - \omega_0)/D_1$), and stimulated Raman scattering (SRS) [123], based on prior work[60] assuming a linear approximation of the Raman response

$$h_R(\tau) \otimes |A|^2 \approx |A|^2 - \tau_R \frac{\partial |A|^2}{\partial \tau} \quad (2.23)$$

and a resonator coupling rate that varies with optical frequency $\kappa_{\text{ex}}(\mu)$, with $\kappa = \kappa_0 + \kappa_{\text{ex}}(\omega)$. The external coupling rate $\kappa_{\text{ex}}(\omega) = \theta(\omega)D_1/2\pi$, where $\theta(\omega)$ is the bus-resonator coupling coefficient (see Fig. 1.6(b) and section 1.2.3). Due to the 30 μm long straight coupling section, $\theta(\omega)$ has a strong decline with increasing optical frequency, which I choose to model with a simple exponential decay (influences by finite-difference time numerical results [124]):

$$\theta(\omega) = \frac{1}{1 + e^{\xi(\omega - \omega_0)/\theta_0}} \quad (2.24)$$

where θ_0 is the coupling coefficient at the pump wavelength ω_0 ($\theta_0 \ll 1$), and ξ is the coupling decay constant. The driving pulse spectrum, on this occasion, is expressed as a rectangular summation of lines

$$\tilde{F}_\mu(t) = \frac{\sqrt{P_0}}{M} \text{rect}(M)_\mu \times \exp\left[i\mu^2 D_1^2 \frac{\tilde{\beta}_2}{2}\right] \times \exp[2\pi i \mu \times \delta f(t)] \quad (2.25)$$

representing M EO-comb lines making a Fourier-transform limited sinc() pulse in the time domain, and including the pre-dispersion (chirp) $\tilde{\beta}_2$ in ps^2 discussed the section 2.2 and Eq. 2.13, and *long-term repetition rate frequency noise* in the form of $\delta f(t)$. All parameter values for this simulation are given in Table C.3.

In Fig. 2.23, the example simulation re-creating the DS generation in the experiment is presented, giving some insight into how strongly perturbed solitons form and the roles played by the higher-order terms in the GLE. In Fig. 2.23(a,b) we show how DS are formed during a scan of the laser frequency over resonance at low power, where $P_0 = 100 \text{ mW}$ or $2.5P_{\text{th}}$. In this scenario, the solitons exist well below the instability thresholds and so do not exhibit any breathing or chaos[79], and they have a small existence range over detuning, as also seen in the corresponding low-power experimental trace shown in Fig. 2.22(a). Formed solitons collapse one by one when the local power level beneath each of them drops below its minimum. Stopping the scan before the last soliton collapse leaves the low energy traces (blue) in Fig. 2.23(e,f), showing a profile very close to the typical sech^2 DS profile, and matching the character of the experimentally generated low-energy DS shown in Fig. 2.21(b).

The formation of a DS at high power is shown in Fig. 2.23(c,d), where $P_0 = 25P_{\text{th}}$. At this driving strength, stable Turing rolls[125] form at a low detuning ($\delta\omega < 0$), before entering into a regime of turbulence [75] up until $\delta\omega < 3\kappa$. At this point solitons form in the region

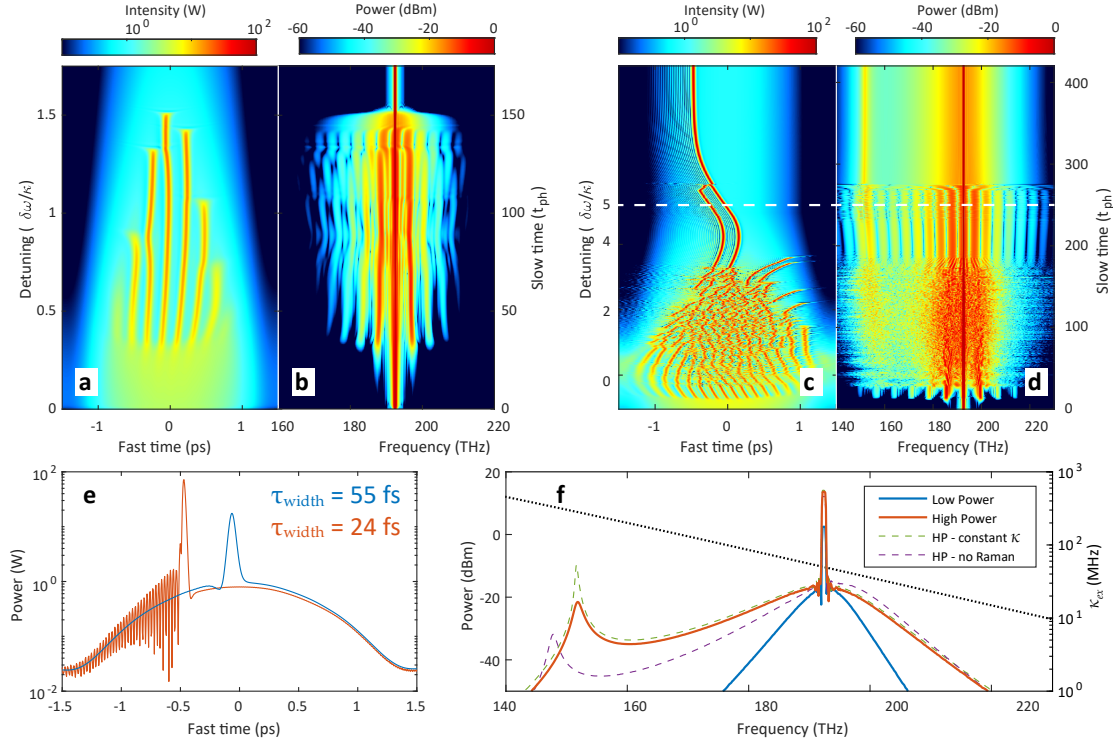


Figure 2.23: Simulation: Pulse-driven dissipative soliton formation based on the generalised Lugiato-Lefever equation. (a) Intracavity optical field and (b) frequency domain output over change in $\delta\omega$ (scan over resonance), at low power. (b,c) Same as (a,b) for high power. Laser frequency tuning stops at white-dashed line. (e) Intracavity time-domain slices of stable single DS state for low (blue) and high (red) power and detuning. (f) Output spectral envelope for single-DS states (solid line), and the same high power DS with perturbations removed (dashed line), along with $\kappa_{ex}(\omega)$ (dotted line). Parameter values for this simulation are given in Table C.3.

of bistability, featuring strong dispersive wave tails. For the rest of scan until $\delta\omega = 5\kappa$, the group velocity of the soliton curves due to the competing shifts in the spectral centre from the counter-acting effects of dispersive-wave induced recoil [67], and the Raman self-frequency shift [61]. For this simulated example, the whole driving pulse profile has a repetition-rate mismatch of $\delta f_{eo} = -50$ kHz so as to contain the shifting solitons inside their locking range with the pulse.

The scan stops at $\delta\omega = 5\kappa$ leaving a bound dual-soliton state moving towards the pulse edge. As has also been observed in numerical work on intensity-trapped solitons in the presence of group-velocity mismatch [115], such a 2-state may not be able to exist on the pulse edge, and so in this example the left soliton is displaced by the right one and collapses. The remaining soliton continues to the edge of the pulse where it becomes locked [114]. The final high power DS is depicted in Fig. 2.23(e,f) in time and frequency respectively. Due to the Raman self-frequency shift, the dispersive-wave recoil of the spectrum centre has been mostly cancelled

as happened in experiment. Moreover, the increase in κ_{ex} at lower optical frequencies has caused the dispersive wave spectrum to broaden to 1.4 THz (3 dB width), agreeable with the experimental dispersive wave peak-width of 1.5 THz. Overall, a stable optical complex is formed comprising the background pulse, the dispersive wave, and the soliton.

2.4.5 Comparison with CW driving

To demonstrate the experimental advantages of the pulse-driving method in generating DS states in this microresonator, experimental results of CW-driving the same resonator are presented in Fig. 2.24, showing behaviour discussed earlier in section 2.1. With a CW pump, the nonlinear threshold for primary sideband generation was 115 mW at the resonator (200 mW on chip facet), effectively about 10 times larger than observed in Fig. 2.21 for pulse driving. I try to generate solitons with CW pumping using a higher power of 310 mW on-facet. Fig. 2.24(a) shows the total transmission from scanning over resonance, including the generated light only with the pump line suppressed. The microcomb spectrum observed at different stationary points during the scan are shown in Fig. 2.24b(i)-(vi). The formation behaviour here is described in better detail in *Karpov et al.* [104], but here only a perfect crystal state is obtained in the soliton regime, each time. In this instance, the soliton count appears to be about 167 in a situation similar to that shown in Fig. 2.6(b). The power is too low for the possibility of number-switching to reduce the soliton count. Fig. 2.24(c) shows the final state accessible at a higher power of 430 mW, the fully chaotic MI state. Likely due to the increased thermal load on the resonator [103], as shown in the scenario Fig. 2.5, the soliton ‘step’ is not accessible via piezo-driven laser tuning, down to the μs scale.

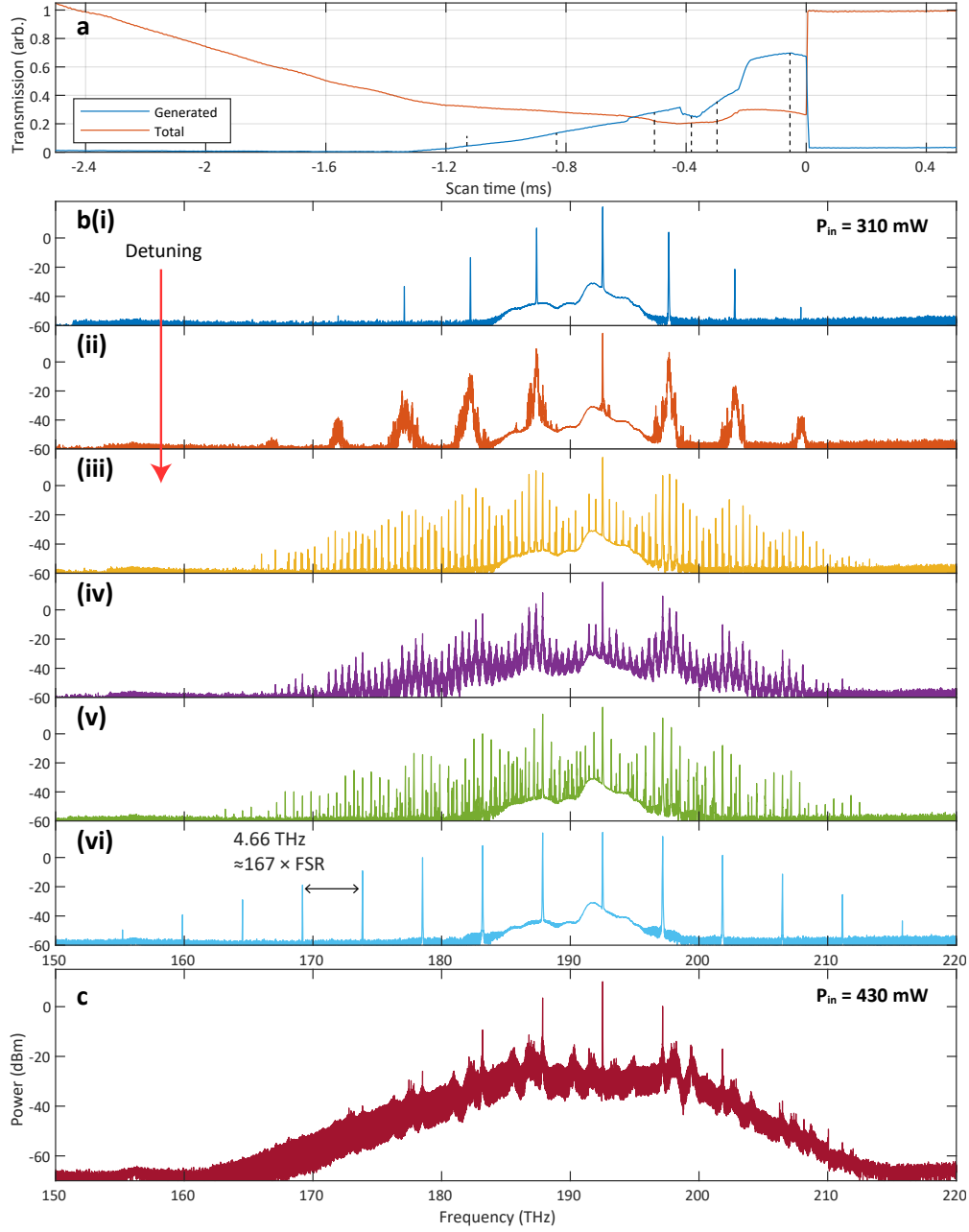


Figure 2.24: **Experimental results from CW-driving the microresonator.** (a) Transmission trace of the microresonator as the laser frequency is swept over resonance, and measured power of ‘generated light’ only, with the pump line suppressed. (b)(i)-(vi) Optical spectra of the states existing at the locations marked in plot (a). (c) Chaotic MI microcomb at maximum reachable detuning with higher power CW pumping.

2.5 Microcomb noise propagation

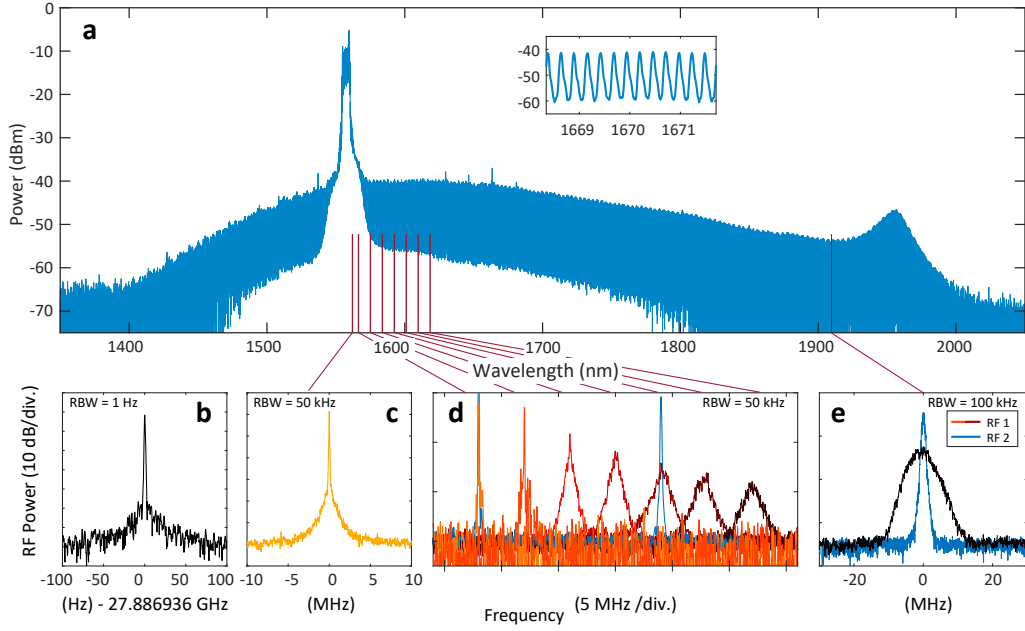


Figure 2.25: **Resonant supercontinuum generation and coherence.** (a) Chosen generated soliton microcomb at maximum detuning, formed using ~ 1 ps pulses with incident average $P_{\text{eff}} = 180$ mW (620 mW total, accounting for insertion loss and $\times 2$ sub-harmonic driving inefficiency). (b) The soliton repetition rate beatnote. (c) Beatnote at the 12th line at the edge of the EO-comb. (d) Beatnotes of μ th comb line, measured between the pump and 1620 nm, from left-to-right $\mu = -45, -88, -132, -175, -217, -259, -300$ (horizontally offset by 4 MHz for clarity). (e) Beatnote at 1908 nm ($\mu = -1300$). Legend applies across (f) and (g), with utilised RF source 1 in red colours, RF source 2 in blue colours.

2.5.1 Coherence measurement, noise multiplication

Turning our attention to the noise and coherence properties of the pulse-driven soliton microcomb, Fig. 2.25 shows a series of heterodyne measurements of the comb. Fig. 2.25(b) shows the repetition rate beatnote of the DS, obtained by suppressing the EO-comb part of the spectrum using a wavelength-division multiplexer. The beatnote corresponds exactly to 2 times the RF source frequency and, with a 1 Hz limited linewidth, demonstrates high repetition rate stability indicating the DS is temporally locked with the driving pulse. For measuring the optical coherence of the comb, heterodyne measurements with a second laser (also *Toptica* CTL 1550) are taken against comb lines of increasing values μ , the comb line index from the centre pump, from 1550 nm to the outer edge at 1908 nm plotted in Fig. 2.25(d-e). Fig 2.25(c) shows a narrow heterodyne beatnote at the edge of the EO-comb. As comb lines become further away from the centre, their linewidth quickly broadens as shown in Fig. 2.25(d) where we plot heterodyne beatnotes up to a range of 70 nm from the comb centre. This noise increase continues to the long-wavelength edge of the comb, where the heterodyne beatnote with a

narrow-linewidth 1908 nm laser (*NKT Photonics*) is plotted in Fig. 2.25(e). Here, the linewidth has expanded to around 7.5 MHz according to Gaussian fitting.

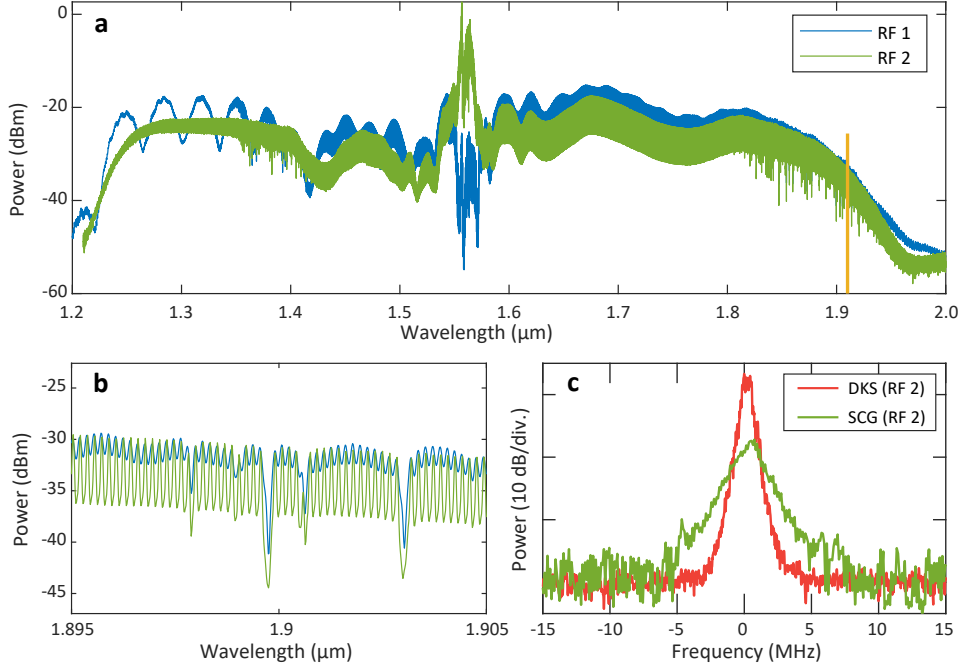


Figure 2.26: Noise filtering comparison with conventional supercontinuum generation. (a) EO-comb based supercontinuum at 14 GHz spacing, derived from the two RF sources. Beatnote measurement at 1908 nm marked in yellow. (b) Close look at the region around 1900 nm, comparing spectral width of comb teeth on OSA. (c) Heterodyne beatnote at 1908 nm measured against the DS- and supercontinuum-based frequency comb, driven by source RF-2 (RBW = 50 kHz, and 1 MHz respectively).

If we switch our RF signal generator from RF-1 to the lower noise source RF-2, and measure the heterodyne comb beatnotes at the same wavelengths (here shown 1560, 1600, and 1908 nm) in Fig. 2.25(d,e), we find that linewidths are decisively more narrow. The linewidth at 1908 nm in particular has reduced by almost a factor of 10, down to 900 kHz. This difference in coherence at the wings of the spectrum, using different EO-comb RF sources, confirms to us that this is the result of RF noise multiplication imposed on the comb spacing through the locking between the input pulse and the DS.

Comparison with conventional supercontinuum generation.

Does this noise multiplication of a pulse-driven soliton microcomb compare differently with a pulse-driven conventional supercontinuum? We decided to answer that question in collaboration with our collaborators Ewelina Obrzud and Tobias Herr at CSEM. At their lab, we formed a supercontinuum from an EO-comb driven with the *same* RF sources as in the DS generation experiment: RF-1 (Rhode & Schwarz SMB100A), and RF-2 (Keysight E8267D). See Fig. 2.20(b)

for the frequency noise spectra of these sources. The supercontinuum is formed through a combination of strong amplification through an EDFA and nonlinear pulse compression through lengths of normal and anomalous dispersion fibre, before creating a supercontinuum in highly-nonlinear optical fibre (HNLF). Details of this SCG method are given in *Obrzud et al.*[36]. The supercontinuum generated from the EO-comb driven by RF-1 and RF-2 are shown in Fig. 2.26(a) and (b). One already noticeable difference in the OSA-measured traces is, particularly in (b) around 1900 nm, at the same spectral resolution of 0.05 nm the apparent definition of the comb lines is far poorer for the comb derived from RF-1 indicating serious decoherence. The fact this decoherence is worst at the spectral edges, also at 1250 nm, suggests line-by-line RF noise multiplication. The heterodyne beatnote detected at 1908 nm (with that same NKT laser) using RF-2 is plotted in Fig. 2.26(c) in comparison with the beatnote measured from the same DS comb line with RF-2 from Fig. 2.25(e). The SCG-based beatnote has a linewidth of ~ 1.8 MHz, approximately double that of the DS. When trying the same measurement with RF-1, the beatnote at 1908 nm was *undetectable* by our experimental means, indicating it was too broad to be resolved with the given equipment and settings. For both RF-1, and RF-2, the measured beatnote at 1908 nm is much more pure for the DS than it is for the SCG. Hence, we concluded that dissipative soliton-based nonlinear filtering of the added noise was taking place for the pulse-driven microcomb experiment.

2.5.2 Numerical modelling of noise transfer

If one were to assume that the soliton is perfectly locked to the driving pulse, we would expect the optical frequency noise of each soliton comb line to be coupled to the RF noise on the coupled pulse repetition rate $f_{e0} = 28$ GHz, such that $S_{\delta\nu}^{(\mu)}(f) = \mu^2 S_f^{(\text{rf})}(f)$, with relative comb index μ (assuming other sources of laser noise are small by comparison). However this is not the case for a DS. The frequency-noise multiplication transfer function can be found in numerical simulations based on the LLE, which for this occasion we simplify and omit higher order dispersion and Raman scattering

$$\frac{\partial A}{\partial t} = \left(i\delta\omega - \frac{\kappa}{2} - i\frac{D_2}{2} \frac{\partial^2}{\partial \varphi^2} + i\Gamma|A|^2 \right) A + \sqrt{\kappa_{\text{ex}}} F(\varphi, t) \quad (2.26)$$

As a reminder, the spatial angular coordinate $\varphi = D_1\tau$ the fast time coordinate. We omit the higher order effects so that we can find understanding of the noise transfer behaviour in the most pure scenario. The input pulse function $F(\varphi, t) = \mathcal{F}[\tilde{F}_\mu]$, referring to Eq. 2.25, with particular attention paid to the frequency noise term $\delta f(t)$. The simulation parameters this time are given in Table C.3. They are chosen to reflect a basic archetypical Si_3N_4 resonator with a more simplified dispersion compared to that of the experiment, rather than perfectly replicating the experiment quantitatively. The relative driving strength is set to $F^2 = 24$, and the detuning $\delta\omega = 6\kappa$. The driving pulse has a pre-chirp of $\tilde{\beta}_2 = +0.3 \text{ ps}^2$ in order to ‘bias’ soliton attraction slightly towards the pulse centre, as it likely is in experiment (see section 2.2).

We apply cycle jitter (ie. repetition rate frequency noise) to the driving pulse function $F(\varphi, t)$, equivalent to a uniform power-spectral density of $S_f^{(rf)}(f) = 1.0 \text{ Hz}^2/\text{Hz}$ over a long period of ‘slow time’ ($t > 4,000\kappa^{-1}$), and the corresponding jitter of the soliton is recorded. For this first simulation, we set $\delta f_{eo} = 0$ corresponding to the driving pulse and the natural soliton repetition rate being equal. The simulation results are shown in Fig. 2.27. In the time domain shown in Fig. 2.27(a,b), the generated soliton is located at its ‘trapping point’ at 0.6 ps at the trailing edge of the pulse[114], but under these synchronous and symmetrical pulse conditions, it could equally find itself at -0.6 ps on the leading edge. As it’s locked to the driving pulse it inherits jitter and gradually walks back and forth in the fast time domain. The noise applied to the input pulse itself during this one example, and its corresponding walk in the time domain, is plotted in Fig. 2.27(c).

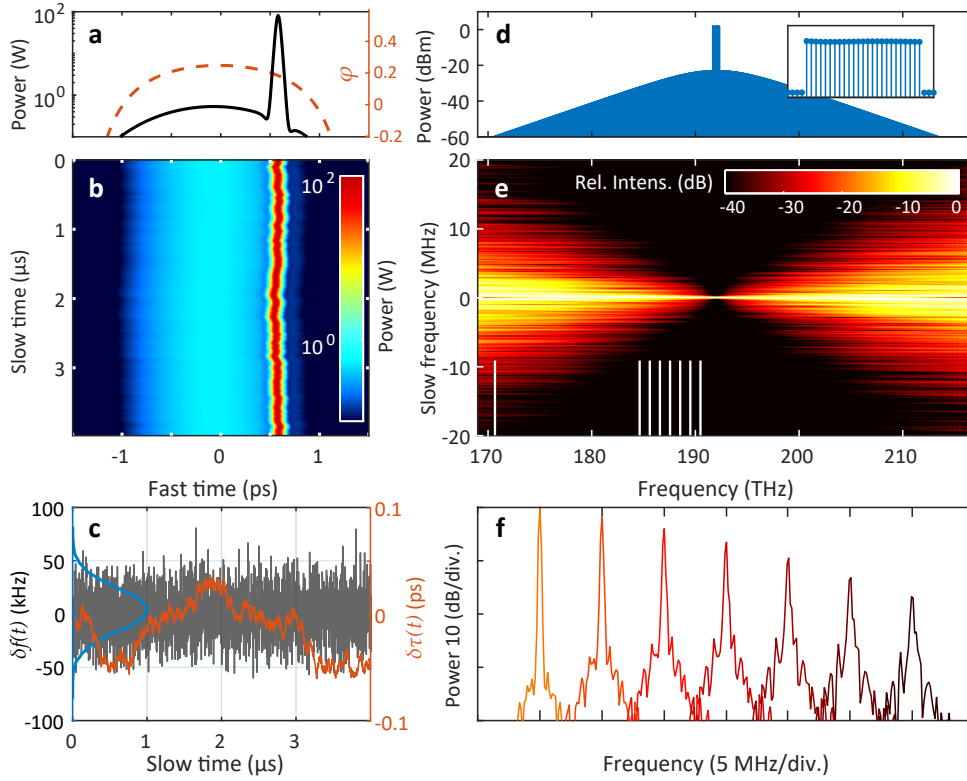


Figure 2.27: **Simulation of input noise multiplication, based on the LLE.** (a) Intracavity field at time t . Instantaneous phase of the background pulse as dashed line. (b) Slow time vs. fast time graph of intracavity field. (c) Frequency noise (grey, histogram in blue), and corresponding absolute timing jitter (orange) imposed on the driving pulse over the period of the simulation. (d) Output spectrum, with inset showing input pulse spectrum. (e) Slow frequency vs. fast frequency graph of the long-term frequency comb, with columns normalised to peak-power spectral density. White marks indicate comb lines depicted in (f) and in Fig. 2.28. (f) Individual noisy comb lines selected from (d), with same comb mode μ as in the experiment Fig. 2.25(d).

The corresponding frequency domain results are shown in Fig. 2.27(d,e). Fig. 2.27(e) in particular is obtained by taking the Fourier transform over both dimensions of the optical field

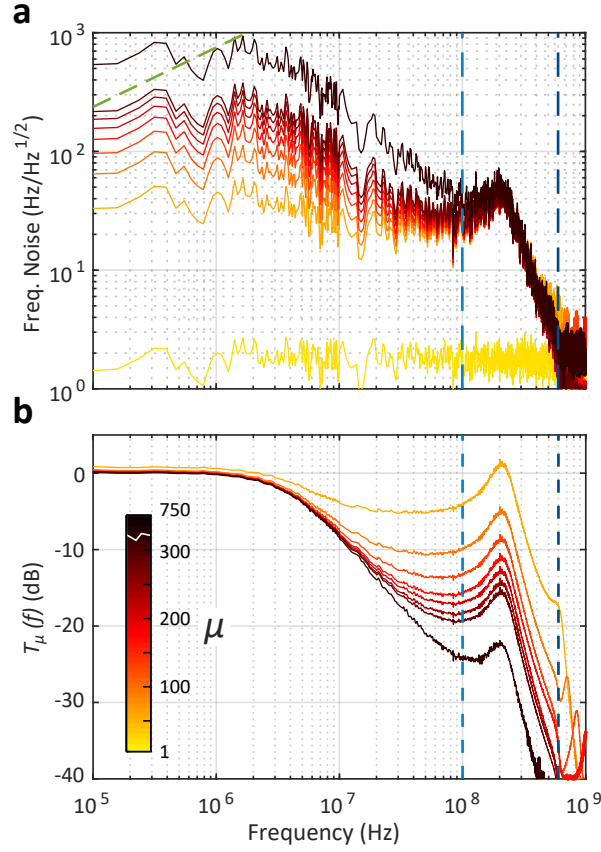


Figure 2.28: **Simulation of noise multiplication and nonlinear filtering, based on the LLE.** (a) Frequency noise spectra and (b) corresponding RF-noise transfer functions for individual comb lines marked in Fig. 2.27, including one comb line far from centre ($\mu = -750$). Dotted lines indicate the linear cavity bandwidth κ (light blue), cavity detuning $\delta\omega$ (dark blue), and the ‘ β -line’ (green). Traces are averaged from 8 simulations for smoothness.

in Fig. 2.27(b), therefore plotting the power spectral densities on the y-axis of each individual comb line along the x-axis – a simulated heterodyne beatnote (normalized to peak). This type of diagram was introduced in chapter 1. Evidently, the linewidth of each comb line widens considerably as they become further from the comb centre. In Fig. 2.27(f), individual beatnotes corresponding to the same comb line measurements shown in Fig. 2.27(f) show good qualitative agreement.

The profile of this frequency noise transfer to individual comb lines is given in Fig. 2.28 where we plot their frequency noise spectra and corresponding normalised transfer functions $T^{(\mu)}(f) = S_{\delta v}^{(\mu)} / (\mu^2 S_f^{(\text{rf})})$ respectively. Frequency-noise power spectra are found by Fourier-transform of the slow-time phase fluctuations of individual comb lines $\tilde{A}_\mu(t)$, as $\delta f_\mu(t) = \frac{d}{dt} \arg(\tilde{A}_\mu(t))$. As expected for low offset frequencies, noise power is fully multiplied by μ^2 , fulfilling the requirement for the soliton to be locked to the driving pulse over the long term. Strikingly however, above some cut-off frequency approximately 3 MHz, the transfer of noise

power drops significantly at a slope of -20 dB/decade, showing how the soliton is able to ‘ignore’ fast background motion of the input pulse despite being locked to it over the long-term. Interestingly, this cut-off frequency is on the order of 100 times lower than the linear cavity bandwidth κ for this simulated Si_3N_4 cavity, of 100 MHz, demonstrating that this filtering is born of the nonlinear DS regime, as has also been observed in MgF_2 crystalline microresonators[126] with single-sideband pumping. Beyond this cut-off point, the transfer function begins to be dominated by the response of the cavity [73], where we see a resonance located after the cavity bandwidth at κ likely corresponding to the soliton’s breathing response[87], and a further strong cut-off at the cavity detuning at $\delta\omega = 2\pi \cdot 600$ MHz. The exact nature of these resonances is beyond the scope of this chapter, though the simulated traces presented here are in excellent qualitative agreement with the numerical and experimental results presented in an independent and concurrent work by *Brasch et al.*[97], where the full linear and nonlinear response is investigated in detail.

2.5.3 Noise transfer reduction with soliton pushing

Returning attention to the experimental heterodyne beatnote measurement at 1908 nm, we have observed an interesting effect when the driving repetition f_{eo} is varied. Fig 2.29(a) shows the 1908 nm beatnote as f_{eo} is swept from the minimum to the maximum of the soliton locking range (0 kHz defined as the minimum). The linewidth appears to narrow, reaching a minimum at the upper edge of the locking range, in this case 50 kHz. To characterize this narrowing phenomenon, we measured the frequency noise spectrum of this beatnote using in-phase/quadrature analysis [127] as f_{eo} is varied across the locking range, which is shown in Fig. 2.29(b). Also overlaid is $2\mu\sqrt{S_f^{(\text{rfl})}}$, where $S_f^{(\text{rfl})}$ here is the independently measured frequency noise spectrum of the signal generator RF-1 at 14 GHz, with comb line $\mu = 1300$, (and factor of 2 from the half rep-rate driving up-scaled to from 14 to 28 GHz). I further plot the corresponding experimental transfer functions $T^{(\mu)}(f)$, as before, in Fig. 2.29(c). As shown, the frequency noise level of the 1908 nm beatnote very closely follows the multiplied RF noise until a certain cut-off frequency, which varies from a maximum of 2 MHz reducing to ~500 kHz at the edge of the locking range. In excellent qualitative agreement with the simulation results in Fig. 2.28, the value of this corner frequency is on the order of 100 times less than the linear cavity bandwidth of 100-150 MHz, experimentally confirming the presence of nonlinear filtering.

Numerical simulations to analyse the synchronisation-dependent nonlinear filtering behaviour are presented next. We apply a mismatch between the input pulse train repetition rate and the native repetition rate of the soliton ($\delta f_{\text{eo}} = f_{\text{eo}} - D_1/2\pi$). Fig. 2.30(b) show the same type of result as Fig. 2.27(e), only now for a DS microcomb with 4 different values of δf_{eo} (manifesting as the gradient in the comb line centres) between -50 and 50 kHz. The effect on the comb linewidth broadening is stark. The simulated comb line for $\mu = -1300$ as δf_{eo} is varied between 0 and 50 kHz (the maximum of the locking range) is displayed in Fig. 2.30(c), showing excellent qualitative agreement with the experimental observation in Fig. 2.29(a).

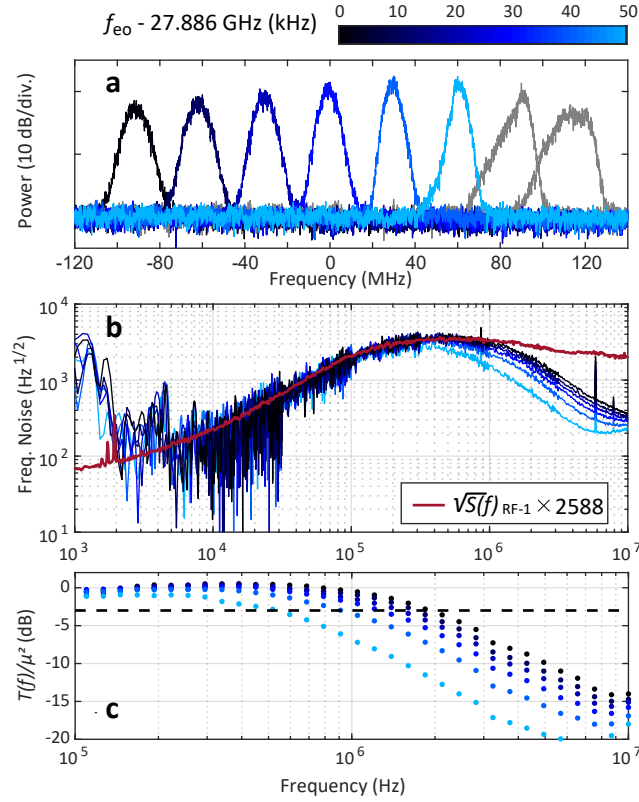


Figure 2.29: **Optimization of soliton-based nonlinear filtering via asynchronous driving: experiment.** (a) Experimental DKS heterodyne beatnote at 1908 nm ($\mu = -1300$) as f_{eo} is varied over a range of 50 kHz. Beatnote signals are horizontally offset each by 30 MHz for clarity. (b) Corresponding measured frequency noise, plotted with the multiplied frequency noise of RF-1. (c) Experimental transfer function based on (b), with 3-dB level marked with dashed line.

Our experimental and simulation results reveal that as the repetition rate mismatch δf_{eo} changes, the ‘trapping’ location of the DS on the driving pulse, as well as the local trapping gradient can change significantly, due to the background driving phase and intensity-driven forces described in section 2.3. In this experiment, the driving field is a mixture of both amplitude modulation (pulse driving) and phase modulation (additional chirping). As a result, the soliton is drawn towards an intermediate trapping location between the intensity-based trap at the edge of the pulse, and the phase-based trap at the peak. This trapping point will be modified by δf_{eo} , which acts as an effective force [128]. In order for a DS to continue to sustain itself, it must follow the pulse at its own shifted repetition rate.

If δf_{eo} is non-zero, the soliton must move to a different location in order to acquire a shifted repetition rate (Eq. 2.16 and 2.18), due the gradient in background phase and/or intensity. Fig. 2.30(a) illustrates these situations from (i) to (iii), where $\delta f_{eo} < 0$, $\delta f_{eo} = 0$, and $\delta f_{eo} > 0$. The soliton is initially positioned on the left, leading edge of the pulse. In Fig. 2.30a(i), the mismatch δf_{eo} and the intensity-based trapping force have combined to shift the soliton to

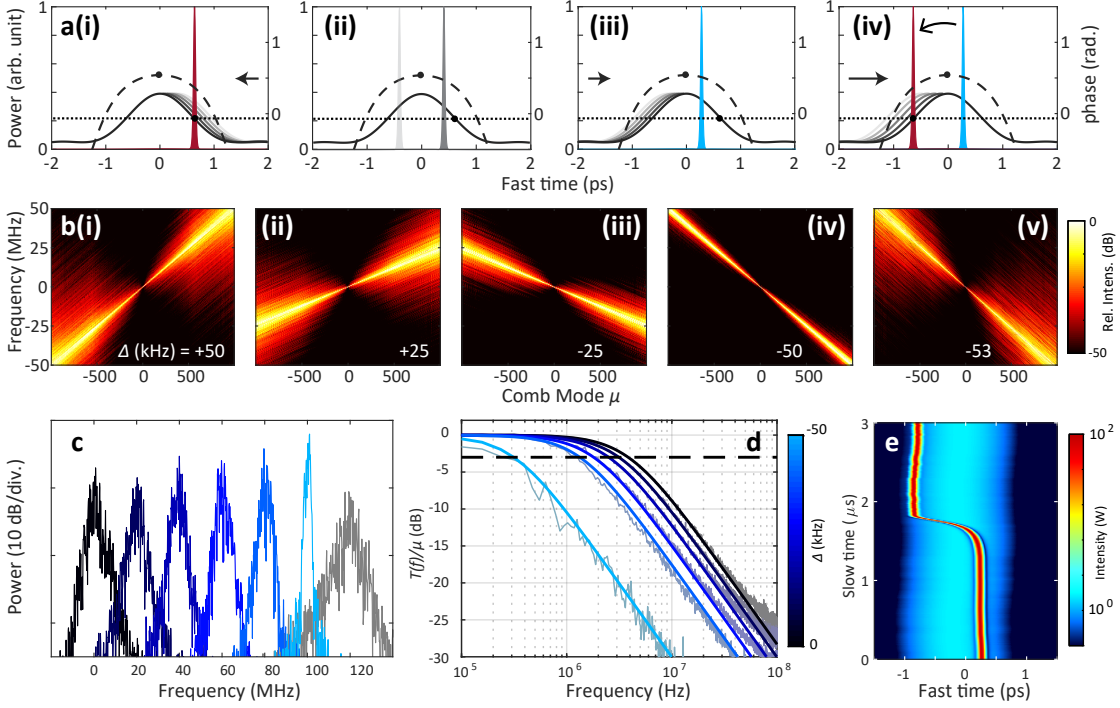


Figure 2.30: **Optimisation of soliton-based nonlinear filtering via asynchronous driving: simulation.** (a)i-iv Conceptual soliton trapping locations on a chirped pulse background under different values of de-synchronised driving δf_{e0} . Arrow indicates driving pulse repetition-rate mismatch, with pulse phase profile (dashed) and the intensity-driven trapping level F_C (dotted). (b)i-v Simulated slow vs. fast frequency graphs for different values of de-synchronisation δf_{e0} . (c) Slice of the simulated $\mu = -1300$ beatnote (1908 nm) in slow frequency for δf_{e0} from 0 to 50 kHz (blue). (d) Simulated noise transfer functions for δf_{e0} from 0 to 50 kHz. Low-pass fit profile in coloured line, original results in grey. (e) Slow time vs. fast time recording of a soliton side-switching event with $\delta f_{e0} = -53$ kHz where, initially, the soliton is ‘quiet’ at its weak trapping point. After falling to the other side, it becomes noisy.

the very left edge of the pulse. In a(ii), the soliton is located at its intermediate trapping point, which is symmetrical with the pulse. In a(iii), the mismatch δf_{e0} adds to the phase-based trapping force, causing the soliton to move closer to the peak.

The observed change in noise transfer bandwidth with varied δf_{e0} can be understood intuitively as being due to the local trapping gradient[115, 97] that gradually decreases from the edge of the pulse to the centre. Somewhat analogous to atoms/particles trapped by optical potential wells[129], a DS trapped at a location closer to the input pulse centre is subject to a shallower potential gradient, thus becoming more ‘free-running’ and less affected by the noise contained in the driving field. For Fig. 2.30b(i) where the soliton is being ‘pulled’ on the edge of the pulse, the transfer broadening is maximised. For b(iv), where the soliton is instead being ‘pushed’ near the peak of the pulse, it has almost reduced to zero. The reduced noise transfer effect is well reproduced by our simulation, as shown in Fig. 2.30(d). As δf_{e0} increases,

the DS gets closer to the pulse centre. Consequently, the cut-off frequency of the noise transfer function decreases, showing qualitative agreement with the experimental measurement in Fig. 2.29(c).

In one additional twist, it was observed in experiment shown in Fig. 2.29(a) that if the δf_{eo} exceeded that ideal point when the soliton was being ‘pushed’ that the measured heterodyne beatnote would reach its most arrow and then, *suddenly*, broaden significantly. This, too, was observed in the simulation demonstrated in Fig. 2.30a(vi), b(v), and (e), where the soliton loses its bond with the driving pulse entirely and basically falls over to the trailing edge which, of course, traps the soliton in a much tighter location, increasing its received jitter.

3 Localised dissipative structures near zero dispersion

Compared with dissipative Kerr solitons (DKS), localised dissipative Kerr structures (LDS) existing in the *normal* dispersion regime, rather than the anomalous, have been covered in greater mystery in the years leading up to the work covered in this chapter. In conservative systems, the opposite dispersion equivalent to the ‘bright’ soliton was the *dark soliton*[89]. In the earlier years of theoretical study into LDS in Kerr cavities, such dark pulses were also found numerically[130, 125, 131] and they were initially associated to those conservative dark solitons. However, as introduced in section 1.3.3, the true underlying dissipative structural component is the switching wave (SW). What appeared to be dark solitons were in fact the lowest-order stable solution of two *interlocked* (SW), inwardly facing[90], a part of an extended family of possible solutions where two inwardly facing SWs would bond to each other based on the quantised potential of their oscillating tails[132], not unlike with DKS and their dispersive wave tails[92].

Experimentally, it was doubtful at first whether dark LDS like this could be formed in Kerr microresonators as, unlike with anomalous dispersion, the intracavity CW field was (almost) always stable[70], and so there would be no opportunity for dark LDS to form in the cavity spontaneously by tuning into resonance as with solitons. The breakthrough demonstration by *Xue et al.* [133] then showed that deviations to the resonator mode spectrum (mode crossings) can provide the phase-matching to allow spontaneous sideband growth – like with MI – to destabilise the CW field and lead to the formation of stable dark pulses [134]. It was also proposed back then by *Lobanov et al.*[131] that stable ‘bright’ pulses can be formed by pumping directly into a deviated cavity mode, something later confirmed to great success[135]

During the pulse-driving soliton microcomb work of the previous chapter, I happened to find that one of the other Si_3N_4 microresonator chips prepared for that experiment happened to have low normal dispersion instead of the low anomalous dispersion as intended. I took the opportunity to pulse-drive the resonator hoping to see SW-based microcomb generation. On that day I was shocked to find, aside from broadband SW-microcomb generation, the formation of a highly broadband apparently stable soliton-like structure with a complex, partially modulated envelope that was unrecognisable to me. This microcomb appeared even

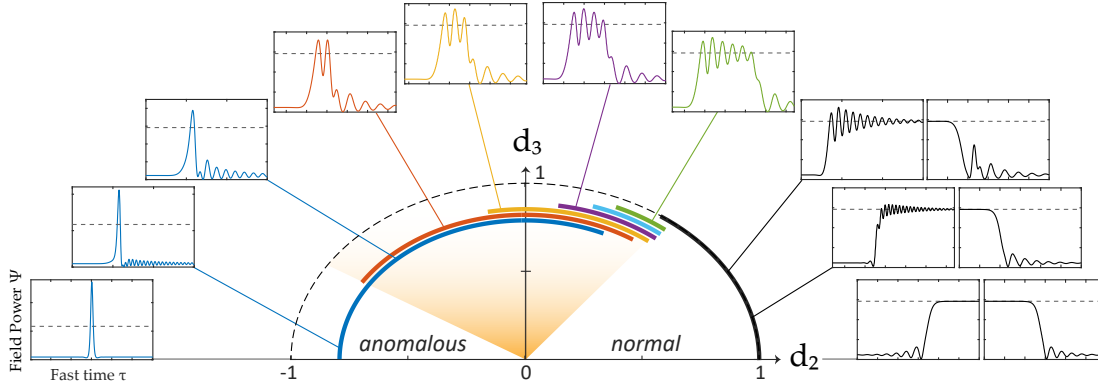


Figure 3.1: Localised Dissipative Structures (LDS) in the second-/third-order dispersion (d_2/d_3) plane. Clockwise from left: conventional dissipative solitons, dissipative solitons with dispersive-wave tails, zero-dispersion solitons with quantized periods (orange area), switching waves with dispersive wave tails, conventional switching wave. Dashed grey line in outer figures represent the CW high-state solution. Thick bands represent the existence range of structures in the circular path. LLE parameters given below in section 3.1.3.

more broadband and efficient than in the conventional soliton microcomb experiment. I then embarked on the work presented below to study this optical object, that I initially did not expect to find, and would choose (along with my co-authors) to term this entity a *zero dispersion soliton* (ZDS).

ZDS exist at the crossing point between conventional dissipative solitons and switching waves, excited in the region of vanishing second-order dispersion (SOD) giving way to pure or dominant third-order dispersion (TOD)[136]. Depicted in Fig. 3.1, ZDS appear as self-stable, multi-peaked pulse structures, existing as a family of solutions of LDS as one traces a circular path of dispersion in the SOD/TOD plane. This ZDS family (here obtained through numerical simulations of Eq. 1.54), is shown to occupy the connection between the diametrically opposed cases, of conventional dissipative solitons on the anomalous dispersion regime, and switching waves on the normal dispersion regime. As one approaches the zero-dispersion region in the center, in both cases of DKS and SW, the dispersive wave tail [137, 69, 120] becomes increasingly dominant until it becomes an essential part of the structure[67], and stable quantised multi-peaked pulses become accessible. We define the two boundaries of this region of ZDS to be where solitons may become multi-peaked on the anomalous side, and where the two switching wave fronts become locked together on the normal side.

This chapter first will cover the theory LDS that exist in all second-order/third-order dispersion space, the definition of the $ZDS^{(n)}$, and how it can be formed using modulated or pulsed-driving. Second, experimental work is presented, firstly with SW generation in the simple dominant second-order dispersion case, followed by ZDS broadband microcomb generation in the near-zero dispersion regime, along with the observation of higher-order dispersive waves.

3.1 Theory

To analyse the optical structures introduced in this section in a universal fashion, as said in the previous chapter, we first consider an optical system described by the dimensionless Lugiato-Lefever Equation (LLE) [85, 70], with a non-CW driving term $F(\tau)$:

$$\frac{\partial \psi}{\partial t} = \left(-d_1 \frac{\partial}{\partial \tau} - i d_2 \frac{\partial^2}{\partial \tau^2} + d_3 \frac{\partial^3}{\partial \tau^3} \right) \psi + (i|\psi|^2 - i\zeta_0 - 1)\psi + F(\tau) \quad (3.1)$$

The form taken by the field solutions are determined solely by the driving strength F and detuning ζ_0 , as well as three parameters d_l describing the relative contributions of the first three orders of dispersion. For simplicity, we set the SOD parameter $d_2 = 1$ here, which corresponds to normal dispersion. Thus, d_3 describes the contribution of TOD relative to d_2 , and the first-order dispersion d_1 corresponds to the offset in group-velocity between the cavity field $\psi(\tau)$ and the static frame of the pulse-driving term $F(\tau)$ (as previously covered in chapter 2, section 2.3). See Eqs. 1.55 for their relationship to real experimental parameters.

3.1.1 Switching wave formation in modulated driving

Firstly, it is necessary to investigate direct SW formation by pulse-driving, in the simplified case of pure SOD ($d_1 = d_3 = 0$). We choose a value of $F_0 = \sqrt{10}$, a typical operating point for practical dissipative structure formation in experiment, and we set a Gaussian pulse as the driving function

$$F(\tau) = F_0 \exp(-\tau^2/\tau_p^2) \quad (3.2)$$

with pulse duration $\tau_p = 100$ so as to ensure any SW is significantly shorter in duration than the envelope of the driving pulse (which is true also in our experiment), and so the driving parameter at each SW location can be considered approximately CW. The detuning is swept linearly from some value $\zeta_0 < 0$ up to $\zeta_0 = 10$. As covered in chapter 1, the cavity resonance becomes tilted as a result of the additional phase acquired over propagation for higher pump power. This creates an expanding range of bistability for steady-state CW solutions, the high state ψ_H and low state ψ_L (the intermediate state is inaccessible). These solutions can be found from Eq. 1.56 and 1.57. In Fig. 3.2(a), these bistable solutions are plotted for the different power levels that exist across the envelope of the driving pulse.

In Fig. 3.2(b) (with spectra in 3.3(a)) we show the intracavity field solutions $\Psi = |\psi(\tau)|^2$ at different values of ζ_0 found using the split-step method [138] (see section 1.2.6). For this direction in ζ_0 , the field initially follows the high-state solution $\psi_H(\tau)$ of the bistable resonance. As ζ_0 crosses 0, there begin to exist parts of the intracavity field where the local Kerr resonance-shift at the edges of the pulse-drive $F(\tau)$ is insufficient to sustain the high-state $\psi_H(\tau)$ (an

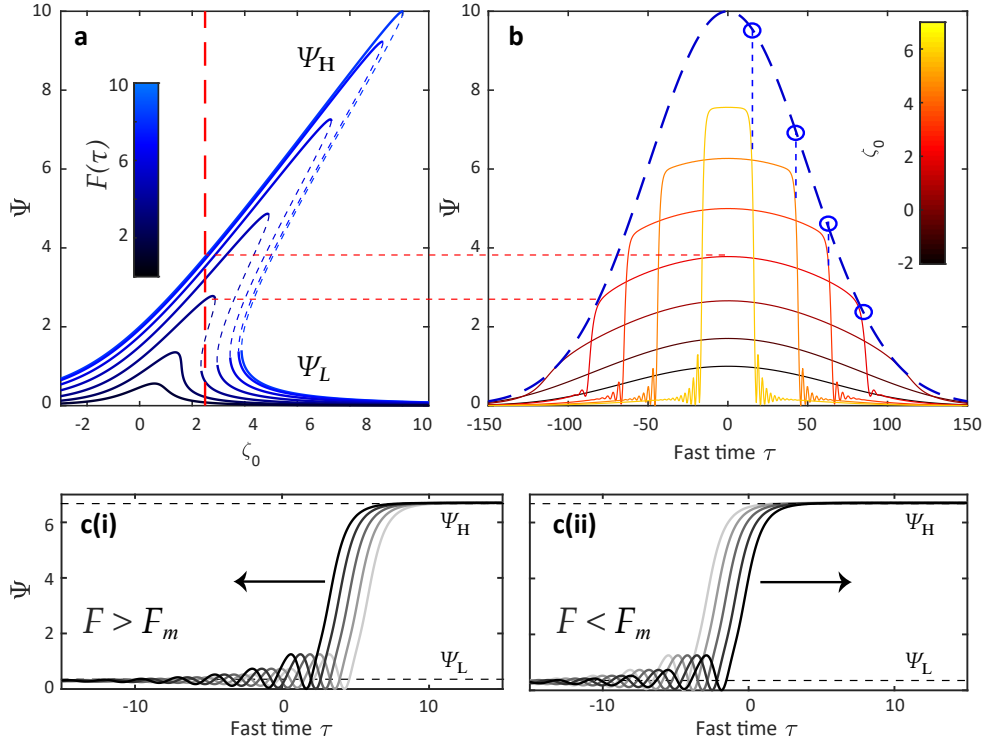


Figure 3.2: **Excitation of switching-waves inside pulse-drive envelope with pure normal dispersion.** (a) Contour of the bistable intracavity CW solutions, plotted for increasing local value of the pump $F(\tau)$, with stable (unstable) solution in solid (dashed) line. Red-dashed line marks detuning after wave-breaking occurs. (b) Development of intracavity field (red-yellow) within the pulse envelope (blue dashed) with increasing detuning ζ_0 . Red-dotted lines connect one field slice with the CW solution in (a). *Maxwell points* on the pulse envelope marked with circles. (c) Expanding (i) and contracting (ii) high-state (dashed) under CW driving.

example detuning of which is marked by the vertical red dashed line in Fig. 3.2(a)). At this stage, the field outside this point falls to the low-state $\psi_L(\tau)$ while the field further inside the pulse background stays on $\psi_H(\tau)$ creating the SW that connects the two states [139].

From here, the two SW locations τ_{SW} follow a location within the pulse-drive envelope $F(\tau) = F_m$, which previous theoretical works on SW stability have termed the “Maxwell Point” [140, 90], until at $\zeta_0 \approx 7$ where there exists no $F(\tau) > F_m$ causing the SWs to meet each other and annihilate, failing to reach their theoretical maximum detuning at $\zeta_0 = 10$. The stability of the SW fronts within the pulse envelope up until this point is due to the effective ‘outward pressure’ manifesting on ψ_H . SWs possess an innate group velocity offset depending on the value of F and ζ_0 [56], where the ψ_H tends to undergo expansion [141], with the SWs moving outward when the driving term is larger than a certain value $F(\tau) > F_m$ for a fixed detuning ζ_0 (see Fig. 3.2(c)). When $F(\tau) < F_m$, the ψ_H contracts and the SWs move inward. Accepting this, it becomes clear that if any intracavity high-state ψ_H existed within a driving pulse envelope, whose peak $F_0 > F_m$, it would undergo expansion until its SW fronts reached a point where

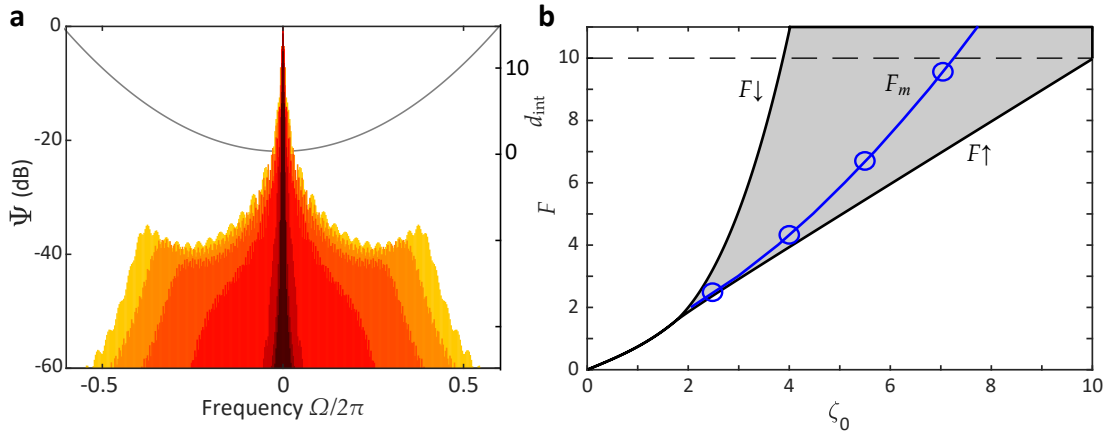


Figure 3.3: **Excitation of switching-waves inside driving pulse envelope with pure normal dispersion.** (a) Microcomb spectra of the fields from Fig. 3.2(a), and integrated dispersion operator. (b) Region of CW bistability in normal dispersion, between CW up- and down-switching points F_{\uparrow}^2 and F_{\downarrow}^2 , with numerically found Maxwell points F_m^2 (solid line) and SW locations from Fig. 3.2(b) (circled).

$F(\tau_{\text{SW}}) = F_m$ and halt its motion. This is how an SW-microcomb finds its definition when driven with a modulated pump [142].

3.1.2 Zero-dispersion formation in pulse-driving

Considering now a Kerr cavity possessing strong TOD, we choose $d_3 = 1$. Fig. 3.4 presents an analogous scenario to Fig. 3.2 and 3.3, now with TOD enabled. We see in Fig. 3.4(b) that the leading-edge SW front (lefthand side) has acquired an upper-state oscillation that corresponds to an enhancement of the spectrum (Fig. 3.4(a)) on the negative frequency side. This enhancement is due to the return to zero of the integrated dispersion function $d_{\text{int}} = d_2\Omega^2 + d_3\Omega^3$ (Ω being the dimensionless angular frequency) [69] (or more accurately the RRC ζ_{L-} shown in section 1.3.3 from Eq. 1.66). This asymmetry in the spectral profile imparts a positive group velocity-shift to the leading-edge SW front, and causes the entire upper-state to collapse at a lower detuning that in the case of pure-SOD.

Overall, the flatness of the dispersion profile on negative frequencies has heavily skewed the generated spectrum to the one side resulting in a negative shift to the group velocity for the SW structure as a whole inside $F(\tau)$. Naturally, introducing a counter-acting group velocity shift in the form of a negative d_1 term should help contain the structure within the centre of $F(\tau)$ as the detuning increases. This scenario is presented in Fig. 3.5. By now setting $d_1 = -1.34$, the time-frame of the cavity field continually moves forward in fast time τ (here to the left), keeping both SWs near to the center of the pulse envelope $F(\tau)$ preventing early collapse. The SW fronts meet together now at $\zeta_0 = 5.1$, where a significant event occurs. Instead of eliminating each other as in the case of pure-SOD, the SWs become locked to each other based on the bonding of the down-SW to the modulated wave of the up-SW forming the stable ZDS.

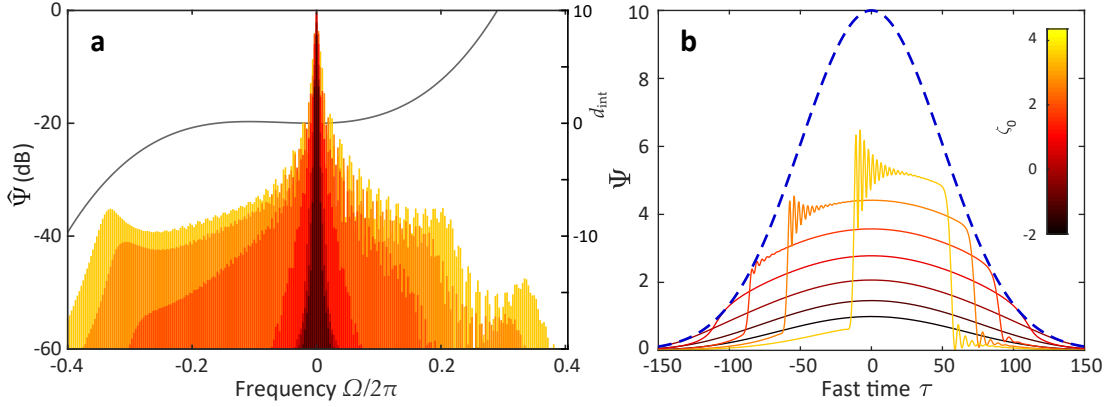


Figure 3.4: **Excitation of switching-waves inside pulse-drive envelope with dominant third-order dispersion.** (a) Intracavity field within the pulse envelope and (b) spectra with increasing detuning ζ_0 .

This structure, forming based on interlocking switching waves, is similar but different to the formation of previously researched ‘dark pulses’ [133]. Such dark pulses form from interlocking in the decaying optical rolls of the low-state ψ_L and can form in the case of pure SOD, whereas these bright ZDS necessarily require strong TOD so that a sufficiently powerful modulation exists on the high-state ψ_H . These ZDS further *distinguish* themselves from the SW state, which exists here at lower detunings for $\zeta_0 < 5.1$, in that the SW is contained overall by the left and right Maxwell points of the pulse-drive envelope $F(\tau)$, whereas the ZDS is *self-stable* akin to a DKS, and can freely exist across the broad background of the driving pulse. As with pulse-driven conventional DKS, the ZDS moves itself towards a single trapping position on one edge of $F(\tau)$ [94, 115, 96, 116], as seen in the previous chapter. In this example, the trapping position is initially on the left edge.

We term the complete structure as a ZDS⁽ⁿ⁾, with n individual peaks. As the detuning here increases past $\zeta_0 > 5.1$, the structure (plotted specifically on levels 3-6 of Fig. 3.5(b)) undergoes progressive inward collapse, reducing its multi-peaked periodicity initially from $n = 5$, down to 2. In the frequency domain (correspondingly in Fig. 3.5(c)), we can determine the value n by the number of spectral periods between the pump and what was initially the SW dispersive wave, here on the left end of the spectrum. It must be pointed out that the bulk of the soliton component of the spectrum continues to exist in the anomalous dispersion region on the left, due to the ‘recoil’ induced by the new powerful dispersive wave component on the right [67, 137]. This is one important explanation as to how the ‘solitonic’ components of the pulse can still exist, allowed by the counter-acting balance of dispersion and nonlinearity, while still being pumped from the normal dispersion region.

Fig. 3.6(a) shows how varying the group velocity shift d_1 (or desynchronisation in terms of pulse-driving) gives rise to a varying maximum detuning for ZDS⁽ⁿ⁾ existence, and with different preferred n . Here (with particular attention to Fig. 3.6(a-iii)), the ZDS⁽³⁾ follows its trapping position on the left-hand slope until it crosses the centre line where a trapping

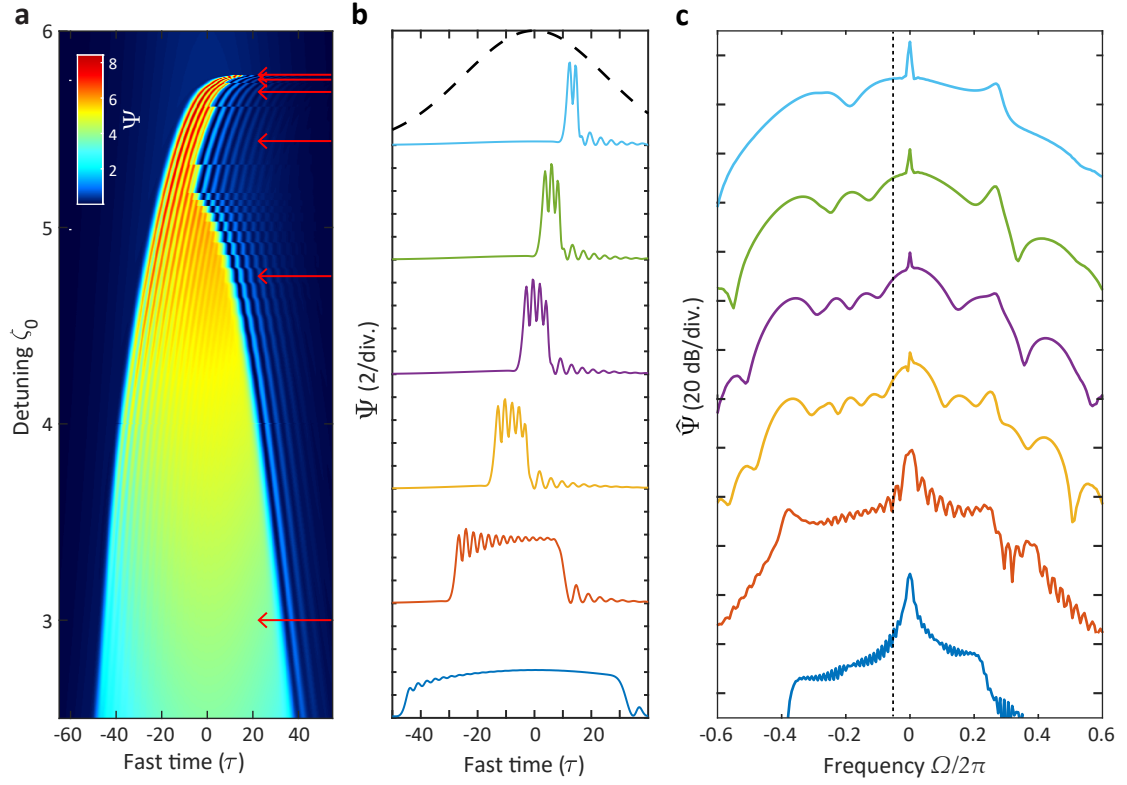


Figure 3.5: **Zero-dispersion soliton formation.** $F_0 = \sqrt{10}$, $d_2 = 1$, $d_3 = 1$ (a) Intracavity field as detuning ζ_0 is increased. $d_1 = -1.34$ (b) Individual time domain and (c) frequency domain of the fields in (a) (red arrows). Pulse-drive envelope $F^2(\tau)$ marked by dashed line in (b), and zero-dispersion frequency marked by dotted line in (c), with normal dispersion on the righthand side.

position no longer exists and falls away to elimination, following an asymmetrical trajectory reminiscent of recent studies on conventional dissipative solitons [115]. The cavity energy trace, plotted in Fig. 3.6(b) for all values of d_1 in the vicinity, shows the asymmetrical unfurling of the characteristic ‘step’ feature we should expect to see in experiment, with a behaviour not too dissimilar to that shown in chapter 2, section 2.3.

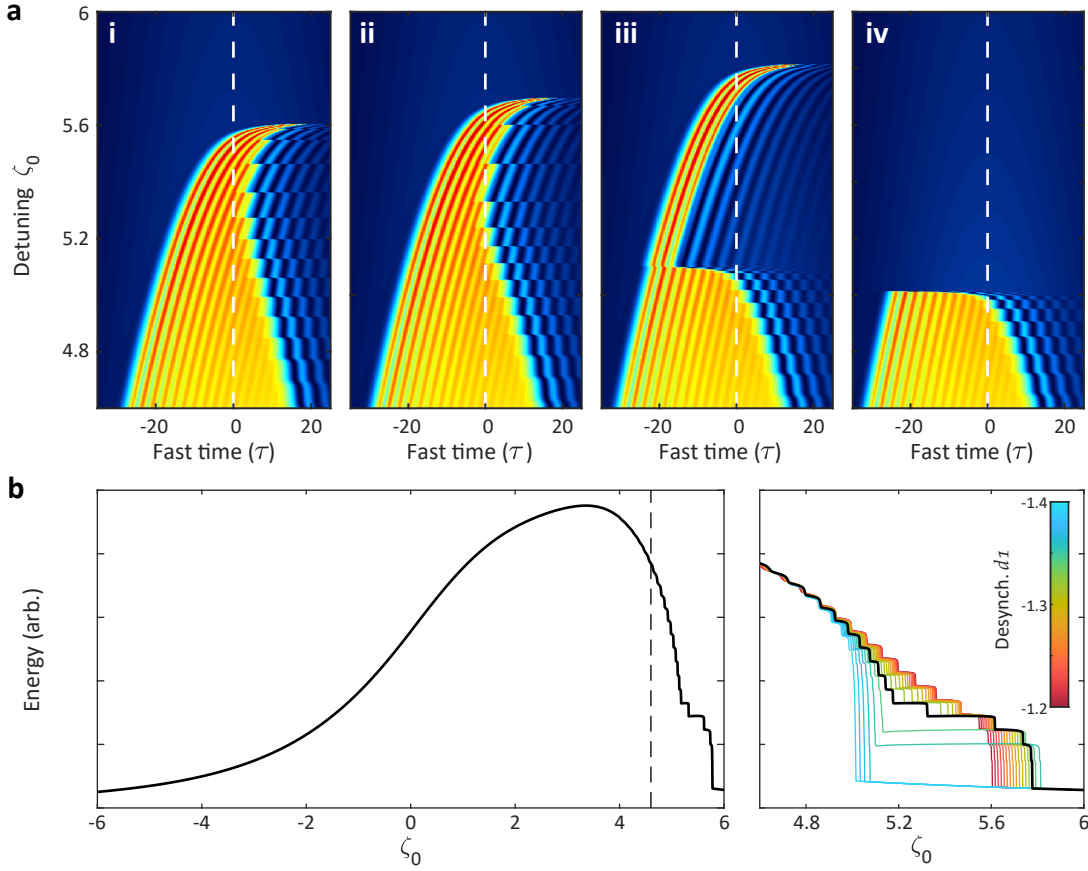


Figure 3.6: **Zero-dispersion soliton formation with desynchronised pulse-driving.** $F_0 = \sqrt{10}$, $d_2 = 1$, $d_3 = 1$ (a) Alternative field formation compared to Fig. 3.5 with (i) $d_1 = -1.20$ (ii) $d_1 = -1.29$ (iii) $d_1 = -1.36$ (iv) $d_1 = -1.37$. White-dashed line marks the pulse-drive centre. (b) (left) Total intracavity energy from Fig. 3.5(a); (right) Close look of the unfurling ‘step’ feature, plotted for different values of desynchronisation d_1 , in a similar fashion to Fig. 2.14.

3.1.3 Zero dispersion existence and discussion

The LDS presented in Fig. 3.1, and in closer detail in Fig. 3.7, are solutions found quasi-statically when simulating Eq 3.1 with SOD and TOD parameters changing over the long time t , where $d_2(t) = \cos(2\pi t/t_p)$ and $d_3(t) = \sin(2\pi t/t_p)$, for one period of $t_p = 11,520$, covering the dispersion semi-circle shown in both directions, forwards and backwards. This time-scale is long enough that the solutions found can be considered to be the long-term stable solutions. A **video** is available showing the continuous journey as a live simulation, found as part of the supplementary material to the paper published on this result[145] and is recommended viewing.

The simulation is pulse-driven with

$$F(\tau) = F_0 \exp(-\tau^2/\tau_p^2) \quad (3.3)$$

where $F_0 = \sqrt{10}$, and $\tau_p = 30$ at detuning $\zeta_0 = 5$, sufficient to sustain an LDS at all dispersion values. The simulation video begins with an SW inside the driving pulse envelope at pure normal dispersion ($d_2 = 1, d_3 = 0$), moves around the dispersion circle anti-clockwise to ($d_2 = -1, d_3 = 0$), and then continues back to terminate at ($d_2 = 1, d_3 = 0$) revealing the hysteresis of the stable ZDS for the forwards and backwards direction. From this, we can see the start and end points for the $ZDS^{(n)}$, including $n = 1$ to $n = 6$. In the video, live plots include the instant dispersion value in the top-right polar-plot and the total intracavity energy value, showing the sharp transitions between states. Further included are live plots of the frequency domain (top-right), real and imaginary values for the time domain field (bottom-left), and the time domain power field (bottom-right). During the simulation, the velocity of the LDS v_s is continuously cancelled by setting $d_1 = v_s$, so that it stays in the centre of the driving pulse envelope in order to maintain its existence.

Specific solutions are highlighted in Fig. 3.7, marked in the top semi-circle diagram with points (A-J), along with their existence ranges within this dispersion circle for this value of F_0 and ζ_0 . The solutions are plotted in the fast time and frequency domain, and the *locus* of the time domain field in the complex plane. Beginning with (A) we have the DKS solution found at pure-anomalous dispersion (Note: in the video, the live solution is in a breathing state, however, the initial stable solution is plotted here). Next at (B), we see the DKS with dispersive wave tail. In row (ii) we see the dispersive wave tail in how the field spirals towards the homogenous low-state solution ψ_L . At (C), the solution of the strongly perturbed DKS able to exist in the *normal dispersion* plane is found. This structure was not able to be obtained in the experiment, but was observed in a concurrent work on these zero-dispersion solitons in fibre-based cavities [144].

At (D), (E), (F), and (G), we find the multi-peaked $ZDS^{(n)}$ states for $n = 2, 3, 4$, and 6 (omitting 5 for brevity). In rows (ii), the complex field is shown to follow a looping excursion around the high-state ψ_H , with each loop forming each of the individual peaks in the time domain pulse. The resulting frequency domain on rows (iii) is highly-structured, but it appears that the number of spectral periods on the negative-frequency side (opposite to the soliton dispersive wave) corresponds to the number of peaks in the time domain pulse. At (H), the two ends of the ZDS in fast time *unlock* from each other, resulting in two free-running SWs that move outward. What used to be the individual peaks of the ZDS has become the high-state dispersive wave tail, seen in row (ii) as a spiral towards the high-state ψ_H . At (I) and (J), this high-state dispersive wave fades away, leaving only the low-state dispersive waves on each switching wave.

On the term ‘zero-dispersion soliton’

A useful given explanation for the ‘zero-dispersion solitons’ seen in this work [143, 146] is that they are two interlocked switching waves forming a self-stable bright pulse. However, an important observation of this simulation which may complicate this explanation is the fact that, for this example value of F_0 and ζ_0 , the ‘single-roll’ soliton solution is able to exist in the

normal dispersion plane (as previously predicted in [67]), and the $ZDS^{(2)}$ and $ZDS^{(3)}$ solutions are likewise able to exist in the anomalous dispersion plane. This would seem to suggest that the single-roll soliton solution could also be thought of as a *single-period interlocked switching wave pair* (?), despite existing continuously with the conventional pure-anomalous soliton solution. Correspondingly, the $ZDS^{(2)}$ for instance, existing continuously in anomalous dispersion, could be thought of as the *dual-cycle* form of the dissipative soliton, given that the single soliton is thought of as a single period of the patterned solution (modulation instability, or Turing rolls) that connects the low state ψ_L with the high state ψ_H in this regime [80]. It is within this *ambiguity* that we define the family for ZDS solutions to be unique from the conventional dissipative solitons and switching waves that exist in the pure or near-pure second-order dispersion regimes.

In terms of nomenclature, the very same entity in prior theoretical and numerical studies has been termed as “bright solitons” existing at zero SOD[67, 147], for instance as a soliton “doublet”[148] and, in recent work more explicitly described as strongly modulated, bright interlocked switching waves [143, 146, 149]. Across all of these prior studies, the terms ‘platicon’, ‘bright soliton’, and ‘locked switching waves’ have all been used together interchangeably to describe the same thing. In this work, we seek to draw a concise and practical distinction from the single-peaked plain soliton on the one hand, and the free-moving switching waves on the other, in order to make an unambiguous entity that exists in the regime near zero dispersion that has a multi-peaked structure.

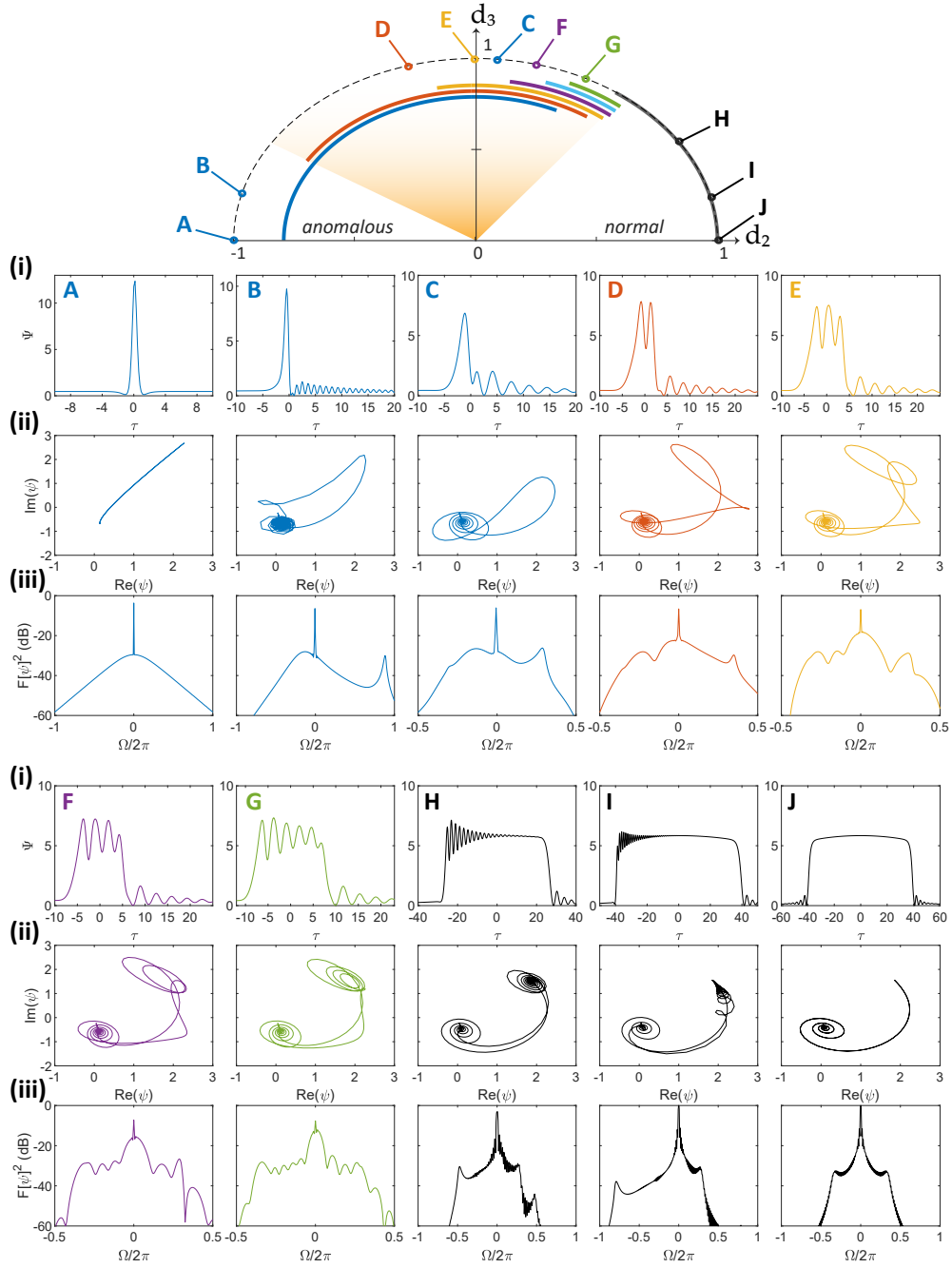


Figure 3.7: **Family of solutions for localised dissipative structures in the second-/third-order dispersion (d_2/d_3) plane.** Top: Unit circle for d_3 vs. d_2 with solutions (A)-(J) marked. Thick colour bands indicate corresponding existence ranges, demonstrating collapsed 'snaking' solutions predicted in [143, 144]. (A)-(C): Dissipative soliton solutions. (D)-(G): Zero-dispersion soliton solutions. (H)-(J): Switching wave solutions. Rows (i): Time domain field $\Psi(\tau) = |\psi(\tau)|^2$ vs. time τ . (ii) Complex field path in the time domain. (iii): Frequency domain.

3.2 Experimental observation and probing of normal- and zero-dispersion solitons and structures

3.2.1 Switching wave microcomb in pure normal dispersion

Before coming to the main experimental results on zero dispersion soliton microcomb generation, it's best to show experimental verification of the scenario presented in section 3.1.1: simple switching wave microcomb generation using a basic amplitude-modulated pump. Creating an SW microcomb with a modulated pump had at the time been reported earlier in a conference paper by *H. Liu*[150] (now published [151]). We wished to gain an understanding of SW behaviour in experiment. While working with Grigory Lihachev on the work with generating a normal dispersion microcomb in Si_3N_4 through *self-injection locking*[152], we decided to observe the SW microcomb accessible in the same resonator via amplitude modulated pumping, in this case bi-tonal. We particularly wanted to see the noise of the microcomb.

A summary of the results of this brief experiment is shown in Fig. 3.8. We experiment on the high- Q Si_3N_4 microresonator used in the self-injection locked microcomb result[152]. It has an FSR of $D_1/2\pi = 26.2$ GHz, normal dispersion $D_2/2\pi = -59.9$ kHz, and a $\kappa/2\pi = 40$ MHz. In order to pump with 2-tones, we send the CW-laser light through a Mach-Zehnder modulator with $f_{\text{eo}} = 13.1$ GHz and the bias level set to fully suppress the carrier component, leaving two laser lines 26.2 GHz apart, forming a cosine driving function inside the microresonator like in Fig. 3.2. At input power $P_{\text{in}} = 200$ mW, when tuning into resonance we observe the formation of a switching wave microcomb as we expected (Fig. 3.8(c)), showing the characteristic growing dual-dispersive wave (DW) profile where the FWM comb grid crosses the lower-state RRC (as depicted in section 1.3.3). Just as with temporally locked dissipative solitons in pulse driven resonators, if the SW fronts are contained by the driving function envelope, then they must also inherit its timing jitter, and this is confirmed by the repetition rate phase noise measurement shown in Fig. 3.8(d). Here, we isolated the SW comb teeth at the edge of the spectrum and compared the phase noise of their intrinsic heterodyne 26 GHz beatnote with $2^2 \times$ the source RF phase noise (the same as RF-1 in chapter 2), showing that they have close correspondence at lower offset frequencies.

3.2 Experimental observation and probing of normal- and zero-dispersion solitons and structures

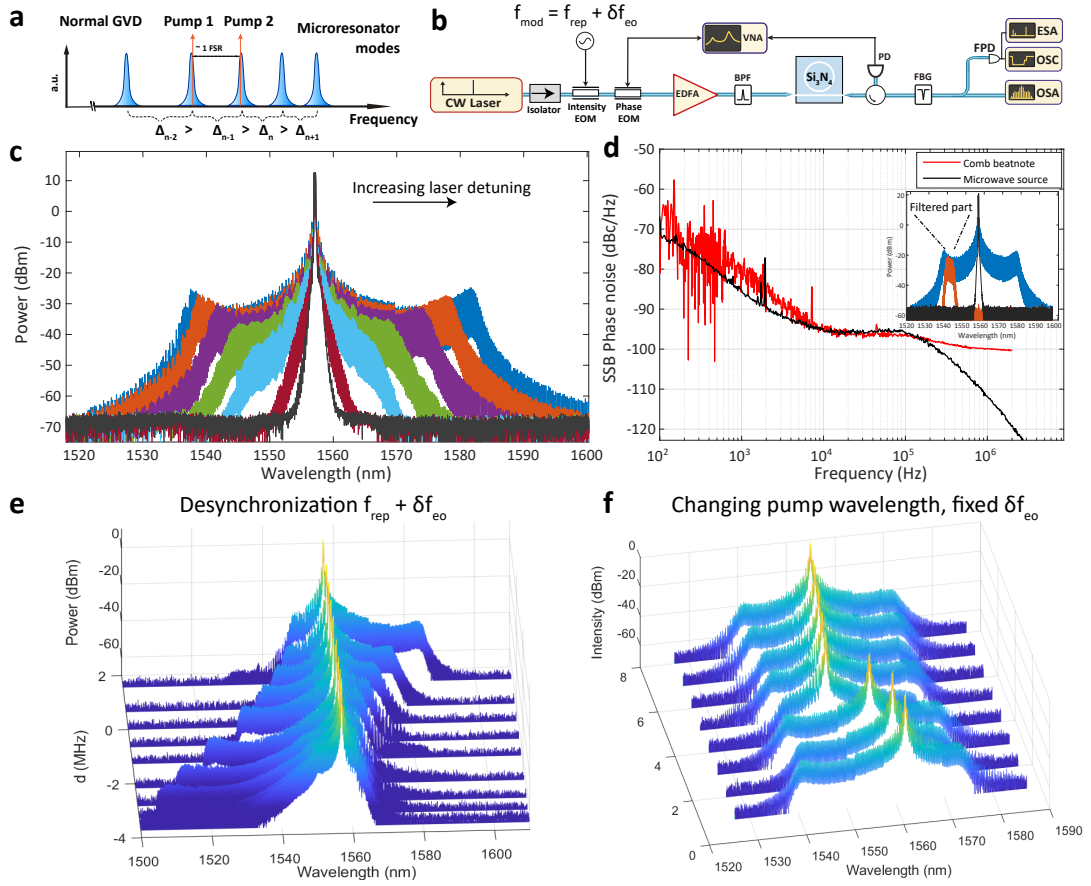


Figure 3.8: Experimental results for 2-tone switching wave microcomb generation in an Si_3N_4 microresonator. (a) 2-tone pumping scheme in a resonator with normal dispersion. (b) Experimental setup. EOM: electro-optic modulator; EDFA: erbium-doped fibre amplifier; BPF: band-pass filter; VNA: vector network analyser; FPD: fast photodiode; FBG: fibre Bragg grating; ESA: electronic spectrum analyser; OSC: oscilloscope; OSA: optical spectrum analyser. (c) The growth of the measured SW microcomb spectrum as the pump frequency is scanned into resonance. (d) Phase noise spectrum of the microwave microcomb repetition rate, obtained from the filtered section of the comb shown in the inset, compared with the RF source of the modulated pump. (e) Change in the microcomb envelope with a constant pump frequency and changing driving relative modulation rate δf_{eo} , and in (f) vice-versa. Figure credit: Grigory Lihachev.

3.2.2 Zero dispersion soliton microcomb

For experimental generation of ZDS microcombs, our experimental setup is in fact exactly the same as the one shown in Fig. 2.20 section 2.4, but without the use of the ‘RF-2’ source for the EO-comb. Details of the EO-comb are given in section 2.2.

Device description

The two microresonators under test this time (internal ID: D42-1.F11.G0.R5 and R6) are part of the same D42 wafer of chips as the soliton experiment in chapter 2, but this chip was located in the outer part of the wafer, and was possibly subject to greater Si_3N_4 waveguide height deviation after the chemical mechanical polishing step (CMP) [153] during the Damascene fabrication [118]. This is conjecture, but likely this chip had a thinner waveguide height, closer to 700 nm than the original target 770 nm, resulting in the overall D_2 decreasing below zero. Both resonators (referred to hereafter as R5 and R6) have the same circular racetrack layout as the resonator in Fig. 2.19, with the same straight-straight coupler section and tapered mode-suppression section (more on that in section 4.2). The measured properties of the two resonators are graphed in Fig. 3.9. As seen in the Eschelle-form linear transmission images in Fig. 3.9(b,d), the apparent D_{int} of R5 and R6 (the resonance deviation in offset frequency) is extremely flat *relative* to the resonance width in the vicinity of the pump location at 192 THz. This is what decides the flatness of the Kerr microcomb to be formed. The dispersion of R6 is less flat than R5 at higher optical frequency, turning anomalous (here positive curvature) quicker, and we will see the difference this makes in the results.

As it happens, only these two resonators gave this zero (cubic) dispersion profile. Resonators higher than R5 had stronger normal dispersion, and resonators below R6 turned back anomalous, demonstrating a greater point about the sensitivity of broadband dispersion engineering to nanofabrication tolerance in Si_3N_4 . The actual polynomial fitting of this dispersion is plotted later along with the obtained microcombs in Fig. 3.13 and 3.12.

3.2 Experimental observation and probing of normal- and zero-dispersion solitons and structures

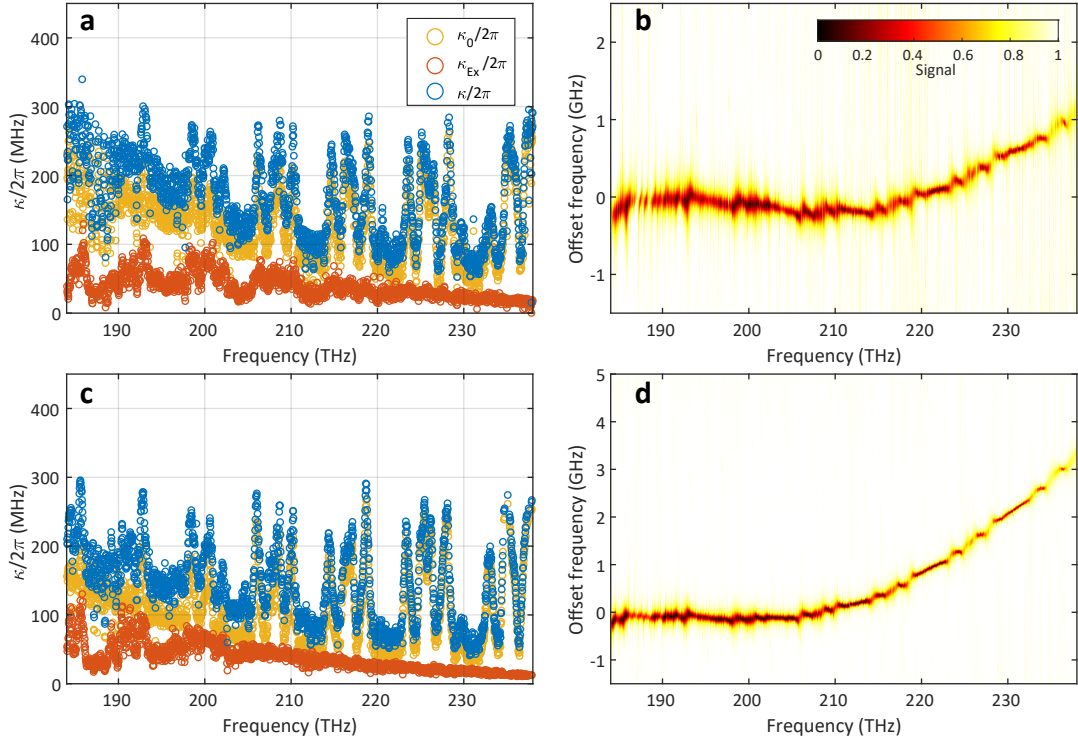


Figure 3.9: **Experimental characteristics for 2 resonators: D42-1.F11.G0.R5 (a/b) and .R6 (c,d).** (a,c) The fitted linewidth values of each measured resonance. (b,d) The total transmission trace measured using the calibrated swept-laser spectroscopy [50], graphed in Eschelle form with a repetition sampling rate of 27.888 GHz.

Formation of ZDS^(4,5)

Starting with R5, in order to ensure that a full range of formation behaviour is observed, and spectral extent maximized, the average pulse-power coupled to the resonator is set to maximum at $P_{in} = 1,200$ mW, or 350 mW considering 2.3 dB insertion loss to the chip, and that only every second EO-comb line spaced at 28 GHz is coupled to the resonator. This is approximately 20 times higher than the observed minimum comb generation threshold. The experiment proceeds in a similar way as shown in theory (section 3.1.2), typical for LDS generation and pulse-driving in Kerr cavities [94, 96]. The native FSR of the microresonator is first found by varying the input repetition rate f_{eo} until the expected unfolding of the ZDS ‘step’ is observed (Fig. 3.10). Here, we see an asymmetrical extension of the step vs. the relative desynchronisation $\delta f_{eo} = f_{eo} - D_1/2\pi$, as expected based on Fig. 3.6(b), although with slightly different form due to unaccounted for higher order effects (the absence of a step at $\delta f_{eo} = 0$ is a coincidence based on shot-to-shot statistical variation of formation probability). Based on this measurement, we find an optimum $f_{eo} = 27.88888$ GHz, with a locking range for ZDS on the order of ± 10 kHz.

For this value of f_{eo} , the EO-comb seed laser frequency ω_p is tuned slowly across a resonance

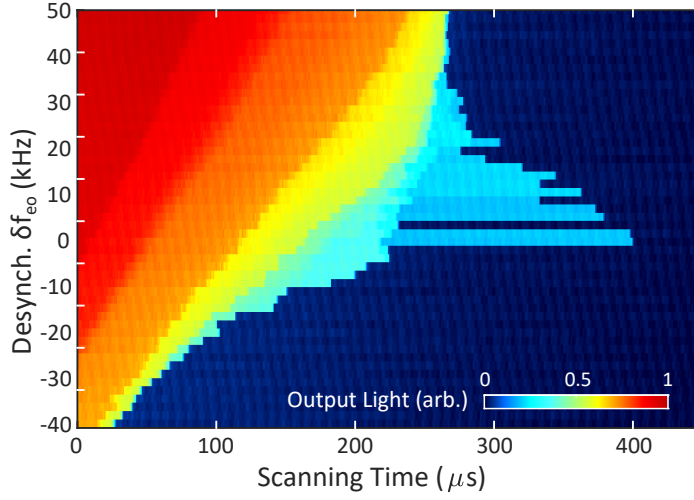


Figure 3.10: **Experimental pulse-driven zero-dispersion step unfurling in device R5.** Graph of the transmission step feature for different desynchronisation about $f_{eo} = 27.888880$ GHz.

frequency ω_0 from the blue-detuned side to the red-detuned side towards the region of Kerr bistability. Fig. 3.11(b) plots the output light from the microresonator during this scan, and at the same time the RF repetition-rate beatnote of the ZDS is recorded (Fig. 3.11(c)). From this we are able to see that throughout this scan over resonance, the RF repetition rate beatnote shows low noise. We pause the scan of the laser at four example locations here in order to observe the steady state solution of the SW and ZDS states. Here the comb spectra measured at the OSA are plotted in Fig. 3.11(a) at four detunings in descending order, after the SW is formed. Qualitatively, the results behave as the simulations in Fig. 3.5(c) predict. Firstly, over the first two rows, we see the spectrum grow wider and with a sharper dispersive-wave ($DW^{(-1)}$) located from 182 to 179 THz. Importantly, we see the spectral interference fringes either side of the pump (spaced by ≈ 1 THz on the first spectrum) increase their period as detuning is increased, indicating the two SW fronts are moving together within the pulse-drive envelope. In the last two rows, we see the SWs have coalesced into the ZDS⁽⁵⁾, a 5-period structure, then reducing to a ZDS⁽⁴⁾, each time moving the location of $DW^{(-1)}$ further out. Stationary states existing in between the 2nd and 3rd rows were not able to be accessed due to them being thermally unstable. In 100% of experimental generations of ZDS in this way, only a single ZDS structure was ever formed. This is naturally as a result of the fact that just two SW fronts are generated at the wave breaking stage with pulse-driving, which go on to lock together forming a single ZDS.

The long term beatnote measured at this final state, plotted in Fig. 3.11(d), is highly stable, inheriting the low-offset phase noise of the f_{eo} as supplied by the RF synthesiser. This confirms that the ZDS has temporally locked to the driving pulse over the long term, just as a conventional bright dissipative soliton would [94, 96]. The ZDS state was able to exist in the microresonator for tens of minutes, eventually collapsing due to uncontrolled thermal drift of the cavity resonance mode away from the laser centre frequency.

3.2 Experimental observation and probing of normal- and zero-dispersion solitons and structures

Fig. 3.12 analyses this final structure in greater detail. the measured integrated dispersion profile $D_{\text{int}} = \omega_{\mu} - \omega_0 - \mu D_1$ of R5 is plotted in Fig. 3.12(a). This data is fitted to a fourth-order polynomial centred at $\omega_0 = 2\pi \times 192.3$ THz where $D_{\text{int}} \approx \mu^2 D_2/2 + \mu^3 D_3/6 + \mu^4 D_4/24$ ($D_2/2\pi = -3.17$ kHz, $D_3/2\pi = 13.8$ Hz, $D_4/2\pi = -15.9$ mHz). In dimensionless parameters (see Fig. 1.55), for a fixed $d_2 = 1$ we have a value $d_3 = 0.38$. We obtain a pump frequency detuning $-\delta\omega/2\pi = -1.2$ GHz by using a live cavity phase-response measurement with a vector network analyser [73]. In Fig. 3.12(b) the entire spectrum of the ZDS⁽⁴⁾ is plotted and features several dispersive waves (DW), the spectral locations of which can be predicted based on where $D_{\text{int}}(\mu) \approx -\delta\omega$ (or see the RRC Eq. 1.66). The predicted DW locations do not match perfectly with experiment however, but this can be explained by the bandwidth-limited dispersion measurement with unknown higher-order values for D_5, D_6 and so forth. The first, DW⁽⁻¹⁾ at 176 THz, will always occur for ZDS formation due to the requirement for powerful TOD. The second, DW⁽⁺¹⁾ at 280 THz, has occurred due to the overall normal fourth-order dispersion of the waveguide [153], but is not required for ZDS formation.

The additional dispersive wave, termed DW⁽⁻²⁾, occurs where the optical comb modes have wrapped by D_1 so that $D_{\text{int}}(\mu) + D_1 = D_{\text{int}}(\mu - 1) = -\delta\omega$ or that, by shifting by one FSR, a linear wave at DW⁽⁻²⁾ has accrued a 2π phase shift relative to the pump wave. This phase-wrapping is commonly known to allow the formation of so called ‘Kelly’ sidebands in soliton fibre lasers [154], and will be investigated more in the next chapter. In brief, due to the longitudinal momentum mismatch $\delta\mu = +1$ between the coupled linear wave and the ZDS comb lines, quasi-phase matching is required to bridge this gap [155]. This microresonator features an aforementioned tapered mode-suppression section where the waveguide width rapidly tapers down to a narrow width in order to stop any higher-order spatial modes from propagating [156] (see Fig. 4.6), where the waveguide dispersion changes sharply. This intra-roundtrip disturbance provides phase modulation to the longitudinal cavity mode wave at DW⁽⁻²⁾, and is sufficient to enable quasi-phase matching to stimulate resonant radiation. This effect has been observed in microresonators with a similar intra-roundtrip modulation of the waveguide width [157], and has long been observed in fibre-based Kerr resonators with longitudinally varying dispersion [158, 159].

Fig. 3.12(c,d) shows numerical LLE simulations using the real experimental parameters of R5 based on the following GLLE:

$$\frac{\partial \tilde{A}_{\mu}(t)}{\partial t} = i\hat{D}_{\mu}\tilde{A}_{\mu} - \frac{\kappa(\mu)}{2}\tilde{A}_{\mu} + i\Gamma\mathcal{F}\left[|A|^2 A\right]_{\mu} + \sqrt{\kappa_{\text{ex}}(\mu)}\tilde{F}_{\mu}(t) \quad (3.4)$$

in a similar fashion to section 2.4.4, demonstrating close agreement with the form taken by the spectrum corresponding to a ZDS⁽⁴⁾ as shown in Fig. 3.12(d). In Fig. 3.12(c), both simulation results take into account either a constant or an oscillating intra-roundtrip dispersion

$$\hat{D}_{\mu}(t) = \delta\omega + 2\pi\delta f_{\text{eo}}\mu + (1 + \Delta(t))\left[\frac{D_2}{2}\mu^2 + \frac{D_3}{6}\mu^3 + \frac{D_4}{24}\mu^4\right] \quad (3.5)$$

with

$$\Delta(t) = \Delta_0 \cos(D_1 t) \quad (3.6)$$

The additional dispersive wave with $DW^{(-2)}$ appears only in the case with longitudinal dispersion modulation on, with $\Delta_0 = 0.2$. Further analysis of this higher-order dispersive is covered more relevantly next chapter in section 4.3, but a full breakdown of the simulation itself is written in section C.3.1 and C.3.4.

Formation of $ZDS^{(2,3)}$

To observe $ZDS^{(n)}$ of lower n we move to R6, which has its zero-dispersion wavelength closer to the pump wavelength at 1560 nm. Here, the dispersion parameters (Fig. 3.13(a)) are fitted to be $D_2/2\pi = -848$ Hz, $D_3/2\pi = 12.8$ Hz, $D_4/2\pi = -15.9$ mHz, corresponding to dimensionless parameters $d_2 = 1$ and $d_3 = 2.11$, further into the zero-dispersion regime (Fig. 3.1). According to Fig. 3.1 and predictions given by Parra-Rivas et al.[143], the existence range for $ZDS^{(n)}$ of lower n is greater in this regime, and so are more likely to form within typical driving parameters. In this microresonator, with the same generation method as above in R5, we generate $ZDS^{(3)}$ and $ZDS^{(2)}$, shown in Fig. 3.13(b). In this microresonator, we do not observe the same $DW^{(+1)}$ or $DW^{(-2)}$. For $ZDS^{(2)}$, spectral measurements are presented taken using three increasing input pump powers, each enabling an increased maximum detuning $\delta\omega$. As shown, as available power is increased, the overall spectral profile expands, with both $DW^{(-1)}$ on the left and the dip in the envelope on the right moving outwards, in a similar manor as for conventional dissipative solitons [74].

3.2 Experimental observation and probing of normal- and zero-dispersion solitons and structures

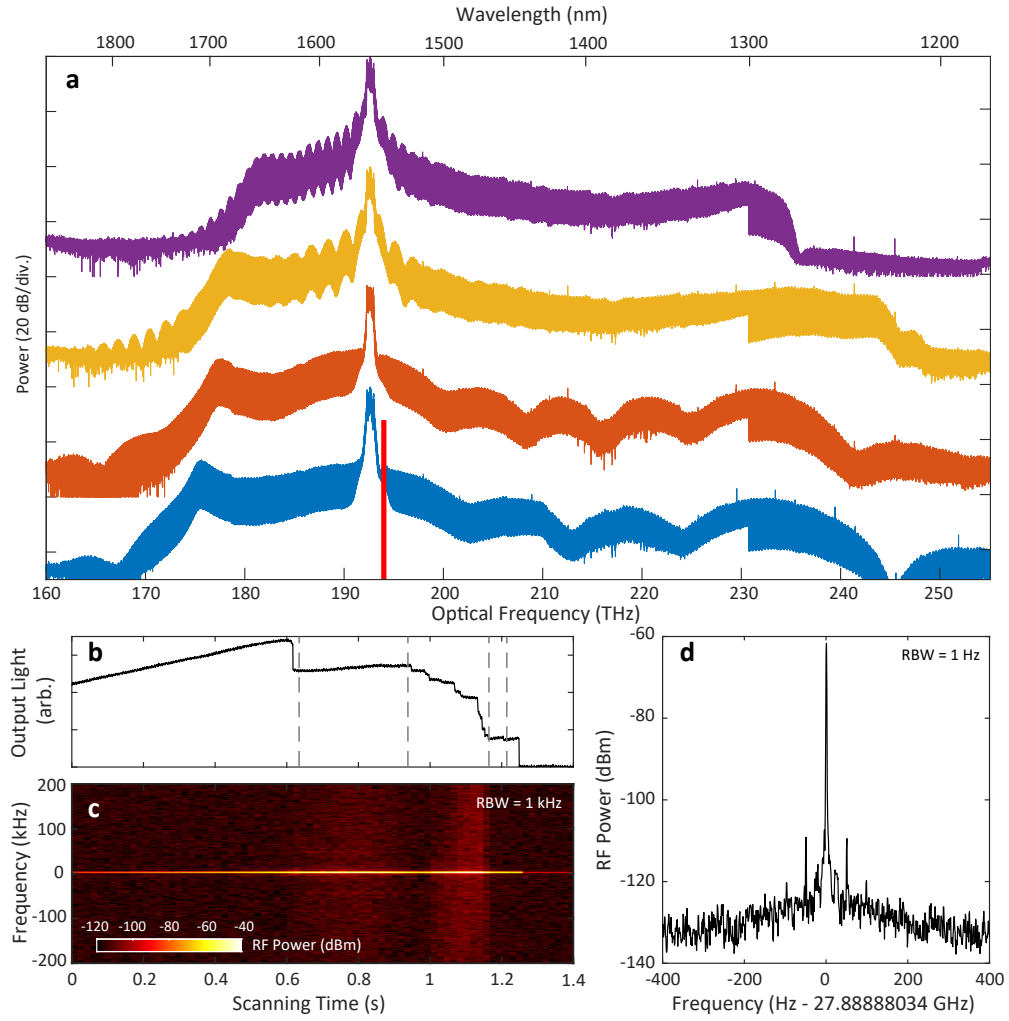


Figure 3.11: Experimental pulse-driven switching wave and zero-dispersion soliton formation. Device D42-1.F11.G0.R5. (a) Stages of comb/spectrum formation in descending order of detuning (40 dB vertical offsets). Red block marks spectral filter for beatnote measurement. (b) Microresonator transmission (with DC value subtracted), with detuning locations from (a) marked with dashed lines. (c) Spectrogram of the repetition-rate beatnote during the laser scan in (b). (d) Long-term beatnote measurement of the final comb state.

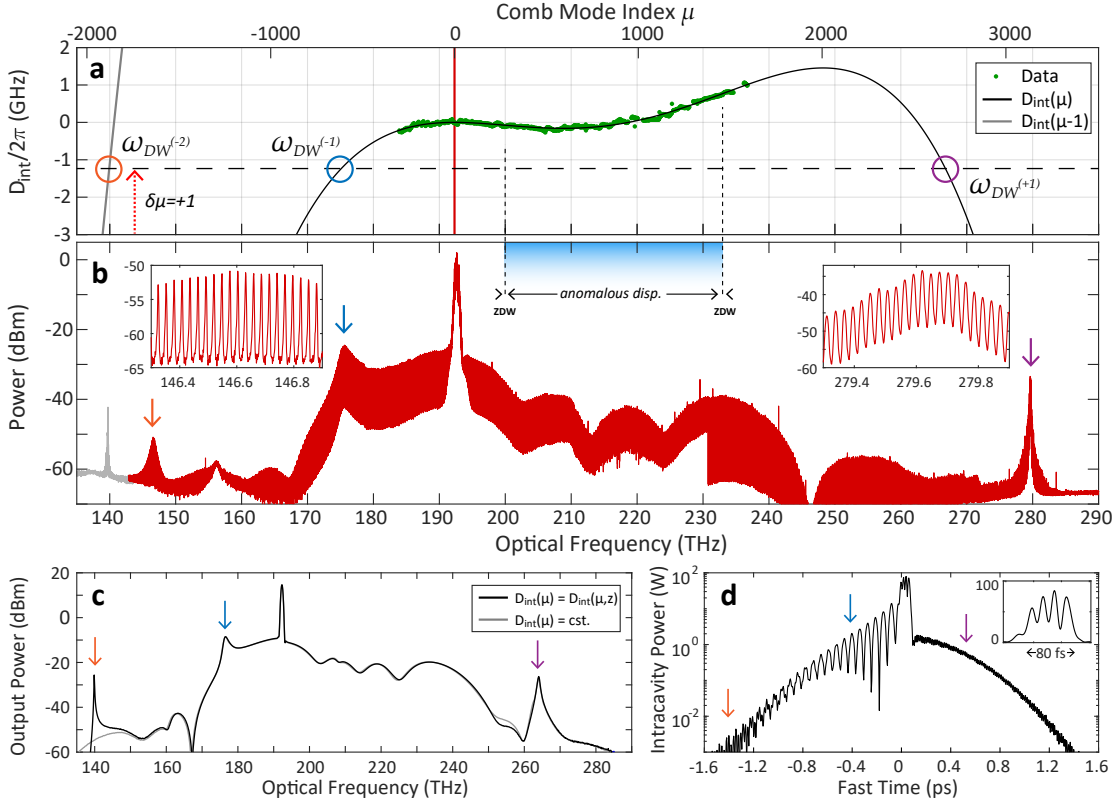


Figure 3.12: Octave spanning zero-dispersion soliton spectrum. Device D42-1.F11.G0.R5. (a) Experimental measurement of the resonator integrated dispersion D_{int} , along with the spectrally extended fitted solution, and solution shifted by $+D_1$. Pump frequency (and pump detuning) marked by the vertical red line (horizontal dashed line). Phase-matched locations of dispersive waves marked by circles, with momentum mismatch in dotted red arrow. (b) Measured spectrum of $ZDS^{(4)}$, with dispersive waves marked with arrows corresponding to the circles in (a). Insets show individual comb lines. The left-most trace is in grey to indicate it is the second-order diffraction spectrum of $DW^{(+1)}$, and not genuine. (c) Frequency domain and (d) time domain simulation of $ZDS^{(4)}$ with dispersive wave tails marked. The close agreement of the central spectral fringes between the experiment and simulation gives us confidence that we are observing a four-peak, 80 fs pulse (showed in linear scale inset). See section C.3.4 for the full breakdown of the modelling with values.

3.2 Experimental observation and probing of normal- and zero-dispersion solitons and structures

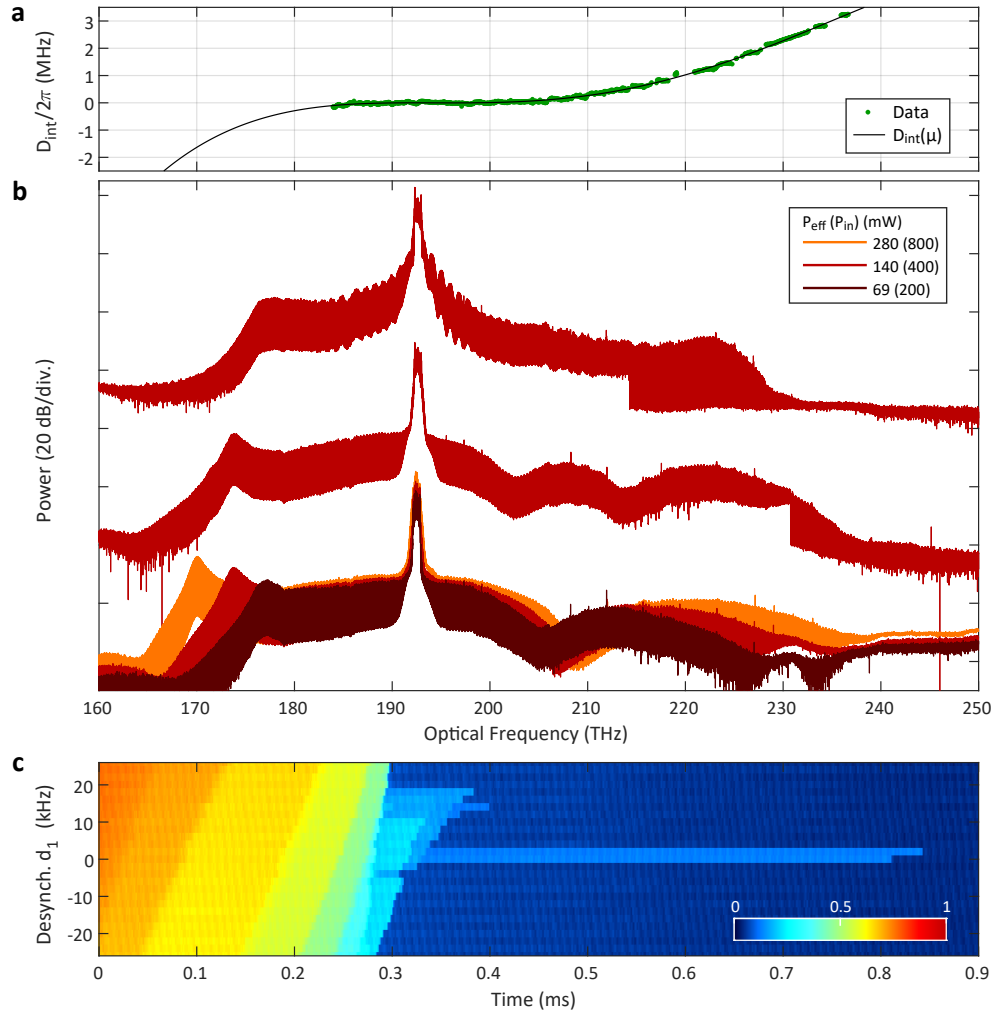


Figure 3.13: **Experimental zero-dispersion soliton formation. Device D42-1.F11.G0.R6.** (a) Experimental measurement of the resonator integrated dispersion D_{int} , and spectrally extended fitted solution. (b) Switching wave, ZDS⁽³⁾, and ZDS⁽²⁾ combs, accessible for different $\delta\omega$ and δf_{e0} . Spectra vertically separated by 50 dB. ZDS⁽²⁾ measured at maximum detuning for each pump powers, noted as effective average power coupled to ring (total power towards chip). (c) Graph of the transmission step feature for different desynchronisation about f_{e0} at maximum power.

4 Microcombs in the dispersion folded zone and Floquet dynamics

Given that a comprehensive understanding of the nonlinear dynamical physics of dissipative Kerr structures in conventional optical microresonators and fibre cavities has emerged, recently significant attention has been devoted to exploring physics and microcomb generation in non-trivial regimes. These regimes include alternative pumping schemes such as the pulse-driving above, or self-injection locked lasers[160, 161], as well as the study of complex dispersion profiles to extend the comb bandwidth of solitons with dispersive waves (DWs) [162]. Indeed, recent work has highlighted the novel dynamics associated with complex resonator structures such as micro-resonators with integrated Bragg gratings, photonic-crystal elements[163], as well as the emergent nonlinear dynamics observed in coupled microring photonic ‘dimers’[86] i.e. photonic ‘molecules’[135].

Yet, in nearly all prior experimental studies of driven nonlinear optical microresonators, the Kerr frequency shift has been, heuristically, less than the free spectral range (FSR). In other words, the spectral extent of the generated coherent dissipative structure exhibits an integrated dispersion that is smaller than the free spectral range. This is predominantly the natural regime for typical microresonators with a large FSR over ~ 50 GHz. Here we study the nonlinear dynamics beyond this realm. Using pulsed optical pumping of low repetition rate optical microresonators, we access the regime where LDS cover a bandwidth whose integrated dispersion exceeds the FSR of the resonator [65]. Akin to electrons in periodic bands that gives rise to the Brillouin zone, we demonstrate how dispersion folding can occur. Specifically, when the dispersion folds back to the zone spanned by the FSR, we show that any periodic perturbation of the soliton during its roundtrip (in our case produced by introducing spatially varying dispersion) enables quasi-phase matching for emergent higher-order structures at the edge of the dispersion ‘zone’. In this way, periodic forcing of the cavity field every roundtrip via the dispersion constitutes a form of parametric driving. For solitons, this gives rise to higher-order dispersive waves [158, 159], also identified as ‘Kelly sidebands’ historically discovered in systems with periodic amplification and later soliton fibre lasers [154, 164, 165]. Additionally, in CW-driven systems, dispersion modulation, or in fact parametric modulation of any system parameter, has long been known to lead to Faraday Instability (FI). FI patterns were most

originally studied in vertically shaken fluid basins[166] and were observed to occur oscillating first at half the forcing frequency. From a general point of view, such dynamics in optical resonators are governed by partial differential equations with periodic coefficients. The associated field of study is called Floquet theory. Floquet dynamics and consequent optical FI has been discussed earlier mostly in the context of fibre-based devices [71, 167, 72, 168] operating in the quasi-CW regime where period-doubling dynamics [169] as well as the competition between Turing and Faraday instability [170, 171] have been observed. The very same dynamics have also been studied for Bose-Einstein condensates [172].

In this chapter, a general model will be laid out describing how light behaves in a parametric Kerr cavity system. Much of the mathematical formulation in this chapter was found by my colleague Aleksandr Tusnin, with significant input from Alexey Tikan. The microresonator having the tapered-waveguide mode suppression section is discussed. Then, the numerical and then experimental treatment of a DKS microcomb in this situation is presented, including the observation of higher-order (5th) dispersive waves. Following that, the normal dispersion regime, switching waves and Faraday instability coexistence is presented with simulations and then experimental results for the generation of FI-driven offset satellite combs, increasing an SW microcomb bandwidth by a factor of ~ 5 .

4.1 Theory

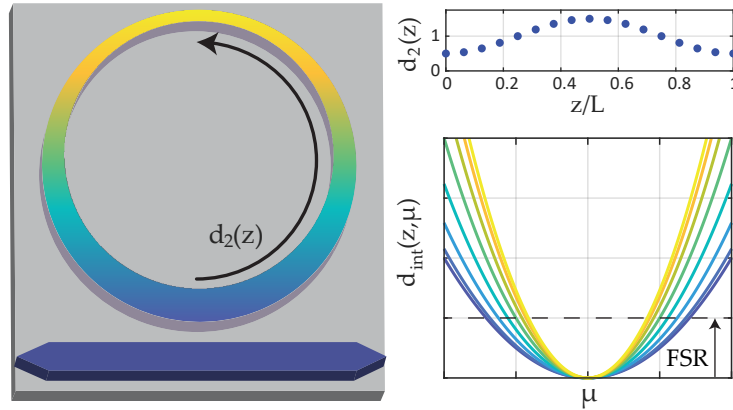


Figure 4.1: **Model for varying dispersion in driven dissipative Kerr nonlinear microresonators.** (a) The simplest case of a passive nonlinear microresonator whose waveguide width, and thus dispersion parameter, undergoes a periodic cycle. (b) In our modelling we consider a simple sinusoidal dispersion modulation, evaluated piece-wise. (c) The integrated dispersion of each resonator mode μ along the resonator's circumference, for each value of d_2 plotted in (b).

The fundamental model underpinning the phenomena presented and discussed in this chapter is depicted in Fig. 4.1. The resonator can be represented as a waveguide ring (Fig. 4.1(a))

whose cross-section varies in such a way that the group velocity dispersion parameter $\mathfrak{d}_2(z)$ ¹ (β_2 as it is in the real experiment) varies periodically over length L with relative amplitude Δ , or in the time domain as $t = z/D_1 R$ for resonator with radius R and free-spectral range (FSR) D_1 . The system can be evaluated piece-wise as in Fig. 4.1(b), where the underlying integrated dispersion operator $\mathfrak{d}_{\text{int}} = \mathfrak{d}_2 \mu^2$ varies for each step in the direction z (Fig. 4.1(c)). The concept of FSR dispersion folding, Fig. 4.2, serves as a visual representation of the requirements for phase-matched FWM in the cavity. The dispersion curve passing FSR/2 is folded back to -FSR/2. In this picture, momentum mismatch between the branches of dispersion is *not compensated* in non-modulated cavities. Thus, FWM interactions with folded modes become resonant *only when* there is a mechanism coupling two neighbouring FSRs.

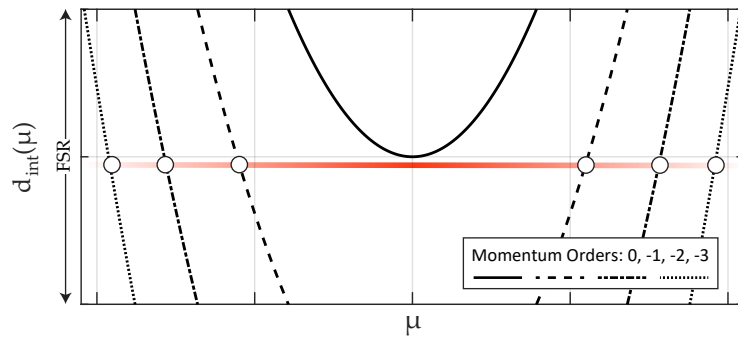


Figure 4.2: **Momentum mismatch.** Roundtrip integrated dispersion of a resonator plotted in the ‘folded zone’ over 1 free-spectral range. The comb spectrum spans multiple orders of dispersion, but each higher order is phase-mismatched. Dispersion modulation is required to quasi-phase match.

To establish a clear line of reasoning and understand the dynamics of this system, we revisit and extend conclusions presented in previous studies [72, 170, 168, 169] looking at them from a different point of view that employs the notion of two-dimensional four-wave mixing (2D FWM).

4.1.1 Quasi-phase matching and Floquet theory

To model the nonlinear dynamics of the cavity with periodically modulated dispersion, we use a form of the Lugiato-Lefever equation (LLE) with a time-dependent dispersion term [72]. In dimensionless units, the equation takes the form:

$$\frac{\partial \psi}{\partial t} = -(1 + i\zeta_0)\psi + i[\mathfrak{d}_2^{(0)} + \mathfrak{d}_2(t)] \frac{\partial^2 \psi}{\partial \varphi^2} + i|\psi|^2 \psi + F(\varphi), \quad (4.1)$$

where $\psi(\varphi, t)$ describes the slowly-varying envelope of the optical field in the microresonator, $F(\varphi)$ the driving function (which may be a pulse profile), φ is the azimuthal coordinate inside

¹In this chapter, dispersion \mathfrak{d}_l normalised to the spatial angular coordinate φ is used, rather than d_l , the dispersion normalised in dimensionless fast time τ

the cavity in the frame moving with velocity $\mathfrak{d}_1 = 2D_1/\kappa$ with $D_1 = 2\pi \cdot \text{FSR}$, $\zeta_0 = 2\delta\omega_0/\kappa$ is the normalised laser-cavity detuning, $\kappa = \kappa_0 + \kappa_{\text{ex}}$ is the total linewidth of the resonator with internal linewidth κ_0 and coupling to the bus waveguide κ_{ex} . Dispersion coefficients $\mathfrak{d}_2^{(0)}$, $\mathfrak{d}_2(t)$ and time t are normalised on the photon lifetime so that $\mathfrak{d}_2 = D_2/\kappa$ and $t = t\kappa/2$ for real lab time t . In this model, we denote $\mathfrak{d}_2^{(0)}$ as the averaged resonator dispersion with periodic modulation $\mathfrak{d}_2(t + \mathfrak{T}) = \mathfrak{d}_2(t)$, where $\mathfrak{T} = T\kappa/2 = \pi\kappa/D_1$ is the normalised roundtrip time. If the driving function $F(\varphi, t)$ is also periodic in time with period \mathfrak{T} , we can assume that the field ψ has the same symmetry $\psi(t + \mathfrak{T}) = \psi(t)$, we can employ the Fourier transform

$$\mathfrak{d}_2(t) = \sum_n \tilde{\mathfrak{d}}_2^{(n)} e^{-i\mathfrak{d}_1 n t}, \quad (4.2)$$

$$\psi(\varphi, t) = \sum_{n\mu} \tilde{\psi}_{n\mu} e^{i\mu\varphi - i\mathfrak{d}_1 n t} \quad (4.3)$$

and obtain an effective two-dimensional equation governing the Floquet dynamics (here F is taken constant for simplicity, but the equation can be readily generalised):

$$\begin{aligned} \frac{\partial \tilde{\psi}_{n\mu}}{\partial t} = & -(1 + i[\zeta_0 - n\mathfrak{d}_1] + i\mathfrak{d}_2^{(0)}\mu^2)\tilde{\psi}_{n\mu} - \\ & - i \sum_m \tilde{\mathfrak{d}}_2^{(n-m)} \mu^2 \tilde{\psi}_{m\mu} + i \sum_{\substack{n_1, n_2, n_3 \\ \mu_1, \mu_2, \mu_3}} \tilde{\psi}_{n_1\mu_1} \tilde{\psi}_{n_2\mu_2} \tilde{\psi}_{n_3\mu_3}^* \delta_{\text{FWM}} \\ & + \delta_{n,0} F, \end{aligned} \quad (4.4)$$

where the conservation law $\delta_{\text{FWM}} = \delta(\mu_1 + \mu_2 - \mu_3 - \mu)\delta(n_1 + n_2 - n_3 - n)$ governs 2D FWM processes in the fast(μ)- slow(n)- frequency space. We can thus conclude that the periodically varying dispersion, which in the LLE leads to a time dependent dispersion term, couples different Floquet orders (n) of the intracavity field.

The dispersionless profile along n (modes are equidistant in this direction having D_1 frequency spacing) protects our system from transverse instabilities [173, 174], allowing us to study and generalise well-known coherent structures such as dissipative Kerr solitons (DKS) and switching waves (SW). However, the presence of periodic dispersion modulation results in linear coupling between different orders of Floquet index n that effectively correspond to FSR-frequency breathing. As shown in Eq. 4.4, the coupling amplitude is proportional to the Fourier coefficients $\tilde{\mathfrak{d}}_2^{(n)}$ and scales *quadratically* with comb index μ , increasingly strengthening the coupling rate for larger mode numbers $|\mu|$.

4.1.2 Upper and lower states resonant radiation curves

To demonstrate the effect of dispersion modulation on the cavity dynamics for all comb modes, we provide split-step simulations [62] of Eq. 4.1, shown in Fig. 4.3. We first investigate the effect of phase-matching on the noise transduction properties of the cavity, in the *absence* of any coherent structure formation to avoid the effect of conventional modulation (Turing) instability [72], we simulate the case of a low average normal dispersion ($\mathfrak{d}_2^{(0)} = 0.0027$). Given

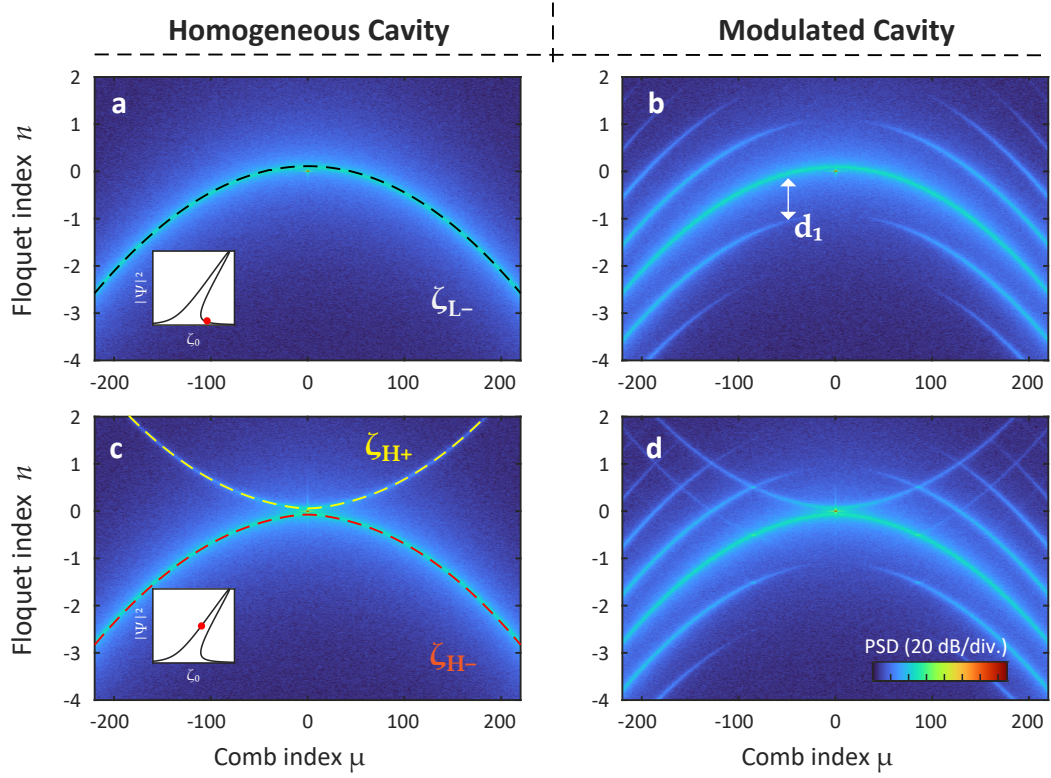


Figure 4.3: **Dispersion curves or Floquet bands for homogeneous and modulated cavity.** (a,c) Simulated 2D Fourier-transform for light propagating in the Kerr lower-state at $\zeta_0 = 5$, and upper-state at $\zeta_0 = 4$ respectively, in a homogeneous cavity with normalized driving strength $F^2 = 10$. The conjugated dispersion curve is only apparent in the upper state. (b,d) Same solution existing in dispersion-modulated cavity with $\Delta = 0.5\vartheta_2^{(0)}$, $d_1/2\pi = 8$, and $\vartheta_2^{(0)} = 0.0027$. Parameter values for this simulation are given in Table C.1.

a CW driving strength of $F^2 = 10$, typical for the generation of solitons or switching waves, the Kerr nonlinear cavity possesses a bistable condition across a range of detuning to approximately $\zeta_0 < 10$, with an upper and lower CW-state solution ψ_H and ψ_L , respectively (solutions of which given in Eq. 1.57 and 1.56). In Fig. 4.3(a,c), corresponding to the respective lower and upper states, we show the long-term response to small noise continuously placed on each comb mode, revealed by taking the 2-D Fourier transform of the output fast-time domain field recorded over a large number of roundtrips, with a numerical integration step smaller than the cavity roundtrip. Such a figure has been referred to as the “nonlinear dispersion relation” (NDR), used in optics and hydrodynamics to describe complex nonlinear systems [175, 86, 63]. It can be expressed as follows:

$$\text{NDR}(\Omega, \mu) = \frac{1}{\sqrt{N_t N}} \sum_{\ell, k} \psi_{\ell, k} e^{i(\Omega t_k - 2\pi \mu \ell / N)}, \quad (4.5)$$

here Ω is a slow frequency, $t_k = \Delta t k$ with $\Delta t = \mathcal{T}_l / N_t = 1 / f_s$ time-step (one over long term sampling frequency), \mathcal{T}_l is simulation time with N_t number of discretisation points. Figure 4.3

presents power spectral density (PSD) of the NDR over Floquet index n vs. μ , which are respectively proportional to the ‘slow’ frequency Ω counted in D_1 and longitudinal mode (comb) index.

Each state carries conjugate pairs of resonant radiation conditions related to the dispersion operator [67, 68], originating from the two states ψ_H and ψ_L : $\zeta_{H\pm}$ and $\zeta_{L\pm}$ respectively

$$\zeta_{L\pm}(\mu) = -\delta\mathfrak{d}_1\mu + \mathfrak{d}_3\mu^3 \mp \sqrt{(\zeta_0 - \mathfrak{d}_2\mu^2 - \mathfrak{d}_4\mu^4 - 2|\psi_L|^2)^2 - |\psi_L|^4} \quad (4.6)$$

$$\zeta_{H\pm}(\mu) = -\delta\mathfrak{d}_1\mu + \mathfrak{d}_3\mu^3 \mp \sqrt{(\zeta_0 - \mathfrak{d}_2\mu^2 - \mathfrak{d}_4\mu^4 - 2|\psi_H|^2)^2 - |\psi_H|^4} \quad (4.7)$$

Which was covered previously in basics section 1.3. Our simulations reveal that the noise within the cavity forms a prominent resonance curve that follows one of those dispersion relations, depending on which bistable state the field is in. We note the conjugated ζ_+ relation appears weakly only on the upper state (depicted as ζ_{H+} in Fig. 4.3(c)) as a result of sufficient FWM with ζ_{H-} . In Fig. 4.3(b,d), we see how rapid dispersion frequency-modulation causes this radiation condition to carry sidebands, hence referred to as Floquet bands, spaced along the n axis spaced by \mathfrak{d}_1 ($n = \zeta/\mathfrak{d}_1$). For this simulated example, $\mathfrak{d}_1/2\pi = 8$ corresponding to 8 times the photon lifetime frequency. For simplicity, we consider an example of $\tilde{\mathfrak{d}}_2^{(1)} = \tilde{\mathfrak{d}}_2^{(-1)} = \Delta/2$ that corresponds to cosine modulation of the dispersion (as it was in Eq. 3.6). In this case, the linear term in Eq. (4.4) couples n and $n \pm 1$ frequency modes with a coupling strength $\Delta\mu^2/2$. This effect is identical to sideband generation in electro-optic modulation, given in Eq. 2.8, in which here efficiency increases with the mode number μ . *Both* upper-state Floquet bands ζ_{H-} and ζ_{H+} are affected by the modulation in a similar way, as shown in Fig. 4.3(d).

4.1.3 Faraday instability

To reveal the emergence of Faraday instability (FI), we modify the simulations presented in Fig. 4.3(d) entering the range of parameters corresponding to the unstable regime. The above-mentioned simplification allows us to further develop an analytical derivation and analyse the linear stability of the system. We use a conventional stability analysis approach [176], but in the new 2D FWM setting created by Eq. 4.4, assuming FSR/2 periodic dynamics of the field. As a result, we obtain that comb indices corresponding to the maximum FI gain can be approximated by the following expression (see extended mathematics section 4.5):

$$\mu \approx \pm \sqrt{\frac{\mathfrak{d}_1}{2\sqrt{(\mathfrak{d}_2^{(0)})^2 - \Delta^2}}} \approx \pm \sqrt{\frac{D_1}{D_2^{(0)}}}. \quad (4.8)$$

Equation 4.8 reveals that in the normal dispersion regime, it is possible to observe formation of sidebands with frequency offset of FSR/2 from the pump which is also highlighted in Fig. 4.4.

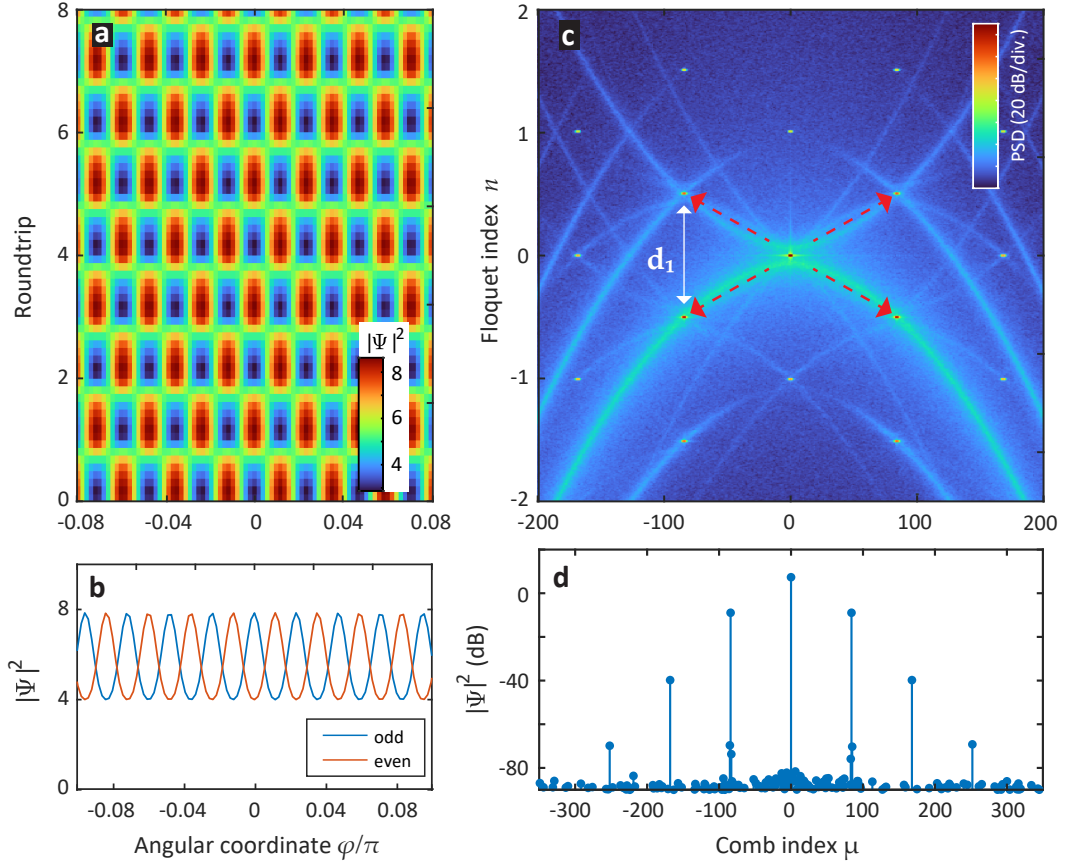


Figure 4.4: **Faraday instability (FI) simulation in CW-driven Kerr cavity with normal dispersion.** For cavity with $F^2 = 10$, $\zeta_0 = 5$, $\Delta = 0.5\vartheta_2^{(0)}$, $\vartheta_1/2\pi = 8$, and $\vartheta_2^{(0)} = 0.0027$. (a) Fluctuating field over roundtrips vs. angular coordinate. (b) Angular coordinate domain showing two consecutive cavity roundtrips. (c) Fast frequency domain snapshot. (d) 2D Fourier-transform (NDR) of (a) for Floquet mode index n vs. comb mode index μ .

Fig. 4.4(a-d) show the result of the numerical simulations. The considered range of parameters correspond to period-doubling dynamics in the resonator with a $2T$ oscillation period, similar to results of Ref. [169]. Fig. 4.4(a,b) show a corresponding spatiotemporal diagram and its cross-sections at two states separated by T . The NDR shown in Fig. 4.4(c) shows the 2D nature of the FWM pathways implying that pump photons can be transferred in the 2D frequency space changing both μ and n indexes. The maximum FI gain (see Fig. 4.5 for the full FI gain diagram) is placed at the modes corresponding to a $\vartheta_1/2$ spacing between the ζ_{H+} and ζ_{H-} Floquet bands.

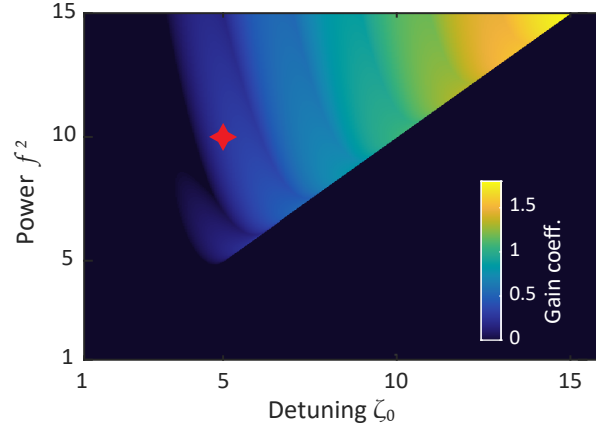


Figure 4.5: **Faraday instability** gain coefficient as a function of detuning and power. Red star marks operating point for Fig. 4.4.

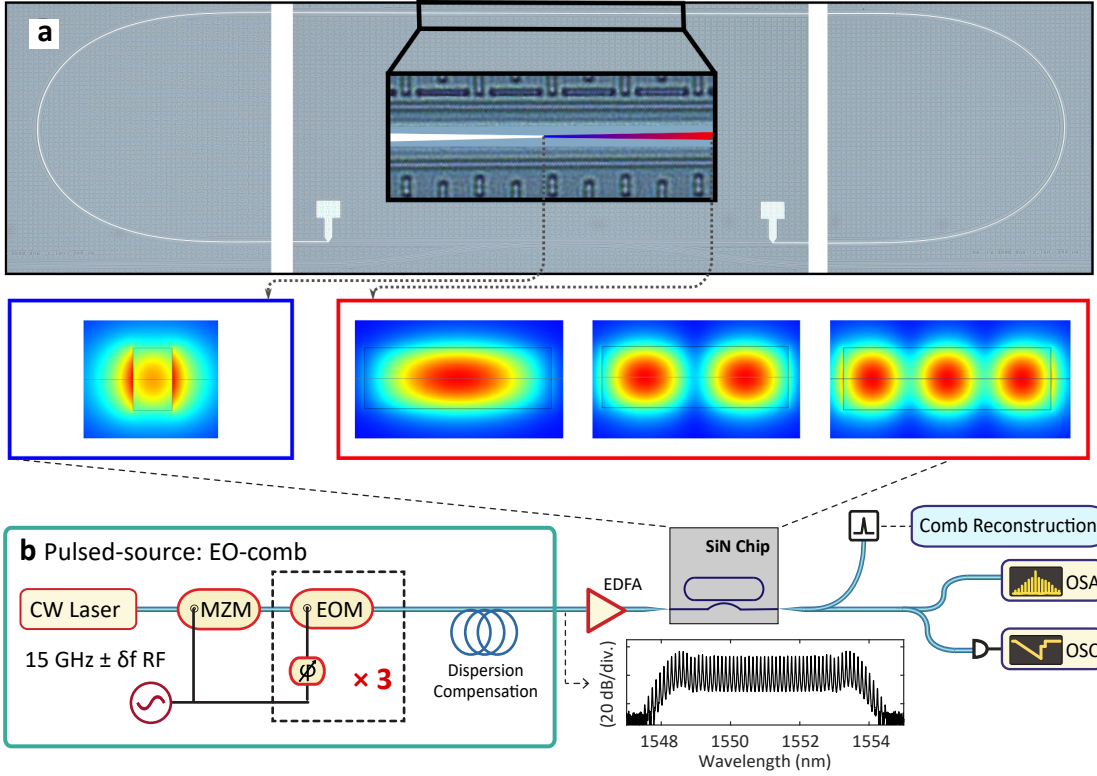


Figure 4.6: **Si₃N₄ photonic chip and experimental setup.** (a) Microscope image of the Si₃N₄ racetrack microresonator having 15 GHz free spectral range. The inset shows the mode suppression section (MSS). The variation of the waveguide width is highlighted by the color gradient. (b) Experimental chip pumping scheme, featuring the EO-comb as a pulsed-source. The input pulse train is coupled into and out of the microresonator chip via lensed fibers. Bottom-inset: Spectrum of the 15 GHz EO-comb before amplification. MZM: Mach-Zehnder modulator, EOM: electro-optic modulator, EDFA: erbium-doped fiber amplifier, OSA: optical spectrum analyzer, OSC: oscilloscope. See Fig. 4.9 for “comb reconstruction” section.

4.2 Microresonators with tapered mode suppression, with anomalous and normal dispersion

The experimental setup used for all the measured results of this work is presented in Fig. 4.6. The resonators of choice (one pictured in Fig. 4.6(a)) are based on the photonic Si_3N_4 waveguide platform, fabricated using the *Damascene process* [177], and have an FSR of 15 GHz, this time native to the repetition rate of the EO-comb and therefore no longer $\times 2$ inefficient. While the ring resonator in the theoretical model is assumed to have a sinusoidally varying second-order dispersion D_2 , the real resonators are more complex. The original motivation for inserting a single mode section into the resonators was to suppress mixing between higher order transverse modes, that can lead to single mode dispersive waves. However, as detailed in this chapter we found that this leads to new dynamics. This was achieved with the use of a higher-order mode suppression section (MSS), a short segment of the resonator where the waveguide tapers from its main waveguide width down to $0.4\text{ }\mu\text{m}$ [156, 178], a width where only the fundamental mode may propagate without strong loss, shown in Fig. 4.6(a).

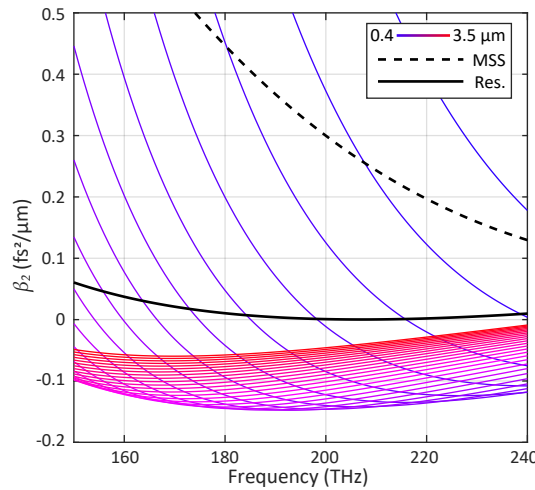


Figure 4.7: The variation of the dispersion over the MSS (Fig. 4.6) for changing waveguide width (height = $820\text{ }\mu\text{m}$), the aggregate dispersion of the whole MSS, and aggregate dispersion for the whole resonator.

In Fig. 4.7, we plot numerically calculated waveguide dispersion values β_2 for several discrete waveguide cross-sections along the MSS, showing how the dispersion transitions from weakly anomalous up to strongly normal. We can retrieve the *average* roundtrip dispersion $\beta_2^{(0)}$ through a weighted sum of β_2 for each waveguide width according to their relative length. In this example resonator design, the final aggregate dispersion calculation comes out close to zero, since the MSS accounts for 13% of the total cavity length. This also means the dispersion modulation duty-cycle is not pure sinusoidal, but rather more pulse-like with many more coupling harmonics in the longitudinal n -space. For numerical modeling presented below, we assume a pure sinusoidal approximation, but a full pulse-like treatment for the dispersion can be found in the extended section.

Resonators fabricated with this architecture for the experiment included a range of average dispersion values from anomalous to normal, providing the results for both regimes in this work. The properties of three in particular, referred to short-hand as D72-A, D72-B, and D72-C, are given in Fig. 4.8. The pumping and measurement setup itself is the same as in the preceding two chapters. In addition, we carry out “comb reconstruction” measurements in order to ascertain both offset frequency, the relative repetition rate, and coherence of the observed comb states, the setup of which is shown in Fig. 4.9. This technique is realized on the linear dispersion measurement tool [50] reconfigured to a heterodyne optical spectrum analyser by superimposing the output of the resonator with the scanning laser on a balanced photodetector. Kerr comb reconstruction provides a high spectral resolution (of the order of 4 MHz) and an extended dynamic range (enhanced by a multistage logarithmic amplifier - Analog Devices 8307) which allow us to obtain full spectral information about the generated comb state.

4.2 Microresonators with tapered mode suppression, with anomalous and normal dispersion

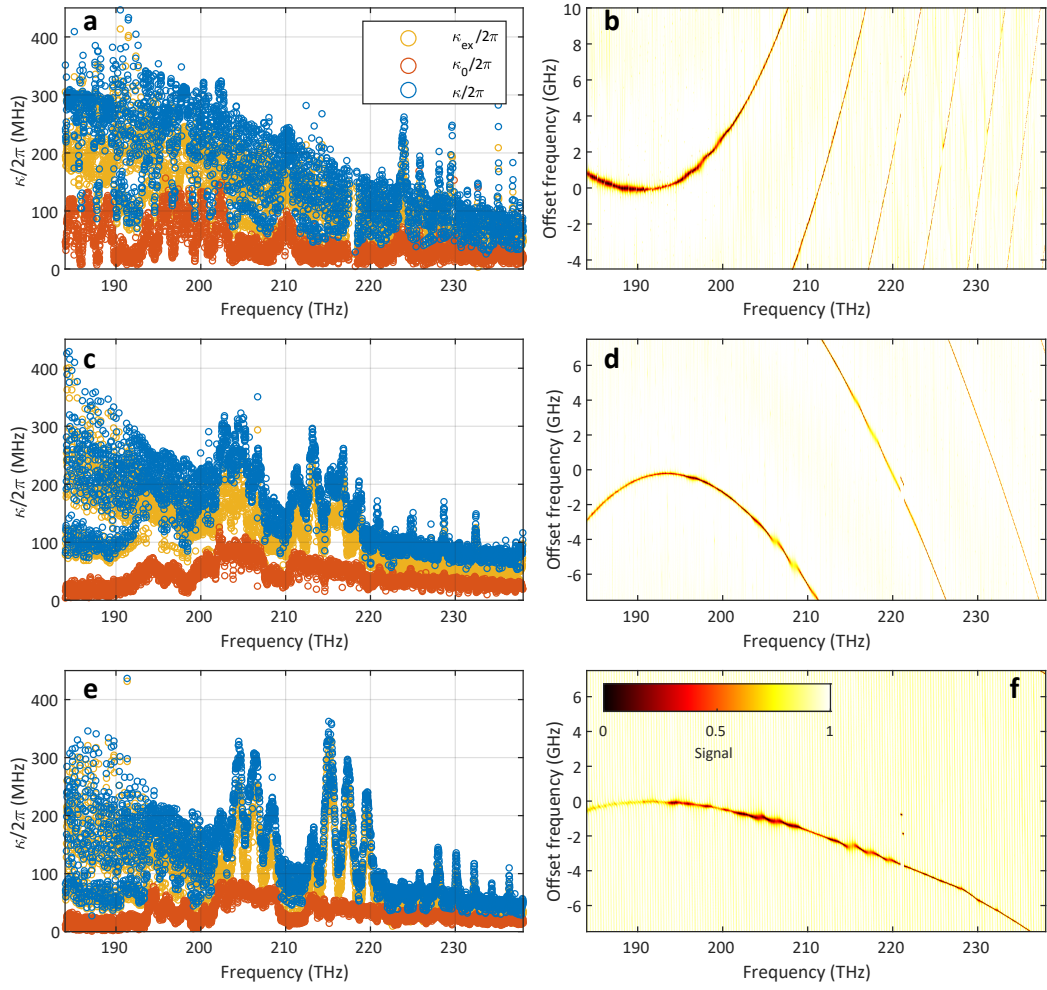


Figure 4.8: **Experimental characteristics for 3 resonators: D72-11.F1.C16.R6(TM) ‘D72-A’ (a/b), D72-11.F9.C15.R6(TE) ‘D72-B’ (c/d), and D72-11.F2.C15.R5(TE) ‘D72-C’ (e/f)** (a,c,e) The fitted linewidth values of each measured resonance. (b,d,f) The total transmission trace measured using the calibrated swept-laser spectroscopy [50], graphed in Eschelle form with a repetition sampling rates of 15.05907, 15.320263, and 15.30877 GHz respectively.

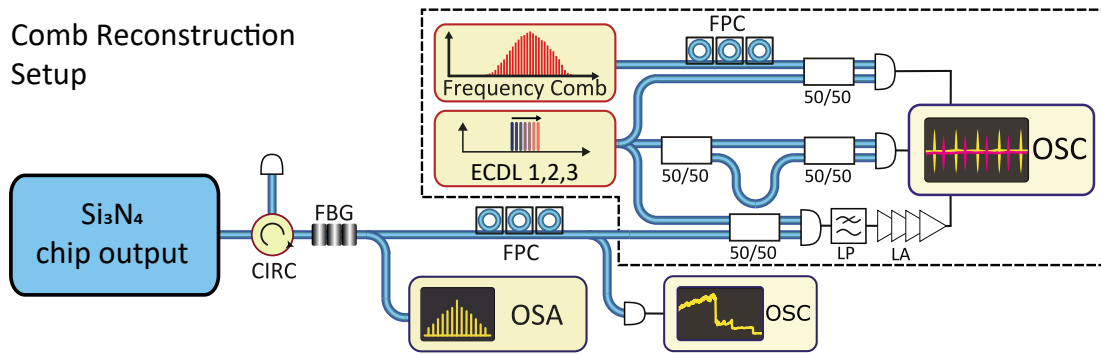


Figure 4.9: **Comb reconstruction experimental setup.** Output microcomb light from the photonic Si_3N_4 chip enters coming from the blue box. FBG: fiber-Bragg grating; OSA: optical spectrum analyzer; OSC: oscilloscope; ECDL: external cavity diode laser; FPC: fiber polarization controller; LP: low-pass filter; LA: logarithmic amplifier.

4.3 The anomalous dispersion case: solitons with higher-order dispersive waves

4.3.1 Theory & Modelling

First, we revisit the effect of the perturbation on the bright DKS formed in the anomalous dispersion cavity. The exact distribution of the modulation along the cavity can affect the position or the amplitude of the instability gain. However, this does not change overall dynamical features [72], which allows us to use the simplest cosine-modulated cavity. Although the Faraday instability gain can be positive, in this case [170], the CW solution on the upper branch is Turing unstable [70] and, in the considered range of parameters, leads to DKS generation. Therefore, dispersion modulation here acts as a roundtrip-periodic perturbation to a stable DKS state. This provides a photon transferring mechanism – quasi-phase matching – resulting in power enhancement in certain modes placed at the same frequency grid as the soliton line. They modify the solitonic spectrum with Fano-shaped sidebands (also known as Kelly sidebands) [159], to which we refer to as here as “higher-order dispersive waves” (HDW). ‘Higher-order’ in this sense is explicitly related to the Floquet dimension (modulation in the longitudinal axis), and should not be confused with higher *polynomial* orders of the dispersion ∂_3, ∂_4 etc.

To illustrate this, we repeat numerical solutions to Eq. (4.1). In Fig. 4.10(a-d), we recall the conventional (unperturbed) DKS features. Fig. 4.10(a) (yellow) shows a cross-section which contains a secant hyperbolic profile on a CW background. The frequency domain of this is shown in Fig. 4.10(b). Taking the 2D Fourier transform of the spatiotemporal data, we obtain the NDR (described above) in Fig. 4.10(d). The NDR of a single unperturbed soliton has two components: a soliton line, and the dispersive resonance curve ζ_{L-} , which is seeded mainly by the cavity noise, and here is approximately equal to the cold-cavity dispersion operator. The detuning of the DKS from the cold cavity resonance ζ_0 is given by the gap between the soliton line and the ζ_{L-} curve. Crucially, even though the cavity dispersion wraps over the FSR line $n = 1$ more than once, *no dispersive wave* is created in this case since the nonlinear photon transfer is forbidden by the momentum conservation law.

When periodic dispersion modulation is introduced, we observe a different picture (Fig. 4.10(a,b,e,f)). The spatiotemporal diagram (e) reveals that the DKS radiates dispersive waves to the cavity, depicted by wavy lines emanating from the DKS and overlapping every roundtrip. They appear as a CW background modulation shown in (a), and in (b) are seen to manifest as several HDW on the spectral wings (ie. Kelly sidebands). The NDR presented in Fig. 4.10(f) reveals that the HDW originate from the intersection between the soliton line and the FSR-folded Floquet bands. This interaction is enabled by the periodic modulation which couples neighbouring modes, appearing in the NDR as copies of the soliton line and dispersive Floquet bands repeated at every FSR. In this way, the momentum conservation law can be satisfied which leads to efficient nonlinear photon transfer at the intersection points, forming the HDW in the spectrum. An extended 3D perspective and a view of the dispersion-folded space can be

found in the supplementary information

While Fig. 4.10 explains the phase-matching behaviour, there are further details that can be seen when taking a 3D view of $\tilde{\psi}_{n\mu}$. Presented again in Fig. 4.11(a,c) is the spatiotemporal field of a soliton propagating in a dispersion-modulated cavity, and its fast vs. slow frequency NDR diagram, the same as in Fig. 4.10(f) this time in 3D. Here we can see the higher orders of the soliton spectra existing at offset frequencies, at non-zero Floquet indices. At the 0th-order, the soliton comb has the vast majority of the energy in the central spectrum, but its higher-order dispersive wave peaks have an asymmetric Fano-resonance profile. At the other orders, the energy of the central spectrum is low, but at the +1st and +2nd Floquet indices, the dispersive waves are fully resonant where they cross the dispersion curve.

This simulation in Fig. 4.11(a,c) was captured by sampling the propagating field solution to Eq. 4.1 at rate of $f_s = 128$, or 8 times the modulation rate (the cavity “FSR”) $\vartheta_1/2\pi = 16$ (more on sampling and evaluation in appendix C.2.1). This is equivalent to measuring the soliton at 8 steps for each circulation of the resonator, revealing the higher-order comb spectra. Doing this is not practical in experiment. Instead, the soliton is measured once per roundtrip as it exits the resonator. *This* outcome is presented in Fig. 4.11(b,d), where the exact same simulation is ran except with $f_s = 16$, equal to the FSR ϑ_1 . Now, it is made clear that the radiating waves of the soliton appear perfectly static at this sampling frequency, just as they would be in experiment. The consequent NDR diagram in Fig. 4.11(d) shows the soliton spectrum now in ‘folded’ space, where all Floquet bands have been collapsed into one, and the dispersive wave peaks appear fully resonant.

4.3 The anomalous dispersion case: solitons with higher-order dispersive waves

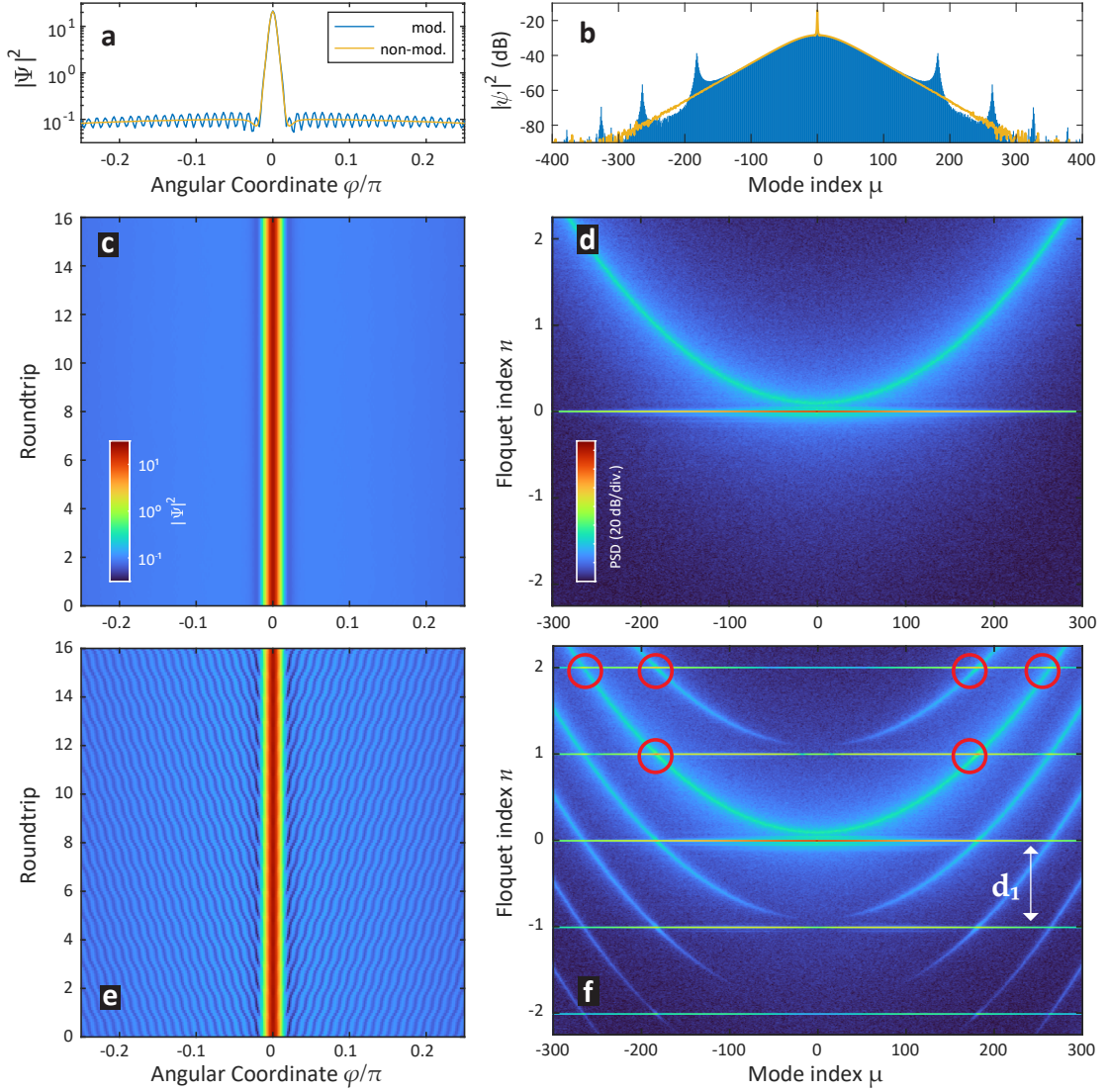


Figure 4.10: **Dissipative Kerr soliton (DKS) simulation in CW-driven modulated cavity.** For $F^2 = 10$, $\zeta_0 = 10$, $\Delta = 0.7\mathfrak{d}_2^{(0)}$, $\mathfrak{d}_1/2\pi = 16$, and $\mathfrak{d}_2^{(0)} = -0.0027$. (a) DKS field in cavity angular coordinate with (blue) and without (yellow) modulation. (b) Corresponding fast frequency power spectrum. (c) Spatiotemporal diagram of the modulated DKS propagating over resonator roundtrips (slow time). (d,e) DKS nonlinear dispersion relations, obtained by taken $\mathcal{F}[\cdot]$ over both dimensions of the spatiotemporal diagram for non-modulated and modulated cases, respectively. Red circles show higher-order dispersive wave positions.

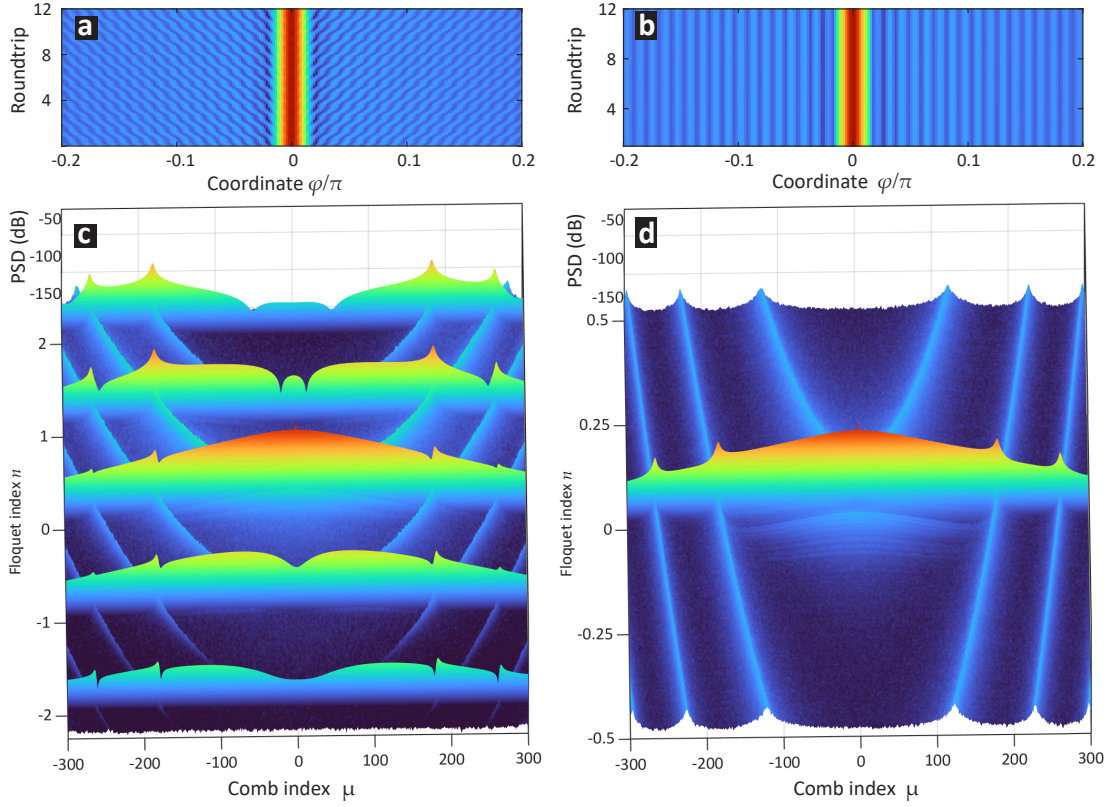


Figure 4.11: **Dispersive resonance analysis simulation.** (a,b) Noisy intracavity optical field in resonator coordinate φ (fast time) over resonator roundtrips (slow time). (c,d) Nonlinear dispersion relation of noisy field taken from 2D Fourier transform of a,b, plotted per comb index μ (fast frequency) over Floquet index n (slow frequency). (a,c) Noisy field solution for cavity in CW Kerr low-state ψ_L , and (b,d) high-state ψ_H . Parameter values for this simulation are given in Table C.1.

4.3.2 Experimental results

First, we verify the excitation of higher order dispersive waves in strongly pulse-driven resonators, that feature periodic dispersion, shown in Fig. 4.12. The resonator device used here, D72-A, has a relatively cubic dispersion profile with coefficients $D_{1,2,3,4}/2\pi = 15.06$ GHz, 14.3 kHz, 6.59 Hz, and -3.84 mHz respectively, with intrinsic loss and coupling $\kappa_{0,\text{ex}}/2\pi = 30$ kHz and 230 kHz respectively as shown in 4.8. The high value of κ_{ex} was selected in order to maximise the output power of the soliton spectrum (according to Eq. 2.1 and 2.3), with a given average power of 720 mW entering the chip waveguide. After the dissipative Kerr soliton (DKS) microcomb was generated stably, by tuning the EO-comb centre frequency across resonance into the bistability region [99], there appeared several Kelly-like sidebands, or HDW, on the short-wavelength side of the spectrum. Remarkably, these higher order dispersive waves were observed up to 5th order and appeared spectrally highly distinct from the DKS. Extrapolating the DKS envelope, we observe that the HDWs exhibit about 25 dB more power compared to the smooth single DKS case. Fig. 4.12(a) shows the integrated dispersion profile of this microresonator measured separately [50], overlaid with its fourth-order polynomial fitting $D_{\text{int}} = \sum_{k=2}^4 D_k \mu^k / k!$, and 5 additional orders of D_{int} separated negatively by nD_1 . In Fig. 4.12(b) the final soliton spectrum is plotted featuring HDW up to the fifth order.

Next, we compare the location of the observed HDW with the theoretical predictions. By taking the frequencies of each HDW in Fig. 4.12(b) and projecting them on to each Floquet order of *folded* integrated dispersion operators in Fig. 4.12(a) (black circles), we retrieve a linear frequency comb grid (black dash). This tilted line gives us the soliton comb relative frequency grid whose repetition rate (comb line spacing) is controlled by the injected EO-comb pulse-train, desynchronised from the cavity FSR slightly by $f_{\text{eo}} = D_1/2\pi + \delta f_{\text{eo}}$ [94]. We directly confirm the comb integrity using the Kerr comb reconstruction technique described above [76], which allows us to experimentally obtain a direct measurement of the NDR (see Fig. 4.9 and section 4.2). The resulting image is shown in Fig. 4.12(c), measured across the bandwidth available to us of ~ 184 -240 THz; although, only the first-order dispersive wave had a sufficient signal-to-noise ratio to be captured. The image shows that every comb line of this spectrum lies on a straight grid spaced by 15.05907 GHz, as sampled in this plot, which did exactly equal the experimentally set EO-comb frequency f_{eo} . In particular, the first HDW seen at 211 THz lies on the very same grid.

It should be pointed out that the soliton spectrum does not match prediction on the long-wavelength side. According to the above dispersion plot, we should see likely two more first-order HDW as the comb grid crosses the $D_{L-} - D_1$ operator ($\approx D_{\text{int}} - D_1$) twice at 169 THz and later below 140 THz. Instead, we see these two features at 148 and 154 THz indicating the polynomial fitting is inaccurate in this region due the lack of measured dispersion values beneath 180 THz.

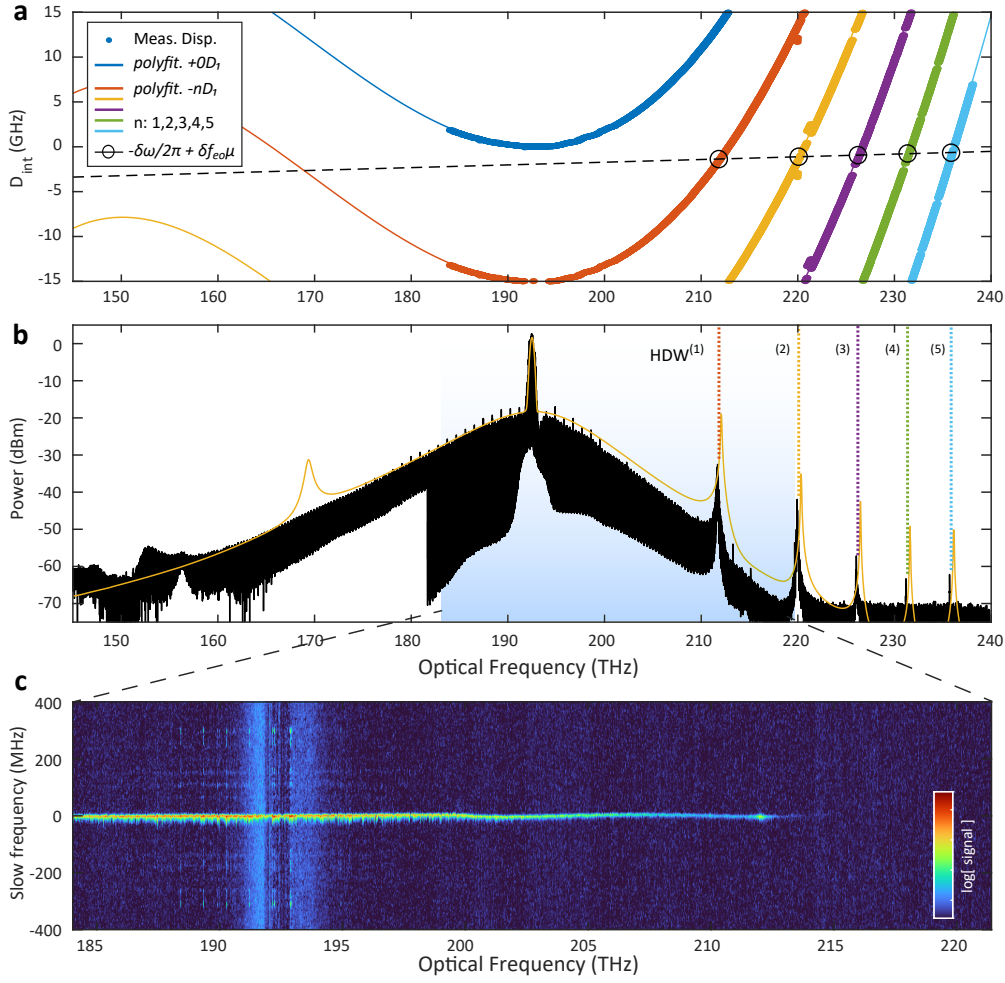


Figure 4.12: **Dissipative soliton with higher-order dispersive waves experiment. Device ‘D72-A’ (D72-11.F1.C16.R6(TM))** (a) Measured integrated dispersion profile overlaid against polynomial fit, including all tranches separated by the FSR D_1 . Dashed line represents comb line array. Where the fit lines are not fully accurate due to lack of measured points, they are gray. (b) Measured single soliton spectrum in resonator device with the above dispersion profile. Observed higher-order DW on high frequency side matched with points on the corresponding dispersion curves. Overlaid is the simulation result using the same resonator values. See appendix C.3.5 for a full breakdown of the simulation with values. (c) Experimental comb reconstruction measurement of the soliton comb in the frequency range 184-220 THz.

4.4 The normal dispersion case: switching waves with satellite structures

4.4.1 Theory & Modelling

Next, we discuss the Floquet dynamics of coherent structures in normal dispersion resonators. In this case the pulse driving, used in our experiments to achieve high peak powers, plays another major role in stabilising SW structures that appear in the resonator (as seen in chapter 3). SW usually have a non-zero relative group velocity that depends on the driving amplitude F . As a reminder from section 3.1.1, there is a particular value of F that corresponds to a stationary SW pattern called a Maxwell point [90, 145]. Pulse driving leads to an intracavity power gradient that depends on the intra-resonator coordinate φ , therefore the edges of a SW lock to the part of the pump corresponding to the Maxwell point. Meanwhile, the dispersion modulation, in this case, leads to the Faraday instability dynamics including the effect of period-doubling[169], resulting in the generation of widely spaced sidebands that originate from the two-dimensional FWM process.

We provide numerical simulations of the LLE Eq. 4.1 and compare homogeneous and modulated cavity cases. Fig. 4.13(a-d) display the ideal SW generated in a synchronously-pumped resonator. The spatiotemporal diagram (Fig. 4.13(c)) shows half of the intracavity field dynamics since there is a mirror symmetry imposed by the pump at $\varphi = 0$. Fig. 4.13(a) (yellow) shows a typical ‘platicon’ profile (ie. SW pair) of a rectangular pulse with oscillating tails. Fig. 4.13(b) is the corresponding spectrum showing the flat-top spectral profile. The NDR plotted in Fig. 4.13(d), particularly the inset panel, clearly reveals the *origin* of such a spectrum. Since both branches of the bi-stable resonance ψ_L and ψ_H are involved in the SW formation, we observe *all* resonant radiation curves ζ_{L-} , ζ_{H-} , and ζ_{H+} on the NDR (ζ_{L+} is again too weak to appear). The ζ_{H-} curve originating from the upper state ψ_H (top of the SW) acquires an additional phase shift due to the Kerr nonlinearity and therefore is shifted down to lower frequencies relative to ζ_{L-} . A coherent structure (the horizontal FWM grid) corresponding to the rising and falling edges of the SW acquires a smaller Kerr shift, and therefore crosses the curve ζ_{L-} . Such a crossing implies the phase-matching between the states and leads to enhanced power at the crossing modes. This creates the characteristic flattened dual-shockwave spectral profile of the SW [179, 145].

When the SW is generated in the modulated cavity, the strong influence of Faraday instability (FI) is observed. Performing numerical simulation with the same parameters as in the Fig. 4.10, but with the sign of $\mathfrak{d}_2^{(0)}$ reversed, we observe *period-doubling* dynamics in Fig. 4.13(a,e). The top part of the SW is patterned with periodic structures, similar to that observed in the CW case (Fig. 4.4), that are direct evidence of FI. Each roundtrip, the patterned profile exhibits a π phase flip as reported in Ref. [71, 169]. The power profiles $|\psi(\varphi, t)|^2$ at two stages of the period-doubling dynamics are displayed in Fig. 4.13(a). Corresponding spectral plot in Fig. 4.13(b) shows the appearance of characteristic *double-peaked* sideband spectra substantially extending the unperturbed SW spectrum. In a microresonator environment,

these sidebands manifest as *satellite combs* drawing energy from the central comb.

Besides the conclusion from the analysis that predicts the position of the modes having maximum FI gain, there is an empirical understanding of the process that can be formulated by analysing the NDR plot shown in Fig. 4.13(f). In the normal dispersion case, conventional modulation instability does not affect the upper state of the bi-stable resonance. Because of the high power, the conjugated upper state dispersive curve ζ_{H+} becomes visible on the NDR. Both curves are experiencing modulation resulting in the FSR-spaced Floquet bands. At the location in the n vs. μ space where ζ_{H-} and ζ_{H+} cross, we observe the formation of satellites. Due to the apparent mirror symmetry between ζ_{H-} and ζ_{H+} , the intersection occurs at $\pm\text{FSR}/2$ in the slow frequency dimension. As explained above, this process can be seen as a two-dimensional FWM process, providing photon transfer from the pump to the sidebands having an $\pm\text{FSR}/2$ offset. The double-peak structure of subcombs can be readily explained with the NDR. This double-feature was in fact seen in numerical simulations shown in *Staliunas et al.* [167] but was not discussed there in further detail. The coherent sub-comb line formed around the unstable mode, sourced from FI, crosses both ζ_{H-} and ζ_{L-} simultaneously, resulting in two peaks, the spacing of which corresponds to the separation between these dispersive curves.

As before in section 4.3.1, we can view interesting features in 3D. Here the scenario is much the same as described above for the soliton case, only now we apply a pulsed envelope to the pump term. Fig. 4.14(a,c) presents the same simulation from Fig. 4.13(e,f), only with $|\tilde{\psi}_{n\mu}|^2$ shown in 3D. In the spatiotemporal plot in (a), we see that the ‘flip-flopping’ of the Faraday Instability (FI) pattern is smooth over slow time. In the NDR diagram in (c), the various different satellite spectra existing at higher Floquet indices are very complex, but possess subtle differences in how they interact with the modulated dispersion bands. That simulation was obtained from a sampling frequency of $f_s = 128$. Again, the same result is presented in the dispersion folded space as one would measure in the real resonator, once per roundtrip with $f_s = 16$, in Fig. 4.14(b,d). Now in the spatiotemporal frame (b), the FI flip-flopping has become completely discrete. In the NDR diagram (d), the central SW spectrum, and its two major satellites, have folded into single orders. For clarity, the slow frequency y-axis has been shifted down by a quarter of an FSR in order to show the precise 0.5FSR ($\mathcal{D}_1/2$) offset of the satellite spectra. It is this FSR-folded domain that corresponds to the real comb reconstruction measurements shown later in in Fig. 4.17, and 4.18(e,f).

4.4 The normal dispersion case: switching waves with satellite structures

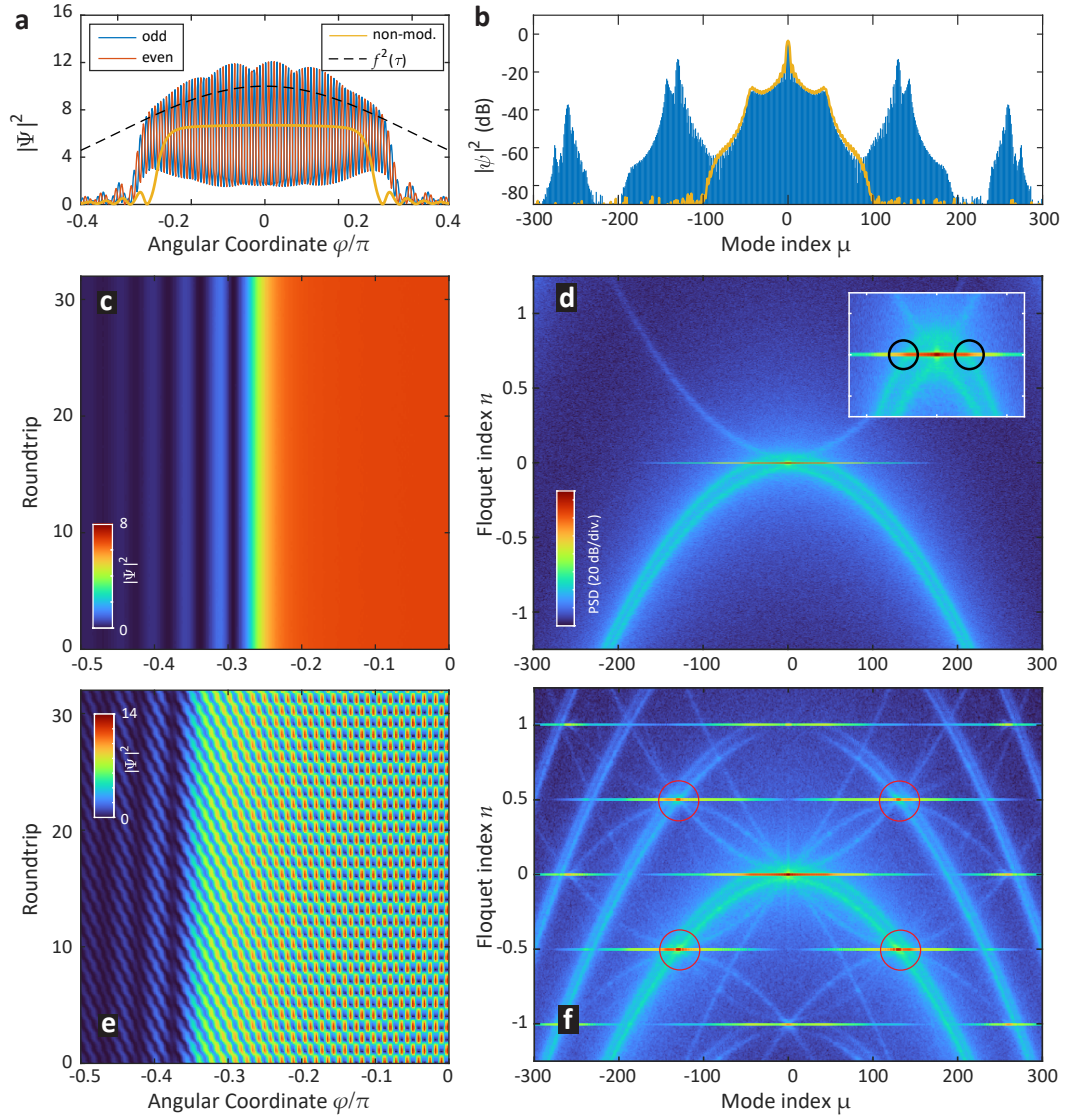


Figure 4.13: **Switching wave (SW) solution in pulse-driven modulated cavity** For $F^2 = 10$, $\zeta_0 = 6$, $\Delta = 0.7\mathfrak{d}_2^{(0)}$, $\mathfrak{d}_1/2\pi = 16$, and $\mathfrak{d}_2^{(0)} = 0.0027$. (a) SW field in cavity angular coordinate with (blue) and without (yellow) modulation. (b) Corresponding power spectrum. (c) Spatiotemporal diagram of an SW in the modulated cavity. (d,e) SW nonlinear dispersion relation, obtained by taken $\mathcal{F}[\cdot]$ over both dimensions of the spatiotemporal diagram for non-modulated and modulated cases, respectively. Black circles show the intersections of a SW line and dispersive parabola resulting in the canonical SW spectral profile. Red circles indicate FI-originated satellites.

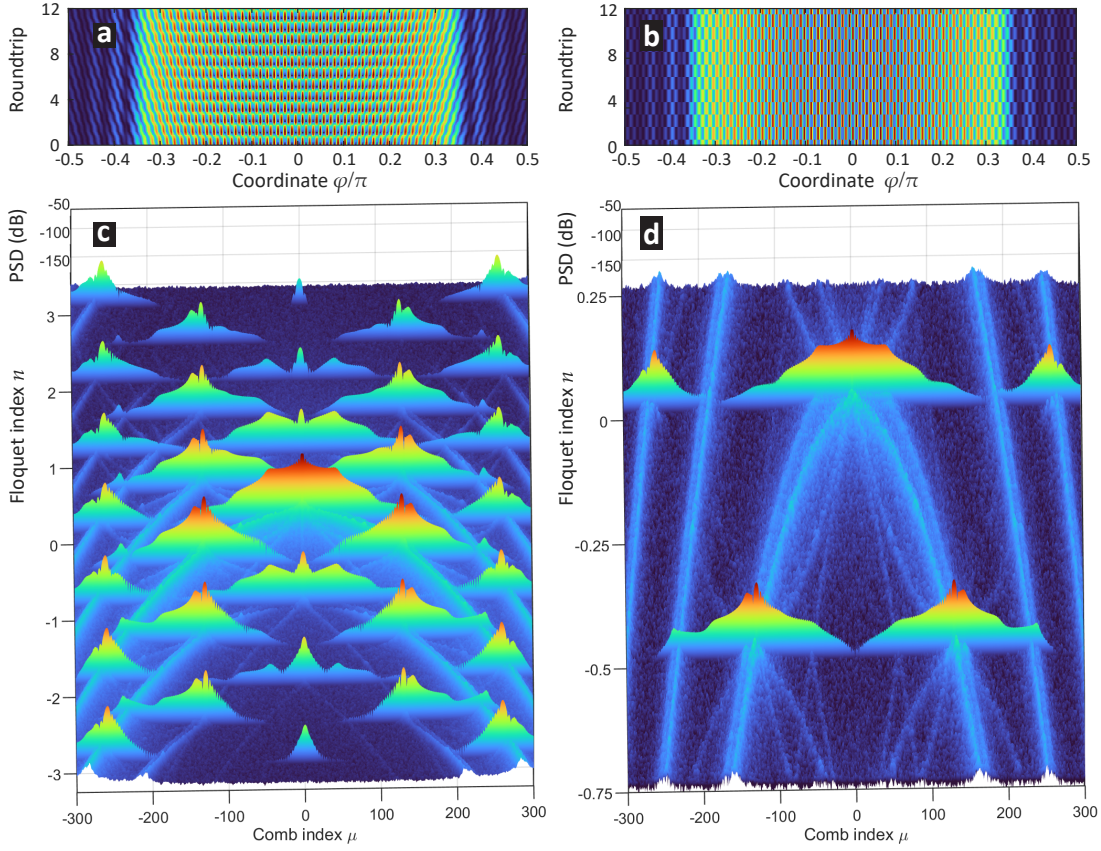


Figure 4.14: **Switching Wave + Satellite Combs in folded space simulation.** (a,b) Switching wave (SW) and Faraday instability (FI) intracavity optical field in resonator coordinate φ (fast time) over resonator roundtrips (slow time). (c,d) Nonlinear dispersion relation of SW+FI taken from 2D Fourier transform of a,b, plotted per comb index μ (fast frequency) over Floquet index n (slow frequency). (a,c) Full temporal super-resolution capture (sampling at $8\times$ cavity repetition rate \mathfrak{d}_1) of field solution showing Floquet bands up to $n = \pm 3$. (b,d) Sampling same field at $1\times$ cavity repetition rate, showing slow-time folded in one FSR \mathfrak{d}_1 . Parameter values for this simulation are given in Table C.1.

4.4.2 Experimental results and comb tuning

Experimental results of switching wave with satellite comb generation in dispersion-modulated resonators is presented here, with the goal of verifying the coherence and comb-like nature of the spectrum as well as the validity of our modelling. For this, two example resonator devices are investigated: D72-B and D72-C. D72-B has relatively strong normal and symmetrical dispersion, with $D_{1,2,3,4}/2\pi = 15.32$ GHz, -12.9 kHz, 5.36 Hz, and -2.39 mHz respectively, and $\kappa_{0,\text{ex}}/2\pi = 30$ kHz and 180 kHz respectively. D72-C, on the other hand, has a flatter and more imbalanced dispersion profile, with $D_{1,2,3,4}/2\pi = 15.31$ GHz, -3.14 kHz, 3.35 Hz, and -2.49 mHz respectively, and $\kappa_{0,\text{ex}}/2\pi = 30$ kHz and 200 kHz respectively. All other experimental details including the driving and detection setup are the same as discussed above at Fig. 4.6.

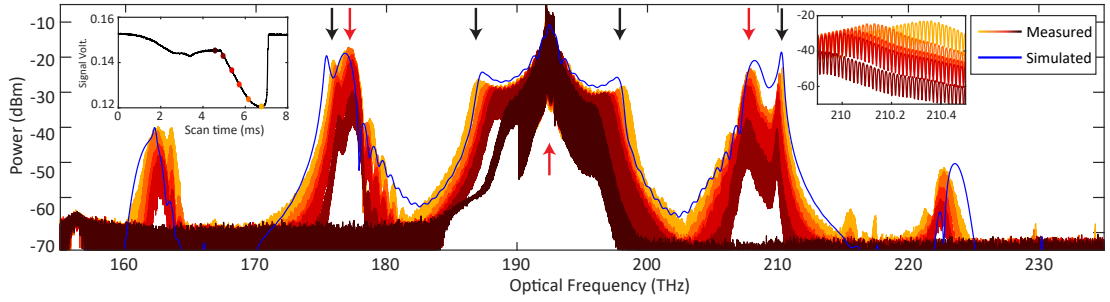


Figure 4.15: **SW microcomb with the emergence of satellite combs in experiment. Device ‘D72-B’ (D72-11.F9.C15.R6(TE))** Measured optical spectra of switching wave affected by FI at different detunings (red-orange scale). Simulated spectral envelope overlaid (blue). Left inset: measured cavity power out during scan of laser detuning over resonance. Red/orange points mark locations of measured spectra. Right inset: zoom-in of comb lines at outer dispersive wave. Black and red arrows correspond to circles from Fig. 4.13 (d) and (f). For complete values used for the simulation, see Table C.4.

Fig. 4.15(f) shows the satellite comb generation results in D72-B, with an average pump power of 230 mW. The left inset in this figure shows the detected power trace from the output of the cavity while the laser centre-frequency is scanned across the cavity resonance from blue-detuned to red-detuned, showing different stages in the way the trace dips in power. The first dip and plateau corresponds to the initial build-up of power in the resonator, and the subsequent formation of the switching wave comb by wave-breaking [145]. The second dip, past halfway, marks the sudden growth of satellite combs. The reason the output power trace decreases in energy during this phase is due to the fact that the photodiode in use does not detect light above 1700 nm (below 176 THz). This indicates energy-transfer from the central comb to the satellite comb. As marked with red-to-orange dots, we stop the laser tuning at the several points here, and plot the spectra measured. Two large satellite combs are observed to rise quickly, *above* even the plateau comb power of the core switching wave. Each satellite comb consists of two features. On the inner side closer to the core spectrum are the sinc() profile-like spectra, marked with red arrows, that represent the origin of the FI pattern sourced from the ‘inside’ of the switching wave, on its upper state, as shown previously in Fig. 4.13.

These are equispaced about the core spectrum at ± 15.5 THz, due to the FI requirement, and appear to agree approximately with the prediction of Eq. 4.8. The second feature is the sharp hook-like dispersive wave on the outer side of the satellite combs, marked with black arrows. These mark the relative location of the lower-state dispersive resonance D_{L-} (where $D_{L-} = \kappa\zeta_{L-}/2$ in dimensionless) with which the FI spectra interact, as also described above in Fig. 4.13. Using the independently measured loss and dispersion values of D72-B given above, we simulated the very same experiment using the LLE with real resonator units. The final simulated spectrum when tuning into resonance is plotted in the same Fig. 4.15 in blue, showing good agreement, particularly with respect to the satellite combs' 'double-feature'.

Moving on to further explore the phase-matching of these satellite combs more deeply, measurements and corresponding simulations of generated satellite combs in resonator device D72-C are shown in Fig. 4.16. The experimental dispersion measurement is shown in Fig. 4.16(a) and its fitting is used to obtain the dispersion parameters listed above, and carry out these verification simulations. When tuning the laser to the point of strongest comb generation, we measure the spectrum shown in Fig. 4.16(b), with average power coupled to the resonator of 60 mW, this time showing satellite comb generation further apart in comparison to Fig. 4.15(f). Re-creating the same experiment in simulation creates the black spectral envelope, showing good agreement. In Fig. 4.15(c), the NDR image for the simulation state is shown, revealing the coherence of the satellite combs and their precise relative position in offset frequency relative to the central switching wave comb, including the three nonlinear dispersion curves D_{L-} , D_{H-} , and D_{H+} that determine this phase matching. According to this figure, the requirement for the FI gain to be equidistant with the pump, and located on the upper-state dispersion curve, causes the satellite combs to originate at 163 THz and 222 THz or ± 29.5 THz relative to the pump, with an offset frequency of ± 3.8 GHz respectively. In a perfectly symmetrical dispersion profile such as in Fig. 4.13 or close to the experiment for D72-B in Fig. 4.15, this offset value would be at or near the FSR/2, 7.66 GHz. In D72-C, due to the positive D_3 , the dispersion landscape has been pulled upwards in the positive optical frequency direction, resulting in this frequency offset value of 3.8 GHz.

To confirm our understanding, we perform comb reconstruction (described above), and plot the image in Fig. 4.17. The data shown here corresponds to the same spectral measurement plotted in Fig. 4.16(b). Superimposed on the density image are the nonlinear dispersion curves calculated for the simulated parameters: the upper- and lower-state curves D_{H-} and D_{L-} respectively (dashed), as well as the conjugated upper-state curve D_{H+} (dashed) and their FSR-shifted Floquet bands (solid). In real units, $D_{\pm} = \kappa\zeta_{\pm}/2$. In this image, we can see the central SW comb spanning 185-203 THz, and we verify that its spectral wings are bound by the lower-state dispersion curve D_{L-} . Crucially, we verify that the short wavelength satellite comb appears at an offset frequency of -3.5 GHz, almost where it is predicted to appear according to the simulated model at the intersection of $D_{H-} = D_{H+} - D_1$. The outer dispersive wave wing of the satellite also appears as this comb's intersection with the lower-state dispersion curve D_{L-} . Both combs appear to be coherent, with optical linewidths limited by the detection resolution of the probing laser (~ 4 MHz). We must acknowledge that the detected offset

frequency of each comb line seems to drift up and down by several MHz across the whole measurement, particularly at the end of the satellite comb. This drift is likely due slow thermal shifts in the pumped resonator mode spectrum (which is not locked) occurring during the 40 second swept-laser scan. This varies from take to take. It is not indicative of the physical frequency comb.

To complete our demonstration of the nature of the satellite comb offset frequency, and its relationship to the dispersion curves, the same series of graphs is presented in Fig. 4.18. This time, however, the frequency of the EO-comb f_{eo} ie. the imposed repetition rate of SW generation inside the cavity, is changed between two limits. In the above Fig. 4.16 results, δf_{eo} was set to 0 in simulation, and in experiment it was set to the point of maximum spectrum-symmetry in the wings of the SW comb, with $f_{eo} = 15.30877$ GHz. In Fig.4.18(a,c,e) we downturn f_{eo} by $\delta f_{eo} = -600$ kHz, and in Fig.4.18(b,d,f) upturn by $\delta f_{eo} = +600$ kHz. In each case, experimentally and in simulation, it is important to observe that the centre of FI gain stays *fixed* at ± 29.5 THz in the optical axis, and at ± 3.8 GHz or ± 3.5 GHz offset frequency in simulation and experiment respectively. These points are highlighted by red lines and circles. While these points remain fixed, the repetition rate (comb line spacing) of the all combs exactly follows the imposed repetition rate, $f_{rep} = f_{eo} + \delta f_{eo}$, causing the visual ‘tilt’ in the combs shown in Fig. 4.18(c-f). Where the tilted comb spectra cross D_{L-} is where the dispersive waves form, highlighted in white circles. By cross-comparing the NDR graphs with the optical spectra shown above in Fig. 4.18(a,b), one can see the direct origin of each comb feature – the edges and enhancements in the spectral envelope.

One final observation for this device D72-C is presented in Fig. 4.19. When the detuning is increased past some threshold, instability in the switching wave and Faraday patterns emerge. Fig. 4.19(a) shows an experimental and simulated trace of the comb spectrum, where the core SW part is merging with the short wavelength satellite. (b) and (c) show the simulated field respectively in frequency and fast time over slow time t , where quasi-periodic bursts are seen erupting from the Faraday waves within the SW fronts. In the simulated slow vs. fast frequency diagram in Fig. 4.19(d), we see that the core comb and the two satellites have begun to connect and form one larger chaotic comb. In Fig. 4.19(e) we present the *experimental* comb reconstruction measurement of this state. The key signatures across the core comb and the short wavelength satellite show remarkable agreement, including signs of a straight line connecting the pump with the strongest part of the satellite, and above, dispersive wave light broadly following the D_{L-} dispersion operator plotted in white.

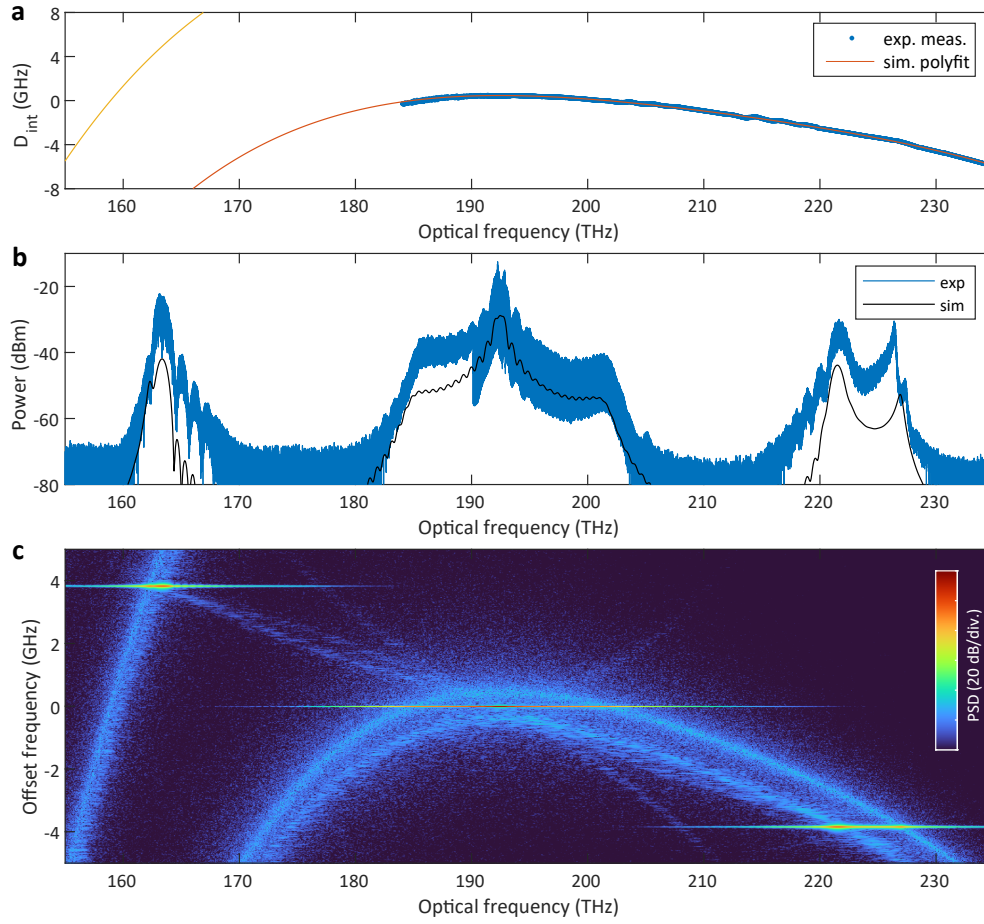


Figure 4.16: **Phase-matching for broadband satellite combs. Device ‘D72-C’ (D72-11.F2.C15.R5(TE)).** (a) Experimentally measured integrated dispersion for resonator D72-C, with fourth-order polynomial fit, used in the following simulation. (b) Experimentally measured spectrum of switching wave with satellite combs, overlaid with simulation result, offset by -15 dB. (c) Nonlinear dispersion relation of the *simulation* above, showing upper and lower dispersion curves and their higher orders. For complete values used for the simulation, see Table C.4.

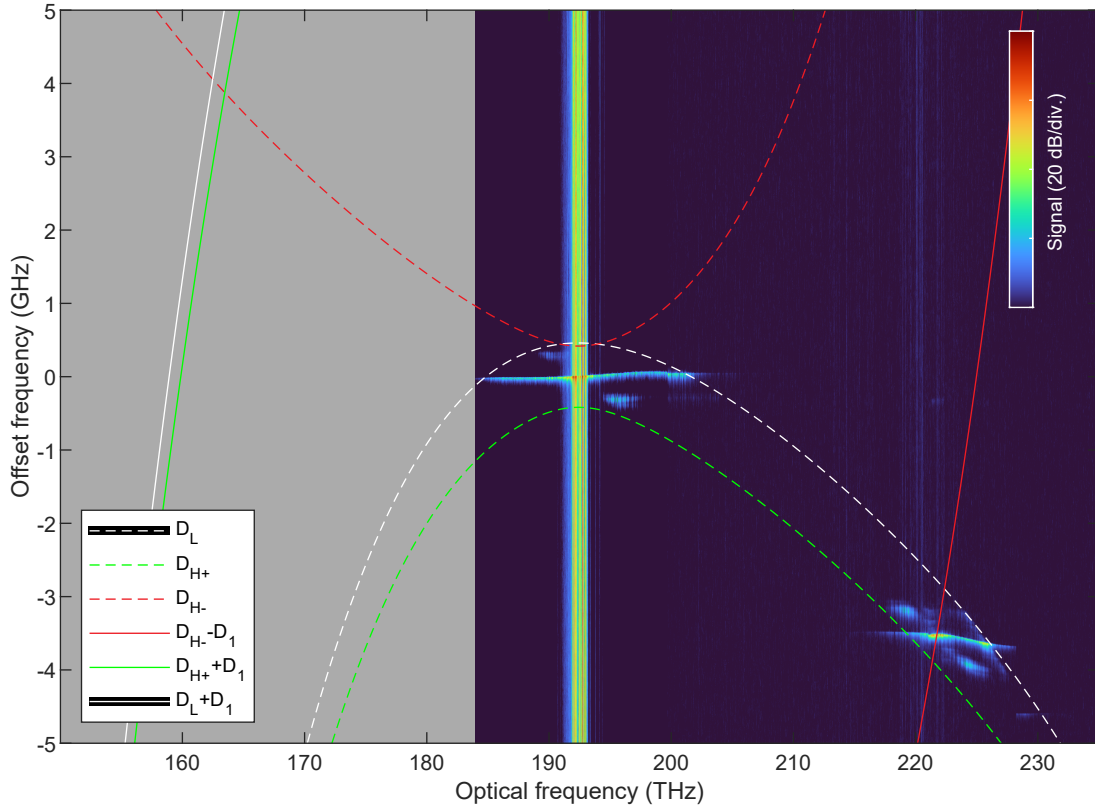


Figure 4.17: **Experimental comb reconstruction of broadband satellite combs. Device ‘D72-C’ (D72-11.F2.C15.R5(TE))**. Experimentally measured comb reconstruction, the equivalent of the image in Fig. 4.16(c), showing the central comb and short wavelength satellite located near the predicted phase-matched frequency offset. The grey area is out of measurement range for our spectroscopy. Overlaid are the analytical dispersion curves used from the simulation. The strong band across 192 THz is excess ASE from the pump spectrum.

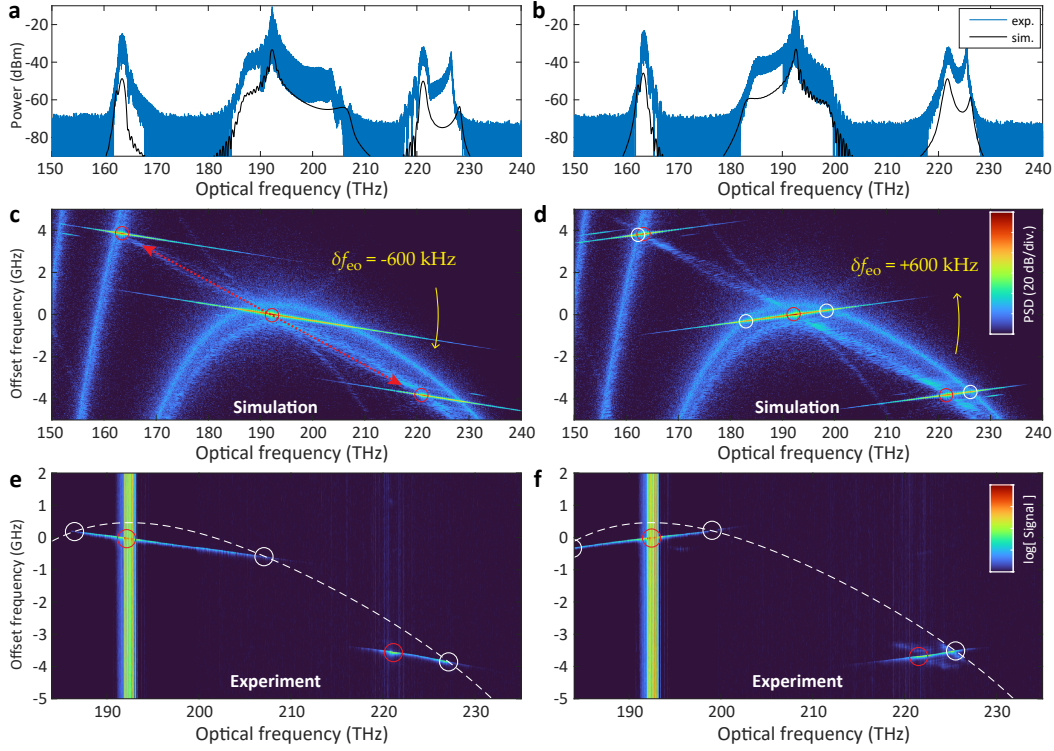


Figure 4.18: Satellite comb repetition rate tuning and phase-matching. Device ‘D72-C’ (D72-11.F2.C15.R5(TE)). Two switching wave + satellite comb generation events where (a,c,e) $\delta f_{eo} = +600$ kHz, and (b,d,f) $\delta f_{eo} = -600$ kHz. (a,b) Spectrum, measured, and simulated using measured resonator parameters. Simulated is offset by -15 dB. (c,d) Nonlinear dispersion relation image for simulated case showing offset satellite comb spectra. (e,f) Measured comb reconstruction image. The strong band across 192 THz is excess ASE from the pump spectrum. Lower-state nonlinear dispersion curve shown in dashed-white. Faraday Instability gain frequency marked in red. Dispersive waves marked in white. For complete values used for the simulation, see Table C.4.

4.4 The normal dispersion case: switching waves with satellite structures

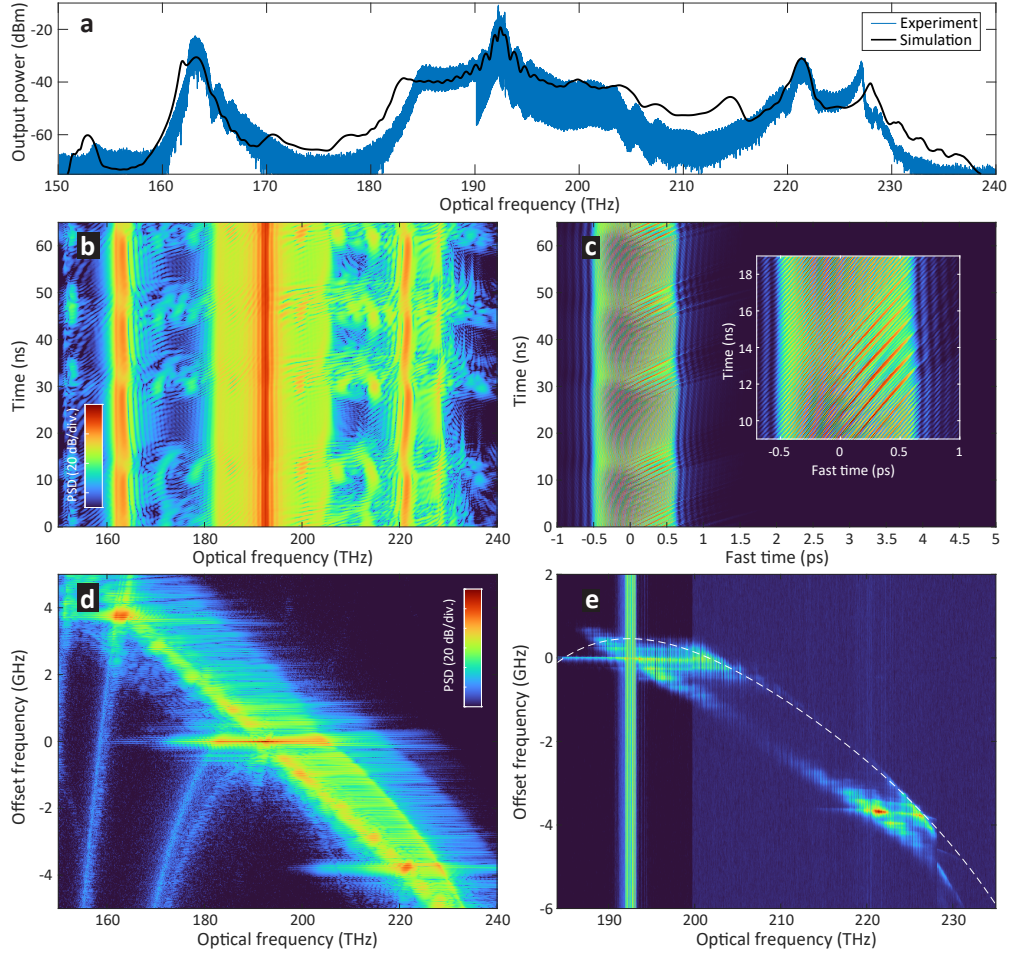


Figure 4.19: Switching wave + satellite comb generation in D72-C in the unstable region, simulation and experiment. (a) Experimental and simulated optical microcomb spectrum of SW and satellite comb generation above the threshold for instability. (b,c) Simulated long-term evolution of (b) microcomb spectral envelope and (c) intracavity field power. (d) Simulated NDR of the long-term states shown in (b,c) plotted in offset frequency vs. optical frequency. (e) Experimental image of the comb reconstruction measurement of the state in (a), corresponding to simulated NDR of (d). White-dashed line is the lower-state dispersive resonance D_{L-} used in the simulation, based on dispersion parameters extracted experimentally. For complete values used for the simulation, see Table C.4.

4.5 Extended mathematics

The following subsection is work done by Aleksandr Tusnin. All credit to him.

Modulation instability analysis

In case of harmonic modulation of the dispersion, Eq. (4.4) indicates linear coupling between the amplitudes $\tilde{\psi}_{n\mu}$ and $\tilde{\psi}_{n\pm 1\mu}$, resulting in breathing of generated structures with period equal to the round-trip time. However, the presence of Kerr nonlinearity gives rise to period multiplication effects that occur due to Faraday instability. In this section we perform a modulation instability analysis for the period-doubled continuous-wave solution.

We assume $\psi_0(\varphi, t)$ to be a solution of Eq. (4.1) with an unmodulated dispersion term. We are interested in dynamics of a small perturbation $\xi(\varphi, t)$ that obeys the linearised equation

$$\begin{aligned} \frac{\partial \xi}{\partial t} = & -(1 + i\zeta_0)\xi + i(\partial_2^{(0)} + \Delta \frac{e^{i\partial_1 t} + e^{-i\partial_1 t}}{2}) \frac{\partial^2}{\partial \varphi^2} \xi + \\ & + i(2|\psi_0|^2 \xi + \psi_0^2 \xi^*) + \Delta \frac{\partial^2 \psi_0}{\partial \varphi^2} \cos \partial_1 t. \end{aligned} \quad (4.9)$$

First, we use the following ansatz $\xi = A(t) \exp i\mu\varphi + B^*(t) \exp -i\mu\varphi$, so the coupled equations for the amplitudes A and B read

$$\begin{cases} \frac{\partial A}{\partial t} = -(1 + i\zeta_0)A - i(\partial_2^{(0)} + \Delta \frac{e^{i\partial_1 t} + e^{-i\partial_1 t}}{2})\mu^2 A + \\ \quad + i(2|\psi_0|^2 A + \psi_0^2 B) + \Delta \frac{\partial^2 \psi_0}{\partial \varphi^2} \cos \partial_1 t, \\ \frac{\partial B}{\partial t} = -(1 - i\zeta_0)B + i(\partial_2^{(0)} + \Delta \frac{e^{i\partial_1 t} + e^{-i\partial_1 t}}{2})\mu^2 B + \\ \quad - i(2|\psi_0|^2 B + \psi_0^2 A) + \Delta \frac{\partial^2 \psi_0}{\partial \varphi^2} \cos \partial_1 t. \end{cases}$$

We continue, assuming $A = \alpha_+ \exp i\partial_1 t/2 + \alpha_- \exp -i\partial_1 t/2$, $B = \beta_+ \exp i\partial_1 t/2 + \beta_- \exp -i\partial_1 t/2$, where the amplitudes obey

$$\frac{d}{dt} \mathbb{Y} = \mathbb{M} \mathbb{Y}, \quad (4.10)$$

where $\mathbb{Y} = [\alpha_+, \alpha_-, \beta_+, \beta_-]^T$ and the matrix

$$\mathbb{M} = \begin{pmatrix} y_{00} & -i\mu^2 \Delta/2 & i\psi_0^2 & 0 \\ -i\mu^2 \Delta/2 & y_{11} & 0 & i\psi_0^2 \\ -i\psi_0^{*2} & 0 & y_{00}^* & i\mu^2 \Delta/2 \\ 0 & -i\psi_0^{*2} & i\mu^2 \Delta/2 & y_{11}^* \end{pmatrix}, \quad (4.11)$$

where $y_{00} = -(1 + i\zeta_0) - i\partial_1/2 - i\mu^2 \partial_2^{(0)} + 2i|\psi_0|^2$ and $y_{11} = y_{00} + i\partial_1$. Real part of the eigenvalues of this matrix give the parametric gain of modulationally unstable solutions. Comb indices of

these solutions can be approximated by the following formula

$$\mu = \pm \sqrt{\frac{\mathfrak{d}_1}{2\sqrt{(\mathfrak{d}_2^{(0)})^2 - (\Delta/2)^2}}} \quad (4.12)$$

5 Outlook and conclusion

In this thesis, Kerr cavity physics were explored as a mutual interplay of simulation and experiment with the aim of generalising and expanding the system to higher orders. The ultimate goal was two-fold: expand understanding of dissipative Kerr dynamics with an intuitive and visual focus; and to exploit these new found effects and strategies to create novel microcombs suitable for use in general applications.

In chapter 2, using the dispersion-engineered Si_3N_4 microresonator platform, we have generated a smooth, resonant supercontinuum based on dissipative soliton formation, comprising over 2,000 comb teeth. By exploiting the resonant enhancement of the high- Q cavity, such a spectrum was generated with pulses 1-6 pJ in energy, >1 ps in duration, and on the order of single-Watt peak power. For future integration, the current EO-comb input could be replaced by an alternative provider of GHz rate, picosecond pulses, such as chip-based silicon or other semiconductor-based mode-locked lasers [180, 181]. Further tailoring of the dispersion landscape and replacing the straight-waveguide coupling section with an adiabatic or curved coupling section [182, 59] will improve the generation and extraction of the short wavelength side of the spectrum. This way, the soliton comb bandwidth can be increased from 2/3rds of an octave to a full octave, enabling $f - 2f$ self-referencing. This work further invites a full exploration of the parameter space for input pulse chirp and flatness parameters in order to find further optimisation of the frequency noise transfer, allowing the use of higher-noise voltage-controlled oscillators for locking the input pulse repetition rate. Overall, this work demonstrated a new chip-based technique for direct access to broadband spectra at microwave repetition rates using a pulsed input, without the use of interleaving, or additional electro-optic modulation after the fact. Importantly, it can provide a way of balancing the fundamental efficiency restrictions between conventional supercontinuum generation, and dissipative soliton microcombs.

In chapter 3, novel class of localized dissipative structures was synthesised, that we term the zero-dispersion soliton. In terms of figures of merit, the generated $\text{ZDS}^{(2-5)}$ -based combs presented here are extremely substantial in terms of the product of their total bandwidth and their total line-count which, as far as we are aware, is a record for a single-structure in

a microresonator. The central body of the ZDS⁽⁴⁾ comb in MR1 spans over 76 THz (1830 and 1260 nm), accounting for more than 2,700 comb teeth, spaced by a detectable 28 GHz repetition rate. When including the DW features, the final bandwidth becomes 136 THz or 97% of an octave. As the repetition rate is directly detectable on photodiode, a future work with fine-tuning of the microresonator dispersion may enable f - $2f$ self-referencing with a single microcomb. We have further demonstrated the direct generation of switching waves via pulse-driving, creating a highly smooth ultra-broadband microcomb under normal dispersion conditions. Such normal dispersion-based microcombs have thus far only been formed in Si₃N₄ via modulation instability enabled by spatial mode-coupling[133], necessitating an extra coupled-microresonator ring with integrated heaters in order to be deterministic [183].

The formation of ZDS-based microcombs more generally has expanded the domain of microcomb generation towards the region of both normal-dispersion and zero-dispersion, previously not often considered ideal. This lifting of strict requirements for anomalous dispersion may give greater flexibility in the Si₃N₄ fabrication process going forward. The result also demonstrates not only that microcomb generation can be achieved in a straight-forward fashion in such waveguide resonators with normal-to-zero dispersion, but that it may be most preferable for highly broadband comb generation due to the superior flatness of the comb in the SW regime, as well as the lack of a high-noise chaotic phase and multi-soliton formation as compared to its anomalous dispersion-based counterpart. In terms of physics, the zero-dispersion soliton can be seen as a bright pulse-like structure which constitutes a link between SW-based and soliton-based localised dissipative structure. Such a structure, the zero-dispersion soliton, defines itself in the regime where third-order dispersion becomes a dominant influence relative to second-order or conventional group-velocity dispersion, and where the dispersive wave components become an essential part of the structure rather than a perturbation. The fact that the ZDS may exist in either anomalous or normal dispersion [149] (referring to Fig. 3.7) presents an ambiguity in explanation for the structure's existence, between being two interlocked switching waves in normal dispersion, or being a multi-peaked dissipative soliton in anomalous dispersion. Further investigation and analysis of ZDS existence will be needed to gain full understanding on this. More widely, this experimental observation may trigger further fundamental research on the nature of dissipative Kerr solitons and switching waves under one umbrella.

In chapter 4, a comprehensive investigation of dissipative structure existence was presented in dispersion-folded Kerr cavities, with a fundamental spatial modulation of the dispersion. The source of additional spectral features is shown directly through 2D analysis of four-wave mixing pathways, in simulation via the slow vs fast frequency NDR diagrams, and in experiment by the comb reconstruction measurement. For the dissipative soliton, the appearance of resonant radiation was observed that we term as higher-order dispersive waves, ie. dispersive waves appearing quasi-phase matched to dispersive resonance curves (or Floquet bands) in FSR-folded space. This is termed as such in relation to conventional 'zeroth-order' dispersive waves that phase-match directly to the base level un-modulated dispersive resonance curve, such as dual-dispersive waves in resonators with quartic dispersion [153]. For the switching

wave structure, we showed direct generation of powerful satellite combs born of the Faraday Instability from the switching wave upper-state. These satellite combs are observed to be mutually locked in repetition rate with the core SW structure. However, the centre frequency of each satellite comb is not determined by this repetition rate, and is instead set fixed by the cavity dispersion, forming at a point up to an FSR/2 offset from the core comb. It was showed how the repetition rate is controllable by varying the injected pulse repetition rate. In terms of applicable value, if assuming that engineering highly flat dispersion is difficult in a given waveguide platform, deliberate modulation of the dispersion instead will automatically generate many higher-order dispersive waves that extend a soliton microcomb spectrum significantly wider beyond the point where the body of the comb disappears into the optical noise floor. Doing so deliberately may extend an already broad soliton microcomb further to the point where it can become octave spanning and able to be f - $2f$ self-referenced. Similarly, and more dramatically, assuming a fixed dispersion profile, dispersion modulation is shown here to effortlessly enable a switching wave microcomb to be extended by multiple times its base level bandwidth. Such combs could in the future find use in spectroscopy [184], telecommunications [13], astro-spectrometer calibration [37], and LiDAR [11]. For these reasons, longitudinal parametric modulation of the resonator waveguide may become a resource for spectrally extending Kerr microcombs.

As an epilogue, whereas these expanded systems were presented here individually with the aim of gaining understanding – pulse-driving, higher-order dispersive wave emission, zero-dispersion structures, Floquet dynamics, and Faraday instability – in the imminent future they can be taken together to achieve the ultimate in microcomb technology, including one true goal of an energy-dense, efficient, and low-noise octave-spanning microcomb at microwave repetition rates. In that vein, included is a brief epilogue (A) with a selection of more cutting-edge microcomb states that require further optimisation to carry on the work.

A Experimental microcomb catalogue

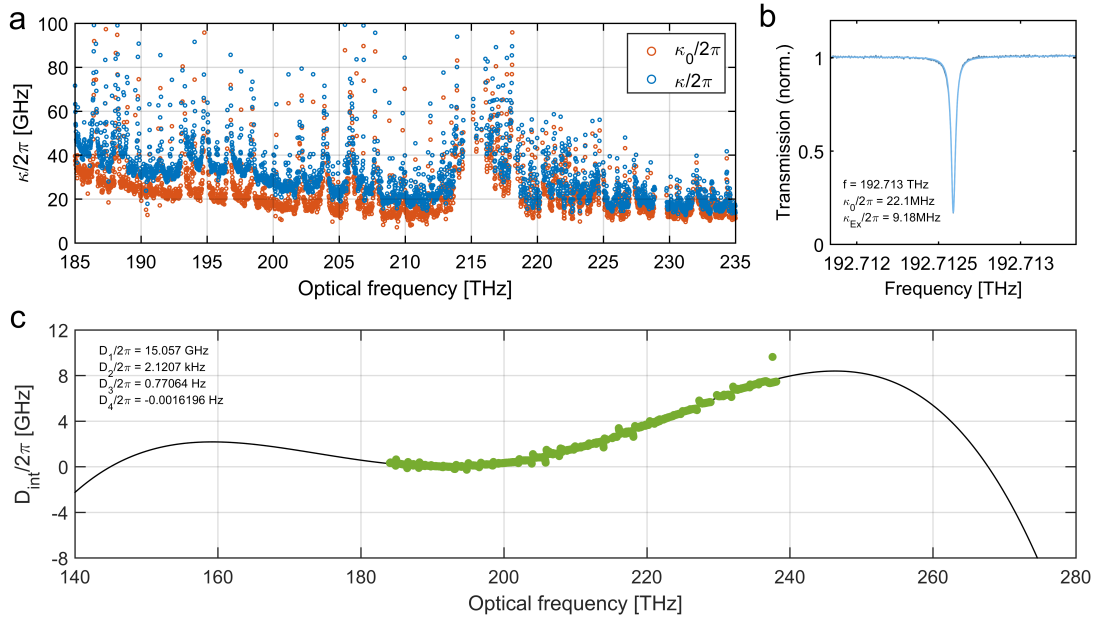


Figure A.1: **Octave-spanning dispersion and linewidth data. Device: D62-2.F8.C6.R4(TE).**

Appendix A. Experimental microcomb catalogue

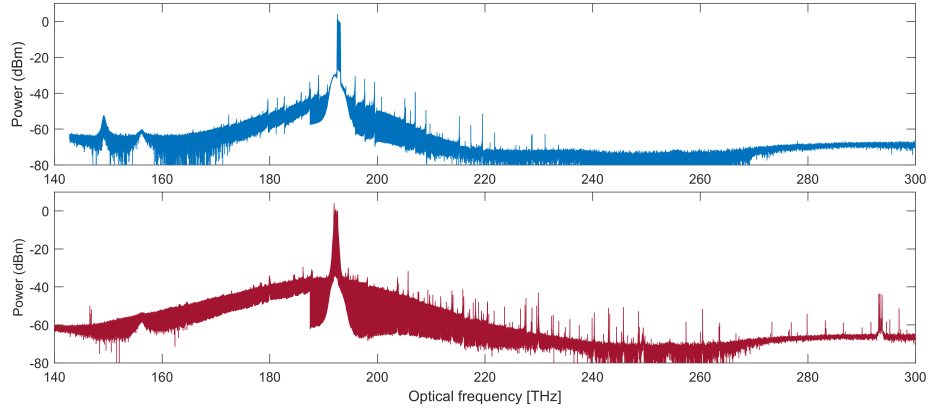


Figure A.2: **Octave-spanning soliton microcombs at 15 GHz line spacing.** (Top) Device: D62-2.F8.C6.R4(TE) (under-coupled). (Bottom) Device: D62-2.F8.C6.R6(TE) (over-coupled).

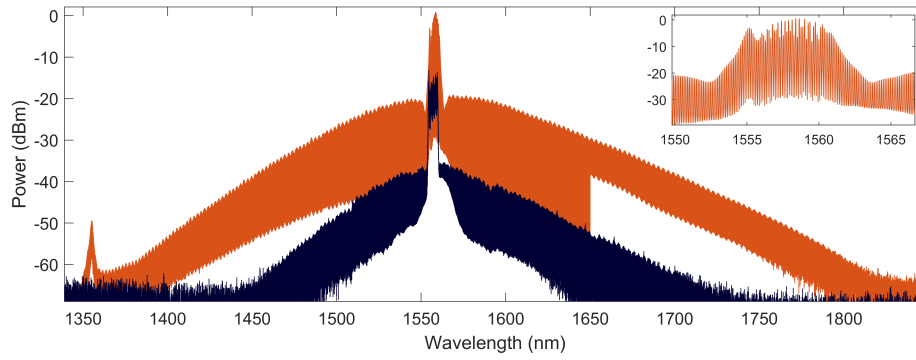


Figure A.3: **Strong soliton microcomb with high conversion efficiency.** (Orange) Device: D72-11.F2.C15.R3(TE). (Blue) For comparison. Device: D42-1.F8.G0.R7(TE).

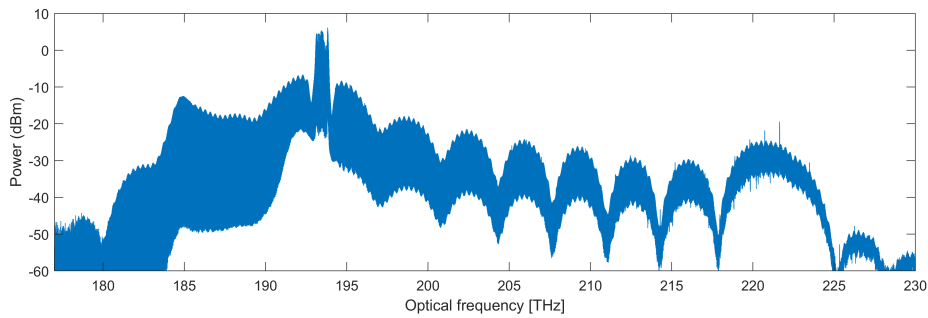


Figure A.4: **Strong zero dispersion soliton microcomb (ZDS⁽⁸⁾).** Device: D72-01.F3.C16.R3(TM).

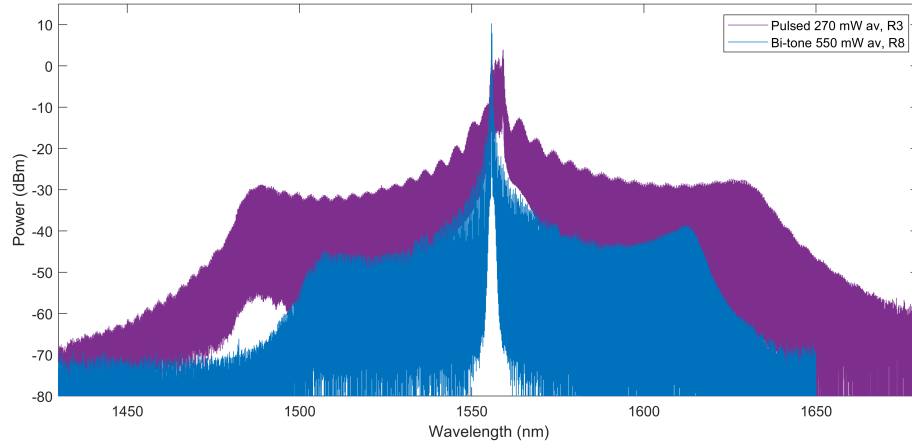


Figure A.5: **Strong switching wave microcomb.** Device: D42-1.F4.A0(TE). (Purple) Resonator R3, over-coupled, pulse-driven. (Blue) For comparison, resonator R8, critically coupled, 2-tone driven.

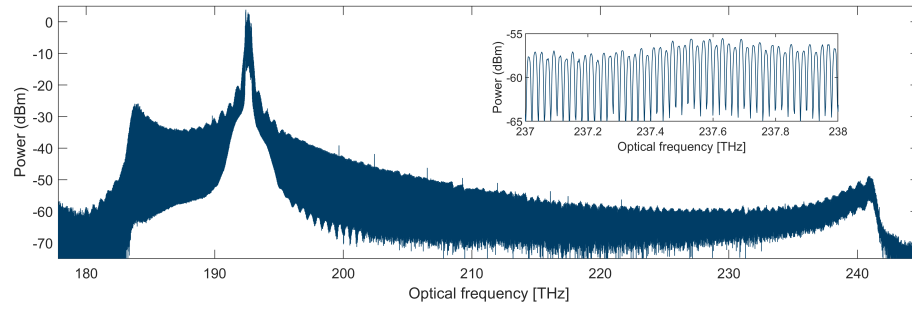


Figure A.6: **Broadband quartic dispersion switching wave microcomb.** Device: D42-1.F4.A0.R8(TE).

B Electro-optic comb components.

This chapter may be read in conjunction with chapter 2, section 2.2 to obtain a complete understanding of the EO-comb for use in the experiment presented in this thesis. This chapter specifically will comment on the parts used and their specific usage guide. See the diagram below for a breakdown and parts.

Summary

The 'Electro-optic comb' (EO-comb) comprises any microwave RF synthesiser plugged into a $\times 4$ RF splitter, going to 4 individual RF phase-shifters, to 4 RF amplifiers, to 4 RF filters (optional), to 3 low- $V\pi$ optical phase modulators and 1 amplitude modulator. It can convert one optical laser line into up to around 50, spaced by around 5 to 17 GHz. The output is a chirped waveform that can be compressed into pulses via dispersion. Having the amplitude modulator going flattens the EO-comb spectrum and extinguishes the residual optical CW when compressed into a pulse train. More on that in section 2.2.

Input RF

Currently, the input RF is provided by a Rhode & Schwarz SMB100A variable RF oscillator <20 GHz, <17 dBm. A 50-line EO-comb can be obtained with around 8-11 dBm seed power going towards the first $\times 4$ RF splitter. Right now, there is a 3-dB attenuator on the output for no particular reason other than to maximise seed power and minimise output noise. In that case the seed power is set to 11-13 dBm.

Phase shifters

Tune the RF phase shifters in order to align the RF waveforms on the 4 modulators to maximise the EO-comb line count at a fixed RF. Currently, the 4 phase shifters are a mix of models. The Weinshel phase shifter is tuned with a jewellery screw inside the housing. It's liable to break so be careful. The golden RF-Lambda phase shifters are tuned by rotating the barrel. Those 3 have a tuning range of around 200 degrees at 15 GHz RF, and go towards the phase modulators.

A Pasternak phase shifter is tuned by turning the knob, and it has a much wider tuning range of

Appendix B. Electro-optic comb components.

around 360 degrees at 15 GHz RF. It goes to the amplitude modulator, as full 360 degree tuning is very convenient. Changing the amplitude modulator phase by 180 degrees determines whether the chirp on the initial waveform is aligned with the dispersion stage, resulting in a pulse or not a pulse (see Fig. 2.11). You can check the four-wave mixing broadening through an output EDFA (>100 mW) to determine whether you have a pulse (Fig. 2.13).

Amplifiers and voltage/power

The RF amplifiers give out a maximum of around 35 dBm or 3 W RF. They tend to heat up. The RF signal sent to the amplifier going to the amplitude modulator is pre-attenuated by 12 dB since only 2 strong amplitude sidebands are needed. Each amplifier has a colour-coded electrical cable going to 2 double-power supplies. They are set to +15 V for the red connection on each amplifier.

Filters

Depending on the RF, the amplifiers are optionally followed by RF filters. There are bandpass filters available around 9-11 GHz and 13-15 GHz, and a low-pass until 17.5 GHz. They each should have a heat-sink attached.

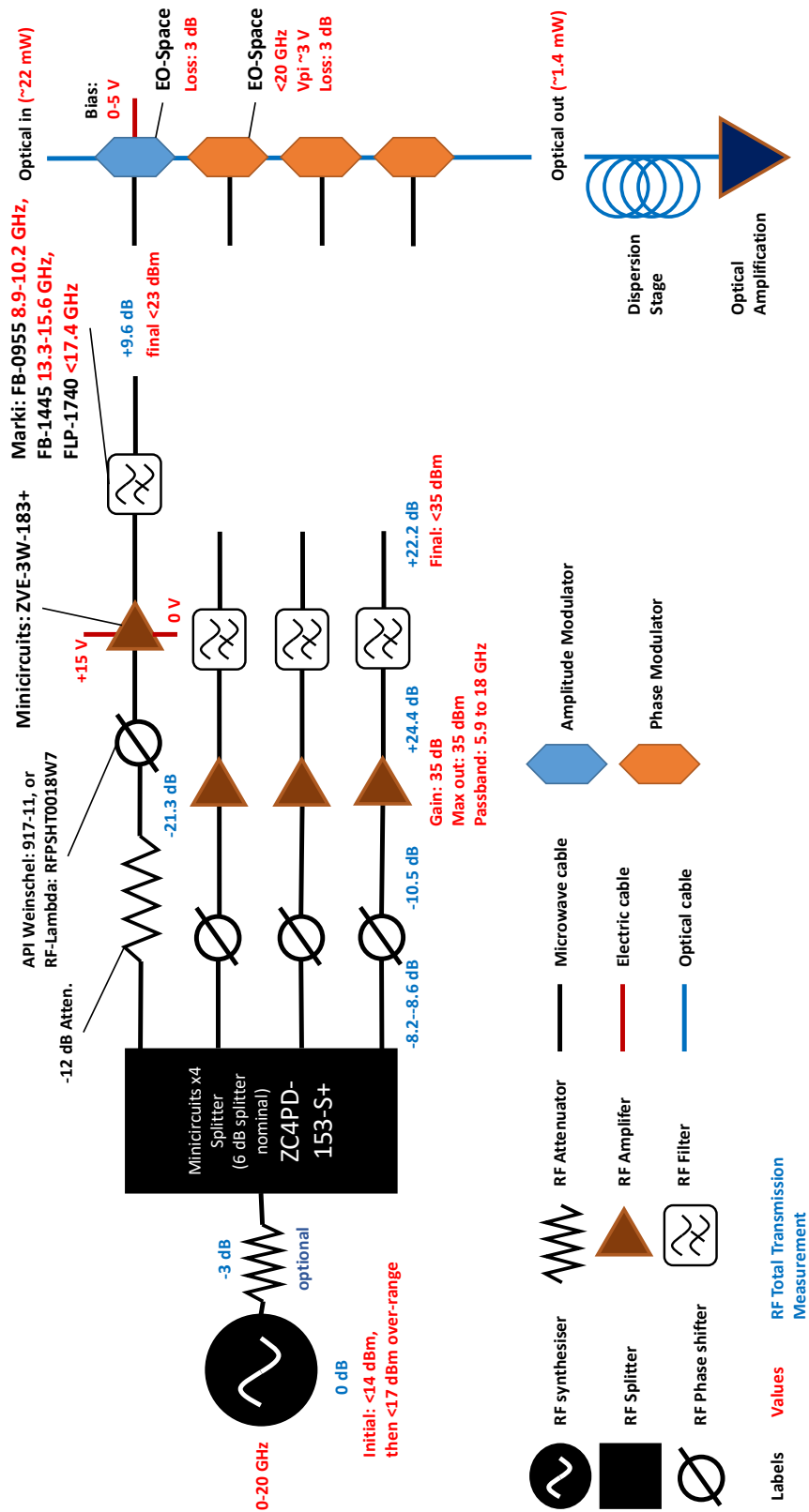
Optical

The 4 EO-space modulators are connected in series, and are arranged in neat loops with the ends labelled (A,B,C etc.). The modulators together suffer an overall optical loss of around 12 dB. If the Toptica CTL is used as input at max power, the output optical EO-comb power will be from 1-2 mW.

The amplitude modulator has a 0-5 V bias input, connected to the additional variable 5 V-out of one of the above two dual-power supply units. Tune this in order to flatten the EO-comb lines and maximise CW/pedestal-extinction for pulse generation.

In order to make pulses, there are SMF-28 fibre spools, and segments of dispersion compensating fibre (DCF) to fine-tune the dispersion. To have minimum duration pulses at 13-15 GHz, use 300 metres of SMF-28. To have such pulses at 10 GHz, use 600 metres of SMF-28 (see following page). Use segments of DCF, and then the exact RF power, to tune the pulse duration and residual chirp.

Switch on/off: 1. Laser; 2. RF Source; 3. RF Amplifier Power Supplies and Bias Voltage; 4. EDFA.



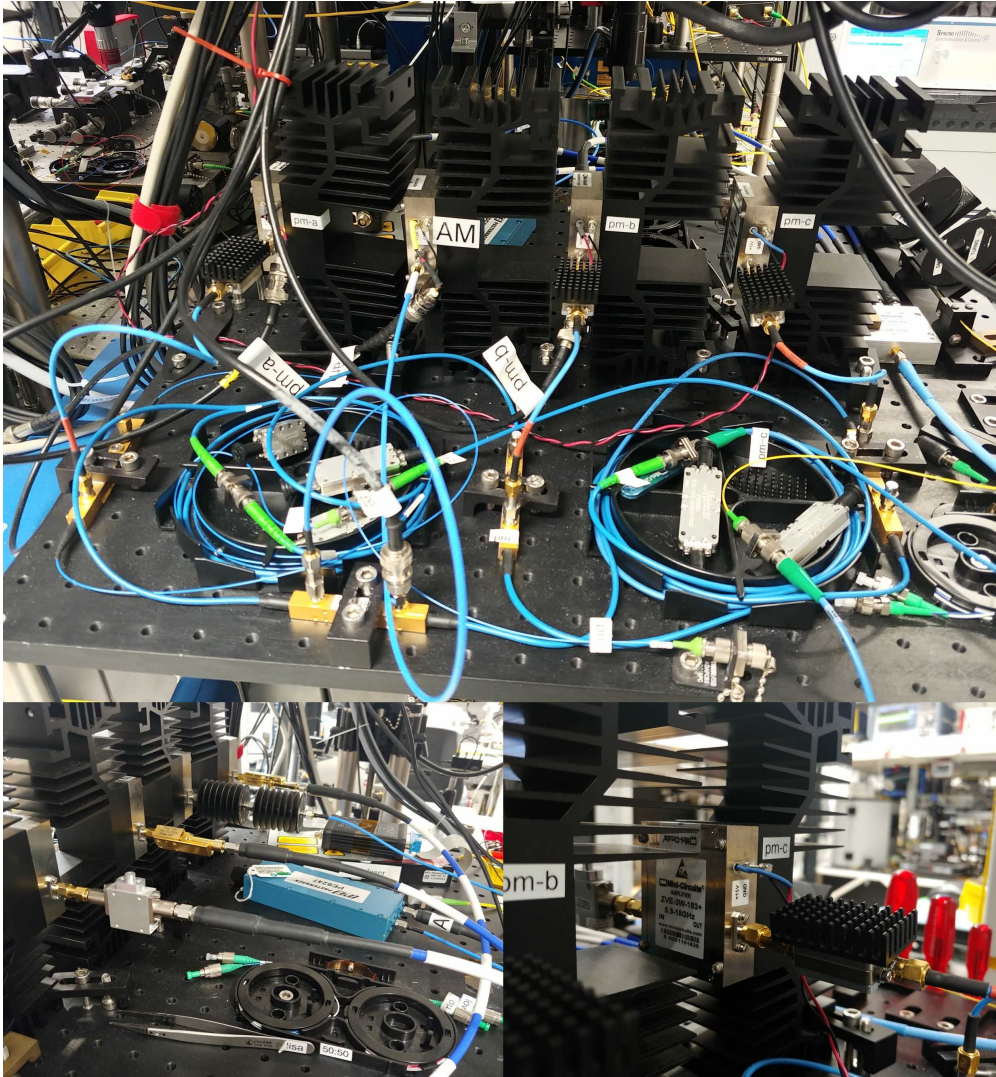


Figure B.1: **Photos of the EO-comb setup.** Top: The output of the 4 RF amplifiers directed towards 4 modulators connected in series fibre-optically. Bottom-left: Input side to the amplifiers. The source RF is split into 4 paths and sent to 4 different phase shifter. Silver (Weinshel), gold (RF-Lambda), and blue (Pasternak). Bottom-right: Close-up of the output filter for one pathway.

C Numerical method

This appendix will detail the numerical methods (based on Matlab) used in this thesis in the form of a written tutorial. The key functions will be briefly explained, and then we will go through a list of *demonstrative* example code scripts ('scenarios'). Together, these scenarios will give the reader the knowledge to replicate specific situations and models presented in this thesis and also, by understanding what parameters and dimensions to change, replicate any of the physics discussed in this work.

The simulation method used in this thesis comes in the form of single Matlab script files, named "lle_cavity_v4_..." for simulations in dimensionless units (Eq. 1.54), and "lle_SiNcavity_v4_..." for simulations in real experimental units (Eqs. 1.49 and 1.51). Each script file contains *all* the information to launch a specific simulation, so every simulation code is saved individually as "lle_cavity_v4_example_1_detail_1" variously.

The general philosophy for this arrangement is putting importance on:

1. **Modularity:** the ability to add and remove any features conveniently.
2. **Rapid feedback:** Live viewing and the ability to cancel and reconfigure simulations at any moment.
3. **Information:** Every parameter value in the workspace.
4. **Vision:** Everything should be plotted.

Throughout this appendix, parameters will be referred to interchangeably by their mathematical symbol (eg. ψ) or their Matlab name (eg. `psi`). For legacy reasons, some of these parameters and quantities may have names that do not match their symbols.

To access the demonstration scripts directly, see this Zenodo entry at [10.5281/zenodo.7939624](https://zenodo.org/record/7939624).

C.1 Functions and split-step method

The vast bulk of the simulation files consist of settings, parameters, inputs, dimensions, and plots programmed in the script. The few function files are detailed thus.

C.1.1 Split-step function

The following mirrors section 1.2.6. The method shown here prioritises simplicity over efficiency.

All work in this thesis on simulating the LLE or GLLE utilises the split-step Fourier method [62], where the LLE is considered analytically solvable over distances short enough that the dispersion and nonlinearity do not contradict each other, and hence are treated *separably*. The nonlinear step in particular is always taken in the time domain, allowing the use of the fast-Fourier transform (FFT) function which offers a level of computational efficiency over the pure coupled-mode equation [185]. This split-step method requires a large amount of steps to stay stable in comparison to supercontinuum generation methods typically making use of ‘ode45’ [186, 187], but here simplicity is prioritised over maximum efficiency. The linear and nonlinear steps may be found by separately solving the LLE with loss, detuning, and dispersion in one step, and nonlinearity and pump term in the second step as an inhomogeneous partial differential equation [66]. The Matlab function is as follows:

```
function C3 = LLE_splitstep(C1,L,S,g,x)

N = 1i*g*abs(C1).^2;

C2 = exp(x*N).*(C1 + S./N) - S./N;

C3 = fft(exp(x*L).*ifft(C2));
```

Here, the LLE is integrated step wise over distance x , g the nonlinear coefficient, and S the driving pump array. The linear operator

$$\hat{L} = i\hat{D} + \hat{K} \quad (\text{C.1})$$

as in Eq. 1.58, including all losses and detuning/dispersion. For when Raman scattering is enabled, the function is very similar but with the Raman contribution factored into the nonlinear operator:

```
function C3 = LLE_splitstepR(C1,L,S,g,fr,ChiR,x)

I = ifft(abs(C1).^2);
N = 1i*g*((1-fr)*abs(C1).^2 + fr*fft(ChiR.*I));
```



```
C2 = exp(x*N).*(C1 + S./N) - S./N;
```

```
C3 = fft(exp(x*L).*ifft(C2));
```

with Raman contribution factor f_R and the Raman response in the frequency domain $\tilde{\chi}_R^{(3)}$ from Fig. 1.13.

In order for the method to be accurate, x should be less than the dispersion length $L_D \approx (\beta_2 \Omega^2)^{-1}$ (for pulse bandwidths of Ω) and the nonlinear length $L_N = (\gamma P)^{-1}$ with P the peak power inside the cavity. Furthermore, for a very broadband simulation with thousands of comb lines to model, the step length has to be sufficiently short so as not to stimulate the growth of false sidebands at the edges of the spectral window. The rapid switching between dispersion step and nonlinear step creates a simulated ‘grating’, and enables quasi-phase matching between the pump and far away modes with very strong phase-shifts due to the dispersion. Ironically, this leads to ‘numerical’ Faraday instability, not unlike the phenomenon discussed in chapter 4. This is discussed further in section C.3.2.

C.1.2 Homogeneous Kerr cavity solution

When launching the integration simulation, time is saved by starting the background field amplitude at or close to the homogenous CW solutions to the LLE (Eq. 1.56), otherwise the cavity field amplitude will have to ‘ring down’ to the equilibrium solution before we start. The following function returns this solution from the roots cubic LLE Eq. 1.57 for dimensionless detuning Z and driving F :

```
function Hom = init_hom(Z,F,root0,root2)

Y = roots([1 -2*Z (Z^2+1) -F]);
if Z>sqrt(3)
    Hom = sqrt(F)/(1+1i*(Z-Y(root2)));
else
    Hom = sqrt(F)/(1+1i*(Z-Y(root0)));
end
```

Depending on Z and F , ie. whether the cavity is bistable, the roots may be real or imaginary and at different array indices, and we only want either the high stable real solution ψ_H , or the low stable real solution ψ_L (see Fig.1.12 or 3.2). See how the function is called in the main script below.

C.1.3 Live plotter

This function is purely a matter of personal preference. As said above, live feedback is important because it allows us to ensure a longer simulation is proceeding stably. Often times

mistakes are made, and if there is a problem part way through the recording it is useful to be able to witness this and cancel the simulation so it can be fixed. Also, even if there is no mistake in the settings dissipative solitons can behave ‘statistically’ (or chaotically), and some outcomes are a matter of chance. Observing a simulation live also makes the process feel much more like a real experiment and, importantly, gives you an intuitive grasp of long term *dynamics* that might not be well grasped in reading the ‘birds-eye-view’ 2-dimensional time and frequency heat-maps. The function is as follows:

```
function [info_label,graph1,graph2,graph3] = cavity_view_v4(figre,...
view_type,dat,axinfo)
% Setting up simulation view screen
% (Miles Cavity Sim v4.0)
% Date: August 2019
% Miles Anderson

figure(figre)
switch view_type
    case 'standard'
        set(figre,'position',[50 50 640 480])
        subplot(211)
        graph1 = stem(dat.mode_x,dat.mode_y,'marker','.', 'basevalue',...
axinfo.mode(3));
        axis(axinfo.mode)
        ylabel('Spectral Power (dB)')
        xlabel(axinfo.zlabl)

        info_label = title(axinfo.labl);

        subplot(212)
        graph2 = plot(dat.space_x,dat.space_y);
        axis(axinfo.space)
        ylabel('Field power')
        xlabel('Fast time')

    case 'amplitude'
        set(figre,'position',[50 50 640 720])
        subplot(311)
        graph1 = stem(dat.mode_x,dat.mode_y,'marker','.', 'basevalue',...
axinfo.mode(3));
        axis(axinfo.mode)
        ylabel('Spectral Power (dB)')
        xlabel(axinfo.zlabl)

        info_label = title(axinfo.labl);

        subplot(312)
        graph2 = plot(dat.space_x,dat.space_y);
        axis(axinfo.space)
        ylabel('Field power')
        xlabel('Fast time')
```

```
        subplot(313)
        graph3 = plot(angle(dat.amplitude),abs(dat.amplitude),'k. ');
        ylabel('amplitude')
        xlabel('phase')

    otherwise
        error('wrong')
end
```

There are two modes. The first live-plots the instantaneous fast frequency envelope (in the form of a stem plot to emphasise the discrete comb nature), and the fast time domain optical field. The second adds a third plot of a single point in the fast time dimension in the complex domain, which may be used to observe the type of dissipative soliton breathing cycles observed in the following works: [79, 88, 87]. Only the first mode is ever used throughout this thesis, however. See below how the function is called.

C.2 Script for simulating the dimensionless LLE & basic scenarios

C.2.1 Program guide and plotting the output

Section 1 (Scan over resonance first example)

The script for simulating the dimensionless LLE is more simple than with real experimental parameters, and the latter is based on exactly the same procedure. The following example starts with generating a crowd of dissipative solitons with a CW pump via scanning the centre frequency (ie. detuning) ‘up’ the tilted Kerr resonance into the region of bistability, as is usually the scenario in experiment[99]. In general this is a fundamental check of the LLE for microcomb simulations.

The procedural code is divided into sections. Many lines are commented out because they are not necessary for the first run, or are for optional observations. After explaining all the sections, running the code, and observing the result, we can then change certain values and settings to observe different dynamics. To begin:

```
% Script for Lugiato-Lefever Split-step Fourier live calculation
% (Miles Cavity Sim v4.1)
% Date: March 2022
% Miles Anderson

% Dimensionless units, (see Dr. Erwan Lucas thesis 2019)

% This script (thesis demo): Excite plain dissipative soliton with d3 tail,
% with default synchronisation.

%% Section 1 - Key parameter definitions
```

Appendix C. Numerical method

```
% Define dimensionless simulation width (dispersed fast time, or angular)
Tw = 24;      % fast time width
N = 2^9;      % number of points

% intracavity field desynchronisation coefficient
% (eg. thermal noise, dispersive wave)
d1 = 0;
% d1 = d1+d_p1;
% d1 = -0.46875;

eta = [0.00 0.05 -1.0 d1 0]; % dispersion operator

F0 = sqrt(10);      % dimensionless forcing term [ sqrt(P/P_thresh) ]
d_p0 = 0;           % desynchronisation rate of drive envelope
coup = 1;           % external coupling factor
% d_p0 = d_p0+d_p1;

% Define detuning boundaries [ 2*delta_omega/kappa ]
zeta0 = -2;         % start
zeta2 = 14;         % finish

% Define simulation duration, in photon lifetime [ 2/kappa ]
if zeta2~=zeta0
    t_end = 20*abs(zeta2-zeta0); % rate of change for scanning
else
    t_end = 20;          % for stationary
end

% Define simulation frequencies
h = 2^-9;           % step length [ fraction of photon lifetime ]
store = 1/h*2^-3;    % data storage period [ no. simulation steps ]
view = store*2^1;     % real-time graphing period [ no. simulation steps ]
plot_time = 0.01;    % plotting duration [ seconds ]
sj = 0;             % initial step for storing (for intracavity evolution)

% Parametric modulation
eta_p = 1/h*2^-4;     % "modulation" time period (for Faraday Instab. etc.)
eta_a = 0.0;          % waveguide modulation amplitude
eta_phi = 0;          % waveguide modulation phase
```

In the first section, we set the fast time span ($Tw:\Delta\tau$) to 24, sufficient to contain several dissipative solitons, where the typical soliton has a region of influence around ~ 1 . This time width needs about $N=2^9$ simulated modes in order to contain the soliton spectrum within the fast frequency window (as we shall see in Fig. C.1), so that it does not allow aliasing artefacts. We next define the dispersion operator η , which is an array of coefficients d_ℓ counting down to $\ell = 0$ on the right end. For anomalous dispersion $d_2 = -1$ and $d_3 = 0.05$ to make things interesting, and to start off with $d_1 = 0$. We define a scan from $\zeta_0 = -2$ to 14. We define a total slow time duration t_end so that $\Delta t/\Delta\zeta_0 = 20$. If the start and finish ζ_0 are equal ('stationary'), then we have a $t_end=20$. This is a sufficient time period for a dissipative soliton to relax

towards equilibrium.

The next part defines the simulation step size, the sampling or storage period, and the live-viewing period in steps. The step size h is set to 2^{-9} , which corresponds to a kind of evaluation or ‘frame rate’ $f_r = 512$ (1/h) per photon lifetime. `store` is set here to be 64 steps, or $1/8^{\text{th}}$ of a photon lifetime, corresponding to a ‘sampling rate’ $f_s = 8$, sufficient to capture breathing dynamics. The main reason to have sampling at all, rather than just saving every single evaluated step, is that typical simulation runs may take millions of steps each having 2^9 points in width (or even up to 2^{14} for some octave-spanning microcomb simulations). Saving every frame may consume Matlab’s memory and make plotting slow. The view period is set to live-plot every second sample. For long running simulations, the view period should ideally be set high enough so that it takes a minority of processing time, so that you know it isn’t impacting the final simulation time.

The part after this concerns parametric modulation of the cavity properties, as explored in chapter 4. The values are set to zero here, but we’ll activate them further below.

Section 2

```
%% Section 2 - Settings
```

```
% Scenario options
```

```
init = 1;           % initial state yes/no
excite = 0;         % hard excitation yes/no
exctr = 1;          % excite step number
pulsed = 0;         % temporally-structured driving function yes/no
```

```
% Additional settings
```

```
external = 0;       % acquire spectrum outside resonator yes/no
% input field (pulse drive) desynchronisation yes/no (eg. rf noise)
desynch = 0;
```

This brief section contains a few yes/no options, the first two being important. When `init` is true, the simulation will begin with the optical field ψ initialised to the homogenous CW solution. If `init` is not true, the field ψ (psi) will stay as it is in the Matlab workspace, assuming that you are following on from a previous initial run. If `excite` is true, then the analytic solution of a dissipative soliton (or an switching wave (SW) or anything) will be added to the intracavity optical field, sometimes referred to as “hard excited” as opposed to “soft” excitation of solitons via scanning/sweeping the detuning.

When `pulsed` is true, the pump function $F(\tau)$ will be one of our chosen pulsed or modulated functions, otherwise it will be CW. The option `external` refers to recording the field that exits the resonator rather than the intracavity field ψ . This is more relevant to the experimental LLE next section. If `desynch` is true, then the driving function $F(\tau)$ will have its own defined drift velocity, otherwise it stays at the centre of the fast time window τ . This is similar to, but not to

Appendix C. Numerical method

be confused with, the drift velocity d_1 imparted to the intracavity field ψ .

Section 3

```
%% Section 3 - Dimensions

% Space/time dimensions
nu = (0:N-1)-N/2;          % mode index
T = linspace(-Tw,Tw,N+1);  % fast time
T = T(1:N);                % the end-piece
dT = T(2)-T(1);            % fast time step
f = nu/(N*dT);             % fast frequency

r = round(t_end/h);        % no. of steps
rs = floor(r/store);       % no. of steps stored/sampled
t = (1:rs)*h*store;        % slow time

dt = h*store;              % slow time step
rf = ((0:rs-1)-rs/2)/(rs*dt); % slow frequency

% RF noise
nf = 0.000001;             % added Gaussian white noise background amplitude
n_band = max(rf);          % injected noise bandwidth
n_trace = lowpass(randn(1,r+store),n_band,1/h,...
    'ImpulseResponse','iir','Steepness',0.9); % noisy trace over slow time
zeta_n = 0.0;              % detuning noise deviation amplitude
F_n = 0.0;                 % pump amplitude noise deviation

% Drive dimensions
% linear detuning function + slow time noise
zeta = linspace(zeta0,zeta2,r) +zeta_n*n_trace(1+store:r+store);
% constant pump drive amplitude + slow time noise
Ft = F0*ones(1,r) +F_n*n_trace(1+store:r+store);
% Ft = F0*(1:r)/r;        % linear pump rise (optional example)

% Slow-time drive envelope desynchronisation rate
d_p = d_p0*ones(1,r); % constant desynch

% Scaling
t_scale = 1;
y_scale = 1;
```

This section defines the time and frequency dimensions according to the above-set time durations in a way that is hopefully self-explanatory. Noise levels given to the simulation is also defined here, and this will be described further below. The values of detuning ζ range linearly from the start and finish values set above and, in this case, the pump amplitude is set to be a constant.

Section 4

```

%% Section 4 - Initial condition

% CW waveform
CW = ones(1,N);

% Pulse waveform
Tp = 16;          % fast time pulse drive width
d2L = +20;        % pulse drive pre-dispersion factor

PA = exp(-T.^2/Tp^2);          % Gaussssian pulse
PA2 = rectangularPulse(-Tp/2,Tp/2,T) +eps;    % Rectangle pulse
% PA = (exp(1i*pi*T*1/(2*Tw))+exp(-1i*pi*T*1/(2*Tw)))/2;    % Bi-tone
% PA = (1+exp(2i*pi*T*1/(2*Tw))+exp(-2i*pi*T*1/(2*Tw)))/3; % Tri-tone

% % sinc pulse (freq. domain)
% PB = (f>-0.5/Tp)&(f<0.5/Tp);
% PB = PB/sum(PB);
% PA = fftshift(fft(fftshift(PB)));

% Pulse pre-dispersion
Dp = ifftshift(1i*d2L*(2*pi*f).^2);
PB = ifft(PA).*exp(Dp);
PA = fft(PB);

% % Additional phase modulation
% d_mod = +0.75i*pi;
% PA = PA.*exp(d_mod*cos(T*pi/Tw));

% Initial solution to the CW LLE, set roots to select branch
psi_h = init_hom(zeta0,Ft(1)^2,3,1);
psi_l = init_hom(zeta0,Ft(1)^2,3,3);
% psi_h for high state, psi_l for low state
psi0 = psi_l;

% Resonant radiation conditions (up to D4)
D_psi_l1 = -eta(4)*(2*pi*f) +eta(2)*(2*pi*f).^3 ...
    -sqrt( (zeta2-eta(3)*(2*pi*f).^2-2*abs(psi_l)^2).^2 -abs(psi_l)^4 );
D_psi_l2 = -eta(4)*(2*pi*f) +eta(2)*(2*pi*f).^3 ...
    +sqrt( (zeta2-eta(3)*(2*pi*f).^2-2*abs(psi_l)^2).^2 -abs(psi_l)^4 );
D_psi_h1 = -eta(4)*(2*pi*f) +eta(2)*(2*pi*f).^3 ...
    -sqrt( (zeta2-eta(3)*(2*pi*f).^2-2*abs(psi_h)^2).^2 -abs(psi_h)^4 );
D_psi_h2 = -eta(4)*(2*pi*f) +eta(2)*(2*pi*f).^3 ...
    +sqrt( (zeta2-eta(3)*(2*pi*f).^2-2*abs(psi_h)^2).^2 -abs(psi_h)^4 );

% Driver, initial run or not, CW or not
if init
    if pulsed
        FT = PA;
    else
        FT = CW;
    end
end

```

Appendix C. Numerical method

```
end
end

% Linear operator [ loss, dispersion ]
D = -1 + 1i*polyval(eta,2*pi*f);

% Manual/arbitrary mode-shifts
% D(N/2+30) = D(N/2+30) + 20i;      % mode-crossing
D = ifftshift(D);
% D(1) = D(1) + 1i*4;                % pump-mode shift

% Initial fast time field noise
noise = nf *h *randn(1,N) .*exp(1i*pi*rand(1,N));
psi0 = psi0 + noise;

% Initial field if this is a first run, else psi carries on from previous
if init
    psi = psi0.*FT;
end

Fr = FT*Ft(1);      % total pump field [ profile * amplitude ]

% Get initial spectrum, 'outside or inside'
if external==1
    psi_f = ifftshift(ifft(Fr-sqrt(coup)*psi));
else
    psi_f = ifftshift(ifft(psi));
end
```

Section 4 creates the initial state of $\psi(\tau)$, the driving field $F(\tau)$, and the linear operator (here marked as D), according to the settings given at the top. If the pulsed option was true, the pulse drive envelope PA is defined here specifically. It may be Gaussian, rectangular, modulated, sinc, or anything. These options are shown here commented out, expect for the default Gaussian. Importantly, pre-dispersion to the pulse ie. *chirp* (as described in section 2.2 and 2.3.2) is also applied to the pulse function to apply a realistic or desired residual phase curvature, in this case negative. This will be relevant in the next part when pulse driving is active. For now we have CW.

The two stable CW states ψ_L (psi_l) and ψ_H (psi_h) of the bistable cavity are found next by using the function defined above, and in this instance we select an initial value of ψ to be the low state so that we can later have hard excitation of a single dissipative soliton. But for now, hard excitation is off regardless.

The resonant radiation conditions (RRC), described in section 1.3 and 4.1.1 are calculated here just for our information's sake.

Next, the pulsed option is applied to the driver envelope. After that, the linear operator is defined with loss set to -1 and the dispersion operator defined as a polynomial from the

values set at the top. At this point, completely arbitrary mode shifts can be applied to the dispersion operator, for instance, to mimic the mode crossing behaviour resulting in soliton crystal state formation shown in Fig. 2.6[104], or intermode breathing[188] for example. The value located at the CW pump index can also be shifted to reproduce the type of dramatic results of spontaneous and super-efficient dissipative soliton formation described in very recent work[163, 107], or for “dark pulse”, “platicon”, or SW front stabilisation shown in many works[133, 131, 183, 135, 189].

If the `init` option is checked, then the optical field $\psi(\tau)$ (`psi`) is set/reset to the initial state. The initial driving pump array is set, and the first spectral envelope is obtained.

Section 5

```
%% Section 5 - Graphing Prep

% Axes limits
SLimit = [-100 0];           % Spectrum y-limit (dB)
if max(zeta)>3                 % Fast time y-limit, if there are high amplitude solitons
    PLimit = [0 2.5*max(zeta)];
else
    PLimit = [0 4*F0];
end
fLimit = [min(f) max(f)];
TLimit = [min(T) max(T)];

% Setting up data to record
Psi = zeros(rs,N);           % fast time vs. slow time array
Psi_f = zeros(rs,N);         % fast frequency vs. slow time array
peak = zeros(1,rs);          % soliton peak for phase space analysis
beat_amp = zeros(1,rs);      % soliton beatote analysis
% k = N/2;                    % initial peak location (for breathing analysis)

% Plot info and data containers
PlotData = struct('space_x',T*t_scale,...
    'space_y',[abs(psi).^2;abs(Fr).^2]*y_scale,...
    'mode_x',f,...
    'mode_y',10*log10(abs(psi_f).^2*y_scale),...
    'amplitude',0);
PlotAxInfo = struct('space',[TLimit*t_scale PLimit*y_scale],...
    'mode',[fLimit/t_scale SLimit+10*log10(y_scale)],...
    'labl',['t_{ph}: 0; zeta = ' num2str(zeta(1))],'zlabl','Frequency');

% Initialise live-view figure
figure(1);clf
set(gcf, 'Renderer','painters')
[info_label,graph1,graph2] = cavity_view_v4(1,'standard',PlotData,PlotAxInfo);
% [info_label,graph1,graph2,graph3] = cavity_view_v4(...
%     1,'amplitude',PlotData,PlotAxInfo); % for breathing analysis
```

Appendix C. Numerical method

```
% Check dispersion/resonant conditions
figure(7)
plot(f,-imag(fftshift(D)), 'k.')
% plot(f,-D_psi_l1, 'g.', f,-D_psi_l2, 'k.', f,-D_psi_h1, 'b.', f,-D_psi_h2, 'r.')
ylabel('d_{int} (arb.)')
xlabel('Fast frequency (arb.)')
grid
% Check pulse drive amplitude/phase
figure(8)
yyaxis left
plot(T,abs(F0*FT).^2)
ylabel('Intensity')
yyaxis right
plot(T,angle(FT))
ylabel('Phase')
xlabel('Fast frequency (arb.)')
grid
% Check injected RF noise
figure(9)
subplot 211
plot((1:r)*h,zeta)
subplot 212
histogram(zeta)
```

The final section before the actual process starts deals with initialising data containers and plots. Firstly, the axis limits of the live-view are set for most convenient observation. Then, zero arrays containing the time and frequency domain frames to be saved are created. After this, axis info and the initial fields are put in structures for the `cavity_view_v4` function. Importantly, the function is only called once here at the start, but it returns the handles containing the YData of the plot graphics so that they can be updated directly inside the for-loop below.

For double-checking, the following plots are made before the process starts: the integrated dispersion (or the RRCs), the pulse drive intensity and phase, and the noisy trace of whichever parameter you choose (in this case detuning) over slow time and in histogram.

Section 6

```
%% Section 6 - Run

% return          % comment out if you don't actually want to run

% Actually run, for every simulation step
for j=1:r

    % Hard excitation
    if (j==exctr&&excite)
%         psi = psi + PA2*(psi_h-psi_l);           % excite SW fronts
```

C.2 Script for simulating the dimensionless LLE & basic scenarios

```
psi = psi + sqrt(2*zeta(j))*...
    sech(sqrt(zeta(j))*(T+0.0*Tw))*exp(0.5*1i); % excite soliton
end

% Driver definition this step
Fr = FT*Ft(j);

% Parametric modulation cycle
dD = 1 + eta_a*cos(eta_phi +2*pi*mod(j,eta_p)/eta_p);

%% actual process %%
psi = LLE_splitstep(psi,real(D)+1i*imag(D)*dD-1i*zeta(j),...
    Fr,1,h);

% Storage sampling / recording
i = j+sj;
if mod(i/store,1)==0
    Psi(i/store,:) = psi; % sample field
%     [~,k] = max(abs(psi)); % peak location for breathing analysis
%     peak(i/store) = psi(k); % for breathing analysis

    % sample spectrum (inside/outside)
    if external==1
        psi_f = ifftshift(ifft(Fr-sqrt(coup)*psi));
        psi_f2 = ifft(abs(Fr-sqrt(coup)*psi).^2); % power spectrum
    else
        psi_f = ifftshift(ifft(psi));
        psi_f2 = ifft(abs(psi).^2); % power spectrum
    end
    Psi_f(i/store,:) = psi_f;
    % microcomb RF repetition rate beatnote signal amplitude
    beat_amp(i/store) = psi_f2(2);

end

% Live-viewing
if mod(i/view,1)==0

    graph1.YData = 10*log10(abs(psi_f).^2*y_scale);
    graph2(1).YData = (abs(psi).^2*y_scale);
    graph2(2).YData = (abs(Fr).^2*y_scale);
%     graph2(2).YData = diff(angle(psi)+2*pi)*N;
%     graph3.XData = angle(peak); % for breathing analysis
%     graph3.YData = abs(peak); % for breathing analysis
    info_label.String = ['t_{ph}: ',num2str(round(j*h)),...
        ' ; \zeta = ',num2str(round(10*zeta(j))/10)];
    pause(plot_time)

end

% Desynchronisation shift
if desynch
```

Appendix C. Numerical method

```

    FT = fft(fftshift( ifftshift(ifft(FT))...
        .*exp(2j*pi*f*d_p(j)*h) ));
end

% Injected fast time noise per simulation step
noise = sqrt(nf *h) *randn(1,N) .*exp(1i*pi*rand(1,N));
psi = psi + noise;

end

% return      % to skip post-processing

```

Here is the looping process, for every step of the LLE over slow time. Firstly, if the `excite` option is true then the structure of choice is added to the field (“hard-excited”), in this case the analytical solution of a dissipative soliton existing at this value of ζ_0 and F , according to Eq. 1.71. Commented out is the rectangular approximation for an SW pair (‘platicon’, section 1.3.3). Since either of these profiles are analytic approximations of the LLE, and not the true equilibrium solutions, they may take a few photon lifetimes to relax to equilibrium. In case the drive amplitude peak or temporal position is changing every step, it is re-defined next. The next part defines the parametric modulation amplitude (represented as $1 + \Delta$ in chapter 4), which here cycles sinusoidally over the “FSR” period (`eta_p`) defined earlier. In the LLE step below, it is applied to the dispersion operator, but it could equally be applied to any value of choice eg. the nonlinear coefficient. In this first simulation it has no effect since `eta_a=0`.

The actual LLE step is called next, taking the field, the step size, the pump, and all the parameters defined up until this point.

Below this the storage (sampling) part is called. If parametric modulation is enabled, it might be interesting to sample the dissipative structure at a different ‘phase’ of its journey around the cavity, hence the integer offset `sj` to the step counter, set earlier. For every store period, the fast time and fast frequency domain fields are saved, and the RF repetition rate ‘beatnote’ amplitude (`beat_amp`, in the complex domain) is taken from the first mode of the power spectrum, symbolically speaking

$$p(t) = [P_1 + \delta P(t)] e^{i\delta\Phi(t)} = \mathcal{F}[\tilde{\psi}^* \tilde{\psi}]_{\mu=1} \quad (\text{C.2})$$

with signal amplitude P_1 , signal amplitude noise $\delta P(t)$ and phase noise $\delta\Phi(t)$. This replicates the experiment where the power envelope of the microcomb light is converted to current on a fast-photodiode, which has a responsive speed faster than the repetition rate, and sampled as an ‘in-phase/quadrature’ signal on the ESA.

Next, the live-viewing part is called. Since the live-view plot has already been created, we just updated the `YData` directly from the plot objects provided earlier. Doing this is *much* faster than calling the `plot` function every step. We also update a title label to show the current

detuning and normalised slow time. This label is how we see how far our progress in the simulation is.

If the `desynch` option is true, then the drive profile is shifted laterally in fast time $F(\tau) \rightarrow F(\tau - \tau_0)$, where the per-photon offset time $\tau_0 = d_p(j) * h$. This part is more relevant in the experimentally-valued simulation described in the next section, where the drive pulse has timing 'jitter'. In this example, it is off. Finally, white-Gaussian noise is recalculated and added to the field in proportion to the step size, and the whole loop continues until finished. The simulation can be cancelled part of the way through on Matlab by pressing ctrl-c, but since this is a script, all of the field data sampled until that point is still ready to be plotted.

Plotting the output, including slow vs. fast frequency, and noise transfer - Section 7

```
%% Section 7 - Post report

% Find average drift of single soliton over total simulation run
[~,mi] = max(abs([Psi(1,:);Psi(rs,:)]),[],2);
To1 = (T(mi(1))-T(mi(2)))/(rs*store);
d_p1 = To1/h;          % get necessary shift to synchronisation

% Find location of moving switching wave front
[~,TxR] = max(heaviside(T(2:end)).*abs(diff(abs(psi).^2)));
SWR_loc = T(TxR);

% "Probe frequency" location for simulated heterodyne comb mode
% measurement
f_prob = 3.0;
[~,mu_dex] = max(1./abs(f-f_prob));

% Necessary window functions to prevent spectral leakage of processed
% noise measurement output
WinLong = window(@hann,rs);      % slow time window
WinShort = window(@hann,N);      % fast time window
% WinLong = ones(rs,1);
% WinShort = ones(N,1);

% Special windows to isolate specific structures in fast time, such as SW
% fronts, optional
WinSlice = 1;                    % field window on/off
T_win = 20;                      % window width
% WinSlice = exp(-T.^2/T_win.^2).^2; % Gaussian window
% WinSlice = exp(-(T-SWR_loc).^2/T_win.^2).^2; % Gaussian window shifted
% WinSlice = fftshift(WinSlice);
% WinSlice = heaviside(T);        % One-sided window

% Process output to take into account external coupling or not, measure
% overall energy, and generate frequency vs. frequency plot ("Nonlinear
% Dispersion Relation")
if external==1 % for getting field exiting cavity
```

Appendix C. Numerical method

```
FTt = Ft((1:rs)*store)*FT; % stored pump function over slow time
Psi_out = (FTt-sqrt(coup)*Psi); % outside fast time field array
% total output field energy
CP = 1/N*trapz(abs([Psi_out,Psi_out(:,1)]')).^2);
% slow freq. vs. fast freq. analysis including windowing
Psi_Ff = fftshift(ifft(WinLong.*ifft(Psi_out.*WinShort'.*WinSlice,[],2)));
else
% total intracavity field energy
CP = 1/N*trapz(abs([Psi,Psi(:,1)]')).^2);
% slow freq. vs. fast freq. analysis including windowing
Psi_Ff = fftshift(ifft(WinLong.*ifft(Psi.*WinShort'.*WinSlice,[],2)));
end
% spectrum of isolated structure only (optional)
psi_fc = ifftshift(ifft(Psi(end,:).*WinSlice,[],2));

% Sampling input noise traces
zeta_amp = zeta(1:store:end); % detuning noise vs. slow time
zeta_sp = fft(zeta_amp)*dt; % detuning noise spectrum
F_amp = Ft(1:store:end); % pump amplitude noise vs. slow time
F_sp = fft(F_amp)*dt; % pump amplitude noise spectrum
beat_sp = fft(detrend(angle(beat_amp)))*dt; % beatnote phase noise
beat_psd = fftshift(fft(WinLong'.*beat_amp)*dt); % rep. rate beatnote
NT = abs(beat_sp)./abs(zeta_sp); % noise transfer

if zeta2>zeta0 % if detuning is swept, plot based on detuning
Zeta = linspace(zeta0,zeta2,rs); % sampled detuning
Y = Zeta;
ylab = '\zeta_0';
else % if detuning is constant, plot based slow time
Y = t;
ylab = 't_{ph}';
end

% Plotting
% Evolution of spectral envelope over slow time
figure(2);
imagesc(f,Y,10*log10(abs(Psi_f).^2));colormap(turbo);
caxis(SLimit)
set(gca,'ydir','normal')
ylabel(ylab)
xlabel('Fast frequency')
cob = colorbar; ylabel(cob,'Power (dB)')

% "Space-time" figure (slow time vs. fast time)
figure(3);
imagesc(T,Y,(abs(Psi).^2).*WinSlice);colormap(turbo);%caxis([-1 1])
set(gca,'ydir','normal')
ylabel(ylab)
xlabel('Fast time')
cob = colorbar; ylabel(cob,'Power')
```

C.2 Script for simulating the dimensionless LLE & basic scenarios

```
% Total/average energy over time
figure(4);
plot(Y,CP)
xlabel(ylab)
ylabel('Power out')

% "Energy-momentum" slow frequency vs. fast frequency figure
figure(5);clf
% plain heat-map
imagesc(f,2*pi*rf,10*log10(abs(Psi_Ff).^2));colormap(hot)
% % 3D view
% surf(f,2*pi*rf,10*log10(abs(Psi_Ff).^2));colormap(turbo);shading interp
% constant peak level for noise/linewidth analysis
% imagesc(f,2*pi*rf,10*log10(abs(Psi_Ff).^2)...
% -ones(rs,1)*max(10*log10(abs(Psi_Ff).^2));colormap(hot);

% % Shifting slow frequency point of view from optical line to resonance line,
% % only valid for static detuning
% Z = fft(fftshift(Psi_Ff));
% MM_Ff = fftshift(iffshift(Z.*exp(-1j*t'*imag(D-1j*zeta2)))); clear Z
% imagesc(f,2*pi*rf,10*log10(abs(MM_Ff).^2));colormap(hot);

set(gca,'ydir','normal')
ylabel('Slow frequency \zeta')
xlabel('Fast frequency')
caxis([SLimit(1)-60 SLimit(2)])
% caxis([-60 0]) % for relative linewidth
% zlim([SLimit(1)-60 SLimit(2)]) % for surf
cob = colorbar; ylabel(cob,'PSD')

% Noise transfer figure (optional)
% Input RF noise
figure(6);
subplot 311
semilogx(iffshift(rf),10*log10(abs(zeta_sp).^2)); % zeta_sp or F_sp
title('Input RF Noise')
ylabel('d\zeta/freq')
grid
% Output RF Noise
subplot 312
semilogx(iffshift(rf),10*log10(abs(beat_sp).^2));
title('Output RF Noise')
ylabel('dB/freq')
xlabel('Slow frequency')
grid
% Transfer function
subplot 313
semilogx(iffshift(rf),10*log10(abs(NT).^2));
title('Transfer - Rep. rate Beatnote')
ylabel('dB')
xlabel('Slow frequency')
grid
```

Appendix C. Numerical method

```
% Beatnote power spectral density ("ESA" measurement)
figure(11);
plot(2*pi*rf,10*log10(abs(beat_psd).^2))
xlabel('Slow frequency (\zeta)')
ylabel('dB')

% Heterodyne beatnote at probe frequency
figure(12);
plot(2*pi*rf,10*log10(abs(Psi_Ff(:,mu_dex)).^2))
xlabel('Slow frequency (\zeta)')
ylabel('dB')

% % Spectral envelope of isolated structure (optional)
% figure(22)
% plot(f,10*log10(abs(psi_fc).^2),f,10*log10(abs(psi_f).^2))
```

This the last important section. Firstly, *assuming* that there is a solitary structure in the cavity field (which will not be the case right now), the peak of this structure at the beginning and end of the simulation is measured here in order to infer its rate of drift, or group-velocity offset d_{p1} . Similarly next, the location of the right-hand SW front is also found, if there is one, which might be useful. Next, a ‘probe’ frequency value is set with the associated comb index found so that its noise can be analysed further below, like in the heterodyne beatnote measurements in section 2.5.

The next chunk sets up the slow vs. fast frequency image, as introduced briefly in section 1.3. See section C.2.2 below for an output demonstration. If the slow vs. fast time optical field picture is analogous to a ‘space-time’ diagram, then this is the conjugate ‘energy-momentum’ picture. It is also sometimes referred to as the nonlinear dispersion relation (NDR) [63, 64, 190] for its ability to directly reveal the nonlinear dispersive phenomenon of the cavity system, such as the RRCs. In order to get the NDR:

$$\tilde{\psi}(\Omega, \zeta) = \mathcal{F}_t \left[W_t \mathcal{F}_\tau \left[W_\tau \psi(\tau, t) \right] \right] \quad (\text{C.3})$$

with the fast Fourier transforms $\mathcal{F}_{t,\tau}$ over both dimensions, and window functions $W_{t,\tau}$ in order to prevent spectral leakage or isolate important structures. By default, W_t (WinLong) is a ‘Hann’ window, standard in signal processing, useful here to clarify long-term offset frequency noise. Setting W_τ (WinShort) also to a Hann window is also useful to fully suppress any discontinuities at the boundaries of the fast time window, but is sometimes unnecessary. W_τ can also be set to be a selective window function (WinSlice) to isolate one particular dissipative structure, for instance one SW front out of a pair. In this script, these are commented out. The following chunk creates $\tilde{\psi}(\Omega, \zeta)$ (Psi_Ff), depending on whether this is intracavity or out of the cavity. It also integrates for the average power, in or out, of the cavity field (CP).

For the purpose of analysing noise transfer, the original pre-made noisy traces for detuning

and power amplitude are re-sampled according to the sample rate f_s . The phase noise over time is obtained from taking $\delta\Phi(t)$ from Eq. C.2 and converting to the frequency domain

$$S_{\delta\Phi}^{\text{rf}} = \mathcal{F}[\Phi(t) - 2\pi f_{\text{rep}}t] \quad (\text{C.4})$$

where the average rise in phase over time due to $2\pi f_{\text{rep}}t$ is subtracted with the detrend function. The power-spectral density (PSD) of the beatnote amplitude are also obtained

$$S_p^{\text{rf}} = \mathcal{F}[W_t p(t)] \quad (\text{C.5})$$

with long-term window function included to prevent spectral leakage and ensure a high fidelity analysis. The transfer function from detuning noise to repetition rate noise, for instance, is done next. It could equally be done with input driving amplitude noise. See section C.2.3 below for an output demonstration.

For the purpose of plotting the slow time axis, either the actual slow time or the re-sampled detuning array Zeta are fine. Firstly, figure(2) and figure(3) plot an image of the instantaneous spectrum and the intracavity optical field envelope over slow time (or detuning). Figure(4) plots the average power internal or external, in this case internal, here showing the characteristic tilted nonlinear rise in intracavity power followed by the soliton ‘step’.

Figure(5) is where we plot the NDR. If the correct window functions are applied, the background noise and the RRCs should be well visible for static dissipative structures. Optionally, in order to observe the growth of noise for each comb line, it is more clarifying to normalise each column to its peak power. This option is commented out here. Additionally, one interesting transformation we can make to this diagram is to shift the y-axis of each column (the slow frequency) by the dispersion operator. This (MM_Ff), puts the cold cavity resonance of each comb mode at the zero slow frequency/detuning, and instead the lasing lines follow the dispersion curve. Setting the colourmap and the caxis/zlim to cover only the relevant signals is essential to make a good picture, naturally.

For noise analysis, figure(6) plots the input noise, output noise, and noise transfer of your choice. This will be relevant further below. Figure(11) and (12) show the PSDs of the repetition rate beatnote, and the “heterodyne” beatnote signal of the probed comb mode respectively.

```
%% Section 8 - Figure tiling

fud = 0.85;
figure(1);
figpos1 = get(gcf,'position');

figure(8);
set(gcf,'position', [100 700*fud figpos1(3:4)*fud])
```

Appendix C. Numerical method

```
title('Incident Waveform F(\tau)')
figure(7);
set(gcf,'position', [150 700*fud figpos1(3:4)*fud])
title('Dispersion Operator')

figure(2);
set(gcf,'position', [680 700*fud figpos1(3:4)*fud])
title('Spectrum Development over Slow Time')
figure(3);
set(gcf,'position', [680 50*fud figpos1(3:4)*fud])
title('Fast Field Development over Slow Time')

figure(5);
set(gcf,'position', [1260 700*fud figpos1(3:4)*fud])
title('Slow vs. Fast Frequency Image')

figure(4);
set(gcf,'position', [1210 50*fud figpos1(3:4)*fud])
title('Cavity Energy over Slow Time')
figure(12);
set(gcf,'position', [1260 50*fud figpos1(3:4)*fud])
figure(11);
set(gcf,'position', [1310 50*fud figpos1(3:4)*fud])
title('Fundamental Comb Beatnote')
```

This last section is handy for organising the numerous figures created when the script is over, but is entirely up to personal preference.

Run this script as written, including the above functions, and you should see output results similar to Fig. C.1, and all the data accessible in the workspace.

C.2.2 Single dissipative soliton analysis

Single dissipative soliton: hard excitation

At this point we want to observe a single dissipative soliton under static driving conditions, so we make the following *changes* to the program:

```
zeta0 = 8;          % start
zeta2 = 8;          % finish

store = 1/h*2^-6;    % data storage period [ no. simulation steps ]
view = store*2^3;    % real-time graphing period [ no. simulation steps ]

excite = 1;          % hard excitation yes/no
```

Firstly, we change the start and finish detuning ζ_0 to be the same, 8, within the bistable soliton existence range. Next we increase the sampling rate to $f_s = 64$ (or every 8 steps), and the view

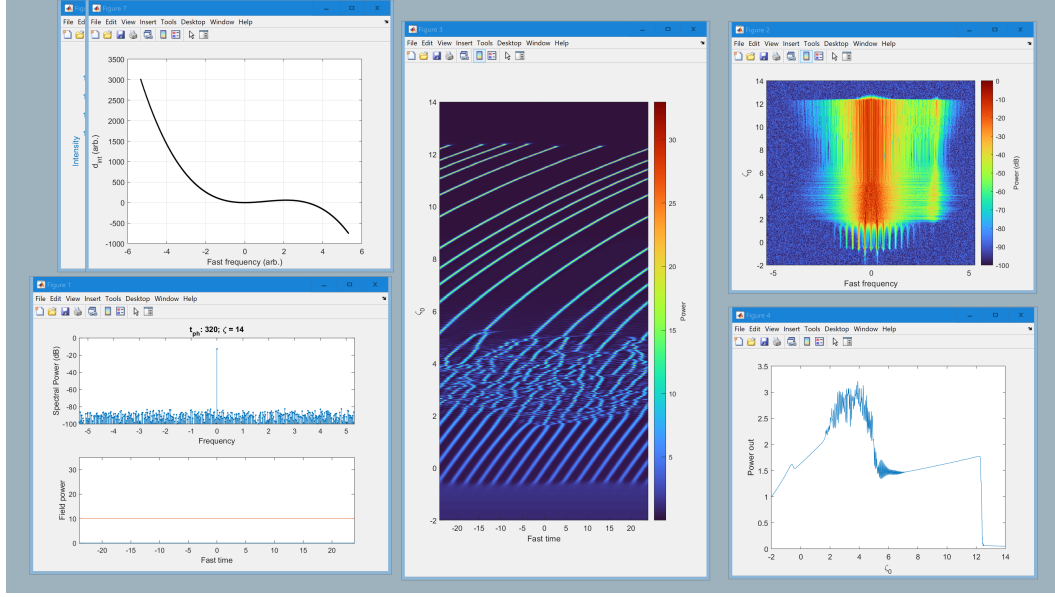


Figure C.1: **Visual output from simple scanning simulation.** Script: "lle_cavity_v4c_SimpleSoliton_1_demo_s1_scan". Figures shown: (Top-left) Integrated dispersion operator $d_{\text{int}}(\Omega)$; (Bottom-left) The live-view plot (now concluded), with frequency domain top and time domain bottom; (Centre) Slow vs. fast time domain image, showing the field going through the MI regime and forming into a group of six solitons; (Top-right) Slow time vs. fast frequency, showing the evolution of the microcomb profile; (Bottom-right) The intracavity average power, showing the stereotypical profile of soliton generation via scanning.

period to every 8 samples. We set `excite` to true to add the solution solution to the field (which is starting in the lower state ψ_L).

After running the script again now, we'll see the output shown in Fig. C.2. Of particular note is the NDR plotted in the top-right. Here we see the bright band corresponding to the dissipative soliton, and it is tilted negatively due to the soliton lagging in fast time due to its dispersive wave (DW) recoil. Since we hard-excited the analytical soliton approximation, there are brief relaxation oscillations seen here as two dim-red sidebands parallel to the soliton band. These relaxation sidelobes are also observed in the repetition rate beatnote in the top-left plot. These are in fact the 'S'-resonance observed in live soliton microcomb probing experiments [73, 74, 97]. In the background of the NDR, we see $\zeta_{L-}(\Omega)$, the RRC of the lower-state intracavity CW component ψ_L . For every comb mode, such as the one shown in the bottom-right plot, this RRC is the 'C'-resonance. Because $|\psi_L|^2$ is small, $\zeta_{L-}(\Omega) \approx d_{\text{int}}(\Omega) + \zeta_0$. Because the sampling frequency $f_s = 64$, we can see that ζ_{L-} is aliased (wrapped) over the slow frequency span $\zeta \in \pi[-f_s, f_s]$, but this is an illusion of the sampling process.

Appendix C. Numerical method

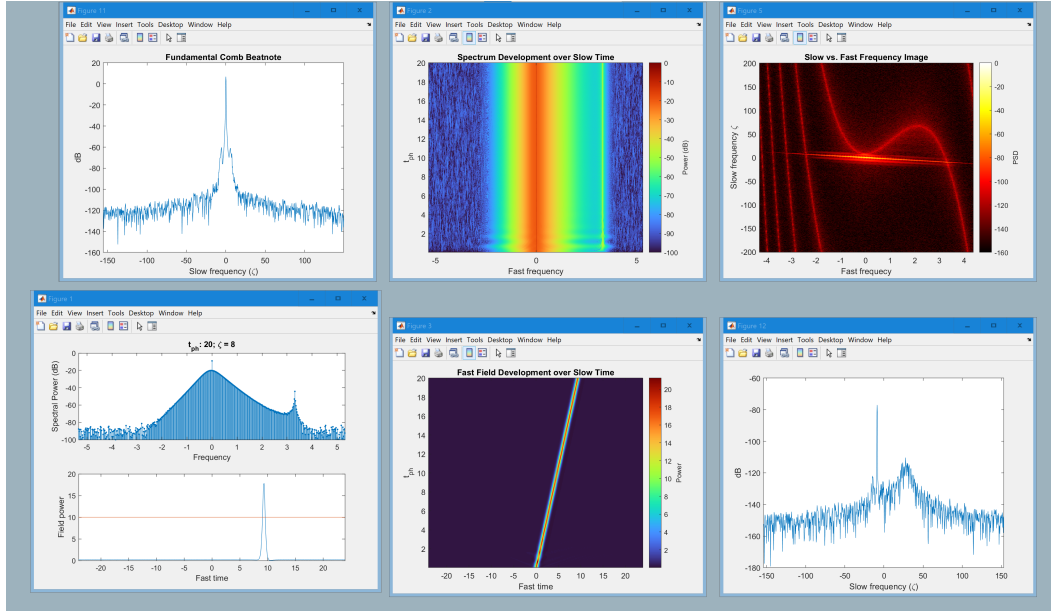


Figure C.2: **Visual output from simple dissipative soliton hard excitation simulation.** Script: "lle_cavity_v4c_SimpleSoliton_1_demo_s2_excite_drift". Figures shown: (Top-left) PSD for the repetition rate beatnote; (Bottom-left) The live-view plot, with frequency domain top and time domain bottom; (Top-centre) Slow time vs. fast frequency, showing the evolution of the microcomb profile; (Bottom-centre) Slow vs. fast time domain image, showing the soliton starting its existence at $\tau = 0$ and drifting towards the right; (Top-right) Slow vs. fast frequency density (log-scale) showing the tilted soliton microcomb and the cubic background RRC; (Bottom-right) PSD for heterodyne beatnote of comb mode at $\Omega/2\pi = 3.0$.

Single dissipative soliton: re-synchronisation

Thanks to us recording the drift velocity of the soliton in section 7, we can restart the simulation, but now with the group velocity corrected. Make the following changes to the program:

```
% d1 = 0;
d1 = d1+d_p1;
```

Run the script again. Now this drift velocity is applied to d_1 to compensate, and the soliton stays 'motionless', and the tilt to the soliton band in the NDR is fully compensated.

Single dissipative soliton: higher-order dispersive waves

For fun, we can enable parametric modulation of the cavity dispersion and observe the result on the same soliton by making the following changes to the program:

```
init = 0;           % initial state yes/no
```

C.2 Script for simulating the dimensionless LLE & basic scenarios

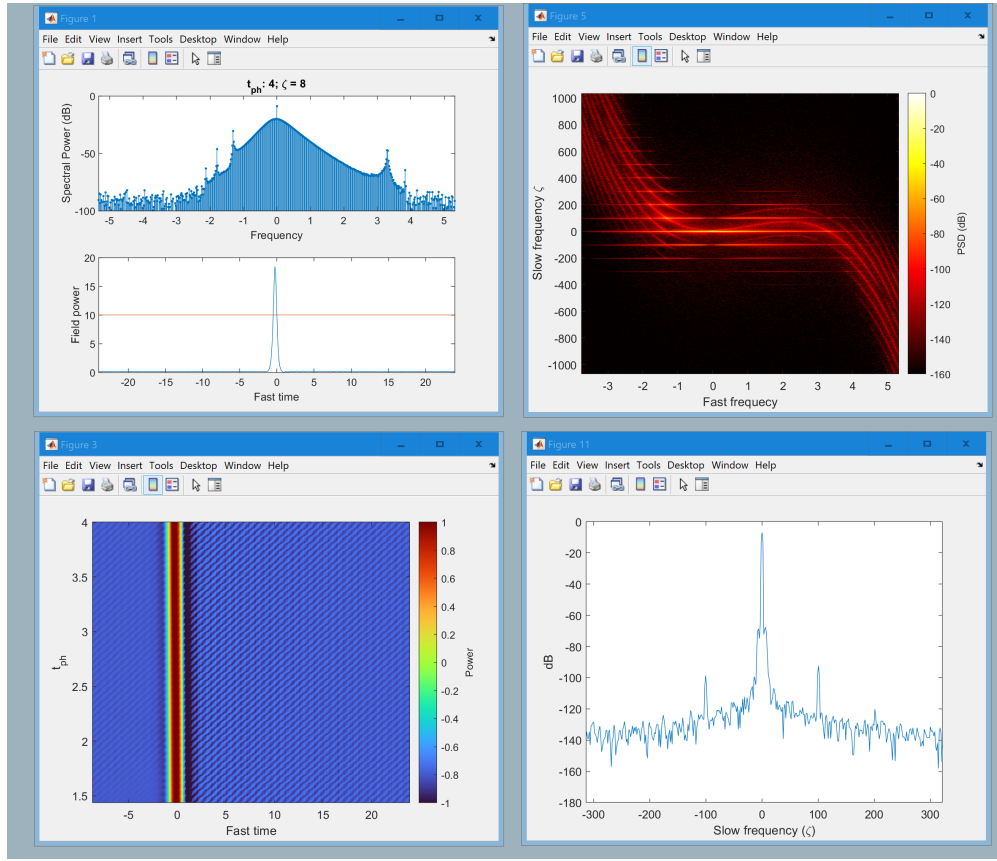


Figure C.3: **Visual output from dispersion modulated dissipative soliton with higher-order dispersive waves (HDW).** Script: "lle_cavity_v4c_SimpleSoliton_1_demo_s4_Kelly_1". Figures shown: (Top-left) The live-view plot, now showing microcomb with HDW ('Kelly sidebands'); (Bottom-left) Slow vs. fast time domain image (in log scale), showing repeatedly radiating waves emanating from the soliton; (Top-right) Slow vs. fast frequency density showing the 'ladder' of Floquet microcombs spaced by ∂_1 in ζ , and the associated Floquet bands of the RRC; (Bottom-right) PSD for the repetition rate beatnote, now sporting apparent sidebands at the 'FSR' of ∂_1 .

```
excite = 0;           % hard excitation yes/no

t_end = 4;           % for stationary

store = 1/h*2^-9;    % data storage period [ no. simulation steps ]

eta_p = 1/h*2^-4;    % "modulation" time period (for Faraday Instab. etc.)
eta_a = 0.5;         % waveguide modulation amplitude

figure(3);
imagesc(T,Y,log10(abs(Psi).^2).*WinSlice);colormap(turbo);caxis([-1 1])
```

First, we elect to *continue* the simulation from the previously excited soliton (assuming psi is

Appendix C. Numerical method

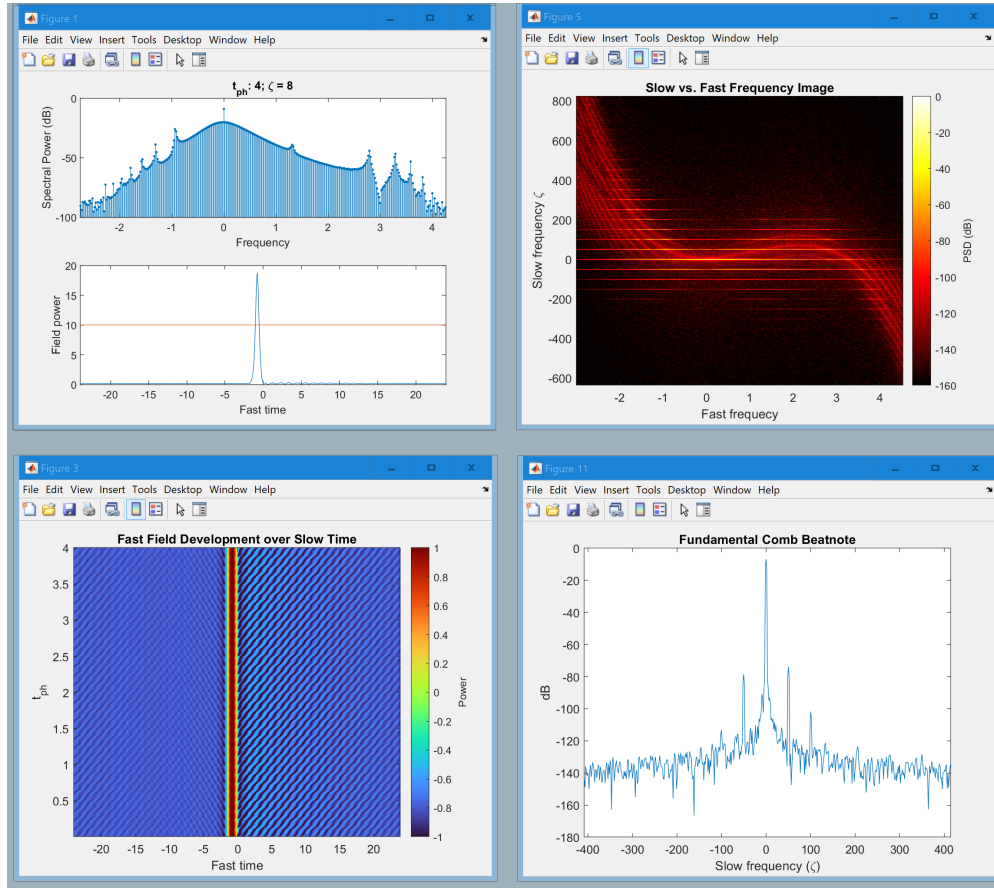


Figure C.4: **Visual output from dispersion modulated dissipative soliton with more HDW.** Script: "lle_cavity_v4c_SimpleSoliton_1_demo_s5_Kelly_2". Figures shown: (Top-left) The live-view plot, showing microcomb with many HDW; (Bottom-left) Slow vs. fast time domain image (in log scale), showing stronger radiating waves; (Top-right) Slow vs. fast frequency density showing a dense microcomb ladder spaced by Δ_1 ; (Bottom-right) PSD for the repetition rate beatnote, with sidebands at $\pm\Delta_1$.

still accessible in the workspace) by setting $\text{init}=0$ and $\text{excite}=0$. Now we won't need to wait for the soliton to reach equilibrium. We reduce the simulation duration to $t = 4$, and increase the sampling rate to the maximum, $f_s = f_r = 512$ per photon lifetime, recording every LLE step.

The modulation period (eta_p) is set to $1/16^{\text{th}}$ of a photon lifetime. This represents an implicit 'FSR' of $\Delta_1/2\pi = 16$. This FSR is entirely independent of the *other* FSR set by the periodic time window of $\Delta\tau = 24$ which is mostly irrelevant in this dimensionless simulation. In an experimental-units simulation, these two quantities should be made equal for the results to make sense. The modulation depth $\Delta = 0.5$ (eta_a). For seeing the radiated waves, we also set a log scale to the time vs. time figure.

When running the script now, the outputs shown in Fig. C.3 appear. About four new higher-

order dispersive waves (HDW) appear on the microcomb profile above the noise level, 3 left and 1 right. During the live-plot, you should be able to see them oscillating in time. The origin of these HDW are seen in the NDR figure where the higher Floquet orders of microcomb cross their corresponding RRCs. The gentle modulation of the soliton is seen in the appearance of sidebands on the repetition rate beatnote located at $\pm\vartheta_1$.

For interest, if we set $\eta_p = 1/h \cdot 2^{-3}$; and run the program again (a couple of times to let things relax), this sets the implicit FSR to $\vartheta_1/2\pi = 8$ and more HDW are added to the microcomb, and with stronger amplitude, seen in Fig. C.4.

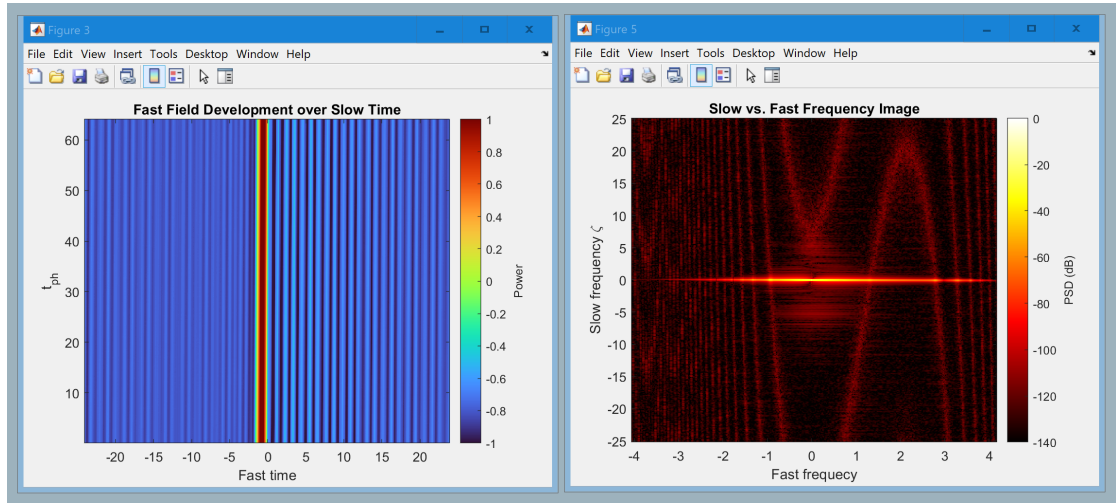


Figure C.5: **Visual output from dispersion modulated dissipative soliton with HDW.** Script: "lle_cavity_v4c_SimpleSoliton_1_demo_s6_Kelly_3". Figures shown: (Left) Slow vs. fast time domain image (in log scale), now showing the HDW apparently frozen in time; (Right) Slow vs. fast frequency density showing the modulated microcomb in the zone folded in ϑ_1 .

To replicate the ‘folded’ view of the soliton microcomb, as would be seen exiting an actual experimental microcavity – once per roundtrip – we can make the following changes:

```
t_end = 64; % for stationary
store = 1/h*2^-3; % data storage period [ no. simulation steps ]
```

This sets the sampling rate equal to the ‘FSR’, $f_2 = \vartheta_1/2\pi$, and we have to run for a longer duration to see sufficient resolution. When running, we’ll see the once-per-roundtrip sampled dissipative soliton picture in Fig. C.5. Now, due to this sampling, all Floquet orders have collapsed into one, just as we see in experiment (for example, Fig. 4.12).

C.2.3 Noise transfer analysis

To test how noise on the driving detuning (ie. laser frequency noise) transfers to the soliton, return to plain dissipative soliton excitation step without HDW (section C.2.2, Matlab file

Appendix C. Numerical method

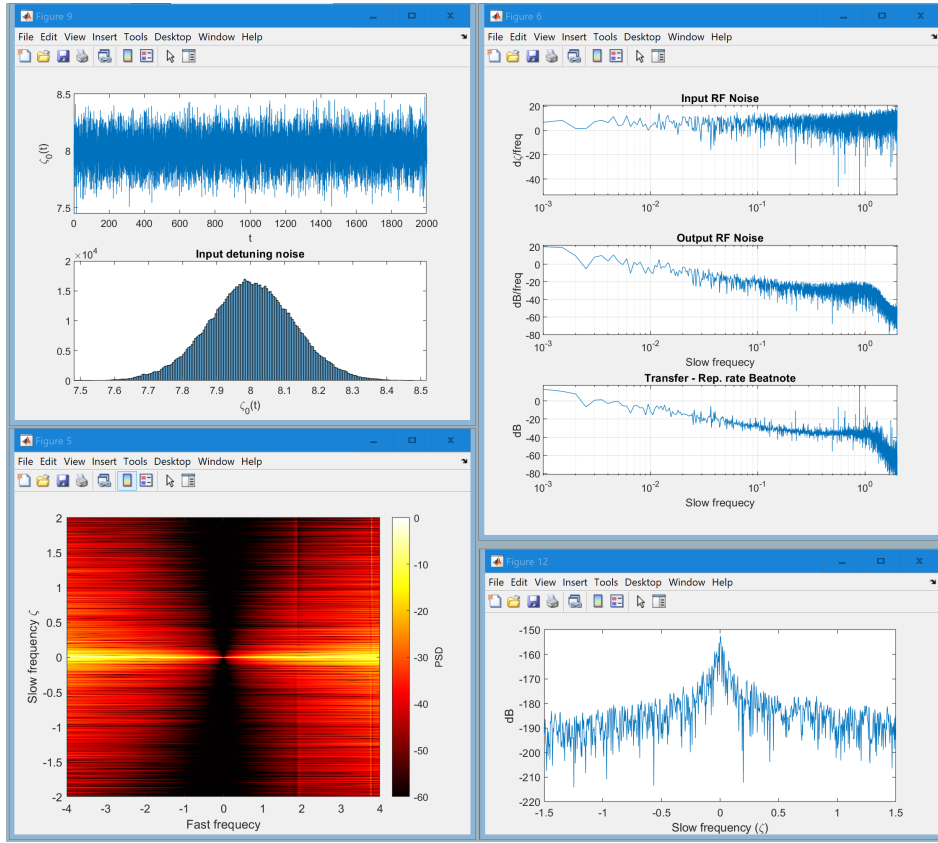


Figure C.6: **Visual output from dispersion modulated dissipative soliton with HDW.** Script: "lle_cavity_v4c_SimpleSolitonNoise_1_demo_s2_example". Figures shown: (Top-left) The pre-made noisy detuning trace $\zeta_0(t)$ over time (top) and in histogram (bottom). (Bottom-left) Slow vs. fast frequency density, normalised to mode-peak. (Top-right) Input frequency noise of the detuning (top), output phase noise of the repetition rate (middle), and the transfer magnitude between the two (bottom). (Bottom-right) Heterodyne beatnote of the particular mode at $\Omega/2\pi = -4$.

"lle_cavity_v4c_SimpleSoliton_1_demo_s2_excite_drift"), and make the following changes:

```
d1 = -1.5920625;
eta = [0.00 0.1 -1.0 d1 0]; % dispersion operator

init = 1;           % initial state yes/no
excite = 1;         % hard excitation yes/no

nf = 0.00;         % added Gaussian white noise background amplitude
```

We adjust the dispersion to make TOD stronger, for the purpose of this demonstration, and we incorporate the drift compensation to d_1 here in advance. We also turn off the added broadband white Gaussian noise. Run this program to excite the soliton and allow it to relax. Next, make the following *changes*:

C.2 Script for simulating the dimensionless LLE & basic scenarios

```

t_end = 2000;                                % for stationary

store = 1/h*2^-2;                            % data storage period [ no. simulation steps ]
view = store*2^5;                            % real-time graphing period [ no. simulation steps ]

init = 0;                                    % initial state yes/no
excite = 0;                                  % hard excitation yes/no

% RF noise
n_band = max(rf);                            % injected noise bandwidth
n_trace = sqrt(store)*lowpass(randn(1,r+store),n_band,1/h,...
'ImpulseResponse','iir','Steepness',0.9);    % noisy trace over slow time
zeta_n = 0.1;                                % detuning noise deviation amplitude

f_prob = -4.0;

figure(5);clf
imagesc(f,2*pi*rf,10*log10(abs(Psi_Ff).^2)...
-ones(rs,1)*max(10*log10(abs(Psi_Ff).^2)));colormap(hot);
caxis([-60 0])

```

We increase the duration to $t = 2000$ in order to see long-term behaviour, and accordingly decrease the sampling rate to $f_s = 4$ to save memory, but still observe noise behaviour just beyond the cavity lifetime frequency. We also increase the view period in order to save time.

For input noise, we introduce a Gaussian-random trace for each simulation step ($1:r$) and *low-pass* it up to the sampling frequency f_s . The reason for this is to not inject unnecessarily high-frequency noise into the simulation, at least not higher than our sampling frequency. This reduces the original noise power by a factor of f_s/f_r , so we compensate this with the factor $\sqrt{\text{store}}$ (equal to $\sqrt{f_r/f_s}$). This noise trace is later added to the detuning array for the LLE process, with an RMS (root mean-square) amplitude of $\text{zeta_n}=0.1$.

Set $\text{f_prob}=-4.0$ to check the heterodyne beatnote of the comb mode at $\Omega/2\pi = -4$, and setup the slow vs. fast frequency picture to normalise each comb mode to its peak (in log scale) with a range of 60 dB. Run the program now. During the run, the soliton will appear to jitter around due to the changing DW recoil, in turn caused by the fluctuating detuning $\zeta_0(t)$.

After the run, the following important plots shown in Fig. C.6 appear. The slow time-domain input noise is summarised in the top left window 'Figure(9)', showing the noisy $\zeta_0(t)$ shown for every simulation step. This figure appears before the simulation starts for pre-inspection. The 'Figure(6)' appearing top-right gives our input and output noise measurements $S_{\delta\zeta_0}^{\text{rf}}$ and $S_{\delta\Phi}^{\text{rf}}$ in semilog-x form. The bottom row plots the transfer function between the two $T^{\text{rf}} = |S_{\delta\Phi}^{\text{rf}}|/|S_{\delta\zeta_0}^{\text{rf}}|$, in this case showing a $1/f^2$ relationship, with a cut-off at ζ_0 . The transfer function in this example is not so smooth, but it can become smooth if the simulation is run 4-8 more times with new input noise traces and T^{rf} is averaged after each run.

The frequency vs frequency picture in the lower left shows the comb mode linewidth broaden

Appendix C. Numerical method

away from the centre as the frequency noise of each line scales as $S^{(\mu)} = \mu^2 \zeta^2 S_{\delta\Phi}^{\text{rf}}$ as demonstrated in the study in section 2.5.2. The lower right figure window shows the individual vertical ‘slice’ at $\Omega/2\pi = -4$, corresponding to the optical frequency noise $S^{(\mu=-191)}(\zeta)$.

Just in case there is confusion at this moment, in dimensionless formalism ‘ $\zeta/2\pi$ ’ is the frequency counterpart to ‘ t ’, and $\Omega/2\pi$ is the frequency counterpart to τ . The comb mode index remains μ .

C.2.4 Dissipative solitons in pulse driving example

This time we shall include pulse driving and observe an example scan, a “soft excitation” of a soliton, that becomes bound to the edge of a driving pulse. Re-creating the example shown in Fig. 2.17, we will also pre-disperse the pulse drive envelope so that it’s chirped (in this case negative phase curvature).

Recall above the setup of a Gaussian pulse with pre-dispersion, in the script program C.2.1 – ‘Section 4’. Restart with the plain dissipative soliton excitation step without HDW (section C.2.2, Matlab file “lle_cavity_v4c_SimpleSoliton_1_demo_s2_excite_drift”). Make the following changes to the program settings:

```
Tw = 32;      % fast time width

d1 = -0.32;
eta = [0.00 0.05 -1.0 d1 0]; % dispersion operator

zeta0 = 2;      % start
zeta2 = 8;      % finish

t_end = 512*abs(zeta2-zeta0); % rate of change for scanning

store = 1/h*2^-1;      % data storage period [ no. simulation steps ]
view = store*2^2;      % real-time graphing period [ no. simulation steps ]

init = 1;      % initial state yes/no
excite = 0;      % hard excitation yes/no
pulsed = 1;      % temporally-structured driving function yes/no

% Pulse waveform
Tp = 16;      % fast time pulse drive width
d2L = +20;      % pulse drive pre-dispersion factor
```

The rest of the program settings should be taken care of already as set up in section C.2.1. Here, we are increasing the fast time span $\Delta\tau$ to 32, pre-setting the desynchronisation $d_1 = -0.32$, and setting $d_3 = 0.05$. We are going to sweep detuning ζ_0 from 2 to 8, with a long duration of $\Delta t/\Delta\zeta_0 = 512$, sampling twice per photon lifetime, viewing every 4 samples. We set $\text{init}=1$ to make sure the run starts anew with the initial field amplitude at the homogenous solution, $\text{excite}=0$ to not hard excite any soliton, and $\text{pulsed}=1$ to use our chirped Gaussian pulse as

the drive term $F(\tau)$. The pulse is set with an initial width of 16, and pre-dispersion equivalent to $+20\Omega^2$.

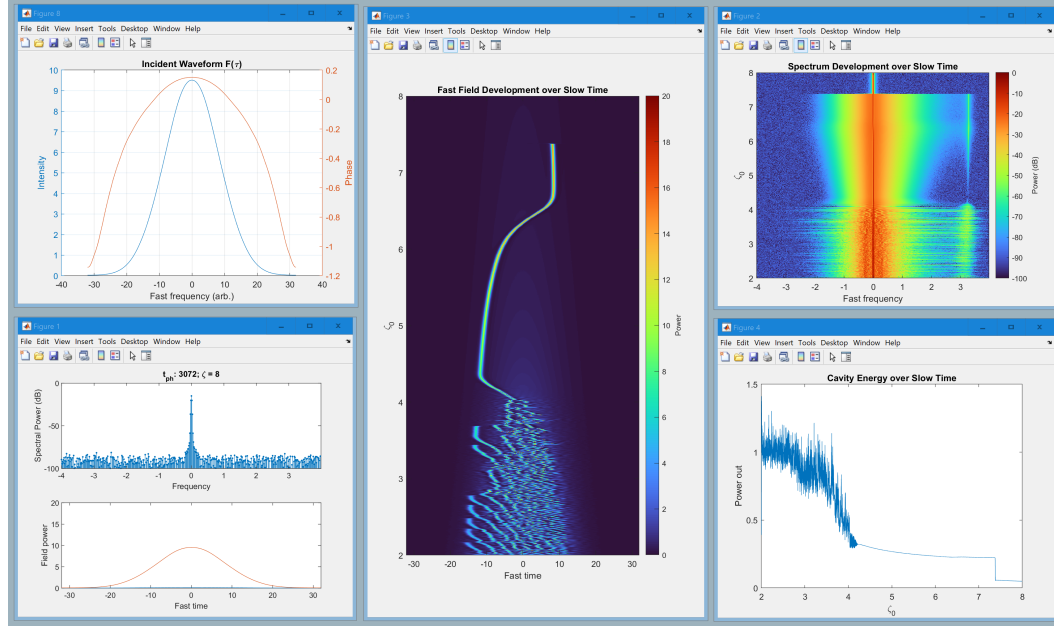


Figure C.7: **Visual output from pulsed scanning simulation.** Script: "lle_cavity_v4c_SimpleSolitonPulsed_1_demo_s1_scan". Figures shown: (Top-left) The driving pulse profile $F(\tau)$ intensity and phase; (Bottom-left) The live-view plot (now concluded), with frequency domain top and time domain bottom; (Centre) Slow vs. fast time domain image, showing the field going through the MI regime and forming one soliton that becomes trapped and changes sides; (Top-right) Slow time vs. fast frequency, showing the evolution of the microcomb profile; (Bottom-right) The intracavity average power, showing the step length in detuning.

Now, run the program. The live-plot should be showing the emergence of MI (Turing patterns) contained within the temporal bounds of the pulse drive. Hopefully, a single soliton will eventually emerge and find itself trapped on the left edge of the pulse due to d_1 . In the unlucky event that no soliton survives, cancel the run and run it again. After some time, the trapped soliton will become unbound from the left edge and switch to the right edge due to the emergence of its DW tail. After the run is completed, we see the output figures in Fig. C.7.

C.2.5 Switching waves and pulse driving

Expanding SW pair

Now we turn our attention to normal dispersion in order to observe switching waves (SW). Once again, return to the plain dissipative soliton excitation step without HDW (section C.2.2, Matlab file “lle_cavity_v4c_SimpleSoliton_1_demo_s2_excite_drift”). Make the following changes to the program settings:

```
Tw = 64;      % fast time width

eta = [0.00 0 1.0 0.0 0];      % dispersion

F0 = sqrt(14);      % dimensionless forcing term [ sqrt(P/P_thresh) ]

zeta0 = 7;
zeta2 = 7;

t_end = 40;      % for stationary

store = 1/h*2^-5;      % data storage period [ simulation steps ]
view = store*2^2;      % real-time graphing period [ simulation steps ]

init = 1;      % initial state yes/no
excite = 1;      % hard excitation yes/no
pulsed = 0;      % temporally-structured driving function yes/no

PA2 = rectangularPulse(-Tw*0.1,Tw*0.1,T);

figure(7)
plot(2*pi*f,-D_psi_l1,'g.',2*pi*f,-D_psi_l2,'k.',...
     2*pi*f,-D_psi_h1,'b.',2*pi*f,-D_psi_h2,'r.')

% Hard excitation
if (j==exctr&&excite)
    psi = psi + PA2*(psi_h-psi_l);      % excite SW fronts
end
```

With this we are going to ‘hard excite’ an SW pair in an expanding regime, like in Fig. 1.19. We set the time span $\Delta\tau = 64$ in order to contain the expanding platicon, and $d_2 = +1$ for normal dispersion, and no other dispersion coefficients. Increase the relative power to $F^2 = 14$, the static detuning to $\zeta_0 = 7$, and the duration to $t = 40$. For slow time resolution, we set $f_s = 32$ (via store), and view period to ever 4 samples. To start the simulation from scratch $\text{init}=1$, and to hard excite a dissipative structure $\text{excite}=1$. This time we are CW driving so $\text{pulsed}=0$.

We are going to excite a SW pair (platicon) by adding a rectangular profile (PA2) to $\psi(\tau)$, with a temporal width of $0.2\Delta\tau$. To make sure of this, down in section 6 of the program, we comment in the line shown here for adding the rectangular front that connects ψ_H with ψ_L , and make sure to comment out the line that adds the soliton solution. Run the program, and you should

C.2 Script for simulating the dimensionless LLE & basic scenarios

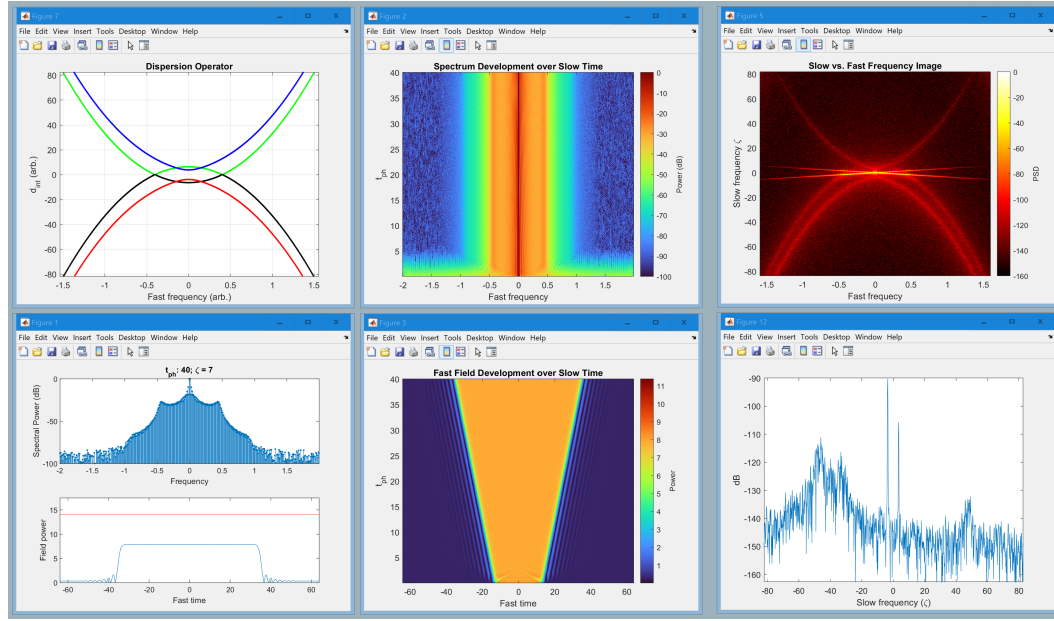


Figure C.8: **Visual output from pulsed scanning simulation.** Script: "lle_cavity_v4c_SimpleSwitchingWave_1_demo_s1_expanding". Figures shown: (Top-left) The resonant radiation conditions (RRC); (Bottom-left) The live-view plot with frequency domain top and time domain bottom; (Top-centre) Slow time vs. fast frequency, showing the evolution of the SW profile; (Bottom-centre) Slow vs. fast time domain image, showing the expanding SW pair (platicon); (Top-right) Slow vs. fast frequency density showing a the pair of SW spectra at opposite tilts, as well as background RRCs; (Bottom-right) The pair of SW heterodyne comb beatnotes located at $\Omega/2\pi = 1$.

see the plots in Fig. C.8.

This time we're looking at the analytically calculated RRCs (from Eq. 1.66) in the plot in the upper left, so we can directly compare with the noisy lines in the frequency vs. frequency plot. In the time vs. time domain shown in the centre-bottom we see the SW pair continuously moving outwards, so that ψ_H is invading the meta-stable ψ_L . Correspondingly, the microcomb band in the frequency vs. frequency picture is split in two, for two different group velocities (and therefore two different f_{rep}). This is also seen with two separate comb teeth shown in the heterodyne measurement plot in the lower right.

Containing expanding SW within pulse drive

Let's turn on pulse driving in order to contain the expanding SWs to form a stable SW microcomb, like in the experiment in section 3.2.1. Make the following changes to the program:

```
pulsed = 1;           % temporally-structured driving function yes/no

% Pulse waveform
Tp = Tw*0.5;         % fast time pulse drive width
```

and run. This time, the expansion of the SWs is gradually halted at the pulse edges. If you set `init=0` and `excite=0` and run again, you will see a stable, single comb profile, shown in Fig. C.9.

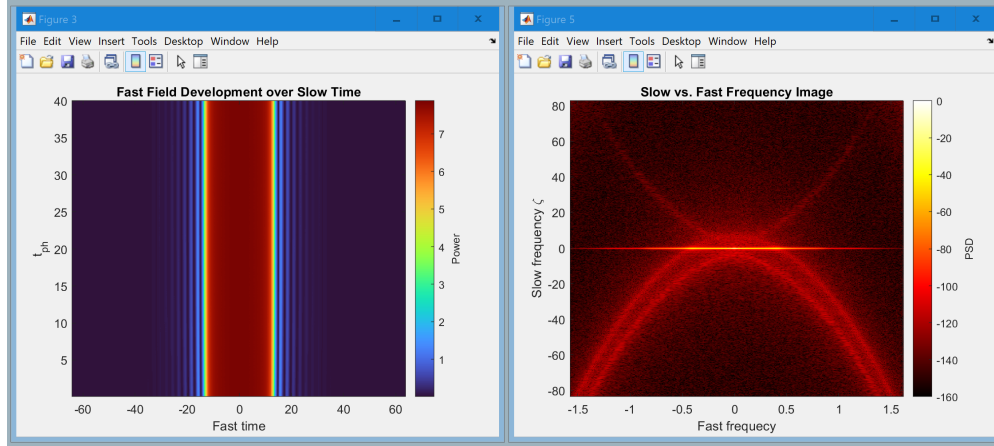


Figure C.9: **Visual output from pulsed scanning simulation.** Script: "lle_cavity_v4c_SimpleSwitchingWave_1_demo_s1_pulsed". Figures shown: (Left) Slow vs. fast time domain image, showing stabilised SW pair (platicon); (Right) Slow vs. fast frequency density now showing single SW microcomb band.

C.3 Script for simulating the realistic LLE in Si_3N_4 with advanced examples

To be clear, the script layout for simulating the LLE with realistic experimental units, as in Eq. 1.58, is essentially the same as for the above script on the normalised LLE. The difference with this script is that all dimensions, parameters, and operators are converted back or forth from normalised/relative units as we go, according to Eqs. 1.55. As such, it may be important to read the above section to understand this one.

The following example program is one used by me to model a future pulse-driven octave-spanning soliton microcomb, based on modelled dispersion in the example shown in Fig. 1.4 (waveguide width \times height: $3.5\times 0.75\mu\text{m}^2$), and with an FSR of 15 GHz.

C.3.1 Program guide and plotting the output

In this program, both frequency units as in Eq. 1.51 and phase per metre units as in Eq. 1.49 are defined in order to maintain full information on the system in terms of theory, design, and experiment. In the actual evaluation however, phase per metre units are used, as in Eq. 1.49.

Section 1 (Octave spanning microcomb example)

```
% Script for Lugiato-Lefever Split-step Fourier live calculation
% (Miles Cavity Sim v4.1)
% Date: March 2022
% Miles Anderson

% Units for silicon nitride resonator.

% Preferring distance in um, and fast time (T) in ps or THz
% (but sometimes fs and PHz is better for fitting)
% Slow time (t) in t_photon or roundtrips, steps
% A is for time field, B for frequency field, S for pump

% This example:
% Hard exciting octave-spanning soliton microcomb in planned design D82

%% Section 1 - Real experimental parameters

c = 2.99792458e2;           % speed of light [ ps/um]
hbar = 6.626e-34/(2*pi);    % planck's constant [ J/Hz ]
n2 = 2.4e-7;                % nonlinear index [ um^2/W ]

% Resonator dimensions
% width = 3500;
% height = 750;
% radius = 750;
fsr = 0.015;
% L = 9640;                % length [ um ]
Aeff = 1.98;               % waeguide nonlinear area [ um^2 ]

f0 = 192.5;                % starting frequency [ THz ]

% Waveguide dispersion fitting parameters \beta(\Omega) [ in fs^k/um ]

f_b=[0.016058573615903;
-0.037616880571321;
0.038393704369802;
-0.002195994841822;
-0.006742435530294;
6.913358229657665;
7.493378829837532];        % polynom. orders 6 to 0 for this device
beta_var = 0.0;             % dispersion modulation index (relative)

% Orders of 'beta', useful to know, converted to ps^k/um.
beta0 = f_b(end);
beta1 = f_b(end-1) *1e-3;
beta2 = f_b(end-2)*2 *1e-6;
beta3 = f_b(end-3)*6 *1e-9;
beta4 = f_b(end-4)*24 *1e-12;

w0 = 2*pi*f0;
```

Appendix C. Numerical method

```

L = 1/(beta1*fsr);      % calculating length from group velocity and FSR
ng = c*beta1;           % group index, for information
n0 = beta0*c*1e-3/w0; % linear index, for information

% Orders of modal dispersion [ 2pi*THz ]
D1 = 2*pi*fsr;
D2 = beta2*L *~-D1/(2*pi) *D1^2;
D3 = beta3*L *~-D1/(2*pi) *D1^3;
D4 = beta4*L *~-D1/(2*pi) *D1^4;

% De-synchronization
de_rf0 = 0;              % external driving desynch [ THz ]
de_rr0 = -1.187324523925781e-06; % internal field desynch [ THz ]
% de_rr0 = de_rr0-de_rf1; % internal field desynch [ THz ]
dbeta1 = -1/(L*fsr) *de_rr0/fsr; % drift velocity compensation

% Loss
kappa0 = 1e-12*2*pi*30e6; % intrinsic linewidth [ THz ]
kappa1 = 1e-12*2*pi*470e6; % external-to-bus linewidth [ THz ]
kappa = kappa0+kappa1;    % total linewidth [ THz ]
kappa_var = 0.0;          % intracavity loss modulation index
kappa_slope = 0.009;      % exponential decay in kappa1 [ 1/THz ]

% Roundtrip parameters
theta0 = kappa0/fsr;      % internal loss [ ]
theta1 = kappa1/fsr;      % external coupling [ ]
alpha = kappa/(2*fsr);    % roundtrip decay [ ]

% Other values for fun
Quality = w0/kappa;
Finesse = D1/kappa;

% Nonlinear coefficients
gamma = n2*w0/(c*Aeff); % waveguide nonlinearity [ /W*um ]
g = hbar*w0*1e12*(fsr*1e12)^2*gamma*L; % Kerr photon coupling [ 2pi*Hz ]
fr_raman = 0.00;        % Raman contribution
t_raman = 0.02;          % Raman time constant [ ps ]

```

This first section is where we set every real experimental or design parameter for the microresonator. In this particular example, we are setting values based on a planned design. The primary unit of fast frequency in the program is THz, however for initial dispersion fitting it is PHz. The unit for field power is Watts and length is μm . We start by defining the FSR (fsr) to be 15 GHz. From finite-element method simulations of the waveguide eigenmode, we find $A_{\text{eff}} = 1.98\mu\text{m}^2$ (see Fig. 1.2, and Eq. 1.22), and the fitted polynomial orders of dispersion $f_b; \beta_\ell/\ell!$ (Eq. 1.11) as a vector of $\ell = 6$ to 0, in units of $\text{fs}^\ell/\mu\text{m}$. For now, the parametric dispersion modulation index $\text{beta_var}=0$. For ‘good-to-know’ purposes, we also convert f_b to value of β_ℓ and D_ℓ , as well as the refractive indices n_0 and n_g . Either calculating or defining the length of the resonator L is important for the dispersion operator. As before in the dimensionless program, we define two desynchronisation/drift values, equivalent to δf_{eo}

here in THz. The value `de_rf0` causes the drive envelope $A_{in}(\tau)$ to drift with the intracavity field $A(\tau)$ neutral, and the value `de_rr0` for vice-versa.

For the cavity loss, in this example we are aiming for a maximally efficient pulse-driven microcomb with a high power, according to Eqs. 2.1 and 2.3. As such, $\kappa_{ex}/2\pi$ is set to a high 470 MHz, which is feasible long straight coupling sections (such as seen in Fig. 4.8), and also plausibly with $\kappa_0/2\pi = 30$ MHz. In case we want to vary the loss every roundtrip the same way we can with dispersion, that modulation depth is also set here. The fall-off parameter of κ_{ex} with short wavelength (`kappa_slope`), due to the waveguide directional coupler, is also set here. See below for the calculation in Section 6. The components of κ are converted to the useful per-roundtrip coefficients θ and α . Finally, the nonlinear propagation constant γ is calculated based on A_{eff} and n_2 . The Raman coefficients are left zero for this example.

Section 2

```
%% Section 2 - Simulation and normalised parameters

% Define simulation width
mode_cut = 2; % only simulated these modes
Tw = 1/(2*mode_cut*fsr); % fast time width [ ps ]
N = 2^13; % number of points/modes [ ]

F0 = sqrt(20); % dimensionless forcing term [ sqrt(P/P_thresh) ]
Pin0 = F0^2/(gamma*L*theta1/alpha^3); % peak power [ W ]

% Define detuning boundaries [ 2*delta_omega/kappa ]
zeta0 = 14.0;
zeta2 = 14.0;
dw0 = zeta0/2*kappa; % frequency detuning [ 2pi*Hz ]
dw2 = zeta2/2*kappa;
de0 = zeta0*alpha; % total phase detuning [ rad. ]
de2 = zeta2*alpha;

% Define simulation duration, in photon lifetime [ 2/kappa ]
if zeta2~=zeta0
    t_end = 10*abs(zeta2-zeta0); % for scanning
else
    t_end = 100; % for stationary
end
t_real = t_end/(alpha*fsr); % real time duration, for information

% Define simulation frequencies
% h = 2^-10; % step length [ fraction of photon lifetime ]
h = 2^-4*alpha; % step length [ discrete to roundtrip ]
h_rate = fsr/(h/alpha); % real maximum frequency of simulation
ntr = alpha/h; % roundtrip step rate.

% store = 1/h*2^-3; % data storage period [ simulation steps ]
store = alpha/h*2^-1; % data storage period [ snap to roundtrip ]
```

Appendix C. Numerical method

```
view = store*2^0;      % real-time graphing period [ simulation steps ]
plot_time = 0.01;      % graph duration [ seconds ]
```

Section 2 is essentially identical to Section 1 of the dimensionless program (see C.2.1) with a few key additions. Simulating an octave-spanning microcomb centred optically at 192 THz with a repetition rate of 15 GHz would require at least 10,000 modes! Thankfully, we are only interested in modelling the one pulse-contained soliton at the centre, in a time window of only about 5 ps out of a total fast time span of 67 ps, so we should be entitled to omit much of the true total fast time span. With that said, there are longer-range DWs that wrap around the cavity causing long-range self-interactions of the soliton and this should be taken into account, or rather in this case, its absence. In such a ‘long’ cavity, the DWs dissipate to very low amplitude by the time they get around, but simulating an even 2^{14} modes is just too slow. Therefore, we will compromise by cutting out half the fast time window and simulating just 2^{13} modes. We define this here with `mode_cut=2`. Throughout the program, this is taken into account for all the dimensional values of ω and μ .

For this example, to ensure a broadband soliton, we *first* set the relative driving strength $F = \sqrt{20}$, and calculated the necessary peak power ($P_0 = 24.7$ W) after based on Eqs. 1.55. Similarly, we set the dimensionless detuning range ζ_0 first, and from it calculate the frequency detuning $\delta\omega$ and the per roundtrip phase ϕ_0 , the latter being used in the LLE evaluation. For the definition of the slow time step length h , we can set this as an arbitrary fraction of t_{ph} since the mean-field LLE model is ideally ignorant of the roundtrip time. Here, more usefully, we set it to a rational fraction of the roundtrip time (recalling $T = \alpha t_{ph}$) meaning here we are evaluating 16 times per roundtrip (`ntr=16`). The consequent real evaluation rate of the simulation `h_rate` in this instance is 240 GHz. We set the sampling period `store` to be 2 times every roundtrip, live-viewing every roundtrip.

Section 3

```
%% Section 3 - Settings

% Scenario
init = 1;          % initial state yes/no
excite = 1;        % hard excitation yes/no
exctr = 1;         % excite step number
pulsed = 1;        % temporally-structured driving function yes/no

% Additional settings
external = 1;      % get spectrum outside resonator yes/no
spectral_loss = 1; % non-uniform spectral kappal
% input field desynchronisation yes/no (eg. rf noise)
desynch = 0;

nf = 0.01;         % noise factor
exT = 0.05;        % where you excite a soliton [ ps ]
```

The settings section is same as in the dimensionless program, but now with another setting `spectral_loss` for whether to make the cavity coupling coefficient κ_{ex} dependent on wavelength.

Section 4

```
%% Section 4 - Dimensions

% Space/time dimensions
% Fast time
nu = ((0:N-1)-N/2);          % mode index
T = linspace(-Tw,Tw,N+1);    % fast time [ ps ]
T = T(1:N);                  % the end-piece
dT = T(2)-T(1);              % time resolution [ ps ]
f = nu/(N*dT);               % fast frequency [ THz ]
nu = nu*mode_cut;            % compensating for omitted modes

% Slow time
% r = round(t_end/h);          % no. of steps
rs = ntr/store*round(t_end/(h*ntr)); % no. of steps stored
r = rs*store;                 % no. of steps
t = (1:rs)*h*store;           % slow time [ t_photon ]
dt = h/(alpha*fsr)*store*1e-12; % slow time resolution (convert to s)
rf = ((0:rs-1)-rs/2)/(rs*dt); % slow frequency [ Hz ]

% Driving dimensions
de = linspace(de0,de2,r);     % linear detuning function
Pin = Pin0*ones(1,r);        % constant pump

% Slow-time input desynchronisation rate
de_rf = de_rf0*ones(r,1);     % constant desynch

% Scaling
t_scale = 1;
y_scale = 1000; % converting W to mW
```

Again, much is the same as in dimensionless, only now in this instance we make sure to ‘snap’ the amount of sampled fields to an integer roundtrip amount, in this case 955. The detuning, driving power, and desynchronisation arrays are created in mind of adding noise to them (but not in this example).

Section 5

```
%% Section 5 - Initial condition

% CW waveform
CW = ones(1,N);
```

Appendix C. Numerical method

```
% Pulse waveform
Tp = 0.85; % Gaussian pulse width [ ps ]
PA = exp(-2*log(2)*T.^2/Tp^2) +eps; % Gaussian pulse

% Phase modulation
d_mod = 1i*pi;
PA = PA.*exp(d_mod*cos(T*pi/Tw));

% Initial solution to the CW LLE, set roots to select branch (3,3) for
% lower branch, probably (3,1) for upper branch.
psi0 = init_hom(zeta0,F0^2,3,3); % dimensionless
Ai = psi0/sqrt(gamma*L/alpha); % real amplitude [ sqrt(W) ]

% Driver definition
if init
    if pulsed
        FT = PA;
        figure(8);yyaxis left
        plot(T,abs(PA).^2)
        ylabel('Intensity (rel.)')
        xlabel('Fast time (ps)')
        yyaxis right
        plot(T,angle(PA))
        ylabel('Phase')
    else
        FT = CW;
    end
end
% average pump power, for information
Pav = trapz(abs(FT).^2)/trapz(abs(CW).^2)/mode_cut*Pin0;

% Noise
noise = nf *h *randn(1,N) .*exp(1i*pi*rand(1,N));
Ai = Ai + noise;

if init % give initial field if this is a first run
    A = Ai.*FT;
end

S = FT*sqrt(Pin(1)); % total pump field [ profile * amplitude ]

if external==1 % get initial spectrum
    B = ifftshift(ifft(S-sqrt(theta1)*A));
else
    B = ifftshift(ifft(A));
end
```

This part is also much the same as in the dimensionless program, but with a few possibilities left out. We also convert the homogenous CW solution ψ_L to a real value $Ai: A_L = \psi_L \sqrt{\alpha/\gamma L}$, to start the pulse peak amplitude near the lower branch CW equilibrium state. After creating the Gaussian driving pulse, with half-maximum width of 0.85 ps, we calculate now the average

incident power P_{av} for our useful information. In this scenario, $P_{av}=0.34$ W. We also pre-plot the incident pulse drive profile.

Section 6

```
%% Section 6 - Operators

% Roundtrip spectral dispersion operator, beta*L [ radians ]
r_phase = polyval([f_b(1:end-2);dbeta1*1e3;0],2*pi*f*1e-3) *L;

% Apply saturable exponential decay to bus-coupling if realistic
if spectral_loss
    r_theta1 = theta1./(exp(kappa_slope*2*pi*f)+theta1);
    r_alpha = (r_theta1+theta0)/2;
else
    r_theta1 = theta1;
    r_alpha = alpha;
end

% Linear operator
D = ifftshift(-r_alpha+1i*r_phase);

% Nonlinear operator
% linear Raman response function
frChiR = 1i*ifftshift(2*pi*f)*fr_raman*t_raman;
wrc = 2*pi*20; % peak frequency
% simplified Raman response function
frChiR = frChiR.*exp(-ifftshift(2*pi*f).^4/wrc^4);
```

This section is where we calculate the LLE operators directly. The dispersion operator is found with the polynomial coefficients f_b , and inserting the intracavity desynchronisation value δf_{eo} (here inserted as $dbeta1$) according to Eq. 1.40. The coefficient units on this line are in fs and μm . For the loss operator, without spectral loss, the roundtrip coupling and dissipation values θ and α are a simple constant, otherwise we calculate $\theta(\omega)$ based on Eq. 2.24.

The Raman impulse response is created here next. In this example, we set up a simplified linear ramp based on t_raman as the model described in section 2.4.4, with a cut-off frequency around ± 15 THz. The impulse response can be made more realistic following the example given in Fig. 1.13. In this scenario regardless, SRS is not used.

Section 7

```
%% Section 7 - Graphing Prep

% Axes limits
SLimit = [-100 30]; % spectrum axis limit [ dBm ]
% intracavity field limit [ 10log(W) ]
```

Appendix C. Numerical method

```
PLimit = [0 10*log10(2.25*max(Pin)*theta1/alpha^2)+10*log10(y_scale)];
fLimit = [min(f) max(f)]/t_scale +f0;
TLimit = [min(T) max(T)]*t_scale;

% Setting data to record
Aa = zeros(rs,N);          % fast time vs. slow time array
Ss = zeros(rs,N);          % same for pump function (if changing every sample)

% Plot info and data containers
PlotData = struct('space_x',T*t_scale,...
    'space_y',10*log10([abs(A).^2;abs(S).^2]*y_scale),...
    'mode_x',f+f0,...
    'mode_y',10*log10(abs(B).^2*y_scale),...
    'amplitude',0);
PlotAxInfo = struct('space',[TLimit PLimit],...
    'mode',[fLimit SLimit],...
    'labl',['t_{ph}: 0; zeta = 'num2str(de(1)/alpha)],'zlabl','Frequency');

% Initialise live-view figure
figure(1);clf
set(gcf, 'Renderer','painters')
[info_label,graph1,graph2] = cavity_view_v4(1,'standard',PlotData,PlotAxInfo);

% Check dispersion and loss profile
figure(7)
yyaxis left
plot(f+f0,-imag(fftshift(D))*D1/(2*pi)^2*1e3,'k')
ylabel('D_{int}/2\pi (GHz)')
xlabel('Fast Frequency (arb.)')
axis([fLimit,1e3*fsr*[-1 1]])
if spectral_loss
    yyaxis right
    semilogy(f+f0,r_theta1*D1/(2*pi)^2*1e6)
    ylabel('\kappa/2\pi (MHz)')
end

% figure(8)
% plot(f,fftshift(imag(frChiR)))
% ylabel('Raman response')
% xlabel('Relative frequency (THz)')
```

This section on graph and data preparation is the same as described earlier, only here we can also plot the linear operators including both dispersion and loss, and SRS.

Section 8

```
%% Section 8 - Run
% return          % if you don't actually want to run

% For accidentally large data setup
```

C.3 Script for simulating the realistic LLE in Si₃N₄ with advanced examples

```
if rs*N>50000000
    disp('Warning! Large Data')
    pause()
end

tic      % measure run time
% Actually run, for ever simulation step
for j=1:r

    % Hard excitation
    if (j==exctr&&excite)
        Ecs = sqrt(2*de(j)/(gamma*L));
        Tcs = sqrt(abs(beta2)*L/(2*de(j)));
        A = A + Ecs*sech((T-exT)/Tcs)*exp(0.5*1i);
    end

    % Driver definition this step
    S = FT*sqrt(Pin(j));

    %%% actual process %%%      parameters in units of per roundtrip
    A = LLE_splitstep(A,D-1i*de(j),sqrt(theta1).*S,gamma*L,h/alpha);
    %      A = LLE_splitstepR(A,D-1i*de(j),sqrt(theta1).*S,gamma*L,frChiR,h/alpha);

    % Storage sampling / recording
    if mod(j/store,1)==0
        Aa(j/store,:) = A;      % sample field
        Ss(j/store,:) = S;      % sample driver
    end

    % viewing
    if mod(j/view,1)==0
        if external==1
            % show out-coupled spectrum
            B = ifftshift(ifft(S))-sqrt(r_theta1).*ifftshift(ifft(A));
        else
            % show internal spectrum
            B = ifftshift(ifft(A));
        end

        graph1.YData = 10*log10(abs(B).^2*y_scale);
        graph2(1).YData = 10*log10(abs(A).^2*y_scale);
        graph2(2).YData = 10*log10(abs(S).^2*y_scale);
        info_label.String = ['t_{ph}: ',num2str(round(j*h)),...
            '\zeta = ',num2str(round(10*de(j)/alpha)/10)];
        pause(plot_time)
    end

    % Driver desynchronisation
    if desynch
        to = -h/alpha*de_rf(j)/fsr^2;      % fast time shift [ ps ]
        FT = fft(fftshift( ifftshift(ifft(FT))...
            .*exp(2j*pi*f*to) ));      % apply temporal shift
    end
end
```

Appendix C. Numerical method

```
end

% Injected fast time noise per simulation step
noise = nf *h *randn(1,N) .*exp(1i*pi*rand(1,N));
A = A + noise;

end
toc

% return      % to skip post-processing
```

The looping process proceeds much the same as in the dimensionless case, only with all units and dimensions evaluated according to the relations given in Eqs. 1.55. There is a brief exception called here in case the number of saved points is going to exceed 50 million, giving you a chance to cancel the run because this will likely case Matlab to become quite slow handling all the following plots. There is the opportunity here to swap the `LLE_splitstep` function for the `LLE_splitstepR` function to include the Raman impulse response, but we won't in this example.

Every time the option `external` is enabled, we apply the spectral out-coupling operator (see Eq. 1.61) to obtain the microcomb as it is measured at the exit of the waveguide device. For clarity in this example, we will live-view the logarithmic scale of the intracavity field which will help us see the decay of the DWs beyond the driving pulse profile. If `desynch` is enabled, then the input drive pulse will laterally move the amount to every evaluation step, calculated here from the value `de_rf` (δf_{eo}) in frequency. The usual random noise is also injected every step here as well.

Plotting the output, including slow vs. fast frequency, and noise transfer - Section 9

```
%% Section 9 - Post report

% Find average drift of single soliton over total simulation run
[~,mi] = max(abs([Aa(1,:);Aa(rs,:)]),[],2);
To1 = (T(mi(1))-T(mi(2)))/(rs*store);
de_rf1 = To1*fsr^2*alpha/h;

% Necessary window functions to prevent spectral leakage
WinLong = window(@hann,rs);
WinShort = window(@hann,N);
% WinLong = ones(rs,1);
% WinShort = ones(N,1);

% Process output to take into account external coupling or not, measure
% overall energy, and generate frequency vs. frequency plot ("Nonlinear
% Dispersion Relation")
if external==1
    % total out-coupled time and frequency domain
```



```

Aout = fft(ifft(Ss,[],2)-ifftshift(sqrt(r_theta1))...
.*ifft(Aa,[],2),[],2);
Bb = ifftshift(ifft(Aout.*WinShort',[],2),2);

Bf = ifft(abs(Aout).^2,[],2);          % power spectrum
% total output power over time
CP = 1/N*trapz(abs([Aout,Aout(:,1)]')).^2);
else
    % total internal spectrum
    Bb = ifftshift(ifft(Aa.*WinShort',[],2),2);
    Bf = ifft(abs(Aa).^2,[],2);
    CP = 1/N*trapz(abs([Aa,Aa(:,1)]')).^2);
end
% slow freq. vs. fast freq. analysis including windowing
I = fftshift(ifft(WinLong.*ifftshift(Bb,2)));

% microcomb RF repetition rate beatnote signal amplitude
beat_amp = Bf(:,2); clear Bf;
beat_sp = fft(detrend(angle(beat_amp)))*dt;      % beatnote phase noise
beat_psd = fftshift(fft(WinLong.*beat_amp)*dt); % rep. rate beatnote

% y-axis for final data presentation
Zeta = linspace(zeta0,zeta2,rs);
if zeta2>zeta0
    Y = Zeta;
    ylab = '\zeta_0';
else
    Y = t;
    ylab = 't_{ph}';
end

% Plotting
% Evolution of spectral envelope over slow time
figure(2);
imagesc(f+f0,Y,10*log10(y_scale*abs(Bb).^2));colormap(turbo);caxis(SLimit)
ylabel(ylab)
xlabel('Frequency (THz)')
cob = colorbar; ylabel(cob,'Power (dBm)')

% "Space-time" figure (slow time vs. fast time)
figure(3);
imagesc(T,Y,log10(abs(Aa).^2));colormap(turbo);caxis([-2 2])
ylabel(ylab)
xlabel('Fast time (ps)')
xlim(1.5*[-1 1])
cob = colorbar; ylabel(cob,'Power (log[W])')

% Total/average energy over time
figure(4);
plot(Y,CP)
xlabel(ylab)
ylabel('Power out')

```

Appendix C. Numerical method

```
% "Energy-momentum" slow frequency vs. fast frequency figure
figure(5);
imagesc(f+f0,rf*1e-6,10*log10(abs(I).^2));colormap(hot);
% surf(f+f0,rf,10*log10(abs(I).^2));colormap(hot);shading interp
% imagesc(f+f0,rf*1e-6,10*log10(abs(I).^2)...
%      -ones(rs,1)*max(10*log10(abs(I).^2)));colormap(hot);
set(gca,'ydir','normal')
ylabel('Slow frequency (MHz)')
xlabel('Fast frequency (THz)')
caxis([-180 -20])
cob = colorbar; ylabel(cob,'Power')

% Average microcomb envelope over time, in case of instability
figure(12);
plot(f+f0,10*log10(mean(abs(Bb).^2)))

% Beatnote power spectral density ("ESA" measurement)
figure(11);
plot(rf*1e-6,10*log10(abs(beat_psd).^2))
xlabel('Slow Frequency (MHz)')
ylabel('dB/Hz')
```

See ‘Section 7’ in C.2.1 for a careful explanation of the post-processing and plotting part. This section here is the same, only with experimental dimensions: eg. the intracavity field over slow time $A(\tau, t)$; the out-coupled field

$$A_{\text{out}}(\tau, t) = A_{\text{in}}(\tau, t) - \Theta(\tau) \otimes A(\tau, t) \quad (\text{C.6})$$

recalling Eqs. 1.58 and 1.61, which you can see in the program is calculated in the Fourier domain; the output microcomb spectrum over slow time

$$B(\omega, t) = \mathcal{F}_\tau [W_\tau A_{\text{out}}(\tau, t)] \quad (\text{C.7})$$

; the slow vs. fast frequency density (NDR)

$$I(\omega)(\omega, f) = \mathcal{F}_t \left[W_t \mathcal{F}_\tau [W_\tau A_{\text{out}}(\tau, t)] \right] \quad (\text{C.8})$$

; and beatnotes such as `beat_psd` obtained in the same way as described in the previous section. For historical reasons, $A_{\text{in}}(\tau, t)$ is represented as `Ss` in the program.

Let’s run the script. You should see in the live-view the narrow dissipative soliton excited upon the Gaussian pulse drive, in log scale. The soliton will emit one particularly strong DW to the right, which will travel around the cavity fast time window and come back into contact with

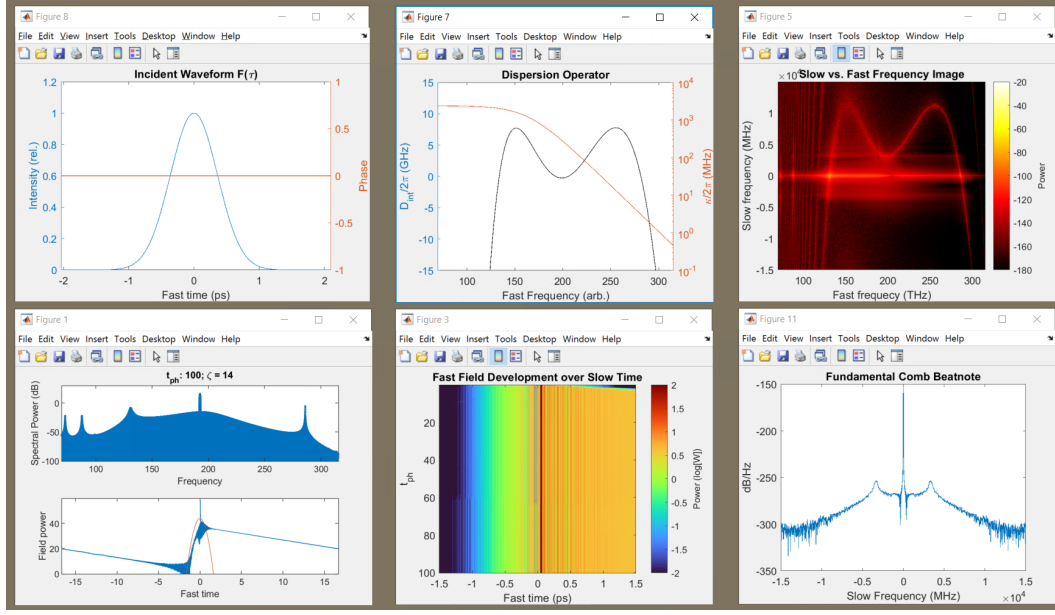


Figure C.10: **Visual output from pulse-driven octave-spanning microcomb simulation.** Script: 'lle_SiNcavity_v4c_Soliton_h750_w3500_15GHz_Example_1_s1'. Figures shown: (Top-left) The driving pulse profile $F(\tau)$ intensity and phase; (Bottom-left) The live-view plot (now concluded), with frequency domain top and time domain bottom; (Top-centre) D_{int} on the left axis and $\kappa(\omega)$ on the right axis. (Bottom-centre) Slow vs. fast time domain image (log scale), showing the soliton emitting a strong DW; (Top-right) Slow time vs. fast frequency, showing the microcomb band and the background quartic RRC; (Bottom-right) The average repetition rate beatnote spectral density.

the soliton on the left, decaying in amplitude as it goes. When the run finished, the following important plots will have been created, highlighted in Fig. C.10.

The plot at the upper middle shows the sextic $D_{\text{int}}(\omega)$ in black, with two zero-crossings approximately an octave apart, promoting DW generation. In orange, the value of $\kappa(\omega)$ is plotted showing our simplified low-pass model, reaching saturation at long wavelengths (since you cannot have $\kappa \geq D_1$). This is noticeable in the final microcomb profile in the lower left, where we can see that the short wavelength dispersive wave is much sharper than the long wavelength one due the higher cavity Q at this location, just as investigated in section 2.4.4. This results in it travelling a further fast-temporal distance around the intracavity window, wrapping around to meet the soliton again. It must be clarified again however that, as said at the start, due to our `mode_cut=2` the fast time span is cut in half, and in the real scenario, this dispersive wave would have decayed much more before wrapping around.

In the upper right we see the slow vs. fast frequency picture, showing the bright microcomb band intersecting with the RRC (in this case D_{L-}) at two points creating the dual-DW. Due to κ_{ex} , the microcomb is seen to be a little bit more noisy on the long wavelength side here. Since the hard-excitation and relaxation of the soliton is included in this run, this has excited

dual comb sidebands (seen as soft-red horizontal bands above and below the microcomb band). These bands coincide with the cavity detuning $\delta\omega$ or the C -resonance, and are also seen clearly in the comb repetition rate beatnote plotted in the lower right.

C.3.2 Beware numerical Faraday Instability and quasi-phase matching!

See the two extra dispersive waves in the final microcomb profile in the lower right in Fig. C.10? They are **fake numerical-HDW**! As said near the beginning of this section, the total evaluation rate of the split-step algorithm, `LLE_splitstep` here, also known as `h_rate`, is 240 GHz. This is effectively a 240 GHz phantom waveguide Bragg grating, where light propagates through alternating dispersion-only and nonlinear-only segments. Just as discussed at length in chapter 4, this creates strong quasi-phase matching in the slow frequency space (Floquet dimension) at this frequency, like a kind of macro-simulated FSR. These two DW appear where the sixth-order polynomial D_{int} wraps or ‘folds’ within the 240 GHz space, and are hence artefacts. We can get rid of them by increasing `h_rate`, but this will slow the simulation. Another way to get rid of them could be to increase $\kappa(\omega)$ towards infinity at these long wavelengths, but right now we don’t mind. One way to make this problem far worse would be model our dispersion with more polynomial orders than 6. This would cause D_{int} to rapidly fold over this split-step zone many more times, leading to artificial instability. Furthermore, with high intracavity CW powers, this phantom phase-matching could promote *numerical Faraday Instability*. Avoiding this is what helps us decide our `h_rate`.

C.3.3 Modelling repetition rate noise transfer in pulse-driven microcombs

Here we will go through an example analysing how repetition rate noise on the input driving pulse transfers to the soliton, depending on where the soliton is trapped on the pulse drive envelope. This example in particular repeats the result presented in the supplementary information to the published pulse-driven microcomb result [191], where a hypothetical ‘depressed’ pulse is used to lock the soliton in the middle of a shallow basin in the pulse drive centre, hence transferring much less jitter compared with at the pulse edge.

Put in the following settings in **Section 1**:

```
% Resonator dimensions
L = 5180;
Aeff = 1.46;

% Waveguide dispersion fitting parameters \beta(\omega) [ in fs^k/um ]
f_b=[-0.02;
6.95;
7.43]; % polynom. orders 6 to 0 for this device

% orders of 'beta', useful to know, converted to ps^k/um just because.
beta0 = f_b(end);
```

C.3 Script for simulating the realistic LLE in Si₃N₄ with advanced examples

```
beta1 = f_b(end-1)*1e-3;
beta2 = f_b(end-2)*2*1e-6;

fsr = 1/(L*beta1);      % Free-spectral range [ THz ]
% Orders of modal dispersion, for information [ 2pi*THz ]
D1 = 2*pi*fsr;
D2 = -beta2*L*D1^3/(2*pi);

% Loss
kappa0 = 1e-12*2*pi*50e6;      % intrinsic linewidth [ THz ]
kappa1 = 1e-12*2*pi*50e6;      % external-to-bus linewidth [ THz ]

% de-synchronization
de_rf0 = 0;      % external driving desynch [ THz ]
de_rr0 = 0;      % internal field desynch [ THz ]
```

This sets up our microresonator from section 2.5.2, with a fixed designed length of 5,180 μm and modelled cross-section $A_{\text{eff}} = 1.46 \mu\text{m}^2$, and a chosen $\beta_2 = -0.04 \text{ fs}^2/\mu\text{m}$. We set $\kappa_0 = \kappa_{\text{ex}} = 2\pi \cdot 50 \text{ MHz}$ and any average desynchronisation to zero.

Where not mentioned here explicitly, keep the settings the same as they are in the above program in section C.3.1, and if there are errors, try to use common sense. Set the following values for **Section 2**:

```
mode_cut = 2;
N = 2^11;      % number of points/modes [ ]

F0 = sqrt(25);      % dimensionless forcing term [ sqrt(P/P_thresh) ]

% Define detuning boundaries [ 2*delta_omega/kappa ]
zeta0 = 15;
zeta2 = 15;

% Define simulation duration, in photon lifetime [ 2/kappa ]
if zeta2~=zeta0

else
t_end = 160;      % for stationary, [do 4000 for example]
end

% Define simulation frequencies
h = 2^-1*alpha;      % step length [ snap to roundtrip ]
store = alpha/h*2^6; % data storage period [ snap to roundtrip ]
view = store*2^5;      % real-time graphing period [ simulation steps ]
```

Meaning that we only model every second comb mode (and cut out half the boundary fast time span) for 2^{11} modes total. We set relative driving strength to 25, relative detuning to 15, initial run duration to 160 photon lifetimes, evaluating twice per roundtrip, sampling only every 64 steps, and viewing every 32 samples. In **Section 3** set:

```
init = 1;      % initial state yes/no
```

Appendix C. Numerical method

```
excite = 1;          % hard excitation yes/no
exctr = 1;          % excite step number
pulsed = 1;         % temporally-structured driving function yes/no

% Extra settings
external = 0;       % get spectrum outside resonator yes/no
spectral_loss = 0;  % non-uniform spectral kappal
nf = 0.001;        % noise factor
exT = +1.0;        % where you excite a soliton [ ps ]
% input field desynchronisation yes/no (eg. rf noise)
desynch = 1;
```

So we are initialising a pulse-driven simulation with a hard-excited soliton, with no external measurement of the microcomb (unnecessary) or spectrally dependent loss. We set a broadband noise to 0 since this is not the noise transfer we are measuring this time, and set the location where we hard-excite the soliton to be $\tau = +1$ ps. Finally, we set `desynch` to true, enabling our pulse drive function to undergo jitter every step. To **Section 4**:

```
rs = round(t_end/(h*store));    % no. of steps stored

% rf noise
n_band = max(rf);
n_trace1 = lowpass(randn(1,r+store),n_band,h_rate*1e12,...
'ImpulseResponse','iir','Steepness',0.9);
rfn2 = 100e3*1e-12;            % rep-rate frequency noise

% slow-time input desynchronisation rate
de_rf = de_rf0*ones(1,r);      % constant desynch
de_rf = de_rf + rfn2*n_trace1(1+store:r+store);
```

Here we make sure we are evaluating so that r/rs is an integer. We prepare a Gaussian noisy trace `n_trace1` for every evaluation step `h`, and then low-pass it below the data recording/sampling rate `max(rf)`, determined by `store`. This is to make sure we are not introducing excessive super-high offset frequency noise into the system, as well as making sure it is not aliased down to our data recording bandwidth. Any low-pass function will achieve this, but here we make use of a Matlab digital filter function "lowpass" (which comes with the signal processing model) to make sure of a hard cut-off beyond our sampling rate. We add an initial padding of `store` to the trace since the lowpass filter is causal in time and can't smoothen the first few points. We give this noisy trace an standard deviation amplitude on the order of 10s kHz and add it to the 'desynchronisation' trace `de_rf`. To **Section 5**:

```
% Pulse
Tp = 1.4/sqrt(2*log(2));        % pulse width [ ps ]
PA = exp(-2*log(2)*(T-0.65*Tp).^2/Tp^2) ...
+exp(-2*log(2)*(T+0.65*Tp).^2/Tp^2) +eps;
PA = PA/PA(N/2);
```

This creates a special pulse profile about 2 ps wide, made up of two Gaussian pulses shifted slightly away from each other, creating a pulse that has a shallow dip 1 ps wide in the centre. In this first run, the soliton is going to be excited on the steep right edge. To **Section 7**:

```
figure(9)
subplot 211
plot((1:r)*h/(alpha*fsr)*1e-6,(de_rf-mean(de_rf))*1e9)
ylabel('\delta f_{eo} (kHz)')
xlabel('Time (\mus)')
subplot 212
histogram((de_rf-mean(de_rf))*1e9)
xlabel('\delta f_{eo} (kHz)')
```

This gives us a pre-run run plot where we can examine the kind of noise we are putting on the input pulse repetition rate. To **Section 9**, the post-processing part, add the following after Bb, Bf, and I are calculated:

```
% Noise Transfer
beat_amp = Bf(:,2); % rep rate signal
NH = ceil(1000/mode_cut);
hetbeat_amp = Bb(:,N/2-NH); clear Bf; % comb mode signal at NH

% df_amp = de(1:store:end)*fsr/(2*pi)+f0; % pump carrier frequency
% de_spf = fft(WinLong'.*df_amp)*sqrt(dt)/rs; % pump carrier spectral density
% df_phase = detrend(cumsum(2*pi*df_amp*dt*1e12)); % pump carrier phase noise
% de_spp = fft(WinLong'.*df_phase)*sqrt(dt)/rs; % pump carrier phase noise spectrum

% Re-sampling the injected RF noise
drf_amp = de_rf(1:store:end)+mode_cut*fsr; % input RF frequency
drf_spf = fft(WinLong'.*drf_amp)*sqrt(dt)/rs; % input RF spectral density
drf_phase = detrend(cumsum(2*pi*drf_amp*dt*1e12)); % input RF phase noise
drf_spp = fft(WinLong'.*drf_phase)*sqrt(dt)/rs; % input RF phase noise spectrum

% Comb repetition rate beatnote phase noise
beat_sp = fft(WinLong.*detrend(unwrap(angle(beat_amp))/mode_cut))*sqrt(dt)/rs;
beat_psd = fftshift(fft(WinLong.*beat_amp)*sqrt(dt)/rs);

% Comb heterodyne beatnote phase noise
hetbeat_sp = fft(WinLong.*detrend(unwrap(angle(beat2_amp))))*sqrt(dt)/rs;
hetbeat_psd = fftshift(fft(WinLong.*hetbeat_amp)*sqrt(dt)/rs);

% Transfer magnitude between input and output noise
% NT = abs(beat_sp)./abs(de_spp)'; % noise transfer
NT = abs(hetbeat_sp)./abs(drf_spp)'; % noise transfer

figure(5);
imagesc(f,rf*1e-6,10*log10(abs(I).^2)-ones(rs,1)*max(10*log10(abs(I).^2)));
colormap(hot);
ylabel('Slow frequency (MHz)')
xlabel('Fast frequency (THz)')
caxis([-40 0])
ylim([-50 50])
cob = colorbar; ylabel(cob,'Power (rel.) (dB)')
```

Appendix C. Numerical method

```
figure(6);
subplot 311
semilogx(fftshift(rf),10*log10(abs(drf_spp).^2));
ylabel('dBc/Hz')
xlabel('Slow frequency (Hz)')
title('Input RF Noise')
grid on

subplot 312;
semilogx(fftshift(rf),10*log10(abs(hetbeat_sp).^2));
ylabel('dBc/Hz')
xlabel('Slow frequency (Hz)')
title('Output RF Noise')
grid on

subplot 313;
semilogx(fftshift(rf),10*log10(abs(NT).^2));
ylabel('dB')
xlabel('Slow frequency (Hz)')
title('Transfer - Rep. rate Beatnote')
grid on
line(n_band*[1 1],ylim,'color','r','linestyle','--','linewidth',1)
line(kappa/(2*pi)*[1 1]*1e12,ylim,...
'color',[0 0.6 0],'linestyle','--','linewidth',1)
line(dw2/(2*pi)*[1 1]*1e12,ylim,...
'color','b','linestyle','--','linewidth',1)

figure(11);
plot(rf*1e-6,10*log10(abs(beat_psd).^2))
xlabel('Slow Frequency (MHz)')
ylabel('dB/Hz')
```

As described in the noise analysis example in section C.2.3, we grab the complex signal amplitude (`beat_amp`) from the first line (first, not zeroth) of the soliton output ‘power spectrum’, the spectrum of the power signal seen in the fast photodiode current. We obtain our microcomb heterodyne beatnote `hetbeat_amp` at the NH mode, in this case $\mu = 1000$, or $\omega/2\pi = 192 + 28$ THz.

Commented out are optional lines where, if we put the noisy trace on the detuning array `de`, we can re-calculate this noise according to our sampling frequency for analysis, but in this example we are studying repetition rate noise from our pulse drive `drf_amp`. For the ‘ESA’ measurement of this, we calculate its spectrum `drf_spf`. We extract the phase from `drf_amp` and integrate to get `drf_phase`, and convert it to the spectrum `drf_spp` (ie. $S_{\delta\phi}^{\text{rf}}(f)$). For the measured heterodyne beatnote phase noise, we convert `hetbeat_amp` to `hetbeat_sp` (ie. $S_{\delta\phi}^{\mu}(f)$), and optionally likewise for the repetition rate beatnote `beat_sp`, but in this example we are looking at transfer to the microcomb laser line phase noise far from the pump centre, as in the experiment (see section 2.5). Finally, we calculate the transfer function `NT`

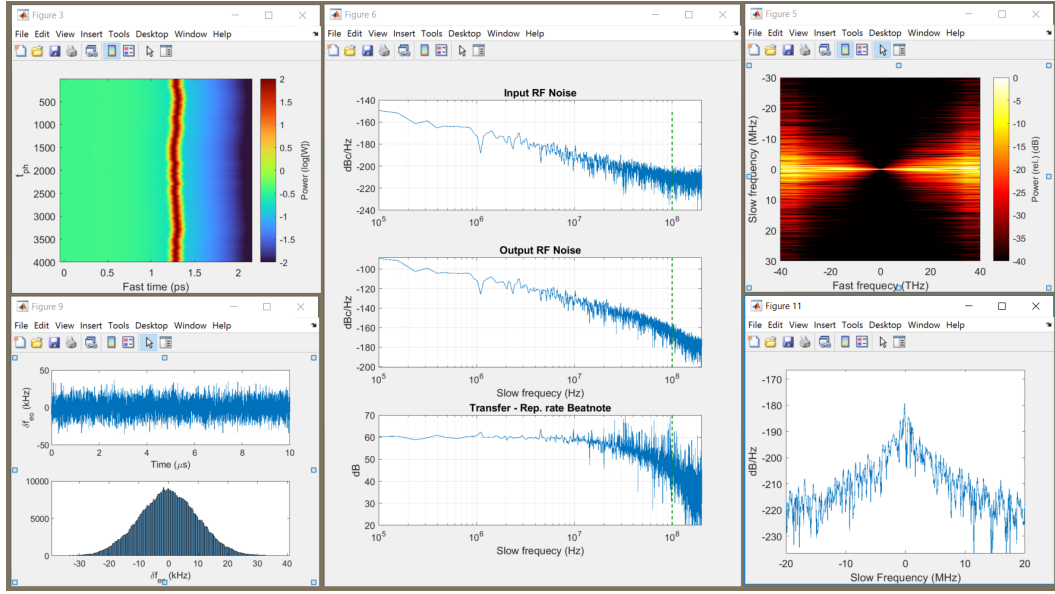


Figure C.11: **Visual output from pulse-driven soliton noise-transfer simulation.** Script: 'lle_SiNcavity_v4c_Soliton_PulsedNoise_28GHz_Example_1_s2'. Figures shown: (Top-left) Slow vs. fast time domain image (log scale) with soliton inheriting jitter from driving pulse; (Bottom-left) The pre-made noise trace for the fluctuations on the input pulse repetition rate over time (top) and in histogram (bottom); (Centre) Input frequency noise of the RF source controlling the driving pulse repetition rate (top), heterodyne beatnote phase noise of the $\mu = 1000^{\text{th}}$ comb mode (middle), and the transfer magnitude between the two (bottom); (Top-right) Slow time vs. fast frequency (ie. comb mode heterodyne beatnote), normalised to peak for each μ ; (Bottom-right) PSD of heterodyne beatnote signal at mode $\mu = 1000$ or $\omega/2\pi = 28$ THz.

$$T^{\mu}(f) = \frac{|S_{\delta\phi}^{\mu}|}{|S_{\delta\phi}^{\text{rf}}|} \quad (\text{C.9})$$

Next, we make sure the slow vs. fast frequency plot (figure(5)) has the correct units, and is normalised to the peak of the beatnote signal of each comb mode μ . Then, in figure(6), we plot the noise input, output, and transfer function in semilog-x fashion.

Run the program. In this first initial run, the dissipative soliton is excited near the right edge of this pulse, and takes some time to move towards its trapping point and halt.

Now, make the following brief changes to the script:

```
t_end = 4000;
init = 0;
excite = 0;
```

and run again to observe low-frequency noise transfer down to . On an average work computer

Appendix C. Numerical method

the simulation should take around 10 minutes give or take. All the while you may observe regular visual updates on the live-view plot. At the conclusion of the run, you should see the important figures in Fig. C.11. In the upper left slow vs. fast time plot, we see the soliton trapped at the right edge of the fast-jittering pulse drive background, and it appears to have inherited most of this jitter. In the upper right slow vs. fast frequency plot, we see the noise *multiplication* from the repetition rate of the pulse drive across every comb mode, and particularly the heterodyne beatnote of the $\mu = 1000$ th mode shown in the lower right. In the centre plots, we see the input and output phase noise, and transfer function between them. The transfer low-pass gain equals 60 dB, or $\mu^2 = 1000^2$ as expected. The bandwidth of this transfer is very large going almost up to the linear cavity bandwidth at 100 MHz, indicating a very ‘tight grip’ on the soliton. This transfer function measured and graphed here appears quite rough, but we have the option of smoothening it out simply by running the simulation again several times (for example 8 times) and averaging this trace. This was done for the plots in Fig. 2.28 to observe the smoother transfer functions.

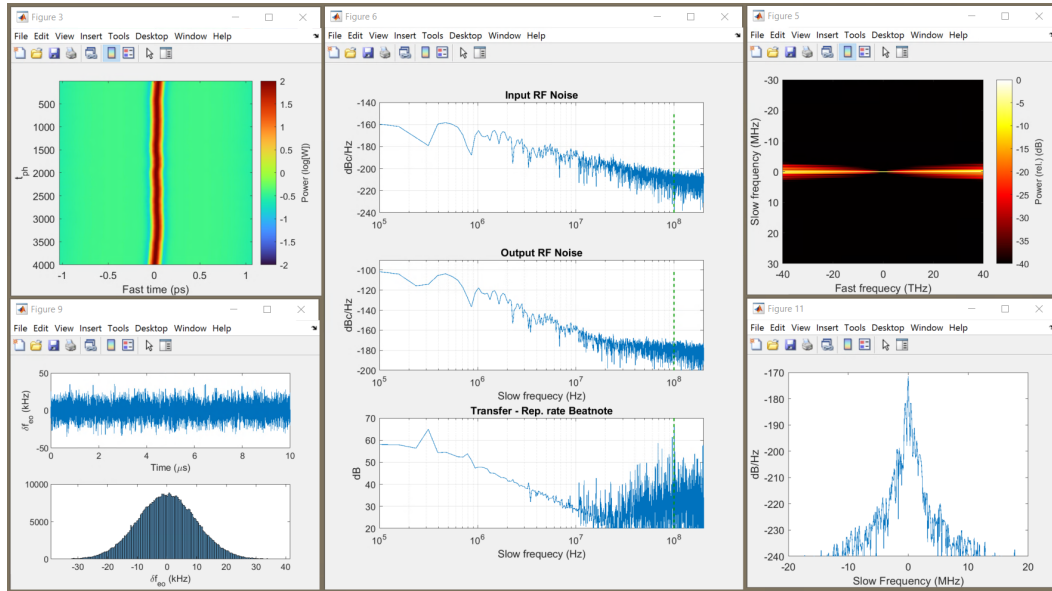


Figure C.12: **Visual output from pulse-driven soliton noise-transfer simulation, flat pulse centre.** Script: ‘lle_SiNcavity_v4c_Soliton_PulsedNoise_28GHz_Example_1_s4’. Figures shown: (Top-left) Slow vs. fast time domain image (log scale) with soliton inheriting less jitter from driving pulse; (Bottom-left) The pre-made noise trace for the fluctuations on the input pulse repetition rate over time (top) and in histogram (bottom); (Centre) Input frequency noise of the RF source controlling the driving pulse repetition rate (top), heterodyne beatnote phase noise of the $\mu = 1000$ th comb mode (middle), and the transfer magnitude between the two (bottom); (Top-right) Slow time vs. fast frequency (ie. comb mode heterodyne beatnote), normalised to peak for each μ ; (Bottom-right) PSD of heterodyne beatnote signal at mode $\mu = 1000$ or $\omega/2\pi = 28$ THz.

Now, go back to reinitialise the simulation as above, with `init=1;_excite=1;_t_end=160` and this time set `exT=0.0` in order to, this time, hard-excite the soliton in the middle of the

driving pulse's 'depression'. Let the soliton relax to its preferred trapping point, then proceed as above now with $t_{\text{end}}=4000$ to observe the long term noise transfer. This time, we see the resulting plots shown in Fig. C.12, and the difference is clear. With the same input jitter on the drive pulse, much less jitter is transferred to the soliton due to the fact that it is balanced within a flatter, shallower basin. In the transfer function trace in the lower centre, we see the corner frequency has shrunk dramatically to about 500 kHz, and noise multiplication over the microcomb linewidth has significantly narrowed.

C.3.4 Generating a zero dispersion soliton microcomb

This section will go through the program to re-create the modelling presented in section 3.2.2, particularly in Fig. 3.12. Here a ZDS⁽⁵⁾ is formed in an overall quartic-dispersion landscape creating a second 'zeroth-order' dispersive wave on the short wavelength side, and also amid a roundtrip-varying dispersion promoting the generation of two additional 'first-order' dispersive waves (ie. HDW).

Start with the program layout described in section C.3.1, and set the following values, **Section 1**:

```
% Resonator dimensions
L = 5180;          % length [ um ]
Aeff = 1.4;        % waeguide nonlinear area [ um^2 ]

% Waveguide dispersion fitting parameters \beta(\Omega) [ in fs^k/um ]
f_b=[0.030684323601653;
-0.018630862980875;
0.002245087483122;
6.922120682156940;
7.408129115638022];
beta_var = 0.2;

% orders of 'beta', useful to know, converted to ps^k/um just because.
beta0 = f_b(end);
beta1 = f_b(end-1)*1e-3;
beta2 = f_b(end-2)*2*1e-6;
beta3 = f_b(end-3)*6*1e-9;
beta4 = f_b(end-4)*24*1e-12;

f0 = 192.3;        % centre frequency [ THz ]
fsr = 1/(L*beta1); % Free-spectral range [ THz ]

% Orders of modal dispersion, for information [ 2pi*THz ]
D1 = 2*pi*fsr;
D2 = -beta2*L*D1^3/(2*pi);
D3 = -beta3*L*D1^4/(2*pi);
D4 = -beta4*L*D1^5/(2*pi);

% Loss
```

Appendix C. Numerical method

```
% real resonator has ~average kappa of 208
kappa0 = 1e-12*2*pi*60e6;      % intrinsic linewidth [ THz ]
kappa1 = 1e-12*2*pi*155e6;     % external-to-bus linewidth [ THz ]

% de-synchronization
de_rf0 = 0;                    % external driving desynch [ THz ]
de_rr0 = -130e-9;              % internal field desynch [ THz ]
```

The dispersion and loss coefficients were found from back-calculation from experimental data found in Fig. 3.9. The value of repetition rate offset `de_rr0` was found through trial and error. Importantly, we set the dispersion modulation depth `beta_var:Δ = 0.2`, which is also a trial value. Next, in **Section 2**:

```
% Define simulation width
mode_cut = 8;

N = 2^10;                % number of points/modes [ ]

F0 = sqrt(16);           % dimensionless forcing term [ sqrt(P/P_thresh) ]

% Define detuning boundaries [ 2*delta_omega/kappa ]
zeta0 = 0;
zeta2 = 8.4;

% Define simulation duration, in photon lifetime [ 2/kappa ]
if zeta2~=zeta0
    t_end = 50*abs(zeta2-zeta0);    % for scanning
else
    t_end = 50;                    % for stationary
end

% Define simulation frequencies
h = 2^-4*alpha;              % step length [ snap to roundtrip ]

store = alpha/h*2^4; % data storage period [ snap to roundtrip ]
view = store*2^1;          % real-time graphing period [ simulation steps ]
```

This time we are saving a lot of computing power by only simulating every 8th comb mode, cutting out 87.5% of the temporal window, which is empty save for relatively weak dispersive wave emissions. If we wanted to double check the result, we can set `mode_cut=1`; $N=2^{13}$ to simulate the the full fast time span but it will take a very long time for little difference. This program will scan the detuning from $\zeta_0 = 0$ to 8.4, at a rate of $\Delta t/\Delta\zeta_0 = 50$, first forming a SW front and ending where the ZDS is able to exist. We are evaluating 16 times per roundtrip, recording every 16 roundtrips, and live-viewing every 2 samples. In **Section 3**:

```
% Scenario
init = 1;                % initial state yes/no
excite = 0;              % hard excitation yes/no
exctr = 1;               % excite step number
pulsed = 1;              % temporally-structured driving function yes/no
```

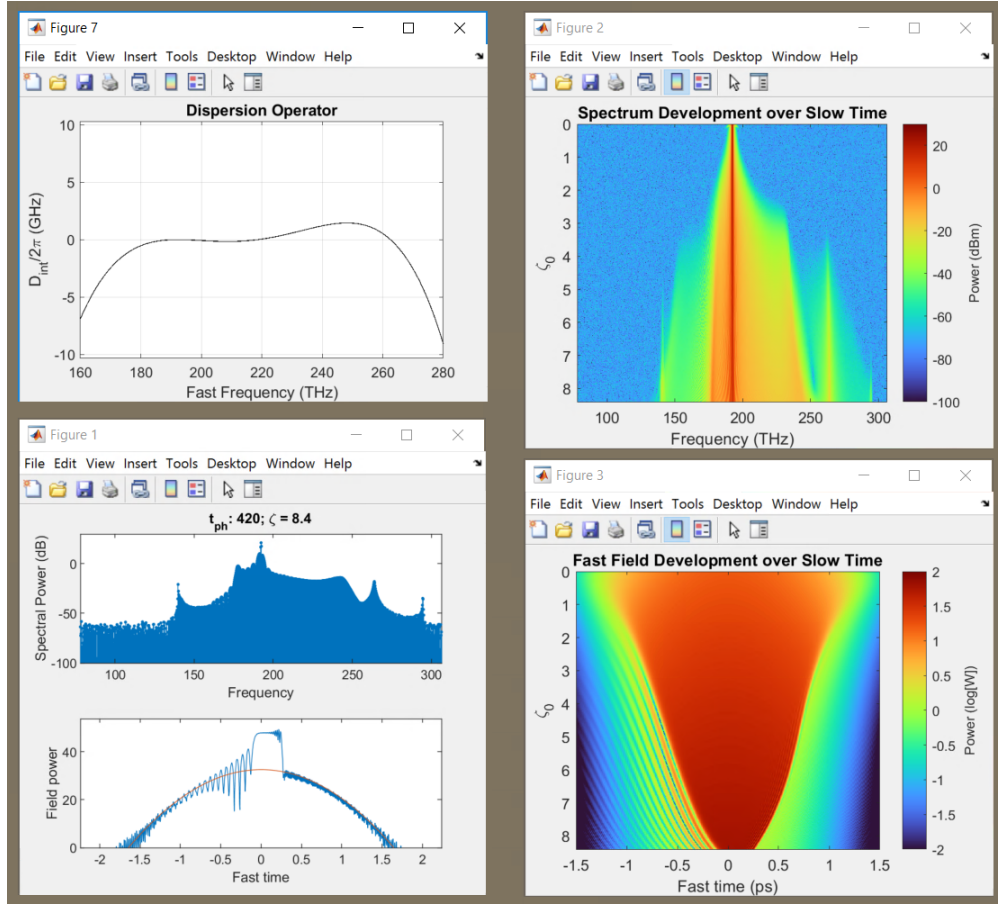


Figure C.13: **Visual output from pulse-driven scan for SW/ZDS generation.** Script: 'lle_SiNcavity_v4c_ZDSFormation_HDW_Example_s1_scan'. Figures shown: (Top-left) The quartic, normal D_{int} profile. (Bottom-left) The live-view plot (now concluded), with frequency domain top and time domain bottom; (Top right) Slow time vs. fast frequency, showing the evolution of the ZDS microcomb profile; (Bottom-centre) Slow vs. fast time domain image, showing the SW formation.

```
% Extra settings
external = 1;           % get spectrum outside resonator yes/no
spectral_loss = 0;      % non-uniform spectral kappa1
nf = 0.1;               % noise factor
% input field desynchronisation yes/no (eg. rf noise)
desynch = 0;
```

This is to start an initialised run, not hard excitation, with pulse driving, out-coupled microcomb measurement, no spectral loss, and no input pulse desynchronisation (although the intracavity field $A(\tau)$ is desynchronised). To **Section 4 and 5**:

```
rs = round(t_end/(h*store)); % no. of steps stored
```

Appendix C. Numerical method

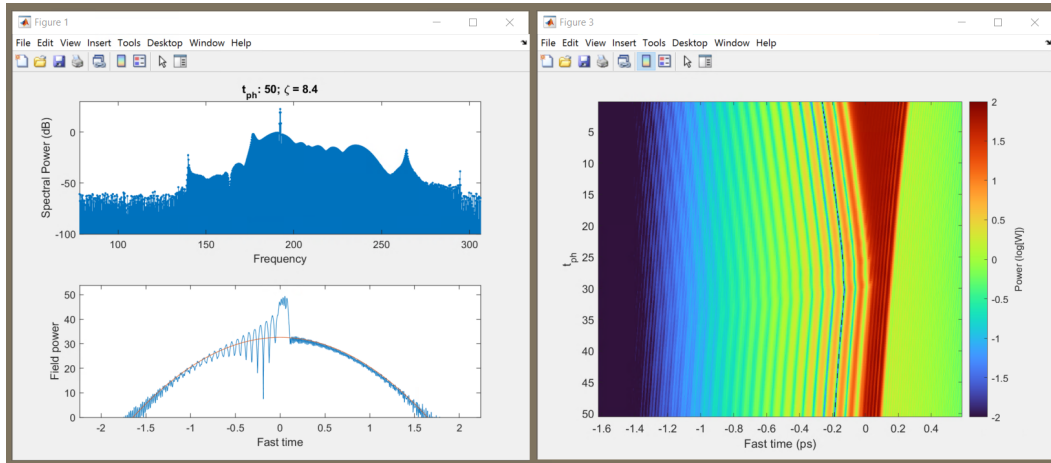


Figure C.14: **Visual output from pulse-driven scan for ZDS formation.** Script: 'lle_SiNcavity_v4c_ZDSFormation_HDW_Example_s2_interlock'. Figures shown: (Left) The live-view plot (now concluded), with frequency domain top and time domain bottom, showing the stable ZDS⁽⁵⁾ microcomb with HDWs; (Right) Slow vs. fast time domain image, showing the two SW fronts coming together and locking on their top level.

```
% Pulse
Tp = 1;
PA = exp(-2*log(2)*T.^2/Tp^2) +eps;

psio = init_hom(zeta0,F0^2,3,1);          % dimensionless
```

for creating our Gaussian pulse drive, and starting the pump amplitude in the stable upper state. To **Section 8** (the looping process), add the following at the LLE split-step line:

```
% Roundtrip perturbation
dbeta = 1+beta_var*(cos(2*pi*mod(j,ntr)/ntr));
A = LLE_splitstep(A,real(D)+1i*imag(D)*dbeta-1i*de(j),sqrt(theta1).*S,...
    gamma*L,h/alpha);
```

This will modulated the total dispersion operator sinusoidally over a 16-step long roundtrip cycle.

Run the program. Assuming there are no errors, you should see in the live-view the gradual formation of the SW front upon the pulse drive as the detuning is increased. When the simulation ends, the SWs should be moving towards each other gradually. We need to stop the scan here to let them coincide and lock without collapsing. You should see the following important plots shown in Fig. C.13. Make the following quick changes to the program:

```
zeta0 = 8.4;

init = 0;          % initial state yes/no
excite = 0;        % hard excitation yes/no
```

and run again. Now, at a static detuning of $\zeta_0 = 8.4$ the two SWs are moving freely inward towards each other. They lock to form a ZDS⁽⁵⁾, in this instance, shown here in Fig. C.14. If the simulation runs for a longer amount of time, the ZDS will probably collapse over the left side of the pulse drive. Changing the value of `de_rr0` carefully can enable a stable trap, but this will require trial and error to achieve authentically.

To analyse the ‘fine’ roundtrip dynamics of the parametrically modulated ZDS and the origin of the two HDW, make the following short changes to the program and run again:

```
% Define simulation duration, in photon lifetime [ 2/kappa ]
if zeta2~=zeta0
else
    t_end = 2;                % for stationary
end

store = alpha/h*2^-3; % data storage period [ snap to roundtrip ]

init = 0;                    % initial state yes/no
excite = 0;                  % hard excitation yes/no
```

Now we are recording the ZDS at rate of 8 times per roundtrip (ie. $f_s = 224$ GHz), which will give us a clear view of the oscillating HDW stimulated by the dispersion modulation. After running the program now, we see the output in Fig. C.15.

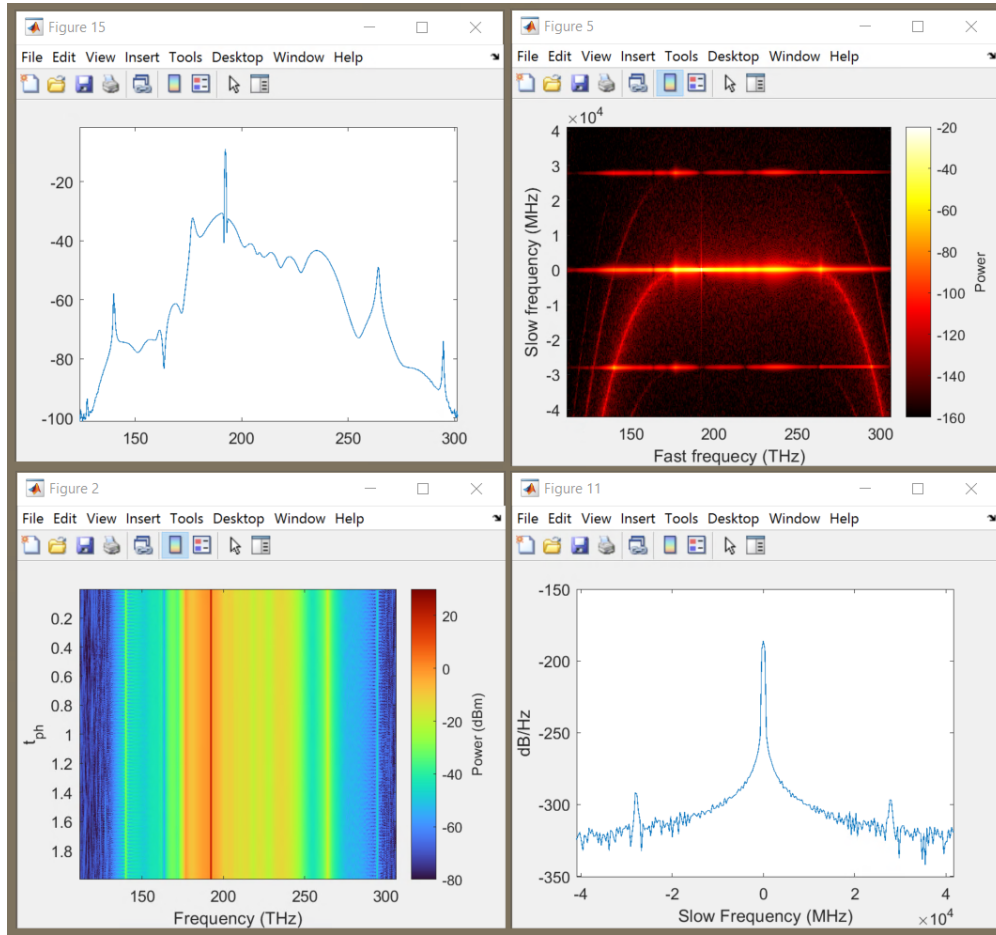


Figure C.15: **Visual output from pulse-driven scan for ZDS formation.** Script: 'lle_SiNcavity_v4c_ZDSFormation_HDW_Example_s3_KellyExamine'. Figures shown: (Top-left) The average ZDS microcomb envelope, obtained over several resonator cycles. (Bottom-left) Slow time vs. fast frequency, showing the evolution of the ZDS spectrum inside several roundtrips, revealing the oscillations of the HDW; (Top-right) Slow vs. fast frequency density, showing the bright microcomb band across the centre, the background quartic RRC, and Floquet bands spaced by $D_1/2\pi = 28$ GHz; (Bottom-right) The average repetition rate beatnote spectral density, showing Floquet sidebands at ± 28 GHz.

C.3.5 Soliton with HDW analysis

In this last advanced scenario, we will analyse the soliton microcomb that exists in the experiment presented in Fig. 4.12, where this time we are implementing the *realistic pulse-like* roundtrip dispersion modulation, due to the short and sharp mode-suppression segment in the resonator (see Fig. 4.6 and 4.7). When looking at the frequency vs. frequency picture, this produces quite a dramatic image.

Start with the above default program in section C.3.1, and set the following, **Section 1**:

C.3 Script for simulating the realistic LLE in Si₃N₄ with advanced examples

```
% Resonator dimensions
Aeff = 2.1;      % waveguide nonlinear area [ um^2 ]

f0 = 192.5;      % starting frequency [ THz ]

% Orders of modal dispersion, from experiment [ 2pi*THz ]
D1 = 2*pi*0.01506085;
D2 = 14.3e-9*(2*pi);
D3 = 6.59e-12*(2*pi);
D4 = -3.84e-15*(2*pi);

fsr = D1/(2*pi);
beta0 = 7.408129115638022;
beta1 = 6.922120682156940*1e-3;
w0 = 2*pi*f0;
L = 1/(fsr*beta1);

% orders of 'beta', useful to know, converted to ps^k/um just because.
beta2 = -D2/(L*D1^3)*(2*pi);
beta3 = -D3/(L*D1^4)*(2*pi);
beta4 = -D4/(L*D1^5)*(2*pi);

% Waveguide dispersion fitting parameters \beta(\omega) [ in fs^k/um ]
f_b=[beta4/24*1e12;
beta3/6*1e9;
beta2/2*1e6;
beta1*1e3;
beta0];
beta_var = -1.7;      % opposite dispersion flip (in case normal to anomalous)

% Loss
kappa0 = 1e-12*2*pi*30e6;      % intrinsic linewidth [ THz ]
kappa1 = 1e-12*2*pi*230e6;      % external-to-bus linewidth [ THz ]
kappa_slope = 0.007;      % exponential decay in kappa1 [ 1/THz ]

% de-synchronization
de_rf0 = 0;      % external driving desynch [ THz ]
de_rr0 = -8.498927970554518e-07;      % internal field desynch [ THz ]
```

This time we are putting in the directly measured values of D_ℓ taken from our dispersion measurement of the experimental device, and converting them to coefficients β_ℓ and f_b . We need to set a highly specific value of de_rr0 in order to keep the soliton on the pulse. This value was found by exciting the same soliton with CW driving under a neutral synchronisation, then using the peak-detect code described earlier to calculate de_rr0 . For **Section 2**:

```
% Define simulation width
mode_cut = 2;

N = 2^13;      % number of points/modes [ ]

F0 = sqrt(15);      % dimensionless forcing term [ sqrt(P/P_thresh) ]
```

Appendix C. Numerical method

```
% Define detuning boundaries [ 2*delta_omega/kappa ]
zeta0 = 15.0;
zeta2 = 15.0;

% Define simulation duration, in photon lifetime [ 2/kappa ]
if zeta2~=zeta0

else
    t_end = 200*alpha;          % for stationary
end

% Define simulation frequencies
h = 2^-6*alpha;               % step length [ snap to roundtrip ]

store = alpha/h*2^0; % data storage period [ snap to roundtrip ]
view = store*2^0;          % real-time graphing period [ simulation steps ]
```

As usual, we are skipping every second comb mode with `mode_cut` to speed things up. We set a static detuning at $\zeta_0 = 15$ with equal pump power. This time with `t_end=200*alpha` we are explicitly setting the time duration to be 200 roundtrips precisely. The evaluation rate is set to be 64 times per roundtrip (ie. $f_r = 964$ GHz) in order to reveal this process. Initially, we set the sampling rate to once per roundtrip ($f_s = 15$ GHz), live-viewing every sample. Next, in **Section 3**:

```
% Scenario
init = 1;          % initial state yes/no
excite = 1;        % hard excitation yes/no
exctr = 1;         % excite step number
pulsed = 1;        % temporally-structured driving function yes/no

% Extra settings
external = 1;      % get spectrum outside resonator yes/no
spectral_loss = 1; % non-uniform spectral kappa1
nf = 0.01;         % noise factor
exT = -0.0;        % where you excite a soliton [ ps ]
% input field desynchronisation yes/no (eg. rf noise)
desynch = 0;
```

to initialise the run with a hard-excited soliton in the pulse drive centre, with out-coupled spectral measurement, and spectral loss enabled. To **Section 5**:

```
% Pulse
Tp = 1.1;
PA = exp(-2*log(2)*T.^2/Tp^2) +eps;

psi0 = init_hom(zeta0,F0^2,3,3); % dimensionless
```

to set up the pulse drive profile and initial amplitude. Add the following to the end of **Section 6**:

```
% Roundtrip dispersion evolution
j = 1:ntr;
nt_z = 1/32*ntr/sqrt(log(2));
e_d = ntr/2;
ddbeta = +exp(-(j-ntr/2).^2/nt_z^2);
ddbeta = ddbeta/abs(sum(ddbeta)) *e_d*beta_var;
dbeta = 1 +ddbeta -mean(ddbeta);

% dbeta = 1+beta_var*(-cos(2*pi*mod(j,ntr)/ntr));

figure(6);bar(0:ntr-1,dbeta,1)
ylim(ntr/2*[-1/2,1])
```

This pre-prepares a 64-step long pulsed profile with which to modulate the magnitude of the dispersion. At this recent stage it is somewhat overcomplicated, but the idea is to make a longitudinal adjustable-width Gaussian pulse that can have either a positive or negative relative amplitude and that retains an even duty-cycle so that the average dispersion $\bar{\beta}_2$ remains constant, and the variance of this excursion is proportional to our parameter `beta_var`. In this specific case, the flat-level of the dispersion will in fact be anomalous ($\beta_2(t=0) < 0$) and then will deviate strongly normal ($\beta_2(t) > 0$) over a short step duration of `nt_z`. Overall, the average dispersion will be anomalous ($\bar{\beta}_2(t) < 0$). This modulation factor (essentially $1 + \Delta(t)$) is plotted further below in Fig. C.16.

In **Section 8**, modify the split-step line to include the modulation:

```
A = LLE_splitstep(A,real(D)+1i*imag(D)*dbeta(mod(j,ntr)+1)-1i*de(j),...
    sqrt(theta1).*S,gamma*L,h/alpha);
```

In **Section 9**, let's arrange a surf-plot to examine the frequency vs. frequency diagram in maximum detail:

```
figure(5);
surf(f+f0,rf,10*log10(abs(I).^2));colormap(hot);shading interp
set(gca,'ydir','normal')
ylabel('Slow frequency (MHz)')
xlabel('Fast frequency (THz)')
caxis([-160 -20])
cob = colorbar; ylabel(cob,'Power')
```

Now, run the program as we have arranged, to excite a dissipative soliton and let it relax into its equilibrium after 200 roundtrips. After this first run is done, set `t_end=10*alpha;`, `store=alpha/h*2^-6;`, and `init=0;excite=0;` to continue the run. This time, the duration will be exactly 10 roundtrips, and now we have set `store` so that $f_s = f_r$, the maximum. Run again now, and observe in the live-view how the microcomb envelope at its wings (but not the central core) and the various HDW undergo a breathing cycle each roundtrip. When the run is completed, we should see the important plots shown in Fig. C.16. What we see here is that in

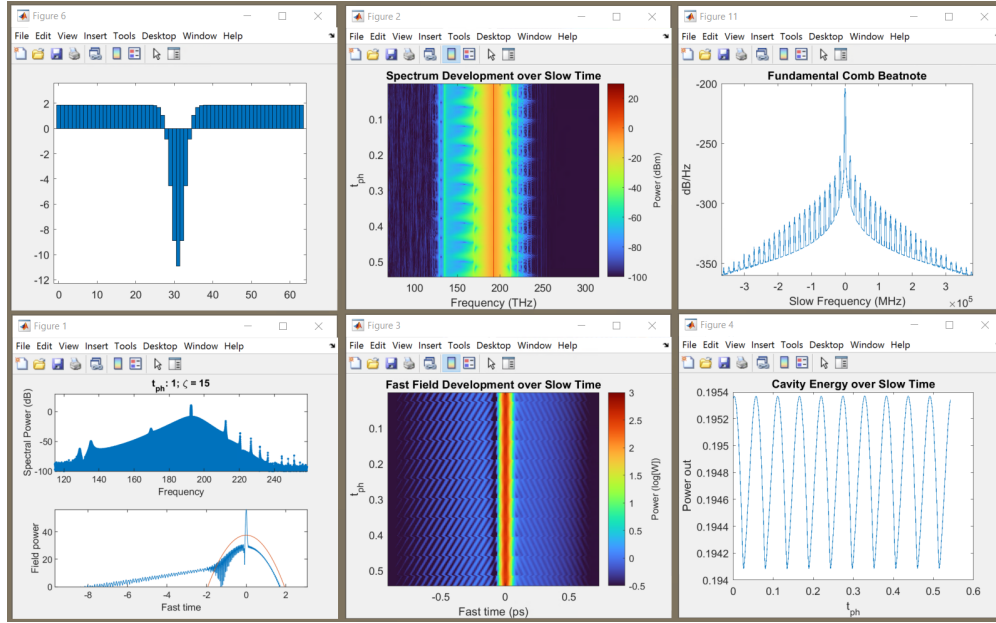


Figure C.16: **Visual output from dispersion-pulsed dissipative soliton microcomb.** Script: 'lle_SiNcavity_v4c_SolitonHDW_F1C16R6TM_Parametric_1'. Figures shown: (Top-left) The dispersion modulation factor $1 + \Delta(t)$, plotted over 64 steps of a roundtrip cycle; (Bottom-left) The live-view plot (now concluded), with frequency domain top and time domain (log scale in dBm) bottom; (Top-centre) Slow time vs. fast frequency, showing the fine evolution of the soliton spectrum over 10 roundtrips of the resonator; (Bottom-centre) Slow vs. fast time domain image (log scale), showing the soliton emitting a periodically varying HDW over 10 roundtrips; (Top-right) The un-folded, super-resolution repetition rate beatnote, showing a whole other comb in the Floquet dimension; (Bottom-right) Average power of the soliton field over the 10 roundtrips.

for much of the roundtrip propagation the soliton is calm, and then for a brief period in the middle of the circuit the soliton is strongly perturbed by this normal-dispersion section. It undergoes a brief breathing cycle, and the main HDW emitted (to the left in this case) rapidly retreats by one period, in a 'saw-tooth' like motion, progressively moving left each roundtrip. In the 'Floquet' dimension, the 'slow' frequency RF domain measured in MHz and GHz this causes many sidebands to emerge all spaced by the FSR, forming a whole new comb in this dimension. Of course, in experiment we cannot see this since we only 'sample' the soliton once per roundtrip at 15 GHz, causing all of these sidebands to collapse into a single repetition rate beatnote. In this simulation, we're sampling at a 'super'-rate of $f_r = 964$ GHz, hence revealing this behaviour.

In Fig. C.17, we highlight especially the slow vs. fast frequency density of this simulation, in 3D this time, showing effectively a 2-dimensional microcomb with a dual-FSR of 15 GHz. Each comb tooth is spaced apart in the optical domain by 15 GHz, but the soliton itself also breathes and emits a pulsating dispersive wave at 15 GHz, meaning every comb mode possesses its own RF microcomb with 15 GHz spacing. The optical-domain profile is smooth since we

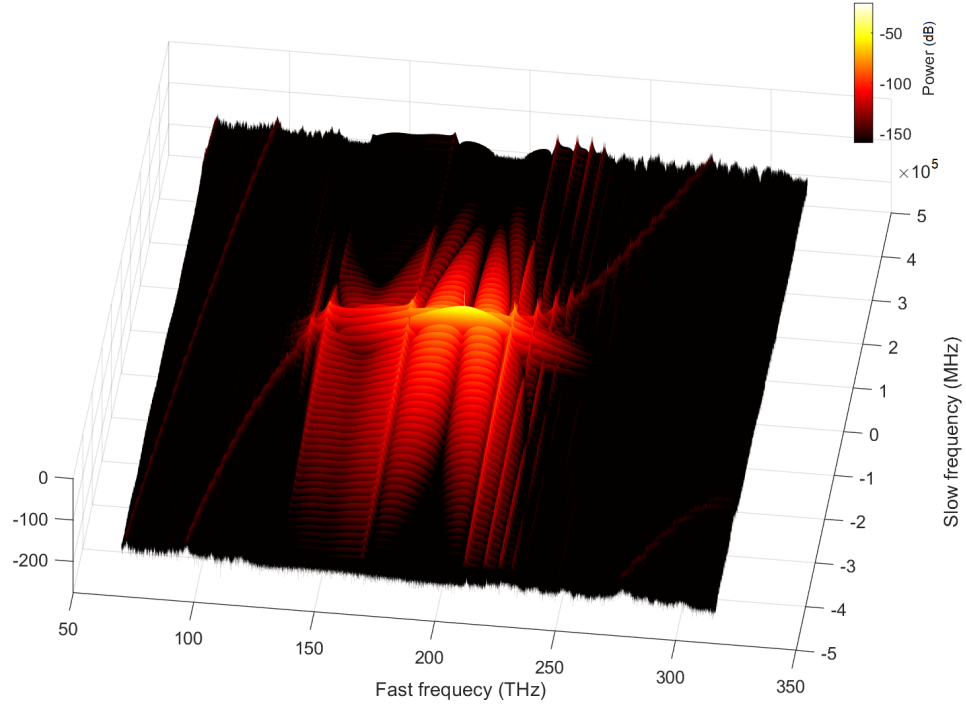


Figure C.17: **Super-resolution view of dispersion-pulsed dissipative soliton microcomb.** Script: 'lle_SiNcavity_v4c_SolitonHDW_F1C16R6TM_Parametric_1'. This is the slow vs. fast frequency density of a dissipative soliton undergoing a pulsating dispersion every roundtrip at 15 GHz, sampled 64 times per roundtrip.

are capturing “one soliton at a time” in the fast time picture, since we are measuring over 10 roundtrips in slow time, the RF domain envelope is sliced into different rows. If you were to run this program one more time and set $\tau_{\text{end}} = \alpha$; ie. measure for a single roundtrip, you will see a completely smooth profile in 3D, representing one space-time event.

Some further specific analysis can be found in the supplementary information to the dispersion-modulated dissipative structures publication: [190].

C.4 Simulation parameter tables

Appendix C. Numerical method

Parameter		Value		
Symbolic	Matlab	Fig. 4.3	Fig. 4.11	Fig. 4.14
N	N	2^{10}	2^{10}	2^{10}
$\delta\tau$	Tw	60	60	60
F_0^2	F0^2	10	10	10
ζ_0	zeta0	5, 4 (for Ψ_L, Ψ_H)	10	6
Δ	eta_a	0.5	0.7	0.7
$\partial_1/2\pi$	1/eta_p	8	16	16
d_2		1	-1	1
f_r	1/h	512	512	512
f_s	1/store/h	64	128, 16	128, 16

Table C.1: **Simulation parameters used for select dimensionless investigations.**

Parameter		Value	
Symbolic	Matlab	Fig. 2.2, 2.3,2.4,2.5,2.6	
n_2 ($\mu\text{m}^2/\text{W}$)	n2	2.4×10^{-7}	
A_{eff} (μm^2)	Aeff	1.98	
$D_1/2\pi$ (GHz)	fsr	20 (2.2,2.6), 1000 (2.3(a)), 10 (2.3(b)), 100 (2.5)	
β_0 (/ μm)	beta2	7.493	
β_1 (fs/ μm)	beta3	6.913	
β_2 (fs ² / μm)	beta2	-0.01348	
β_3 (fs ³ / μm)	beta3	0	
δf_{eo} (kHz)	de_rr0	0	
$\kappa_{\text{ex}}/2\pi$ (MHz)	kappa1/2/pi	25	
$\kappa_0/2\pi$ (MHz)	kappa0/2/pi	25	
ξ (/THz)	kappa_slope	0	
f_R	fr_raman	0	
τ_R (fs)	t_raman	20	
Simulated modes (1 out of every -)	mode_cut	1	
Number of modes	N	2^8 (2.3(a)), 2^{14} (2.3(b)), 2^{10} (2.5), 2^{13} (2.6)	
τ_p (ps)	Tp	CW or 1.1	
F_0^2	F0^2	10, or see figure	
ζ_0	zeta0	10, or see figure	
$\Delta t/\Delta\zeta_0$	10, or stationary		
Duration (t)	t_end	10, unless scanning	

Table C.2: **Parameters used for simulations modelling pulse drive scaling scenarios.**

C.4 Simulation parameter tables

Parameter		Value	
Symbolic	Matlab	Fig. 2.23	Fig. 2.27,2.28,2.30
n_2 ($\mu\text{m}^2/\text{W}$)	n2	2.4×10^{-7}	"
L (μm)	L	5180	"
A_{eff} (μm^2)	Aeff	1.46	"
$D_1/2\pi$ (GHz)	fsr	28	"
β_2 ($\text{fs}^2/\mu\text{m}$)	beta2	-0.0110	-0.04
β_3 ($\text{fs}^3/\mu\text{m}$)	beta3	-0.1382	0
δf_{eo} (kHz)	de_rr0	-49	see figure
$\kappa_{\text{ex}}/2\pi$ (MHz)	kappa1/2/pi	50	
$\kappa_0/2\pi$ (MHz)	kappa0/2/pi	50	
ξ (/THz)	kappa_slope	0.007	0
f_R	fr_raman	0.2	0
τ_R (fs)	t_raman	20	20
Simulated modes (1 out of every -)	mode_cut	4	2
Number of modes	N	2^{11}	2^{11}
M EO-comb lines	M	26 (at 28 GHz)	26
$\tilde{\beta}_2$ (ps^2)	chirp	0.4	0.3
F_0^2	F0^2	2.5 (low), 25 (high)	24
ζ_0	zeta0	see figure	12
$\Delta t/\Delta\zeta_0$		20	
Duration (t)	t_end		20000
f_r (GHz)	h_rate	FSR*2	FSR*2
f_s (GHz)	h_rate/store	FSR/32	FSR/8

Table C.3: Parameters used for simulations modelling select experimental results.

Appendix C. Numerical method

Parameter		Value	
Symbolic	Matlab	Device D72-B	Device D72-C
$D_1/2\pi$ (GHz)	D1/2/pi	15.321	15.308
$D_2/2\pi$ (kHz)	D2/2/pi	-12.925	-3.1405
$D_3/2\pi$ (Hz)	D3/2/pi	5.3638	3.345
$D_4/2\pi$ (mHz)	D4/2/pi	-2.3788	-2.4926
$\kappa_{\text{ex}}/2\pi$ (MHz)	kappa1/2/pi	180	200
$\kappa_0/2\pi$ (MHz)	kappa0/2/pi	30	30
$\Gamma/2\pi$ (MHz/W)		10.6	10.6
N	N	2048	2048
$\delta\tau$ (time window) (ps)	Tw	± 8	± 8
τ_p (ps)	Tp	0.9	0.9
F_0^2	F0^2	26	16
P_0 (W)	Pin0	6.4	4.7
ζ_0	zeta0	scan: [-4,14], stop: 8	stable: 4, unstable: 7
$\delta\omega/2\pi$ (GHz)	dw2/2/pi	scan: [-0.42,1.47], stop: 0.84	stable: 0.46, unstable: 0.81
δf_{eo} (kHz)	de_rr0	0	0, ± 600
Δ	beta_var	0.9	0.7
f_r (GHz)	h_rate	FSR*8	FSR*8
f_s (GHz)	h_rate/store	scan: FSR/16, static: FSR	FSR

Table C.4: **Parameters used for simulations modelling select experimental results.**

C.5 Tutorial videos online!

C.5.1 Dispersion modelling with COMSOL

At <https://www.youtube.com/watch?v=Xh6Tax7NgGc>, the video titled *COMSOL simulation tutorial: Dispersion Engineering in Micro-ring Resonators* part of the channel “Optomechanical Technologies - ETN”.

This tutorial by me was recorded at the FEM workshop organized by EPFL in October 2017, part of the OMT ETN workshop series. In it I give a basic tutorial on how to calculate the broadband dispersion of photonic waveguides, straight or bent, with COMSOL Multiphysics and Matlab. In the tutorial the example is a silica-cladded silicon nitride waveguide.

C.5.2 Simulating the GNLSE for supercontinuum generation on Matlab

At https://www.youtube.com/watch?v=oWf_dA8X3fw, the video titled *Introduction to NLSE simulation / supercontinuum generation* part of the channel “K-LAB”.

This tutorial and lecture by me was recorded during the MICROCOMB ITN – CMEP workshop (Computational Methods for Nonlinear Photonics), February 2020, hosted by our research group. In it I give a basic overview of the nonlinear optics of the Generalised Nonlinear Schrödinger Equation (GNLSE) and how it is modelled in Matlab using `ode45`, along the lines given by *John Dudley et al.*[192]. I give several key examples of SCG processes.

Bibliography

- [1] S. Haykin and M. Moher. *Communication Systems*. Wiley, Mar. 2009.
- [2] S. T. Cundiff and J. Ye. “Colloquium: Femtosecond Optical Frequency Combs”. *Reviews of Modern Physics* 75.1 (2003), p. 325.
- [3] J. Reichert, R. Holzwarth, Th. Udem, and T. W. Hänsch. “Measuring the Frequency of Light with Mode-Locked Lasers”. *Optics Communications* 172.1 (Dec. 1999), pp. 59–68. DOI: 10.1016/S0030-4018(99)00491-5.
- [4] D. J. Jones, S. A. Diddams, J. K. Ranka, A. Stentz, R. S. Windeler, J. L. Hall, and S. T. Cundiff. “Carrier-Envelope Phase Control of Femtosecond Mode-Locked Lasers and Direct Optical Frequency Synthesis”. *Science* 288.5466 (Apr. 2000), pp. 635–639. DOI: 10.1126/science.288.5466.635.
- [5] S. A. Diddams, K. Vahala, and T. Udem. “Optical Frequency Combs: Coherently Uniting the Electromagnetic Spectrum”. *Science* 369.6501 (July 2020). DOI: 10.1126/science.aay3676.
- [6] Th. Udem, J. Reichert, R. Holzwarth, and T. W. Hänsch. “Absolute Optical Frequency Measurement of the Cesium D 1 Line with a Mode-Locked Laser”. *Physical Review Letters* 82.18 (May 1999), pp. 3568–3571. DOI: 10.1103/PhysRevLett.82.3568.
- [7] S. A. Diddams, D. J. Jones, J. Ye, S. T. Cundiff, J. L. Hall, J. K. Ranka, R. S. Windeler, R. Holzwarth, T. Udem, and T. W. Hänsch. “Direct Link between Microwave and Optical Frequencies with a 300 THz Femtosecond Laser Comb”. *Physical Review Letters* 84.22 (May 2000), pp. 5102–5105. DOI: 10.1103/PhysRevLett.84.5102.
- [8] S. Schiller. “Spectrometry with Frequency Combs”. *Optics Letters* 27.9 (May 2002), pp. 766–768. DOI: 10.1364/OL.27.000766.
- [9] T. Steinmetz et al. “Laser Frequency Combs for Astronomical Observations”. *Science* 321.5894 (Sept. 2008), pp. 1335–1337. DOI: 10.1126/science.1161030.
- [10] J. E. Stalnaker, V. Mbele, V. Gerginov, T. M. Fortier, S. A. Diddams, L. Hollberg, and C. E. Tanner. “Femtosecond Frequency Comb Measurement of Absolute Frequencies and Hyperfine Coupling Constants in Cesium Vapor”. *Physical Review A* 81.4 (Apr. 2010). DOI: 10.1103/PhysRevA.81.043840.

- [11] J. Riemensberger, A. Lukashchuk, M. Karpov, W. Weng, E. Lucas, J. Liu, and T. J. Kippenberg. “Massively Parallel Coherent Laser Ranging Using a Soliton Microcomb”. *Nature* 581.7807 (May 2020), pp. 164–170. DOI: 10.1038/s41586-020-2239-3.
- [12] P. Marin-Palomo et al. “Microresonator-Based Solitons for Massively Parallel Coherent Optical Communications”. *Nature* 546.7657 (June 2017), pp. 274–279. DOI: 10.1038/nature22387.
- [13] A. Fülöp et al. “High-Order Coherent Communications Using Mode-Locked Dark-Pulse Kerr Combs from Microresonators”. *Nature Communications* 9.1 (Apr. 2018), p. 1598. DOI: 10.1038/s41467-018-04046-6.
- [14] L. Lundberg, M. Karlsson, A. Lorences-Riesgo, M. Mazur, V. Torres-Company, J. Schröder, and P. A. Andrekson. “Frequency Comb-Based WDM Transmission Systems Enabling Joint Signal Processing”. *Applied Sciences* 8.5 (May 2018), p. 718. DOI: 10.3390/app8050718.
- [15] R. Holzwarth, Th. Udem, T. W. Hänsch, J. C. Knight, W. J. Wadsworth, and P. St. J. Russell. “Optical Frequency Synthesizer for Precision Spectroscopy”. *Physical Review Letters* 85.11 (Sept. 2000), pp. 2264–2267. DOI: 10.1103/PhysRevLett.85.2264.
- [16] D. T. Spencer et al. “An Optical-Frequency Synthesizer Using Integrated Photonics”. *Nature* 557.7703 (May 2018), pp. 81–85. DOI: 10.1038/s41586-018-0065-7.
- [17] M. Kourogi, K. Nakagawa, and M. Ohtsu. “Wide-Span Optical Frequency Comb Generator for Accurate Optical Frequency Difference Measurement”. *IEEE Journal of Quantum Electronics* 29.10 (Oct. 1993), pp. 2693–2701. DOI: 10.1109/3.250392.
- [18] S. A. Diddams et al. “An Optical Clock Based on a Single Trapped $^{199}\text{Hg}^+$ Ion”. *Science* 293.5531 (Aug. 2001), pp. 825–828. DOI: 10.1126/science.1061171.
- [19] T. Rosenband et al. “Frequency Ratio of Al^+ and Hg^+ Single-Ion Optical Clocks; Metrology at the 17th Decimal Place”. *Science* 319.5871 (Mar. 2008), pp. 1808–1812. DOI: 10.1126/science.1154622.
- [20] N. Hinkley, J. A. Sherman, N. B. Phillips, M. Schioppo, N. D. Lemke, K. Beloy, M. Pizzocaro, C. W. Oates, and A. D. Ludlow. “An Atomic Clock with 10^{-18} Instability”. *Science* 341.6151 (Sept. 2013), pp. 1215–1218. DOI: 10.1126/science.1240420.
- [21] A. D. Ludlow, M. M. Boyd, J. Ye, E. Peik, and P. O. Schmidt. “Optical Atomic Clocks”. *Reviews of Modern Physics* 87.2 (June 2015), pp. 637–701. DOI: 10.1103/RevModPhys.87.637.
- [22] M. A. Norcia, J. R. K. Cline, J. A. Muniz, J. M. Robinson, R. B. Hutson, A. Goban, G. E. Marti, J. Ye, and J. K. Thompson. “Frequency Measurements of Superradiance from the Strontium Clock Transition”. *Physical Review X* 8.2 (May 2018), p. 021036. DOI: 10.1103/PhysRevX.8.021036.
- [23] C. W. Chou, D. B. Hume, T. Rosenband, and D. J. Wineland. “Optical Clocks and Relativity”. *Science* 329.5999 (Sept. 2010), pp. 1630–1633. DOI: 10.1126/science.1192720.
- [24] C. Lisdat et al. “A Clock Network for Geodesy and Fundamental Science”. *Nature Communications* 7.1 (Aug. 2016), p. 12443. DOI: 10.1038/ncomms12443.

- [25] M. Lezius et al. “Space-Borne Frequency Comb Metrology”. *Optica* 3.12 (Dec. 2016), pp. 1381–1387. DOI: 10.1364/OPTICA.3.001381.
- [26] T. Schuldt et al. “Optical Clock Technologies for Global Navigation Satellite Systems”. *GPS Solutions* 25.3 (Apr. 2021), p. 83. DOI: 10.1007/s10291-021-01113-2.
- [27] J. Grotti et al. “Geodesy and Metrology with a Transportable Optical Clock”. *Nature Physics* 14.5 (May 2018), pp. 437–441. DOI: 10.1038/s41567-017-0042-3.
- [28] W. Liang, D. Eliyahu, V. S. Ilchenko, A. A. Savchenkov, A. B. Matsko, D. Seidel, and L. Maleki. “High Spectral Purity Kerr Frequency Comb Radio Frequency Photonic Oscillator”. *Nature Communications* 6 (Aug. 2015), p. 7957. DOI: 10.1038/ncomms8957.
- [29] X. Xie et al. “Photonic Microwave Signals with Zeptosecond-Level Absolute Timing Noise”. *Nature Photonics* 11.1 (Jan. 2017), pp. 44–47. DOI: 10.1038/nphoton.2016.215.
- [30] E. Lucas, P. Brochard, R. Bouchand, S. Schilt, T. Südmeyer, and T. J. Kippenberg. “Ultralow-Noise Photonic Microwave Synthesis Using a Soliton Microcomb-Based Transfer Oscillator”. *Nature Communications* 11.1 (Jan. 2020), pp. 1–8. DOI: 10.1038/s41467-019-14059-4.
- [31] K. Beha, D. C. Cole, P. Del’Haye, A. Coillet, S. A. Diddams, and S. B. Papp. “Electronic Synthesis of Light”. *Optica* 4.4 (Apr. 2017), pp. 406–411. DOI: 10.1364/OPTICA.4.000406.
- [32] D. T. Spencer et al. “Towards an Integrated-Photonics Optical-Frequency Synthesizer With <1 Hz Residual Frequency Noise”. In: *Optical Fiber Communication Conference (2017), Paper M2J.2*. Optical Society of America, Mar. 2017, M2J.2. DOI: 10.1364/OFC.2017.M2J.2.
- [33] D. R. Carlson, D. D. Hickstein, W. Zhang, A. J. Metcalf, F. Quinlan, S. A. Diddams, and S. B. Papp. “Ultrafast Electro-Optic Light with Subcycle Control”. *Science* 361.6409 (Sept. 2018), pp. 1358–1363. DOI: 10.1126/science.aat6451.
- [34] M. T. Murphy et al. “High-Precision Wavelength Calibration of Astronomical Spectrographs with Laser Frequency Combs”. *Monthly Notices of the Royal Astronomical Society* 380.2 (Sept. 2007), pp. 839–847. DOI: 10.1111/j.1365-2966.2007.12147.x.
- [35] R. A. McCracken, É. Depagne, R. B. Kuhn, N. Erasmus, L. A. Crause, and D. T. Reid. “Wavelength Calibration of a High Resolution Spectrograph with a Partially Stabilized 15-GHz Astrocomb from 550 to 890 Nm”. *Optics Express* 25.6 (Mar. 2017), pp. 6450–6460. DOI: 10.1364/OE.25.006450.
- [36] E. Obrzud et al. “Broadband Near-Infrared Astronomical Spectrometer Calibration and on-Sky Validation with an Electro-Optic Laser Frequency Comb”. *Optics Express* 26.26 (Dec. 2018), pp. 34830–34841. DOI: 10.1364/OE.26.034830.
- [37] Ewelina Obrzud et al. “A Microphotonic Astrocomb”. *Nature Photonics* 13.1 (Jan. 2019), p. 31. DOI: 10.1038/s41566-018-0309-y.
- [38] M.-G. Suh et al. “Searching for Exoplanets Using a Microresonator Astrocomb”. *Nature Photonics* 13.1 (Jan. 2019), pp. 25–30. DOI: 10.1038/s41566-018-0312-3.

Bibliography

- [39] P. Roztocki and R. Morandotti. “Astrocombs for Extreme-Precision Spectroscopy”. *Nature Astronomy* 3.2 (Feb. 2019), pp. 135–136. DOI: 10.1038/s41550-019-0698-y.
- [40] R. A. Probst et al. “A Crucial Test for Astronomical Spectrograph Calibration with Frequency Combs”. *Nature Astronomy* 4.6 (June 2020), pp. 603–608. DOI: 10.1038/s41550-020-1010-x.
- [41] A. A. Jørgensen et al. “Petabit-per-Second Data Transmission Using a Chip-Scale Microcomb Ring Resonator Source”. *Nature Photonics* 16.11 (Nov. 2022), pp. 798–802. DOI: 10.1038/s41566-022-01082-z.
- [42] A. Rizzo et al. “Petabit-Scale Silicon Photonic Interconnects With Integrated Kerr Frequency Combs”. *IEEE Journal of Selected Topics in Quantum Electronics* (2022), pp. 1–21. DOI: 10.1109/JSTQE.2022.3197375.
- [43] P. Trocha et al. “Ultrafast Optical Ranging Using Microresonator Soliton Frequency Combs”. *Science* 359.6378 (Feb. 2018), pp. 887–891. DOI: 10.1126/science.aao3924.
- [44] A. Lukashchuk, J. Riemensberger, M. Karpov, J. Liu, and T. J. Kippenberg. “Dual Chirped Microcomb Based Parallel Ranging at Megapixel-Line Rates”. *Nature Communications* 13.1 (June 2022), p. 3280. DOI: 10.1038/s41467-022-30542-x.
- [45] A. Lukashchuk, J. Riemensberger, A. Tusnin, J. Liu, and T. Kippenberg. *Chaotic Micro-Comb Based Parallel Ranging*. Dec. 2021. DOI: 10.48550/arXiv.2112.10241.
- [46] A. B. Fallahkhair, K. S. Li, and T. E. Murphy. “Vector Finite Difference Modesolver for Anisotropic Dielectric Waveguides”. *Journal of Lightwave Technology* 26.11 (June 2008), pp. 1423–1431. DOI: 10.1109/JLT.2008.923643.
- [47] L. G. Wright, Z. M. Ziegler, P. M. Lushnikov, Z. Zhu, M. A. Eftekhar, D. N. Christodoulides, and F. W. Wise. “Multimode Nonlinear Fiber Optics: Massively Parallel Numerical Solver, Tutorial, and Outlook”. *IEEE Journal of Selected Topics in Quantum Electronics* 24.3 (May 2018), pp. 1–16. DOI: 10.1109/JSTQE.2017.2779749.
- [48] M. Anderson. “Dynamics of Temporal Kerr Cavity Solitons: Chaos, Instability, and Multi-Resonant Solutions”. Thesis. The University of Auckland, 2016.
- [49] P. Del’Haye, O. Arcizet, M. L. Gorodetsky, R. Holzwarth, and T. J. Kippenberg. “Frequency Comb Assisted Diode Laser Spectroscopy for Measurement of Microcavity Dispersion”. *Nature Photonics* 3.9 (Sept. 2009), pp. 529–533. DOI: 10.1038/nphoton.2009.138.
- [50] J. Liu, V. Brasch, M. H. P. Pfeiffer, A. Kordts, A. N. Kamel, H. Guo, M. Geiselmann, and T. J. Kippenberg. “Frequency-Comb-Assisted Broadband Precision Spectroscopy with Cascaded Diode Lasers”. *Optics Letters* 41.13 (July 2016), pp. 3134–3137. DOI: 10.1364/OL.41.003134.
- [51] K. Ikeda. “Multiple-Valued Stationary State and Its Instability of the Transmitted Light by a Ring Cavity System”. *Optics Communications* 30.2 (Aug. 1979), pp. 257–261. DOI: 10.1016/0030-4018(79)90090-7.

-
- [52] L. A. Lugiato and R. Lefever. “Spatial Dissipative Structures in Passive Optical Systems”. *Physical Review Letters* 58.21 (May 1987), pp. 2209–2211. DOI: 10.1103/PhysRevLett.58.2209.
 - [53] M. Anderson, Y. Wang, F. Leo, S. Coen, M. Erkintalo, and S. G. Murdoch. “Coexistence of Multiple Nonlinear States in a Tristable Passive Kerr Resonator”. *Physical Review X* 7.3 (Aug. 2017), p. 031031. DOI: 10.1103/PhysRevX.7.031031.
 - [54] M. Conforti and F. Biancalana. “Multi-Resonant Lugiato-Lefever Model”. *Optics Letters* 42.18 (Sept. 2017), pp. 3666–3669. DOI: 10.1364/OL.42.003666.
 - [55] S. Coen. “Passive Nonlinear Optical Fiber Resonators Fundamentals and Applications”. Thesis. UNIVERSITÉ LIBRE DE BRUXELLES, 2000.
 - [56] S. Coen, M. Tlidi, Ph. Emplit, and M. Haelterman. “Convection versus Dispersion in Optical Bistability”. *Physical Review Letters* 83.12 (Sept. 1999), pp. 2328–2331. DOI: 10.1103/PhysRevLett.83.2328.
 - [57] T. Herr, V. Brasch, J. D. Jost, I. Mirgorodskiy, G. Lihachev, M. L. Gorodetsky, and T. J. Kippenberg. “Mode Spectrum and Temporal Soliton Formation in Optical Microresonators”. *Physical Review Letters* 113.12 (Sept. 2014), p. 123901. DOI: 10.1103/PhysRevLett.113.123901.
 - [58] E. G. A. Lucas. “Physics of Dissipative Kerr Solitons in Optical Microresonators and Application to Frequency Synthesis”. PhD thesis. Lausanne: EPFL, 2019. DOI: 10.5075/epfl-thesis-9109.
 - [59] G. Moille et al. “Broadband Resonator-Waveguide Coupling for Efficient Extraction of Octave-Spanning Microcombs”. *Optics Letters* 44.19 (Oct. 2019), pp. 4737–4740. DOI: 10.1364/OL.44.004737.
 - [60] M. Karpov, H. Guo, A. Kordts, V. Brasch, M. H. P. Pfeiffer, M. Zervas, M. Geiselmann, and T. J. Kippenberg. “Raman Self-Frequency Shift of Dissipative Kerr Solitons in an Optical Microresonator”. *Physical Review Letters* 116.10 (Mar. 2016), p. 103902. DOI: 10.1103/PhysRevLett.116.103902.
 - [61] X. Yi, Q.-F. Yang, K. Y. Yang, and K. Vahala. “Theory and Measurement of the Soliton Self-Frequency Shift and Efficiency in Optical Microcavities”. *Optics Letters* 41.15 (Aug. 2016), pp. 3419–3422. DOI: 10.1364/OL.41.003419.
 - [62] G. P. Agrawal. *Nonlinear Fiber Optics*. Ed. by P. L. Christiansen, M. P. Sørensen, and A. C. Scott. Lecture Notes in Physics. Springer Berlin Heidelberg, 2000.
 - [63] A. Tikan, F. Bonnefoy, G. Ducrozet, G. Prabhudesai, G. Michel, A. Cazaubiel, É. Falcon, F. Copie, S. Randoux, and P. Suret. “Nonlinear Dispersion Relation in Integrable Turbulence”. *Scientific Reports* 12.1 (June 2022), p. 10386. DOI: 10.1038/s41598-022-14209-7.
 - [64] A. Tikan, A. Tusnin, J. Riemensberger, M. Churaev, X. Ji, K. N. Komagata, R. N. Wang, J. Liu, and T. J. Kippenberg. “Protected Generation of Dissipative Kerr Solitons in Supermodes of Coupled Optical Microresonators”. *Science Advances* 8.13 (Apr. 2022), eabm6982. DOI: 10.1126/sciadv.abm6982.

Bibliography

- [65] M. H. Anderson, A. Tikan, A. Tuszynski, J. Riemensberger, R. N. Wang, and T. J. Kippenberg. *Dissipative Solitons and Switching Waves in Dispersion Folded Kerr Cavities*. May 2022. DOI: 10.48550/arXiv.2205.09957.
- [66] J. Jang. “Temporal Cavity Solitons in Optical Fibres Dynamics, Interactions and Temporal Tweezing”. Thesis. The University of Auckland, 2015.
- [67] C. Milián and D. V. Skryabin. “Soliton Families and Resonant Radiation in a Micro-Ring Resonator near Zero Group-Velocity Dispersion”. *Optics Express* 22.3 (Feb. 2014), pp. 3732–3739. DOI: 10.1364/OE.22.003732.
- [68] Y. He, S. Wang, and X. Zeng. “Dynamics of Dispersive Wave Emission From Dark Solitons in Kerr Frequency Combs”. *IEEE Photonics Journal* 8.6 (Dec. 2016), pp. 1–8. DOI: 10.1109/JPHOT.2016.2626004.
- [69] J. K. Jang, M. Erkintalo, S. G. Murdoch, and S. Coen. “Observation of Dispersive Wave Emission by Temporal Cavity Solitons”. *Optics Letters* 39.19 (Oct. 2014), pp. 5503–5506. DOI: 10.1364/OL.39.005503.
- [70] M. Haelterman, S. Trillo, and S. Wabnitz. “Dissipative Modulation Instability in a Nonlinear Dispersive Ring Cavity”. *Optics Communications* 91.5 (Aug. 1992), pp. 401–407. DOI: 10.1016/0030-4018(92)90367-Z.
- [71] S. Coen and M. Haelterman. “Modulational Instability Induced by Cavity Boundary Conditions in a Normally Dispersive Optical Fiber”. *Physical Review Letters* 79.21 (Nov. 1997), pp. 4139–4142. DOI: 10.1103/PhysRevLett.79.4139.
- [72] M. Conforti, A. Mussot, A. Kudlinski, and S. Trillo. “Modulational Instability in Dispersion Oscillating Fiber Ring Cavities”. *Optics Letters* 39.14 (July 2014), p. 4200. DOI: 10.1364/OL.39.004200.
- [73] H. Guo, M. Karpov, E. Lucas, A. Kordts, M. H. P. Pfeiffer, V. Brasch, G. Lihachev, V. E. Lobanov, M. L. Gorodetsky, and T. J. Kippenberg. “Universal Dynamics and Deterministic Switching of Dissipative Kerr Solitons in Optical Microresonators”. *Nature Physics* 13.1 (Jan. 2017), pp. 94–102. DOI: 10.1038/nphys3893.
- [74] E. Lucas, H. Guo, J. D. Jost, M. Karpov, and T. J. Kippenberg. “Detuning-Dependent Properties and Dispersion-Induced Instabilities of Temporal Dissipative Kerr Solitons in Optical Microresonators”. *Physical Review A* 95.4 (Apr. 2017), p. 043822. DOI: 10.1103/PhysRevA.95.043822.
- [75] S. Coulibaly, M. Taki, A. Bendahmane, G. Millot, B. Kibler, and M. G. Clerc. “Turbulence-Induced Rogue Waves in Kerr Resonators”. *Physical Review X* 9.1 (Mar. 2019), p. 011054. DOI: 10.1103/PhysRevX.9.011054.
- [76] T. Herr, K. Hartinger, J. Riemensberger, C. Y. Wang, E. Gavartin, R. Holzwarth, M. L. Gorodetsky, and T. J. Kippenberg. “Universal Formation Dynamics and Noise of Kerr-frequency Combs in Microresonators”. *Nature Photonics* 6.7 (July 2012), pp. 480–487. DOI: 10.1038/nphoton.2012.127.

- [77] P. Del’Haye, A. Schliesser, O. Arcizet, T. Wilken, R. Holzwarth, and T. J. Kippenberg. “Optical Frequency Comb Generation from a Monolithic Microresonator”. *Nature* 450.7173 (Dec. 2007), pp. 1214–1217. DOI: 10.1038/nature06401.
- [78] P. Del’Haye, T. Herr, E. Gavartin, M. L. Gorodetsky, R. Holzwarth, and T. J. Kippenberg. “Octave Spanning Tunable Frequency Comb from a Microresonator”. *Physical Review Letters* 107.6 (Aug. 2011), p. 063901. DOI: 10.1103/PhysRevLett.107.063901.
- [79] F. Leo, L. Gelens, P. Emplit, M. Haelterman, and S. Coen. “Dynamics of One-Dimensional Kerr Cavity Solitons”. *Optics Express* 21.7 (Apr. 2013), pp. 9180–9191. DOI: 10.1364/OE.21.009180.
- [80] P. Parra-Rivas, D. Gomila, M. A. Matías, S. Coen, and L. Gelens. “Dynamics of Localized and Patterned Structures in the Lugiato-Lefever Equation Determine the Stability and Shape of Optical Frequency Combs”. *Physical Review A* 89.4 (Apr. 2014), p. 043813. DOI: 10.1103/PhysRevA.89.043813.
- [81] P. Parra-Rivas, D. Gomila, L. Gelens, and E. Knobloch. “Bifurcation Structure of Localized States in the Lugiato-Lefever Equation with Anomalous Dispersion”. *Physical Review E* 97.4 (Apr. 2018), p. 042204. DOI: 10.1103/PhysRevE.97.042204.
- [82] S. Wabnitz. “Suppression of Interactions in a Phase-Locked Soliton Optical Memory”. *Optics Letters* 18.8 (Apr. 1993), pp. 601–603. DOI: 10.1364/OL.18.000601.
- [83] I. V. Barashenkov and Yu. S. Smirnov. “Existence and Stability Chart for the Ac-Driven, Damped Nonlinear Schrödinger Solitons”. *Physical Review E* 54.5 (Nov. 1996), pp. 5707–5725. DOI: 10.1103/PhysRevE.54.5707.
- [84] A. B. Matsko, A. A. Savchenkov, W. Liang, V. S. Ilchenko, D. Seidel, and L. Maleki. “Mode-Locked Kerr Frequency Combs”. *Optics Letters* 36.15 (Aug. 2011), pp. 2845–2847. DOI: 10.1364/OL.36.002845.
- [85] S. Coen and M. Erkintalo. “Universal Scaling Laws of Kerr Frequency Combs”. *Optics Letters* 38.11 (June 2013), pp. 1790–1792. DOI: 10.1364/OL.38.001790.
- [86] A. Tikan et al. “Emergent Nonlinear Phenomena in a Driven Dissipative Photonic Dimer”. *Nature Physics* 17.5 (May 2021), pp. 604–610. DOI: 10.1038/s41567-020-01159-y.
- [87] E. Lucas, M. Karpov, H. Guo, M. L. Gorodetsky, and T. J. Kippenberg. “Breathing Dissipative Solitons in Optical Microresonators”. *Nature Communications* 8.1 (Sept. 2017), p. 736. DOI: 10.1038/s41467-017-00719-w.
- [88] M. Anderson, F. Leo, S. Coen, M. Erkintalo, and S. G. Murdoch. “Observations of Spatiotemporal Instabilities in the Strong-Driving Regime of an AC-driven Nonlinear Schrödinger System”. *Optica* 3.10 (Oct. 2016), p. 1071. DOI: 10.1364/OPTICA.3.001071.
- [89] Y. S. Kivshar and B. Luther-Davies. “Dark Optical Solitons: Physics and Applications”. *Physics Reports* 298.2 (May 1998), pp. 81–197. DOI: 10.1016/S0370-1573(97)00073-2.

Bibliography

- [90] P. Parra-Rivas, D. Gomila, E. Knobloch, S. Coen, and L. Gelens. “Origin and Stability of Dark Pulse Kerr Combs in Normal Dispersion Resonators”. *Optics Letters* 41.11 (June 2016), pp. 2402–2405. DOI: 10.1364/OL.41.002402.
- [91] A. U. Nielsen, Y. Xu, M. Ferré, M. G. Clerc, S. Coen, S. G. Murdoch, and M. Erkintalo. “Engineered Discreteness Enables Observation and Control of Chimera-like States in a System with Local Coupling”. *arXiv:1910.11329 [nlin, physics:physics]* (Oct. 2019).
- [92] Y. Wang, F. Leo, J. Fatome, M. Erkintalo, S. G. Murdoch, and S. Coen. “Universal Mechanism for the Binding of Temporal Cavity Solitons”. *Optica* 4.8 (Aug. 2017), pp. 855–863. DOI: 10.1364/OPTICA.4.000855.
- [93] S. Coen, M. Haelterman, P. Emplit, L. Delage, L. M. Simohamed, and F. Reynaud. “Experimental Investigation of the Dynamics of a Stabilized Nonlinear Fiber Ring Resonator”. *JOSA B* 15.8 (Aug. 1998), pp. 2283–2293. DOI: 10.1364/JOSAB.15.002283.
- [94] E. Obrzud, S. Lecomte, and T. Herr. “Temporal Solitons in Microresonators Driven by Optical Pulses”. *Nature Photonics* 11.9 (Aug. 2017), nphoton.2017.140. DOI: 10.1038/nphoton.2017.140.
- [95] V. Brasch, E. Lucas, J. D. Jost, M. Geiselmann, and T. J. Kippenberg. “Self-Referenced Photonic Chip Soliton Kerr Frequency Comb”. *Light: Science & Applications* 6.1 (Jan. 2017), e16202. DOI: 10.1038/lsa.2016.202.
- [96] M. H. Anderson, R. Bouchand, J. Liu, W. Weng, E. Obrzud, E. Obrzud, T. Herr, and T. J. Kippenberg. “Photonic Chip-Based Resonant Supercontinuum via Pulse-Driven Kerr Microresonator Solitons”. *Optica* 8.6 (June 2021), pp. 771–779. DOI: 10.1364/OPTICA.403302.
- [97] V. Brasch, E. Obrzud, S. Lecomte, and T. Herr. “Nonlinear Filtering of an Optical Pulse Train Using Dissipative Kerr Solitons”. *Optica* 6.11 (Nov. 2019), pp. 1386–1393. DOI: 10.1364/OPTICA.6.001386.
- [98] A. Ishizawa, T. Nishikawa, A. Mizutori, H. Takara, A. Takada, T. Sogawa, and M. Koga. “Phase-Noise Characteristics of a 25-GHz-spaced Optical Frequency Comb Based on a Phase- and Intensity-Modulated Laser”. *Optics Express* 21.24 (Dec. 2013), pp. 29186–29194. DOI: 10.1364/OE.21.029186.
- [99] T. Herr, V. Brasch, J. D. Jost, C. Y. Wang, N. M. Kondratiev, M. L. Gorodetsky, and T. J. Kippenberg. “Temporal Solitons in Optical Microresonators”. *Nature Photonics* 8.2 (Feb. 2014), pp. 145–152. DOI: 10.1038/nphoton.2013.343.
- [100] C. Bao et al. “Nonlinear Conversion Efficiency in Kerr Frequency Comb Generation”. *Optics Letters* 39.21 (Nov. 2014), p. 6126. DOI: 10.1364/OL.39.006126.
- [101] X. Yi, Q.-F. Yang, K. Y. Yang, M.-G. Suh, and K. Vahala. “Soliton Frequency Comb at Microwave Rates in a High-Q Silica Microresonator”. *Optica* 2.12 (Dec. 2015), pp. 1078–1085. DOI: 10.1364/OPTICA.2.001078.

-
- [102] V. B. Braginsky, M. L. Gorodetsky, and V. S. Ilchenko. “Optical Whispering-Gallery Microresonators”. In: *Laser Applications*. Vol. 2097. SPIE, Aug. 1994, pp. 283–288. DOI: 10.1117/12.183155.
 - [103] Q. Li, T. C. Briles, D. A. Westly, T. E. Drake, J. R. Stone, B. R. Ilic, S. A. Diddams, S. B. Papp, and K. Srinivasan. “Stably Accessing Octave-Spanning Microresonator Frequency Combs in the Soliton Regime”. *Optica* 4.2 (Feb. 2017), pp. 193–203. DOI: 10.1364/OPTICA.4.000193.
 - [104] M. Karpov, M. H. P. Pfeiffer, H. Guo, W. Weng, J. Liu, and T. J. Kippenberg. “Dynamics of Soliton Crystals in Optical Microresonators”. *Nature Physics* 15.10 (Oct. 2019), pp. 1071–1077. DOI: 10.1038/s41567-019-0635-0.
 - [105] D. C. Cole, E. S. Lamb, P. Del’Haye, S. A. Diddams, and S. B. Papp. “Soliton Crystals in Kerr Resonators”. *Nature Photonics* 11.10 (Oct. 2017), pp. 671–676. DOI: 10.1038/s41566-017-0009-z.
 - [106] C. Bao, Y. Xuan, D. E. Leaird, S. Wabnitz, M. Qi, and A. M. Weiner. “Spatial Mode-Interaction Induced Single Soliton Generation in Microresonators”. *Optica* 4.9 (Sept. 2017), pp. 1011–1015. DOI: 10.1364/OPTICA.4.001011.
 - [107] Ó. B. Helgason, M. Girardi, Z. Ye, F. Lei, J. Schröder, and V. T. Company. “Power-Efficient Soliton Microcombs”. *arXiv:2202.09410 [physics]* (Feb. 2022).
 - [108] M. Malinowski, A. Rao, P. Delfyett, and S. Fathpour. “Optical Frequency Comb Generation by Pulsed Pumping”. *APL Photonics* 2.6 (May 2017), p. 066101. DOI: 10.1063/1.4983113.
 - [109] W. Weng, A. Kaszubowska-Anandarajah, J. He, P. D. Lakshmijayasimha, E. Lucas, J. Liu, P. M. Anandarajah, and T. J. Kippenberg. “Gain-Switched Semiconductor Laser Driven Soliton Microcombs”. *Nature Communications* 12.1 (Mar. 2021), p. 1425. DOI: 10.1038/s41467-021-21569-7.
 - [110] T. Kobayashi, H. Yao, K. Amano, Y. Fukushima, A. Morimoto, and T. Sueta. “Optical Pulse Compression Using High-Frequency Electrooptic Phase Modulation”. *IEEE Journal of Quantum Electronics* 24.2 (Feb. 1988), pp. 382–387. DOI: 10.1109/3.135.
 - [111] M. Fujiwara, M. Teshima, J. Kani, H. Suzuki, N. Takachio, and K. Iwatsuki. “Optical Carrier Supply Module Using Flattened Optical Multicarrier Generation Based on Sinusoidal Amplitude and Phase Hybrid Modulation”. *Journal of Lightwave Technology* 21.11 (Nov. 2003), pp. 2705–2714. DOI: 10.1109/JLT.2003.819147.
 - [112] J. Liu et al. “Monolithic Piezoelectric Control of Soliton Microcombs”. *Nature* 583.7816 (July 2020), pp. 385–390. DOI: 10.1038/s41586-020-2465-8.
 - [113] W. Weng, M. H. Anderson, A. Siddharth, J. He, A. S. Raja, and T. J. Kippenberg. “Coherent Terahertz-to-Microwave Link Using Electro-Optic-Modulated Turing Rolls”. *Physical Review A* 104.2 (Aug. 2021), p. 023511. DOI: 10.1103/PhysRevA.104.023511.

Bibliography

- [114] I. Hendry, W. Chen, Y. Wang, B. Garbin, J. Javaloyes, G.-L. Oppo, S. Coen, S. G. Murdoch, and M. Erkintalo. “Spontaneous Symmetry Breaking and Trapping of Temporal Kerr Cavity Solitons by Pulsed or Amplitude-Modulated Driving Fields”. *Physical Review A* 97.5 (May 2018). DOI: 10.1103/PhysRevA.97.053834.
- [115] I. Hendry, B. Garbin, S. G. Murdoch, S. Coen, and M. Erkintalo. “Impact of Desynchronization and Drift on Soliton-Based Kerr Frequency Combs in the Presence of Pulsed Driving Fields”. *Physical Review A* 100.2 (Aug. 2019), p. 023829. DOI: 10.1103/PhysRevA.100.023829.
- [116] M. Erkintalo, S. G. Murdoch, and S. Coen. “Phase and Intensity Control of Dissipative Kerr Cavity Solitons”. *Journal of the Royal Society of New Zealand* 52.2 (Mar. 2022), pp. 149–167. DOI: 10.1080/03036758.2021.1900296.
- [117] J. K. Jang, M. Erkintalo, S. Coen, and S. G. Murdoch. “Temporal Tweezing of Light through the Trapping and Manipulation of Temporal Cavity Solitons”. *Nature Communications* 6 (June 2015), p. 7370. DOI: 10.1038/ncomms8370.
- [118] M. H. P. Pfeiffer, C. Herkommer, J. Liu, T. Morais, M. Zervas, M. Geiselmann, and T. J. Kippenberg. “Photonic Damascene Process for Low-Loss, High-Confinement Silicon Nitride Waveguides”. *IEEE Journal of Selected Topics in Quantum Electronics* 24.4 (July 2018), pp. 1–11. DOI: 10.1109/JSTQE.2018.2808258.
- [119] J. Liu, A. S. Raja, M. H. P. Pfeiffer, C. Herkommer, H. Guo, M. Zervas, M. Geiselmann, and T. J. Kippenberg. “Double Inverse Nanotapers for Efficient Light Coupling to Integrated Photonic Devices”. *Optics Letters* 43.14 (July 2018), pp. 3200–3203. DOI: 10.1364/OL.43.003200.
- [120] V. Brasch, M. Geiselmann, T. Herr, G. Lihachev, M. H. P. Pfeiffer, M. L. Gorodetsky, and T. J. Kippenberg. “Photonic Chip-Based Optical Frequency Comb Using Soliton Cherenkov Radiation”. *Science* 351.6271 (Jan. 2016), pp. 357–360. DOI: 10.1126/science.aad4811.
- [121] J. P. Gordon. “Theory of the Soliton Self-Frequency Shift”. *Optics Letters* 11.10 (Oct. 1986), pp. 662–664. DOI: 10.1364/OL.11.000662.
- [122] M. Anderson, F. Leo, M. Erkintalo, S. Coen, and S. G. Murdoch. “Measurement of the Raman Self-Frequency Shift of a Temporal Cavity Soliton”. In: *Photonics and Fiber Technology 2016 (ACOFT, BGPP, NP) (2016), Paper NW4A.4*. Optical Society of America, Sept. 2016, NW4A.4. DOI: 10.1364/NP2016.NW4A.4.
- [123] Y. Wang, M. Anderson, S. Coen, S. G. Murdoch, and M. Erkintalo. “Stimulated Raman Scattering Imposes Fundamental Limits to the Duration and Bandwidth of Temporal Cavity Solitons”. *Physical Review Letters* 120.5 (Jan. 2018), p. 053902. DOI: 10.1103/PhysRevLett.120.053902.
- [124] M. H. P. Pfeiffer, J. Liu, M. Geiselmann, and T. J. Kippenberg. “Coupling Ideality of Integrated Planar High-Q Microresonators”. *Physical Review Applied* 7.2 (Feb. 2017), p. 024026. DOI: 10.1103/PhysRevApplied.7.024026.

-
- [125] C. Godey, I. V. Balakireva, A. Coillet, and Y. K. Chembo. “Stability Analysis of the Spatiotemporal Lugiato-Lefever Model for Kerr Optical Frequency Combs in the Anomalous and Normal Dispersion Regimes”. *Physical Review A* 89.6 (June 2014), p. 063814. DOI: 10.1103/PhysRevA.89.063814.
 - [126] W. Weng, E. Lucas, G. Lihachev, V. E. Lobanov, H. Guo, M. L. Gorodetsky, and T. J. Kippenberg. “Spectral Purification of Microwave Signals with Disciplined Dissipative Kerr Solitons”. *Physical Review Letters* 122.1 (Jan. 2019), p. 013902. DOI: 10.1103/PhysRevLett.122.013902.
 - [127] M. Schiemangk, S. Spießberger, A. Wicht, G. Erbert, G. Tränkle, and A. Peters. “Accurate Frequency Noise Measurement of Free-Running Lasers”. *Applied Optics* 53.30 (Oct. 2014), pp. 7138–7143. DOI: 10.1364/AO.53.007138.
 - [128] J. Javaloyes, P. Camelin, M. Marconi, and M. Giudici. “Dynamics of Localized Structures in Systems with Broken Parity Symmetry”. *Physical Review Letters* 116.13 (Mar. 2016). DOI: 10.1103/PhysRevLett.116.133901.
 - [129] W. D. Phillips. “Nobel Lecture: Laser Cooling and Trapping of Neutral Atoms”. *Reviews of Modern Physics* 70.3 (July 1998), pp. 721–741. DOI: 10.1103/RevModPhys.70.721.
 - [130] A. Coillet, I. Balakireva, R. Henriët, K. Saleh, L. Larger, J. M. Dudley, C. R. Menyuk, and Y. K. Chembo. “Azimuthal Turing Patterns, Bright and Dark Cavity Solitons in Kerr Combs Generated With Whispering-Gallery-Mode Resonators”. *IEEE Photonics Journal* 5.4 (Aug. 2013), pp. 6100409–6100409. DOI: 10.1109/JPHOT.2013.2277882.
 - [131] V. E. Lobanov, G. Lihachev, T. J. Kippenberg, and M. L. Gorodetsky. “Frequency Combs and Platicons in Optical Microresonators with Normal GVD”. *Optics Express* 23.6 (Mar. 2015), pp. 7713–7721. DOI: 10.1364/OE.23.007713.
 - [132] P. Parra-Rivas, E. Knobloch, D. Gomila, and L. Gelens. “Dark Solitons in the Lugiato-Lefever Equation with Normal Dispersion”. *Physical Review A* 93.6 (June 2016), p. 063839. DOI: 10.1103/PhysRevA.93.063839.
 - [133] X. Xue, Y. Xuan, Y. Liu, P.-H. Wang, S. Chen, J. Wang, D. E. Leaird, M. Qi, and A. M. Weiner. “Mode-Locked Dark Pulse Kerr Combs in Normal-Dispersion Microresonators”. *Nature Photonics* 9.9 (Sept. 2015), pp. 594–600. DOI: 10.1038/nphoton.2015.137.
 - [134] X. Xue, Y. Xuan, P.-H. Wang, Y. Liu, D. E. Leaird, M. Qi, and A. M. Weiner. “Normal-Dispersion Microcombs Enabled by Controllable Mode Interactions”. *Laser & Photonics Reviews* 9.4 (2015), pp. L23–L28. DOI: 10.1002/lpor.201500107.
 - [135] Ó. B. Helgason, F. R. Arteaga-Sierra, Z. Ye, K. Twayana, P. A. Andrekson, M. Karlsson, J. Schröder, and Victor Torres-Company. “Dissipative Solitons in Photonic Molecules”. *Nature Photonics* 15.4 (Apr. 2021), pp. 305–310. DOI: 10.1038/s41566-020-00757-9.
 - [136] P. K. A. Wai, C. R. Menyuk, H. H. Chen, and Y. C. Lee. “Soliton at the Zero-Group-Dispersion Wavelength of a Single-Model Fiber”. *Optics Letters* 12.8 (Aug. 1987), pp. 628–630. DOI: 10.1364/OL.12.000628.

Bibliography

- [137] P. K. A. Wai, H. H. Chen, and Y. C. Lee. “Radiations by “solitons” at the Zero Group-Dispersion Wavelength of Single-Mode Optical Fibers”. *Physical Review A* 41.1 (Jan. 1990), pp. 426–439. DOI: 10.1103/PhysRevA.41.426.
- [138] S. Coen, H. G. Randle, T. Sylvestre, and M. Erkintalo. “Modeling of Octave-Spanning Kerr Frequency Combs Using a Generalized Mean-Field Lugiato–Lefever Model”. *Optics Letters* 38.1 (Jan. 2013), pp. 37–39. DOI: 10.1364/OL.38.000037.
- [139] N. N. Rozanov, V. E. Semenov, and G. V. Khodova. “Transverse Structure of a Field in Nonlinear Bistable Interferometers. I. Switching Waves and Steady-State Profiles”. *Soviet Journal of Quantum Electronics* 12.2 (1982), p. 193. DOI: 10.1070/QE1982v012n02ABEH005474.
- [140] I. Ganne, G. Sleky, I. Sagnes, and R. Kuszelewicz. “Optical Switching Waves in III-V Semiconductor Microresonators”. *Physical Review B* 63.7 (Feb. 2001), p. 075318. DOI: 10.1103/PhysRevB.63.075318.
- [141] H. Wang et al. “Self-Regulating Soliton Switching Waves in Microresonators”. *Physical Review A* 106.5 (Nov. 2022), p. 053508. DOI: 10.1103/PhysRevA.106.053508.
- [142] V. E. Lobanov, G. Lihachev, and M. L. Gorodetsky. “Generation of Platicons and Frequency Combs in Optical Microresonators with Normal GVD by Modulated Pump”. *EPL (Europhysics Letters)* 112.5 (2015), p. 54008. DOI: 10.1209/0295-5075/112/54008.
- [143] P. Parra-Rivas, D. Gomila, and L. Gelens. “Coexistence of Stable Dark- and Bright-Soliton Kerr Combs in Normal-Dispersion Resonators”. *Physical Review A* 95.5 (May 2017), p. 053863. DOI: 10.1103/PhysRevA.95.053863.
- [144] Z. Li, Z. Li, Y. Xu, Y. Xu, S. Coen, S. Coen, S. G. Murdoch, S. G. Murdoch, M. Erkintalo, and M. Erkintalo. “Experimental Observations of Bright Dissipative Cavity Solitons and Their Collapsed Snaking in a Kerr Resonator with Normal Dispersion Driving”. *Optica* 7.9 (Sept. 2020), pp. 1195–1203. DOI: 10.1364/OPTICA.400646.
- [145] M. H. Anderson, W. Weng, G. Lihachev, A. Tikan, J. Liu, and T. J. Kippenberg. “Zero Dispersion Kerr Solitons in Optical Microresonators”. *Nature Communications* 13.1 (Aug. 2022), p. 4764. DOI: 10.1038/s41467-022-31916-x.
- [146] V. E. Lobanov, N. M. Kondratiev, A. E. Shitikov, R. R. Galiev, and I. A. Bilenko. “Generation and Dynamics of Solitonic Pulses Due to Pump Amplitude Modulation at Normal Group-Velocity Dispersion”. *Physical Review A* 100.1 (July 2019), p. 013807. DOI: 10.1103/PhysRevA.100.013807.
- [147] J. H. Talla Mbé, C. Milián, and Y. K. Chembo. “Existence and Switching Behavior of Bright and Dark Kerr Solitons in Whispering-Gallery Mode Resonators with Zero Group-Velocity Dispersion”. *The European Physical Journal D* 71.7 (July 2017), p. 196. DOI: 10.1140/epjd/e2017-80132-8.
- [148] C. Bao, H. Taheri, L. Zhang, A. Matsko, Y. Yan, P. Liao, L. Maleki, and A. E. Willner. “High-Order Dispersion in Kerr Comb Oscillators”. *JOSA B* 34.4 (Apr. 2017), pp. 715–725. DOI: 10.1364/JOSAB.34.000715.

-
- [149] J. H. T. Mbé and Y. K. Chembo. “Coexistence of Bright and Dark Cavity Solitons in Microresonators with Zero, Normal, and Anomalous Group-Velocity Dispersion: A Switching Wave Approach”. *JOSA B* 37.11 (Nov. 2020), A69–A74. DOI: 10.1364/JOSAB.396610.
- [150] H. Liu, S.-W. Huang, J. Yang, M. Yu, D.-L. Kwong, and C. W. Wong. “Bright Square Pulse Generation by Pump Modulation in a Normal GVD Microresonator”. In: *2017 Conference on Lasers and Electro-Optics (CLEO)*. May 2017, pp. 1–1.
- [151] H. Liu, S.-W. Huang, W. Wang, J. Yang, M. Yu, D.-L. Kwong, P. Colman, and C. W. Wong. “Stimulated Generation of Deterministic Platicon Frequency Microcombs”. *Photonics Research* 10.8 (Aug. 2022), pp. 1877–1885. DOI: 10.1364/PRJ.459403.
- [152] G. Lihachev et al. “Platicon Microcomb Generation Using Laser Self-Injection Locking”. *Nature Communications* 13.1 (Apr. 2022), p. 1771. DOI: 10.1038/s41467-022-29431-0.
- [153] M. H. P. Pfeiffer, C. Herkommer, J. Liu, H. Guo, M. Karpov, E. Lucas, M. Zervas, and T. J. Kippenberg. “Octave-Spanning Dissipative Kerr Soliton Frequency Combs in Si_3N_4 Microresonators”. *Optica* 4.7 (July 2017), pp. 684–691. DOI: 10.1364/OPTICA.4.000684.
- [154] S. Kelly. “Characteristic Sideband Instability of Periodically Amplified Average Soliton”. *Electronics Letters* 28.8 (Apr. 1992), pp. 806–807. DOI: 10.1049/el:19920508.
- [155] D. D. Hickstein, G. C. Kerber, D. R. Carlson, L. Chang, D. Westly, K. Srinivasan, A. Kowligy, J. E. Bowers, S. A. Diddams, and S. B. Papp. “Quasi-Phase-Matched Supercontinuum Generation in Photonic Waveguides”. *Physical Review Letters* 120.5 (Feb. 2018), p. 053903. DOI: 10.1103/PhysRevLett.120.053903.
- [156] A. Kordts, M. H. P. Pfeiffer, H. Guo, V. Brasch, and T. J. Kippenberg. “Higher Order Mode Suppression in High-Q Anomalous Dispersion SiN Microresonators for Temporal Dissipative Kerr Soliton Formation”. *Optics Letters* 41.3 (Feb. 2016), pp. 452–455. DOI: 10.1364/OL.41.000452.
- [157] S.-W. Huang, A. K. Vinod, J. Yang, M. Yu, D.-L. Kwong, and C. W. Wong. “Quasi-Phase-Matched Multispectral Kerr Frequency Comb”. *Optics Letters* 42.11 (June 2017), pp. 2110–2113. DOI: 10.1364/OL.42.002110.
- [158] K. Luo, Y. Xu, M. Erkintalo, and S. G. Murdoch. “Resonant Radiation in Synchronously Pumped Passive Kerr Cavities”. *Optics Letters* 40.3 (Feb. 2015), pp. 427–430. DOI: 10.1364/OL.40.000427.
- [159] A. U. Nielsen, B. Garbin, S. Coen, S. G. Murdoch, and M. Erkintalo. “Invited Article: Emission of Intense Resonant Radiation by Dispersion-Managed Kerr Cavity Solitons”. *APL Photonics* 3.12 (Dec. 2018), p. 120804. DOI: 10.1063/1.5060123.
- [160] A. S. Raja et al. “Electrically Pumped Photonic Integrated Soliton Microcomb”. *Nature Communications* 10.1 (Feb. 2019), p. 680. DOI: 10.1038/s41467-019-08498-2.
- [161] B. Stern, X. Ji, Y. Okawachi, A. L. Gaeta, and M. Lipson. “Battery-Operated Integrated Frequency Comb Generator”. *Nature* 562.7727 (Oct. 2018), p. 401. DOI: 10.1038/s41586-018-0598-9.

Bibliography

- [162] G. Moille, E. F. Perez, J. R. Stone, A. Rao, X. Lu, T. S. Rahman, Y. K. Chembo, and K. Srinivasan. “Ultra-Broadband Kerr Microcomb through Soliton Spectral Translation”. *Nature Communications* 12.1 (Dec. 2021), p. 7275. DOI: 10.1038/s41467-021-27469-0.
- [163] S.-P. Yu, D. C. Cole, H. Jung, G. T. Moille, K. Srinivasan, and S. B. Papp. “Spontaneous Pulse Formation in Edgeless Photonic Crystal Resonators”. *Nature Photonics* 15.6 (June 2021), pp. 461–467. DOI: 10.1038/s41566-021-00800-3.
- [164] W. Zhao, C. Yang, and M. Shen. “Enhanced Kelly Sidebands of Mode-Locking Fiber Lasers for Efficient Terahertz Signal Generation”. *Optics & Laser Technology* 137 (May 2021), p. 106802. DOI: 10.1016/j.optlastec.2020.106802.
- [165] C. Wang et al. “High Energy and Low Noise Soliton Fiber Laser Comb Based on Non-linear Merging of Kelly Sidebands”. *Optics Express* 30.13 (June 2022), p. 23556. DOI: 10.1364/OE.460609.
- [166] T. B. Benjamin and F. Ursell. “The Stability of the Plane Free Surface of a Liquid in Vertical Periodic Motion”. *Proceedings of the Royal Society of London. Series A. Mathematical and Physical Sciences* 225.1163 (Sept. 1954), pp. 505–515. DOI: 10.1098/rspa.1954.0218.
- [167] K. Staliunas, C. Hang, and V. V. Konotop. “Parametric Patterns in Optical Fiber Ring Nonlinear Resonators”. *Physical Review A* 88.2 (Aug. 2013), p. 023846. DOI: 10.1103/PhysRevA.88.023846.
- [168] A. Mussot, M. Conforti, S. Trillo, F. Copie, and A. Kudlinski. “Modulation Instability in Dispersion Oscillating Fibers”. *Advances in Optics and Photonics* 10.1 (Mar. 2018), pp. 1–42. DOI: 10.1364/AOP.10.000001.
- [169] F. Bessin, F. Copie, M. Conforti, A. Kudlinski, A. Mussot, and S. Trillo. “Real-Time Characterization of Period-Doubling Dynamics in Uniform and Dispersion Oscillating Fiber Ring Cavities”. *Physical Review X* 9.4 (Nov. 2019), p. 041030. DOI: 10.1103/PhysRevX.9.041030.
- [170] F. Copie, M. Conforti, A. Kudlinski, A. Mussot, and S. Trillo. “Competing Turing and Faraday Instabilities in Longitudinally Modulated Passive Resonators”. *Physical Review Letters* 116.14 (Apr. 2016). DOI: 10.1103/PhysRevLett.116.143901.
- [171] J. Yang, S.-W. Huang, Z. Xie, M. Yu, D.-L. Kwong, and C. W. Wong. “Coherent Satellites in Multispectral Regenerative Frequency Microcombs”. *Communications Physics* 3.1 (Jan. 2020), pp. 1–9. DOI: 10.1038/s42005-019-0274-x.
- [172] C.-X. Zhu, W. Yi, G.-C. Guo, and Z.-W. Zhou. “Parametric Resonance of a Bose-Einstein Condensate in a Ring Trap with Periodically Driven Interactions”. *Physical Review A* 99.2 (Feb. 2019), p. 023619. DOI: 10.1103/PhysRevA.99.023619.
- [173] M. J. Ablowitz and J. T. Cole. “Transverse Instability of Rogue Waves”. *Physical Review Letters* 127.10 (Sept. 2021), p. 104101. DOI: 10.1103/PhysRevLett.127.104101.
- [174] V. E. Zakharov and A. M. Rubenchik. “Instability of Waveguides and Solitons in Nonlinear Media”. *Journal of Experimental and Theoretical Physics* 38.3 (1974), p. 794.

-
- [175] K. P. Leisman, D. Zhou, J. W. Banks, G. Kovačič, and D. Cai. “Effective Dispersion in the Focusing Nonlinear Schrödinger Equation”. *Physical Review E* 100.2 (Aug. 2019), p. 022215. DOI: 10.1103/PhysRevE.100.022215.
 - [176] Y. K. Chembo, I. S. Grudinin, and N. Yu. “Spatiotemporal Dynamics of Kerr-Raman Optical Frequency Combs”. *Physical Review A* 92.4 (Oct. 2015), p. 043818. DOI: 10.1103/PhysRevA.92.043818.
 - [177] J. Liu, G. Huang, R. N. Wang, J. He, A. S. Raja, T. Liu, N. J. Engelsen, and T. J. Kippenberg. “High-Yield, Wafer-Scale Fabrication of Ultralow-Loss, Dispersion-Engineered Silicon Nitride Photonic Circuits”. *Nature Communications* 12.1 (Apr. 2021), p. 2236. DOI: 10.1038/s41467-021-21973-z.
 - [178] S.-W. Huang, H. Liu, J. Yang, M. Yu, D.-L. Kwong, and C. W. Wong. “Smooth and Flat Phase-Locked Kerr Frequency Comb Generation by Higher Order Mode Suppression”. *Scientific Reports* 6.1 (May 2016), p. 26255. DOI: 10.1038/srep26255.
 - [179] Y. Xu et al. “Frequency Comb Generation in a Pulse-Pumped Normal Dispersion Kerr Mini-Resonator”. *Optics Letters* 46.3 (Feb. 2021), pp. 512–515. DOI: 10.1364/OL.413585.
 - [180] M. L. Davenport, S. Liu, and J. E. Bowers. “Integrated Heterogeneous Silicon/III-V Mode-Locked Lasers”. *Photonics Research* 6.5 (May 2018), pp. 468–478. DOI: 10.1364/PRJ.6.000468.
 - [181] P. J. Delfyett, A. Klee, K. Bagnell, P. Juodawlkis, J. Plant, and A. Zaman. “Exploring the Limits of Semiconductor-Laser-Based Optical Frequency Combs”. *Applied Optics* 58.13 (May 2019), pp. D39–D49. DOI: 10.1364/AO.58.000D39.
 - [182] G. F. R. Chen, J. R. Ong, T. Y. L. Ang, S. T. Lim, C. E. Png, and D. T. H. Tan. “Broadband Silicon-On-Insulator Directional Couplers Using a Combination of Straight and Curved Waveguide Sections”. *Scientific Reports* 7.1 (Dec. 2017). DOI: 10.1038/s41598-017-07618-6.
 - [183] B. Y. Kim, Y. Okawachi, J. K. Jang, M. Yu, X. Ji, Y. Zhao, C. Joshi, M. Lipson, and A. L. Gaeta. “Turn-Key, High-Efficiency Kerr Comb Source”. *Optics Letters* 44.18 (Sept. 2019), pp. 4475–4478. DOI: 10.1364/OL.44.004475.
 - [184] I. Coddington, N. Newbury, and W. Swann. “Dual-Comb Spectroscopy”. *Optica* 3.4 (Apr. 2016), pp. 414–426. DOI: 10.1364/OPTICA.3.000414.
 - [185] T. Hansson, D. Modotto, and S. Wabnitz. “On the Numerical Simulation of Kerr Frequency Combs Using Coupled Mode Equations”. *Optics Communications* 312 (Feb. 2014), pp. 134–136. DOI: 10.1016/j.optcom.2013.09.017.
 - [186] J. Hult. “A Fourth-Order Runge–Kutta in the Interaction Picture Method for Simulating Supercontinuum Generation in Optical Fibers”. *Journal of Lightwave Technology* 25.12 (Dec. 2007), pp. 3770–3775. DOI: 10.1109/JLT.2007.909373.
 - [187] J. Travers. *SCGBookCode*. Feb. 2023.

Bibliography

- [188] H. Guo, E. Lucas, M. H. P. Pfeiffer, M. Karpov, M. Anderson, J. Liu, M. Geiselmann, J. D. Jost, and T. J. Kippenberg. “Intermode Breather Solitons in Optical Microresonators”. *Physical Review X* 7.4 (Dec. 2017), p. 041055. DOI: 10.1103/PhysRevX.7.041055.
- [189] S.-P. Yu, E. Lucas, J. Zang, and S. B. Papp. “A Continuum of Bright and Dark-Pulse States in a Photonic-Crystal Resonator”. *Nature Communications* 13.1 (June 2022), p. 3134. DOI: 10.1038/s41467-022-30774-x.
- [190] M. H. Anderson, A. Tikan, A. Tusnin, J. Riemensberger, A. Davydova, R. N. Wang, and T. J. Kippenberg. “Dissipative Solitons and Switching Waves in Dispersion-Modulated Kerr Cavities”. *Physical Review X* 13.1 (Mar. 2023), p. 011040. DOI: 10.1103/PhysRevX.13.011040.
- [191] M. Anderson, R. Bouchand, J. Liu, W. Weng, E. Obrzud, T. Herr, and T. Kippenberg. “Supplementary Document for Photonic Chip-Based Resonant Supercontinuum - 4930365.Pdf” (May 2021). DOI: 10.6084/m9.figshare.14428871.v2.
- [192] J. M. Dudley, G. Genty, and S. Coen. “Supercontinuum Generation in Photonic Crystal Fiber”. *Reviews of Modern Physics* 78.4 (Oct. 2006), pp. 1135–1184. DOI: 10.1103/RevModPhys.78.1135.

Contact

miles.anderson@epfl.ch

www.linkedin.com/in/miles-anderson-829370105 (LinkedIn)
people.epfl.ch/miles.anderson (Company)

Top Skills

Research

Physics

Matlab

Honors-Awards

Faculty of Science Masters Award

Summer Research Scholarship

First in Course Award: Physics 340
Electronics and Signal Processing

First in Course Award: Physics 726
Optoelectronics

Scholarship Calculus

Publications

Coexistence of Multiple Nonlinear States in a Tristable Passive Kerr Resonator

Photonic chip-based resonant supercontinuum via pulse-driven Kerr microresonator solitons

Observations of spatiotemporal instabilities of temporal cavity solitons.

Zero-dispersion Kerr solitons in optical microresonators

Integrated gallium phosphide nonlinear photonics

Miles Anderson

Doctoral Assitant at EPFL (École polytechnique fédérale de Lausanne)

Lausanne, Vaud, Switzerland

Summary

PhD Worker in nonlinear optics and photonics. In particular: microchip-based frequency comb laser generation, and the formation of fundamental dissipative optical structures.

Simulation, design, experiment, theory. I enjoy presenting and teaching.

Next to physics, I'm also interested in history and philosophy.

Experience

EPFL (École polytechnique fédérale de Lausanne)

6 years 7 months

Doctoral Assistant

March 2017 - March 2023 (6 years 1 month)

Lausanne Area, Switzerland

Investigation of cavity soliton phenomena, Kerr frequency-comb generation, and applications in crystalline or photonic chip-microresonators.

Intern

September 2016 - March 2017 (7 months)

Lausanne Area, Switzerland

The University of Auckland

3 years 3 months

Research Assistant

April 2016 - September 2016 (6 months)

Experiments and simulations into the dynamics of optical, passively driven nonlinear cavities.

Graduate Teaching Assistant

July 2013 - September 2016 (3 years 3 months)

229

Running tutorials and lab experiments for Stage I physics students, including marking reports.

Currently a supervisor and examiner for the Stage II-III physics labs. Have also been involved in updating and testing new student experiments.

Masters Student

March 2015 - March 2016 (1 year 1 month)

See education section.

Summer Research Student

December 2013 - March 2014 (4 months)

Construction and characterisation of a high-power ytterbium fibre-optic amplifier for use with an ultra-fast pulsed 1030nm source, and replicating research on Stimulated Brillouin-Scattering in optical fibres.

Kotahi Logistics LP Ltd

Vessels Booking Coordinator

December 2011 - June 2012 (7 months)

Booking Fonterra dairy product containers on outgoing sea vessels according to an optimised freight plan.

Education

University of Auckland

Master's Degree, Nonlinear Optics · (2015 - 2016)

University of Auckland

Bachelor's Degree, Engineering Physics/Applied Physics · (2011 - 2014)

Rangitoto College

High School · (2006 - 2010)